Vanadium interaction with FCC catalysts

Thesis

Vanadium Interaction with FCC Catalysts

A Thesis Presented to The Open University

for the Degree of Doctor of Philosophy

James Stanley Sarginson, B.Sc. (Chem.)

Department of Chemistry

The Open University

June, 1997

EX12

RESEARCH DEGREES CENTRE

LIBRARY AUTHORISATION FORM

Please return this form to the The Research Degrees Centre with the two bound copies of your thesis to be deposited with the University Library.
All students should complete Part 1. Part 2 only applies to PhD students.

Student: JAMES STANLEY SARGINSON PI: H7164579

Degree: PhD

Thesis title: VANADIUM INTERACTION WITH FCC CATALYSTS

Part 1 Open University Library Authorisation [to be completed by all students]

I confirm that I am willing for my thesis to be made available to readers by the Open University Library, and that it may be photocopied, subject to the discretion of the Librarian.

Signed: J.S. Sarginson Date: 25/2/98

Part 2 British Library Authorisation [to be completed by PhD students only]

If you want a copy of your PhD thesis to be available on loan to the British Library Thesis Service as and when it is requested, you must sign a British Library Doctoral Thesis Agreement Form. Please return it to the Research Degrees Centre with this form. The British Library will publicise the details of your thesis and may request a copy on loan from the University Library. Information on the presentation of the thesis is given in the Agreement Form.

The University has agreed that your participation in the British Library Thesis Service should be voluntary. Please tick either (a) or (b) to indicate your intentions.

[a] ☑ I am willing for the Open University to loan the British Library a copy of my thesis.
A signed Agreement Form is attached.

[b] ☐ I do not wish the Open University to loan the British Library a copy of my thesis.

Signed: J.S. Sarginson Date: 25/2/98

I wish to dedicate this thesis to

the memory of my parents

Abstract

Fluidised cracking catalysts, which contain a form of zeolite-Y as the main catalytically active component, are widely used commercially for the conversion of crude oil into more profitable product streams. During the cracking reaction, these catalysts are contaminated with vanadium which has a marked effect on the crystallinity of the zeolite-Y component and, as a consequence, activity and selectivity for hydrocarbon processing is degraded. The purpose of this work has been to carry out a detailed investigation, on the laboratory scale, of the effect of vanadium contamination on both commercial and model rare earth ion-exchanged zeolite-Y catalysts. Vanadium contamination was achieved using a standard (Mitchell) method and catalysts were subject to treatment conditions similar to those found in the regenerator part of a fluidised catalytic cracking unit using a specially constructed furnace. Investigations of the solid state chemical reactions between vanadium and rare earth compounds, both in the presence and absence of silica and alumina support materials typical of those found in commercial catalysts, extend the study. Extensive use is made of magic-angle-spinning nuclear magnetic resonance spectroscopy (^{51}V and ^{27}Al), X-ray powder diffraction and surface area measurements for sample characterisation. The apparatus for surface area measurements was constructed during the course of the work.

It is suggested that the reduction in crystallinity of rare earth ion-exchanged zeolite-Y in the presence of vanadium is associated with the removal of rare earth ions from the cage structure of the zeolite. The extent of this process depends upon the details of the treatment conditions and important factors are identified. The observation of the formation of $LaVO_4$ in a range of hydrothermally treated lanthanum ion-exchanged zeolite-Y samples supports the proposed model.

Acknowledgements

I am especially grateful to my supervisor, Dr. Michael Mortimer, for his academic guidance in this work and his encouragement throughout these studies. I must also thank Dr. Nick Gudde of B.P. Oil International for his help and advice during the work and for making my visits to Sunbury so informative and enjoyable. I gained a great deal from experiencing work in a industrial laboratory environment and all of the staff were more than helpful.

EPSRC and B.P. Oil International are thanked for financial assistance in the form of a case award.

Finally, I would like to thank Professor F.T. Berry for the use of the facilities of the Chemistry Department and also a special thank you to the technical staff of the Department without whose help my studies would not have run as smoothly as they did.

Contents

Chapter 1

Introduction

1 Introduction

The chemistry of zeolite-Y in the presence of vanadium has been investigated under a number of different reaction conditions. Zeolite-Y is used by the petroleum industry for the conversion of oil fractions into more profitable product streams and it is the main catalytic component of the composite catalyst (fluid cracking catalyst). It is during the main cracking reaction that the various components of the fluid cracking catalyst have vanadium, and other contaminants, deposited upon their surfaces. The main aim of this thesis is to investigate in detail the effect of the presence of vanadium on the zeolite-Y component of the catalyst. It is known that this metal causes a reduction in the level of zeolite-Y crystallinity and, on an industrial scale, if vanadium contamination was allowed to continue unchecked then complete loss of crystallinity would be the end result. As the petroleum industry is increasingly forced to convert poor quality crudes and heavier distilled fractions, where vanadium levels are greater, then the need for a more vanadium tolerant catalyst becomes essential. If an effective vanadium tolerant catalyst is to be designed then a better understanding of the mechanism by which vanadium interacts with zeolite-Y is required.

A variety of samples have been investigated in the present work. These include two types of zeolite-Y based sample: a commercial fluid cracking catalyst and zeolite-Y by itself as a model system. Rare earth vanadium chemistry has also been investigated in a series of solid state reactions as well as on the surfaces of different support materials (α-alumina and silica). A mechanism for the interaction of vanadium with rare earth (RE) stabilised zeolite-Y is proposed and supporting evidence is provided. It is suggested that the formation of lanthanum vanadium (V) oxide is intrinsically involved in the destruction of the lanthanum stabilised zeolite-Y.

The thesis is divided into a number of chapters. Chapter 2 provides a general overview, based on the current literature, of the vanadium/fluid cracking catalyst system. Details of the different components of the fluid cracking catalyst and the role they play within the composite catalyst are given. Particular attention is given to the zeolite-Y component of

the catalyst, together with the different forms of zeolite-Y that can be incorporated into the final fluid cracking catalyst. Current understanding of the interaction of vanadium with fluid cracking catalysts is reviewed, including details of how vanadium is deposited upon the catalyst, its location throughout the catalyst, suggested mechanisms of vanadium attack, and the efforts made to overcome the loss of zeolite-Y crystallinity in the presence of vanadium.

Three major techniques have been used for the characterisation of samples throughout the work. Magic-angle-spinning nuclear magnetic resonance spectroscopy (^{27}Al and ^{51}V) and X-ray diffraction have been extensively used, on all classes of sample, to monitor and identify new phases formed as a function of reaction conditions. Surface area measurements have been limited to samples which contain zeolite-Y and have been used to quantify the loss of zeolite-Y crystallinity. X-ray diffraction was used to investigate changes to the unit cell constant of the zeolite-Y based samples. Magic-angle-spinning nuclear magnetic resonance proved to be particularly useful since the identity of both amorphous compounds as well as crystalline compounds could be probed. A theoretical outline for all three techniques, together with details of the apparatus used, and experimental methods employed, is given in Chapter 3.

Chapter 4 gives details of the methods used for the preparation of all classes of sample studied throughout the course of the work. This includes the ion-exchange procedure for the model zeolite-Y based samples and the vanadium contamination procedure. A detailed account of the methods used to treat the samples is given including descriptions of the vertical tube furnace for the treatment of support based samples and the horizontal tube furnace arrangement for carrying out solid state reactions.

The results from the various classes of sample are extensively discussed in Chapter 5. Sections 5.1 to 5.3 describe the results from zeolite-Y based samples. A particularly important result is the observation that the amount of destruction caused to the zeolite-Y lattice, in the presence of vanadium, is dependent upon the rare earth ion-exchange level present within the sample. This observation, together with the detection of the presence of

lanthanum vanadium (V) oxide, is important in suggesting a mechanism for vanadium/zeolite-Y interaction (Section 5.2). Sections 5.4 and 5.5 discuss the results from experiments where the chemistry of vanadium with rare earths was investigated. A key feature of all these experiments was the observation of lanthanum vanadium (V) oxide for all different combinations of reactants under conditions which favoured the oxidation of vanadium.

The results presented in Chapter 5 are collated and discussed in terms of the overall aims of the project in Chapter 6.

Chapter 2

Literature Survey

2 Literature Survey

The introduction, by the petroleum industry, of zeolite-based cracking catalysts in the early 1960s for the conversion of crude oil into gasoline and light olefin products heralded a new era. Zeolite catalysts offered the petroleum industry better yields and selectivities for these products with no increase in coke yield.[1] Miale and co-workers[2] reported that modified zeolites are about 10 000 times more active for the conversion of *n*-hexane than amorphous silica-alumina. The scientific interest in these catalysts has continued to grow with the design and improvement of the next generation of fluidised cracking catalyst (FCC), both by refiners and catalysts manufactures, still of considerable commercial importance. The volume of published literature in the field is large. As a consequence the content of the present literature survey has been restricted to two specific areas. Firstly, to give a brief introduction to the commercial processes and the demands that these put on the zeolite catalyst, together with some of the improvements made by the industry to meet these demands. Secondly to give a more detailed account of the available open literature specific to the effect of vanadium on zeolite FCC operations. It is the zeolite-vanadium interaction that is the main focus of the present work, with a particular interest in the mechanism by which the vanadium reacts destructively with the zeolite causing collapse of the zeolite structure.

2.1 Introduction to Fluid Cracking Catalysis

This section provides an introduction to the form of the FCC, together with a description of its various components and the role they play within the catalyst as a whole. Emphasis is given to the main component of the FCC which is the zeolite. Details of the necessary physical properties of the FCC particle that make it an effective catalyst are also given.

Crude oil, and other distilled fractions, are converted into more useful products by FCCs within a fluidised catalytic cracking unit (FCCU). Figure 2.1 gives a simplified schematic diagram of a typical Esso-designed riser cracker.[3]

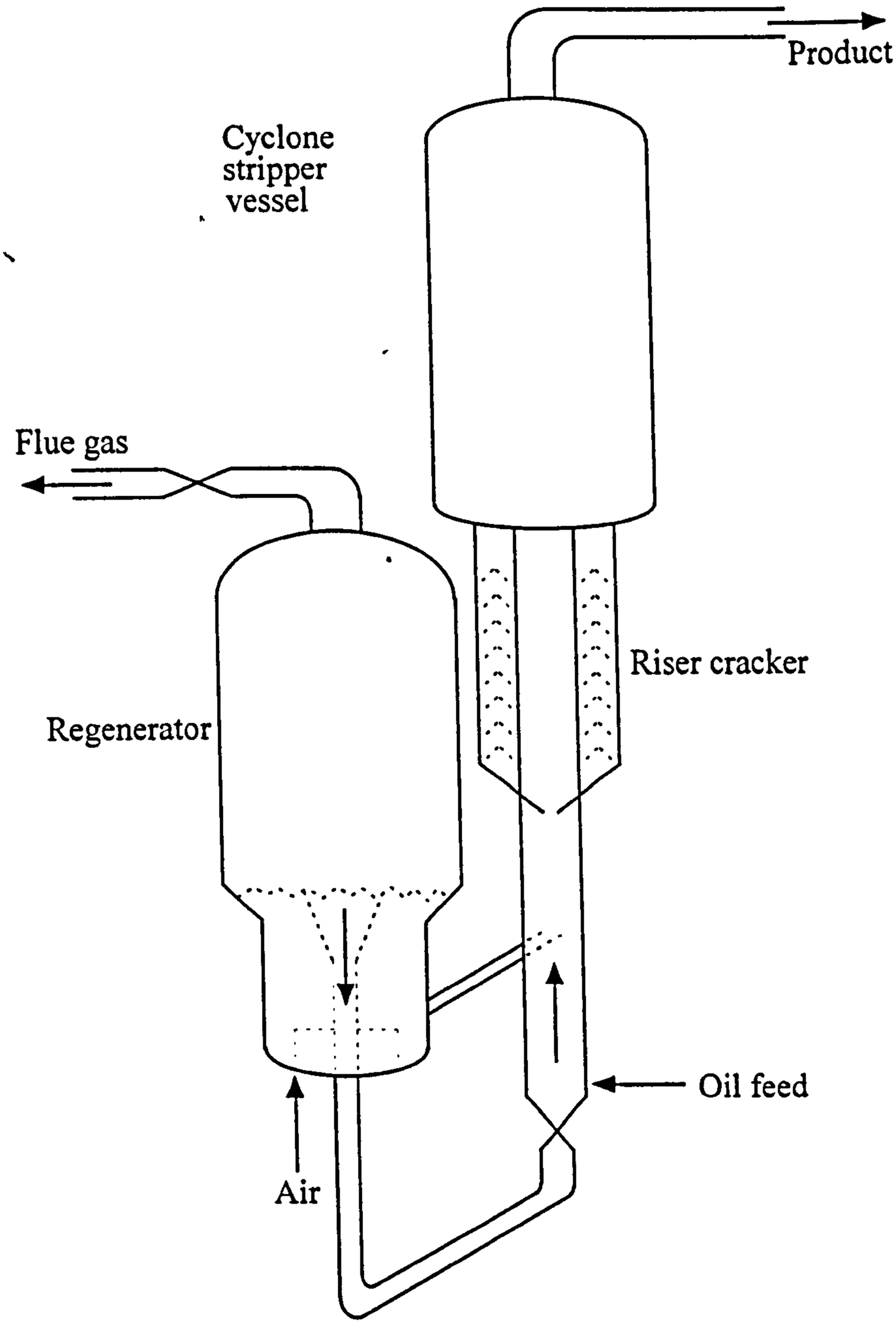

Figure 2.1 Schematic diagram of an Esso-designed riser cracker.

Most modern FCCUs are composed of two major components, a riser cracker and a regenerator. Within the riser cracker, the catalyst and oil fractions are mixed and it is here that the cracking chemistry occurs. Within the regenerator, the catalyst is hydrothermally treated to remove the coke deposited on the surface of the catalyst during the cracking reaction. Riser cracker conditions are reducing and generally maintained in the temperature range 500-600°C; regenerator conditions are oxidising and temperatures are typically in the range 700-800°C. Details of an FCCU cycle will be discussed later in this section.

Fluidised cracking catalysts

An FCC is used by the petroleum industry for the conversion of crude oil into a more useful and profitable product stream. A wide variety of commercial FCCs are available and so general statements regarding their properties must be treated with caution. Any one commercial FCC can differ from another in a number of ways (for example, amount and type of zeolite present within the catalyst, type of matrix present and type of binder). However, it is fair to say that a 'typical' FCC is composed of two major components, a matrix and zeolite. These components are held together with a silicate and/or aluminate binder. A typical FCC would contain 10-20% zeolite, by mass, and the particle size of the composite catalyst would be approximately 60μm.

There are two major classes of FCC based on the porosity of the matrix within which the zeolite component is embedded.[1,3] The types of matrix are of (i) high porosity, such as amorphous silica/alumina and related gelled materials including semisynthetic clay, and (ii) low porosity, such as the naturally-occurring clays. The zeolite component is almost exclusively a synthetic zeolite-Y with the faujasite structure. The final form of zeolite-Y that is incorporated into a FCC can be of various types. The nature of these types is discussed in more detail in Section 2.1.1.

The most catalytically active component within an FCC is the zeolite-Y component. The zeolite-Y is so active that it is necessary to dilute its activity with other material so that as already indicated the zeolite concentration within FCCs is typically 10-20%, by mass.[3] The zeolite component ultimately determines the flow of products from the FCCU, but the matrix component of the FCC can also be catalytically active as will be described shortly. Zeolite/matrix combinations are specifically chosen to give the desired product stream. The zeolite chemistry is related to the complex pore structure and the nature, distribution and concentration of the active sites within the zeolite.[4,5] The mechanism of catalytic cracking is dominated by carbocation chemistry; these ions are formed on the acid sites of the cracking catalysts. Important carbocation reactions are cracking, hydrogen transfer and isomerisation. The final composition of the cracking products depends on the relative rates of the various competing reactions.

The matrix component of the FCC is generally catalytically active providing active sites for molecules that are too large to enter the pore structure of the zeolite. Once fragmented, these hydrocarbons can then gain access to the internal zeolite structure where selective hydrocarbon processing occurs. The choice of matrix depends greatly on the feed oil quality. For example, a feed which contains quantities of large hydrocarbons, such as the heavier distilled fractions, would need a matrix of large pore structure, as well as high surface area, for effective conversion to occur.

Figure 2.2 shows a simplified flow chart of a typical FCC preparation involving a silica/alumina, gel-based matrix.[3] Full details of the individual steps can be found in reference 3, although it can be noted that the acid neutralising conditions control the bulk pore structure in the finished catalyst. Alumina addition results in both the silicon and aluminium having tetrahedral co-ordination. This step is important since it determines the activity and stability of the amorphous silica/alumina catalyst. The spray dryer atomises an aqueous dispersion of the solid into a heated chamber (520-600°C), where the solids are converted, in seconds, into particles of ~60μm diameter. After spray drying, the particles are washed with hot ammonium salts to remove cations that are harmful to the catalyst, for example, Na^+. The final drying (280-360°C) stage serves two purposes: both the removal of water from the catalyst and the breakdown of ammonium ions liberating NH_3. The finished catalyst has ~12% volatile content which is mostly adsorbed water not liberated during the drying process.[3]

Catalyst particles within the FCCU experience a variety of physically and chemically hostile environments and all components of the FCC must be able to withstand these extremes. For example FCC particles are (i) continually held at elevated temperatures (typically 500-800°C) and so the different components must have high thermal stability; (ii) exposed to steam in the regenerator part of the FCCU so the particles must have high hydrothermal stability; and (iii) subject to many collisions with other catalysts particles, as well as with the reactor walls, so the particles require considerable mechanical strength (erosion of the particles to < 30μm can result in the loss of particles to the atmosphere[3]).

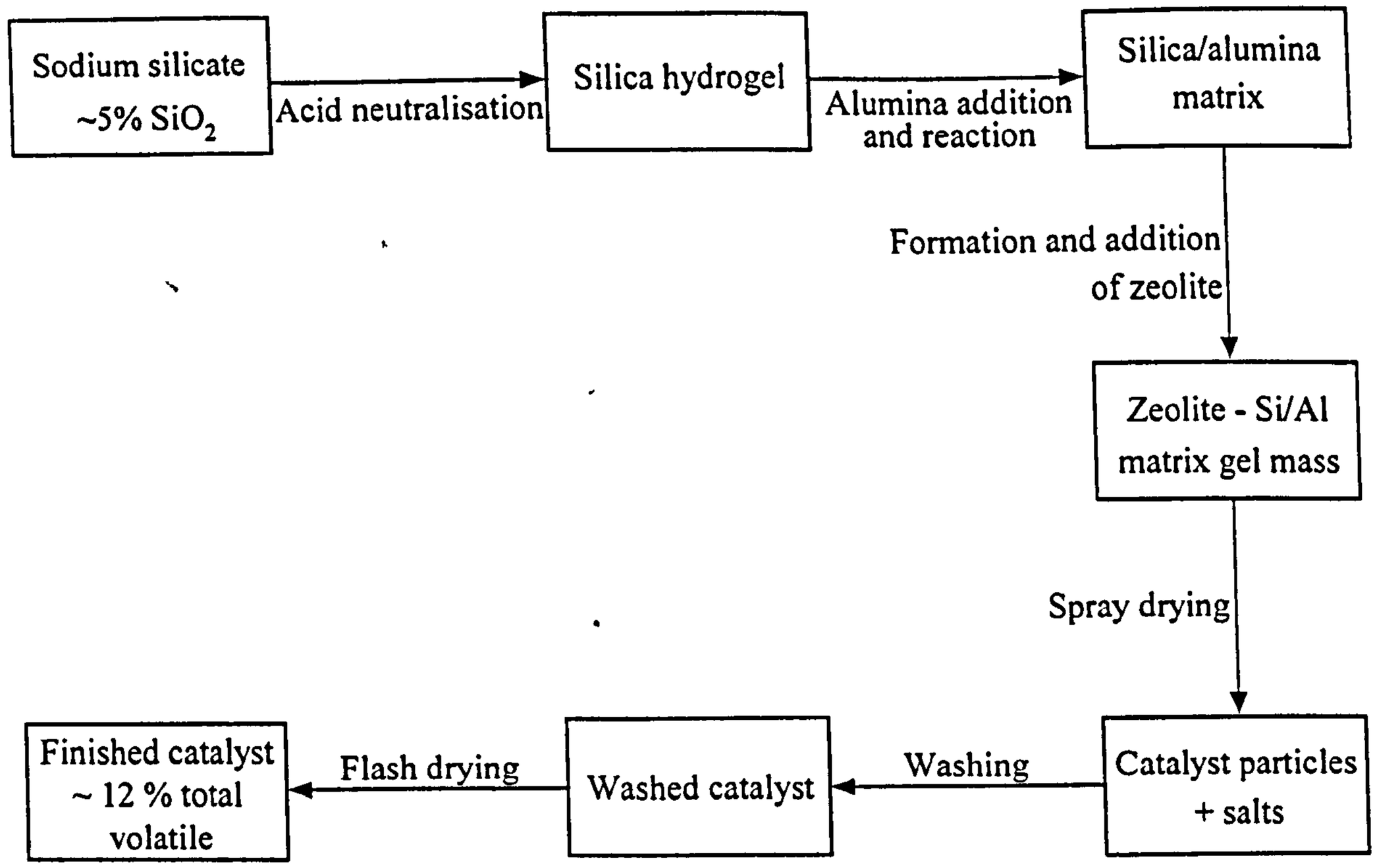

Figure 2.2 Simplified flow chart showing the preparation of a typical FCC involving a silica/alumina, gel-based matrix.

As already indicated (Figure 2.1) there are two major components to an FCCU: a riser cracker and regenerator. Within the riser cracker, where the atmosphere is reducing, the FCC particle is sprayed with hot crude oil at elevated temperatures (typically 500-600°C). This has the effect of forcing the particle upwards where it is continually colliding with other catalyst particles and the walls of the riser cracker. It is during the breakdown of the crude oil that the particle has vanadium and other contaminants deposited onto its surface (Section 2.2). During the cracking reaction the FCC becomes coated with coke, and other debris, and this limits its catalytic activity since these products effectively block fresh reactants from the surface of the FCC. To overcome this fouling catalyst particles are transferred to the regenerator where the coke is steam stripped hydrothermally at elevated temperatures (typically 700-800°C). When regenerated the catalyst particles are returned to the riser cracker for the start of another cycle. It is in the regenerator where the zeolite is placed under most risk of destruction due to the presence of metal contaminants, together with the oxidising steam/air atmosphere at elevated temperatures.

Before an FCC is used in an FCCU it is subject to an array of measurements and tests, relating to its physical and chemical properties. These include surface area, pore volume,

pore size distribution, density, attrition resistance, particle size distribution, thermal stability and hydrothermal stability. It is essential that, as far as possible, the performance of an FCC batch is known before it reaches the FCCU. Laboratory tests have been developed to meet this need.

When a catalyst is introduced into the FCCU it is known that certain physical properties will change, for example, a loss of surface area is observed. Catalysts that are working in an FCCU are referred to as 'equilibrium catalysts', since they are continually being used and regenerated. In order, therefore, to simulate the behaviour of an FCC within an FCCU it is necessary to deactivate fresh catalysts to the more realistic behaviour of equilibrium catalysts. This can be achieved by hydrothermally treating the samples at temperatures usually greater than that found normally in the FCCU.[6] Mitchell[6] found that deactivation treatments at higher temperatures than normally found in an FCCU gave catalysts with similar physical characteristics (unit cell constant, surface area etc.) to those that were obtained from working FCCUs. (Experimental details of the methods used in this work for the deactivation of samples are given in Chapter 4). Once deactivated, the catalyst activity and selectivity can be determined using a microactivity unit.[7,8] The microactivity test (MAT) gives a rapid and efficient method for the screening of catalysts and is widely used in industrial testing laboratories.[1]

2.1.1 Zeolite-Y and Modifications

The structure of zeolite-Y is described in this section and details are given of the various modifications that are used in FCCs. In particular an account of some of the advances and important structural and chemical considerations that have lead to the development of a modified form of zeolite-Y, for use in recent forms of FCC, will be given.

Structure and preparation of zeolite-Y

Zeolite-Y is a synthetic crystalline aluminosilicate with the faujasite structure.[9] As with all zeolites it consists of rings of tetrahedral units built up into a three-dimensional structure via oxygen bridges between the tetrahedral centres (Al or Si). More specifically the structure is based upon a secondary building unit, composed of linked 4- and 6-rings forming a truncated octahedron or sodalite unit (Figure 2.3(a)). These sodalite units, linked via oxygen bridges, through four of the eight 6-rings in a tetrahedral array, yield the framework structure of faujasite (Figure 2.3(b)). The sodalite unit building blocks can be said to be linked via hexagonal prisms. This can correspond to zeolite X or Y depending on the ratio of silicon to aluminium (Si/Al); zeolite-Y is silicon rich and so has a high Si/Al ratio typically greater than 2.5.

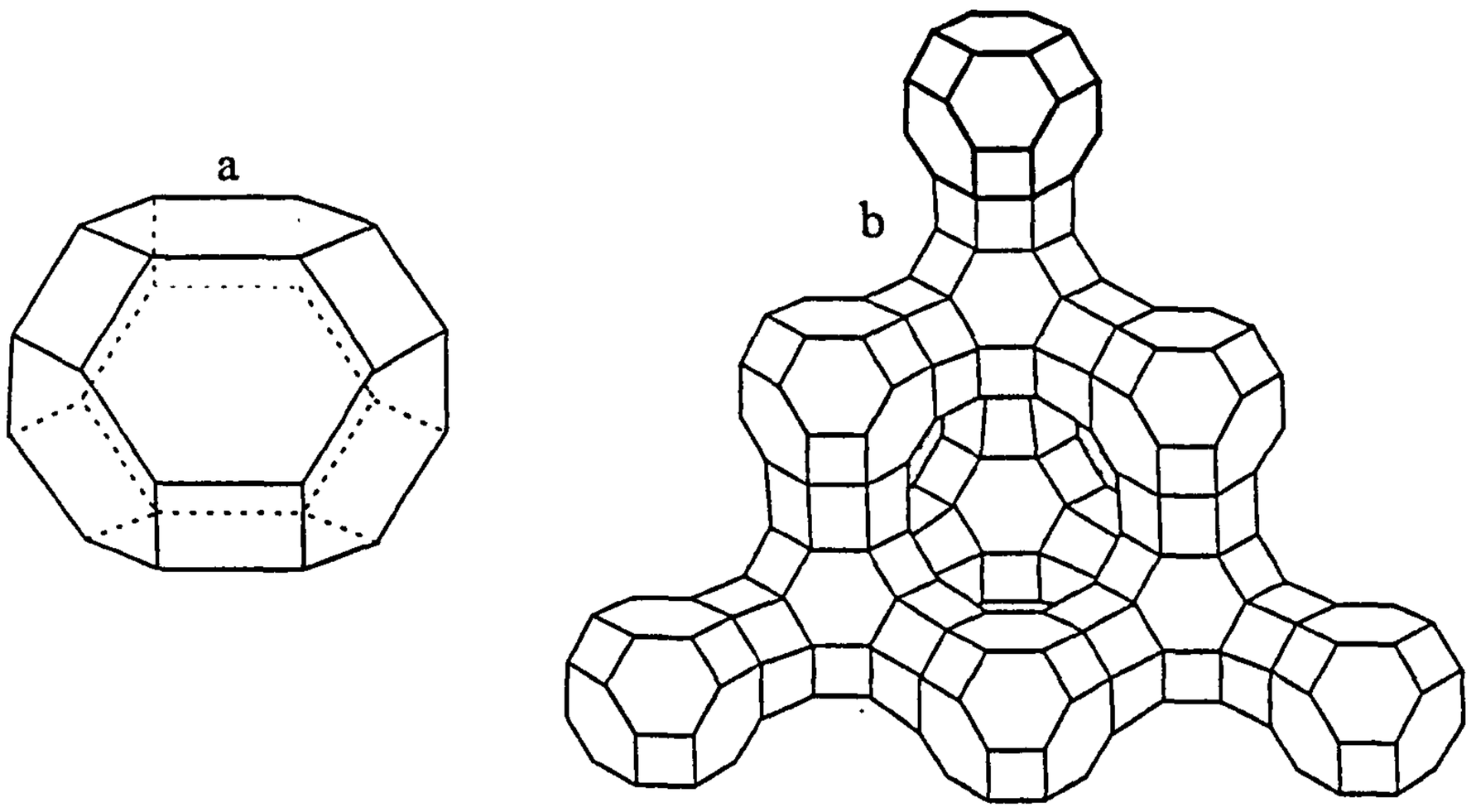

Figure 2.3 Schematic structures for (a) the sodalite unit building block and (b) the faujasite structure.

The faujasite framework is very open and encloses a system of large cages (known as supercages, with diameters of 1180 pm) linked by four windows of 12-rings to adjacent pores. Looking out from a supercage there are eighteen 4-rings, four 6-rings and four 12-rings, as indicated in Figure 2.3(b). Within the structure both silicon and aluminium are tetrahedrally co-ordinated to oxygens (Figure 2.4). Each aluminium substituted into an all silicon structure introduces a negative charge and so, therefore, the total negative charge on

the whole zeolite-Y lattice is dependent on the Si/Al ratio. The charge can be balanced by any number of cations, but commercially H^+, or rare earth (Ce^{4+}, La^{3+}) cations, are generally used.

The faujasite structure has a cubic unit cell which encloses 8 supercages, there are 192 T (Si or Al) atoms per unit cell and faujasite has the general formula

$$M^{y+}_{x/y}[(AlO_2)_x(SiO_2)_{192-x})].zH_2O$$

Values of x range from 74 to 96 for zeolite-X and from 48 to 74 for zeolite-Y.[4] The size of the unit cell constant is dependent upon the framework Si/Al ratio and reflects the different lengths of the Si-O and Al-O bonds. The Si-O bond length, which is 0.18 nm, is slightly smaller than the Al-O bond length, which is 0.19 nm. As a consequence as the Si/Al ratio increases (decreasing framework aluminium) the size of the unit cell constant decreases. This is shown graphically in Figure 2.5.

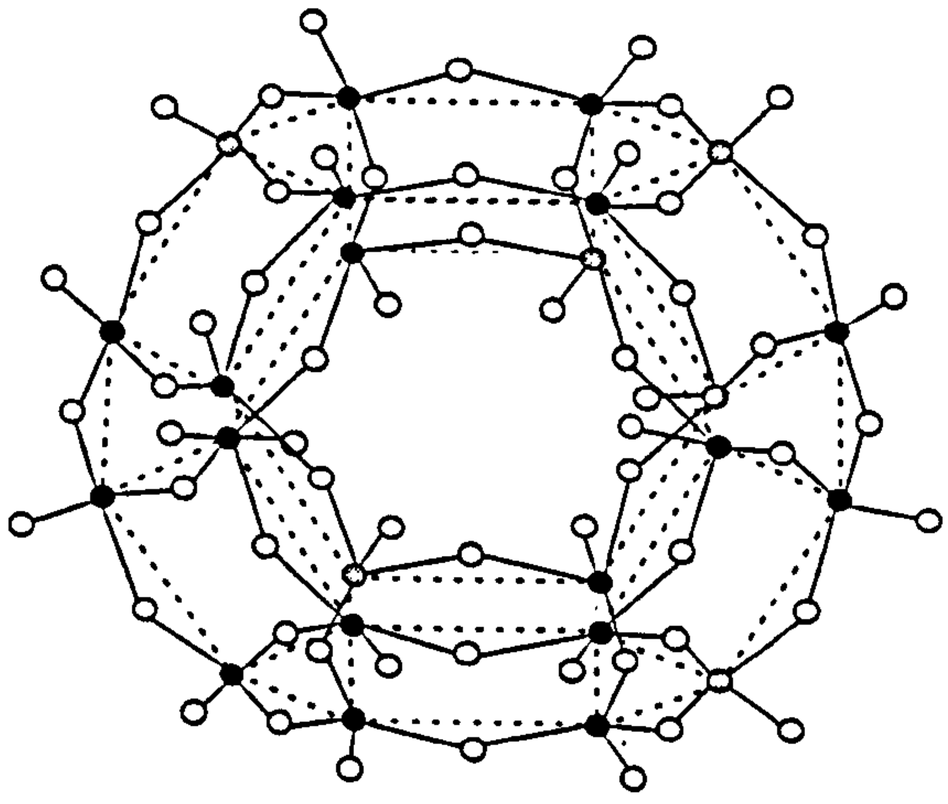

Figure 2.4 Diagram illustrating how silicon (●), aluminium (○) and oxygen (○) are arranged within a sodalite unit building block (illustrated by dotted lines). This sodalite unit will have associated with it a total negative charge of -6; this is due to the presence of six aluminium units.

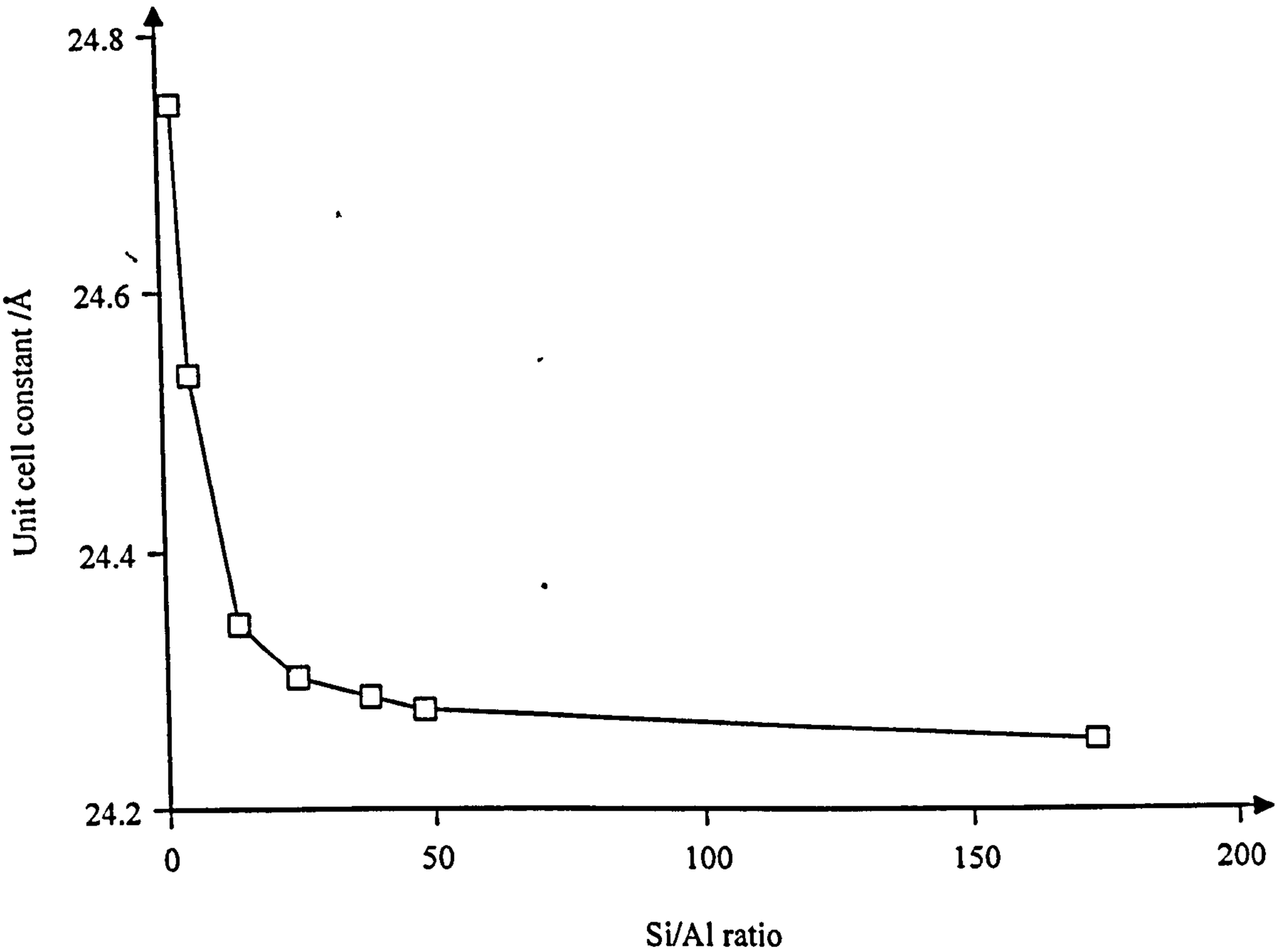

Figure 2.5 Graph illustrating the decrease in the unit cell constant as the framework Si/Al ratio increases, (data taken from reference 10).

Zeolite-Y is prepared by heating a mixture of silicate and aluminate solution near the boiling point of the mixture for several hours until crystallisation occurs.[1,11] Maher and co-workers[12] have shown that crystallisation time and product purity can be improved by seeding the mixture with zeolite precursors. Figure 2.6 shows a simplified flow chart for the production of zeolite-Y.

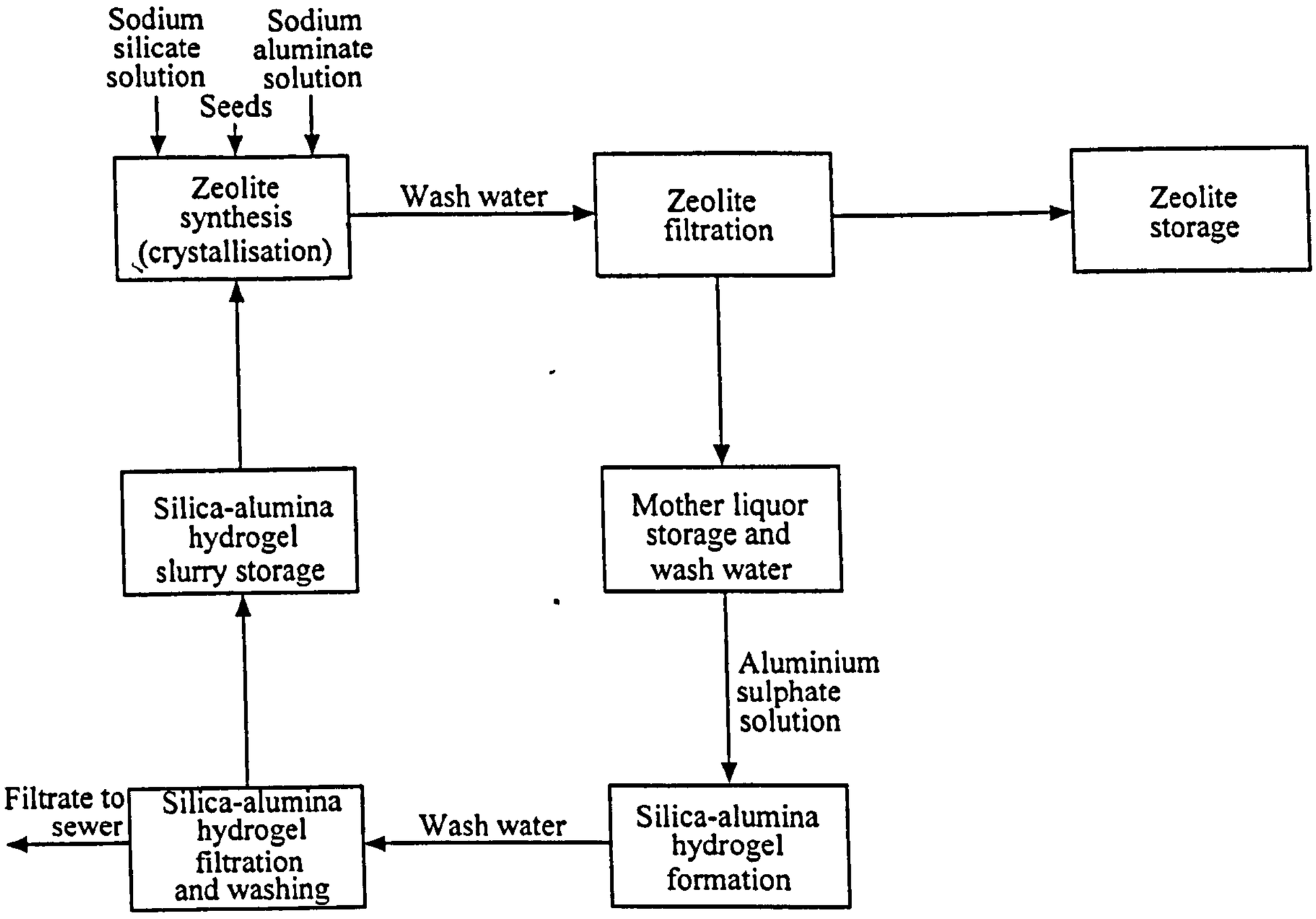

Figure 2.6 Flow chart showing the production of sodium exchanged zeolite-Y.[13]

Crystallisation times vary from 12-30 hours depending upon the synthesis mixture and the kind of hydrogel prepared. Reaction temperatures are in the range of 90-100°C.[13] This synthesis utilises the mother liquor, which is a weak solution of sodium silicate. Addition of aluminium sulphate solution forms a silica-alumina hydrogel, this is used as a starting material for the next synthesis.

The zeolite is usually prepared with sodium counter-ions balancing the net charge on the zeolite lattice; hence the common label Na-Y.

Ion-exchange: modifications, properties and structures

Na-Y is not thermally stable at typical FCCU conditions. Shiralkar and Kulkarni[14] reported Na-Y to be thermally stable up to 810°C; similar values have been reported by other workers.[15,16] The thermal stability can be greatly enhanced by ion-exchange with different counter-ions. This observation has led to a whole area of investigation into the

ion-exchange properties of Na-Y and the effect that different counter-ions have on the chemical properties, as well as the thermal and hydrothermal stabilities of the exchanged zeolite.[14-36] Some of these results, particularly those concerned with thermal and hydrothermal behaviour, and relevant to the present work, are outlined below.

Bremer and co-workers[20] reported three different and distinct types of thermal behaviour depending on cation with respect to Na-Y. These were (i) minimal stability at 20-40% exchange, (ii) continually increasing stability with increasing degree of exchange, and (iii) continually decreasing stability with increasing degree of exchange. An explanation of these results was put forward in terms of the relative distortions caused in the zeolite lattice by accommodating different counter-ions in non-lattice positions. For example, for case (i), of which Mg^{2+}, Ca^{2+}, Co^{2+}, Ni^{2+} and Zn^{2+} are examples, the decrease in thermal stability at exchanges less than 40% was attributed to the ions occupying sites in and near the hexagonal prisms; this results in significant lattice distortions to the hexagonal prisms. As the exchange level increases these distortions are compensated for by the counter-ions occupying sites within the sodalite units.

Interestingly for a cerium-exchanged zeolite, it has been suggested[20] that additional thermal stability could be due to the formation of a cerium complex. Other workers have also reported such complexes being formed with other rare earths, in particular lanthanum.[24,37] Thus, for example, Maugé and co-workers[24] gave evidence, based on X-ray crystal structure studies, for a dimeric species in a lanthanum-exchanged system involving extra framework bridging hydroxyls and framework oxygens. Figure 2.7 shows a proposed lanthanum linkage formed across sodalite cages.

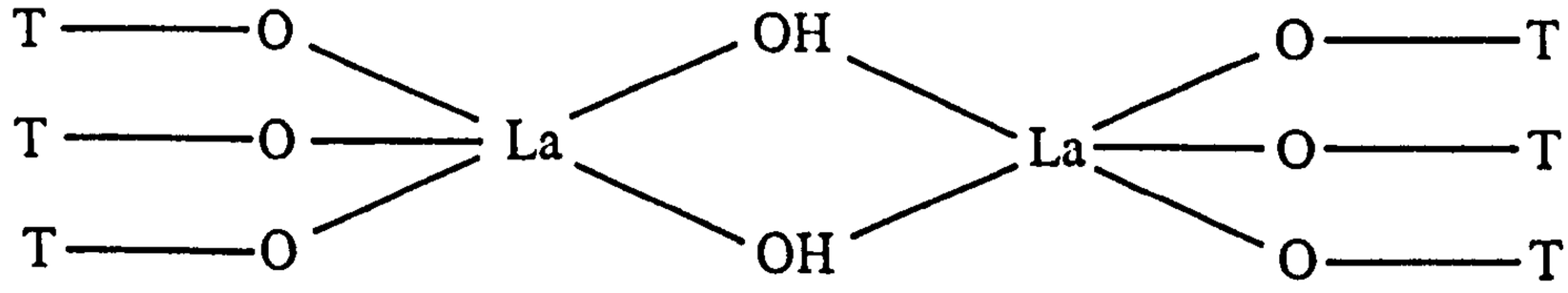

Figure 2.7 Diagram showing the system of lanthanum linkages across sodalite cages proposed by Maugé and co-workers.[24] T refers to framework silicon or aluminium.

Ion-exchange has lead to two of the three major classes of zeolite used commercially today; that is zeolite-Y in a protonated form, denoted H-Y, and zeolite-Y in a rare earth exchanged form, denoted RE-Y (RE refers to rare earth). The third form is a highly dealuminated form of H-Y type zeolite, referred to as an ultrastable zeolite: this is described later. Both H-Y and RE-Y zeolites exhibit superior thermal and hydrothermal stabilities over their Na-Y parent zeolites. Table 2.1 illustrates the thermal stabilities of two modified forms of the parent Na-Y zeolite.[16] The values quoted are taken as the first exothermic peak in the differential thermal analysis (DTA) curve. This is taken to reflect the collapse of the zeolite-Y structure.

Zeolite-Y type	Thermal stability /°C
Na-Y	830
RE-Y	960
H-Y	1000

Table 2.1 The thermal stabilities of two modified forms of Na-Y. All three entries have a Si/Al ratio ~ 10. The RE ion-exchange level was 12.98 mass%, expressed in terms of RE_2O_3.

Na-Y is converted to its protonated form (H-Y) by exhaustive ion exchange with NH_4^+ salts. Zeolite-Y is not directly exchanged with H^+ ions as zeolite-Y is not stable under strong acidic conditions.[4] The NH_4^+ counter-ion is thermally broken down, evolving NH_3, leaving the zeolite in the H-Y form. The extent of ion-exchange can be improved by an intermediate calcination step (200-600°C) which allows rearrangement of ions within the zeolite lattice, this makes more of the Na^+ ions accessible to exchange with NH_4^+.[38]

Similarly RE-Y forms are prepared by exhaustive ion exchange with the appropriate rare earth salt in solution. An intermediate calcination step (~540°C) has been shown to increase the degree of ion exchange.[39] RE-Y zeolites are sometimes further stabilised by a calcination step (~550°C) after ion exchange and washing; these zeolites are referred to as CREY (calcined rare earth Y-type zeolites).[3] Commercially RE-Y zeolites are typically

found in a mixed rare earth form, with the actual composition of rare earth dependent upon the source. If oxides are used as starting materials then the variation can be as shown in Table 2.2.[3] In general cerium, lanthanum and neodymium are usually present in the greatest quantities. The similarity of rare earth distribution in a typical zeolite-Y after exchange compared with the rare earth ion distribution in solution has been taken to indicated that no preferential exchange of one ion over the other takes place.[1]

	Monazite /mass%	Bastnaesite /mass%
Cerium	46	50
Lanthanum	24	24
Neodymium	17	10
Praseodymium	6	4
Samarium	3	1
Gadolinium	2	0.5
Others	2	0.5

Table 2.2 The breakdown of rare earth oxides from two different sources.

The extent of ion-exchange has been shown to be very important in determining the thermal and hydrothermal stability of an exchanged zeolite, particularly with reference to residual sodium levels. Various authors[24,28-30] have carried out investigations in this area. Thus Maugé and co-workers[24] mixed sodium (in the form of sodium chloride) at 10 mass% with a lanthanum-exchanged zeolite-Y and gradually heated to 1000°C. The structure was observed to breakdown some 250°C lower than the lanthanum-exchanged zeolite-Y itself, heated under the same conditions. Analysis of the sample after salt occlusion, that is the point at which diffraction peaks due to sodium chloride disappear, but before complete breakdown of the zeolite-Y lattice, showed that no lanthanum complex of the type shown in Figure 2.7 was present. These authors concluded that the removal of this type of complex due to the presence of sodium was probably the cause of the increased instability.

Ultrastable zeolites

Investigation into the stability of zeolite-Y has shown that this is related to the framework Si/Al ratio.[16,28,29] There is general agreement that the thermal stability of zeolite-Y is increased as the Si/Al ratio increases, that is decreasing framework aluminium. Figure 2.8 illustrates the dependence of thermal stability on the Si/Al ratio for Na-Y zeolites.[38]

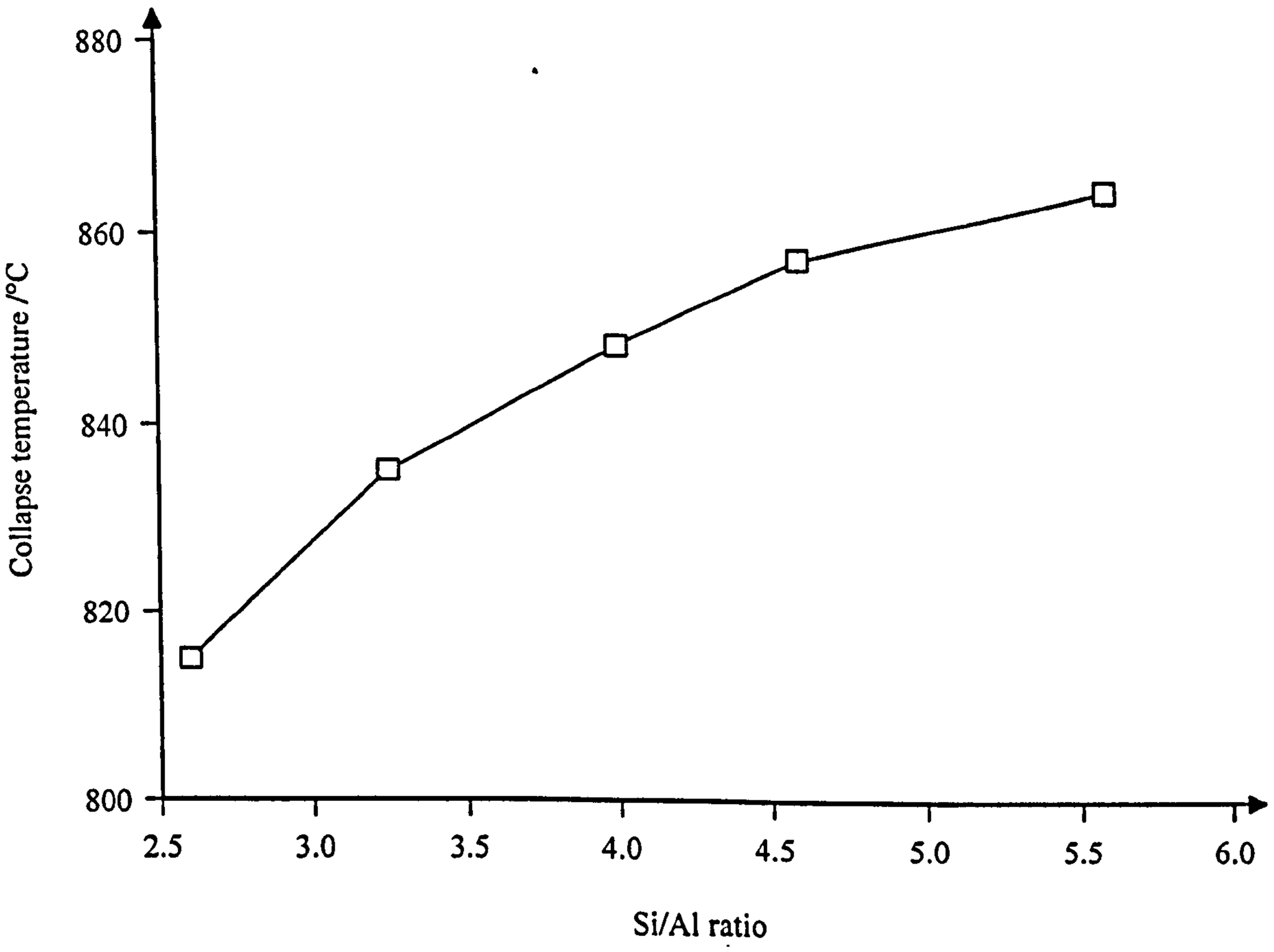

Figure 2.8 Variation of Na-Y collapse temperature with the Si/Al ratio.

The level of framework aluminium forms the basis for establishing the third of the three major classes of commercial zeolite-Y; as already indicated this is a highly dealuminated form of H-Y type zeolite. Many authors[40-50] have investigated this type of zeolite-Y with an emphasis on relating the effect of dealumination to changes in physical and chemical properties. As a class, dealuminated zeolites are known as ultrastable zeolites and are denoted US-Y. US-Y zeolites can be prepared by a number of routes, either chemical or hydrothermal, and all involve the removal of aluminium from framework positions.

Kerr[42,43] described a chemical method for the production of ultrastable zeolites. His method involved the acid leaching of the tetrahedral framework aluminium using ethylenediaminetetraacetic acid. The acid is added slowly (at least 18 hours) to a refluxing aqueous zeolite slurry and the modified zeolite is then filtered and calcined in air or nitrogen. The resultant crystalline aluminium-deficient zeolite was shown to have a superior thermal stability over its parent zeolite. A reduction in unit cell constant was also observed for the ultrastable zeolite. Kerr[42,43] suggested that this was due to the formation of new Si-O-Si linkages where Si-O-Al-O-Si sites existed in the parent zeolite.

Beyer and co-workers[51] described an alternative chemical method of preparation involving silicon tetrachloride ($SiCl_4$). A saturated $SiCl_4$/nitrogen mixture is passed through a bed of zeolite at elevated temperatures (250-450°C). The degree of dealumination was found to be dependent upon the reaction temperature and the contact time. This mechanism of dealumination involves the direct substitution of the extracted aluminium with the external silicon source.

McDaniel and Maher[38] discussed two other methods for the formation of US-Y, Figure 2.9. These two methods are very similar with the second method differing from the first only by an intermediate calcination step during the ion-exchange process: this increases the ease with which sodium levels can be decreased. A characteristic reduction in the unit cell constant, similar to that observed by Kerr,[42,43] was observed.

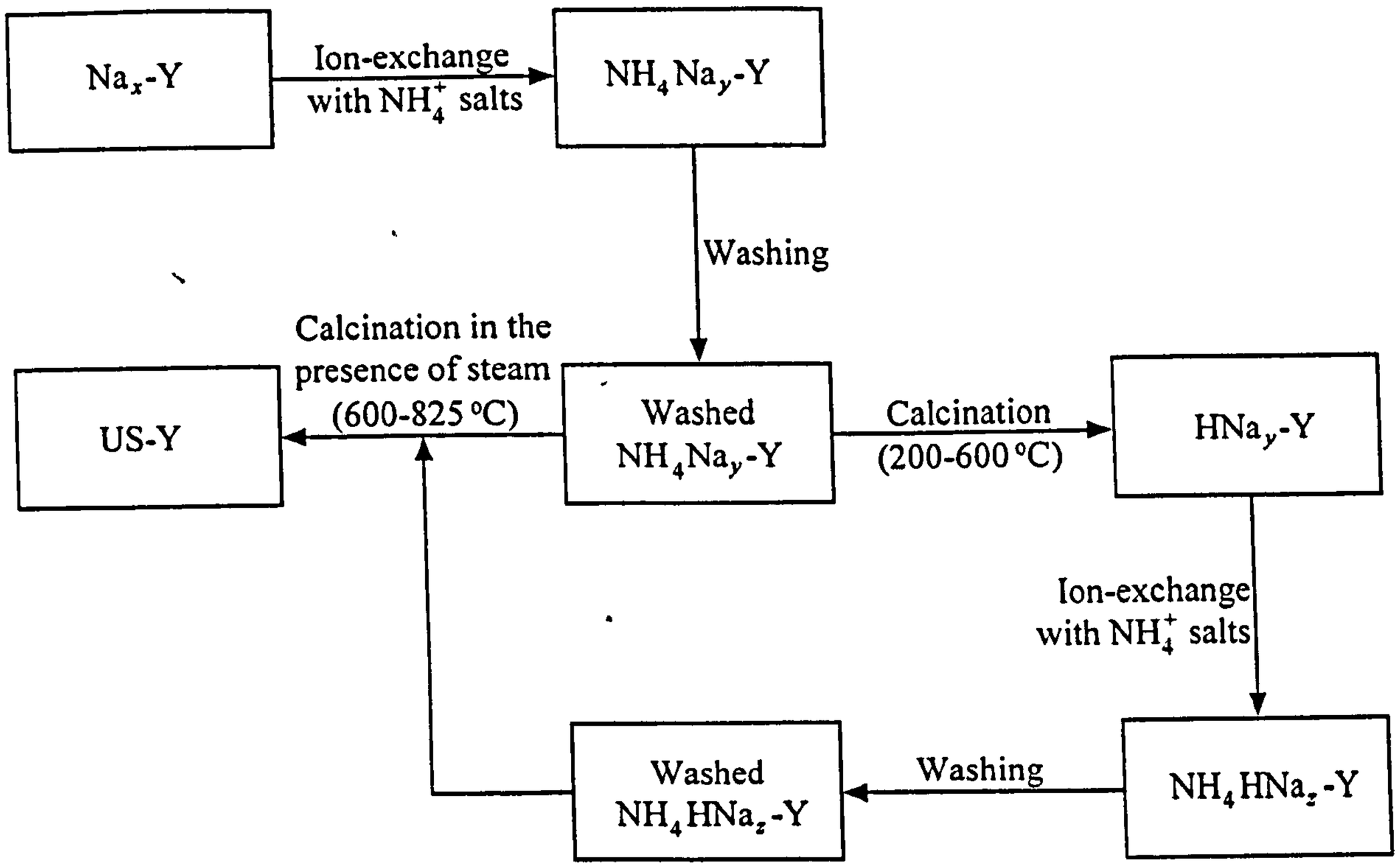

Figure 2.9 Flow chart showing two methods of forming US-Y from Na-Y.[38] *x*, *y* and *z* show the relative amounts of Na^+ in the zeolites at each stage, where *x*>*y*>*z*. If *x* represents 100% sodium ions, values of *y* can be reduced to 10-15% depending on the extent of ion-exchange, values of *z* can be extremely low (<1%) again the final value depends upon the extent of ion-exchange.

The additional stability of US-Y zeolites has been attributed to a number of different factors. Jacobs and Uytterhoven[52] suggested that the additional stability was due to the extra-framework aluminium present as a result of the dealumination process. Kerr[42,43] proposed that the additional stability was due to the formation of new Si-O-Si bonds. Gallezot and co-workers[53] demonstrated that silicon can migrate to fill the voids resulting from aluminium extraction. Calculation of the occupancy factor for T (Si or Al) atoms in a dealuminated sample was not found to deviate significantly from unity. If vacancies remained where aluminium ions had been removed, then an occupancy factor of 0.84 would have been expected. It was concluded that dealumination was followed by local recrystallisation in the framework. The process involved the formation of new 'SiO_4 tetrahedra' in the framework positions damaged by aluminium removal.

2.2 Vanadium-Zeolite Chemistry

Modified zeolite-Y catalysts can be prepared that are thermally and hydrothermally capable of withstanding the rigours of a modern FCCU. However, catalysts still suffer from the detrimental effects of vanadium and other metals which reduce their performance. This section provides a general review of the literature concerned with vanadium-zeolite chemistry. Particular emphasis is given to mechanistic proposals which may account for the destruction of the catalyst by vanadium; but the deposition, distribution, mobility and the efforts to prevent the harmful effects of this metal will also be discussed. Reference is also made to work on related systems which may give insight into possible vanadium species responsible for zeolite lattice destruction. In some places, where appropriate, reference is made to work to be reported later in this thesis. Finally a point concerning nomenclature is useful at this stage: the general term 'zeolite' will be used in those places where a detailed description of the form of a particular modified zeolite-Y would be cumbersome.

The area of vanadium-zeolite chemistry has attracted considerable interest: the petroleum industry would benefit greatly from a more metal-tolerant catalyst and there is basic interest in understanding the chemistry of the interaction between vanadium and the zeolite lattice. Overall the need for an improved FCC is emphasised by the increasing need for refiners to convert heavier distilled fractions which contain higher levels of vanadium.

Vanadium together with other metal contaminants (in particular nickel, copper and iron) are present as organometallic compounds such as porphyrins and naphthenates within crude oil.[54-57] Figure 2.10 gives a few of the structures of metal-containing species that have been positively identified (via nuclear magnetic resonance spectroscopy) within crude oil.[57] These organometallic compounds come into contact with the FCC during the cracking reactions. The organo-skeletal framework is broken down by the FCC and the metal remains on the FCC surface. Metals are continually being deposited in this way and, with time, build to levels that seriously affect the activity and selectivity of the catalyst.

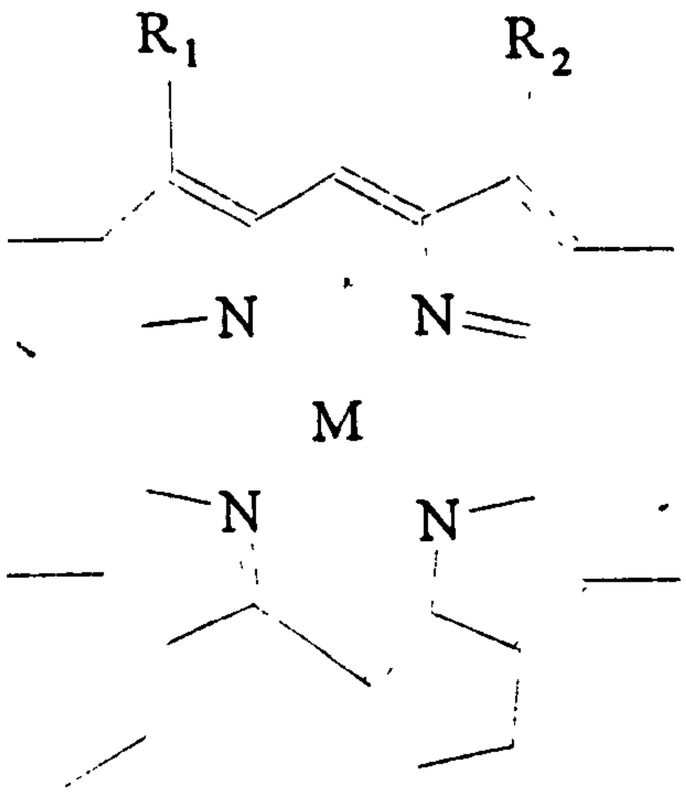

R_1 = Et, R_2 = Me; R_1 = Et, R_2 = H;

R_1 = R_2 = Me

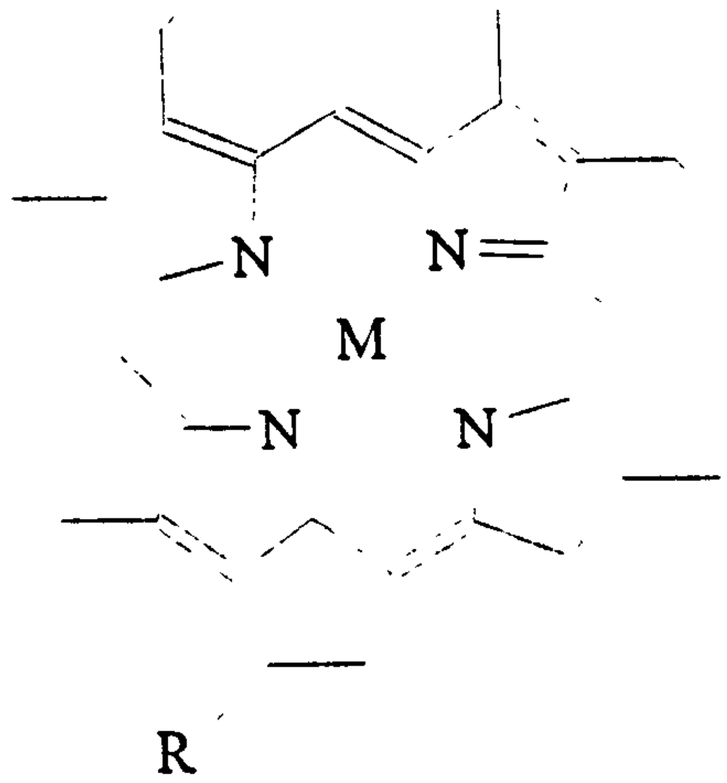

R = Et, Me

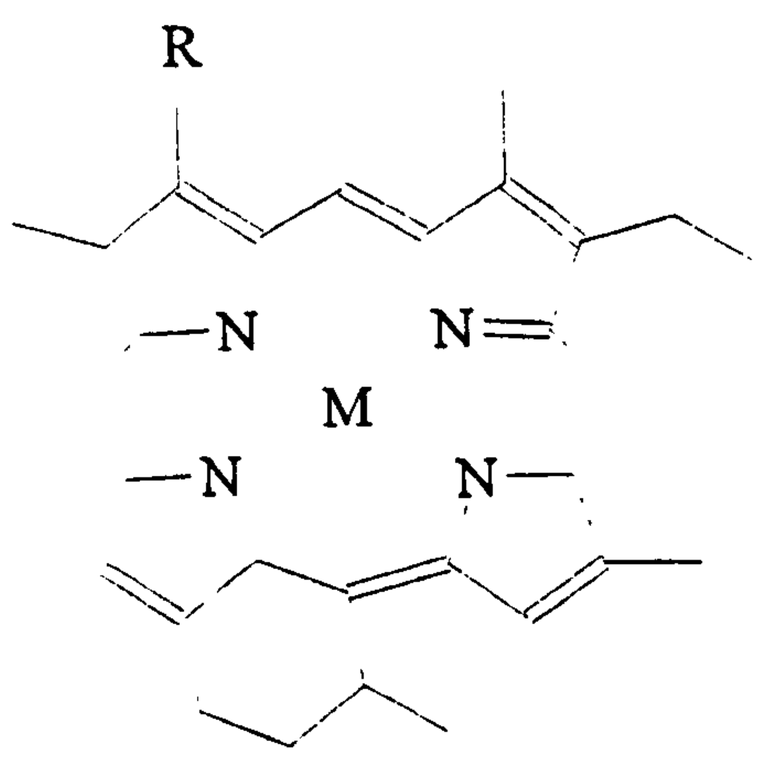

R = Me, —CH_2—COOH

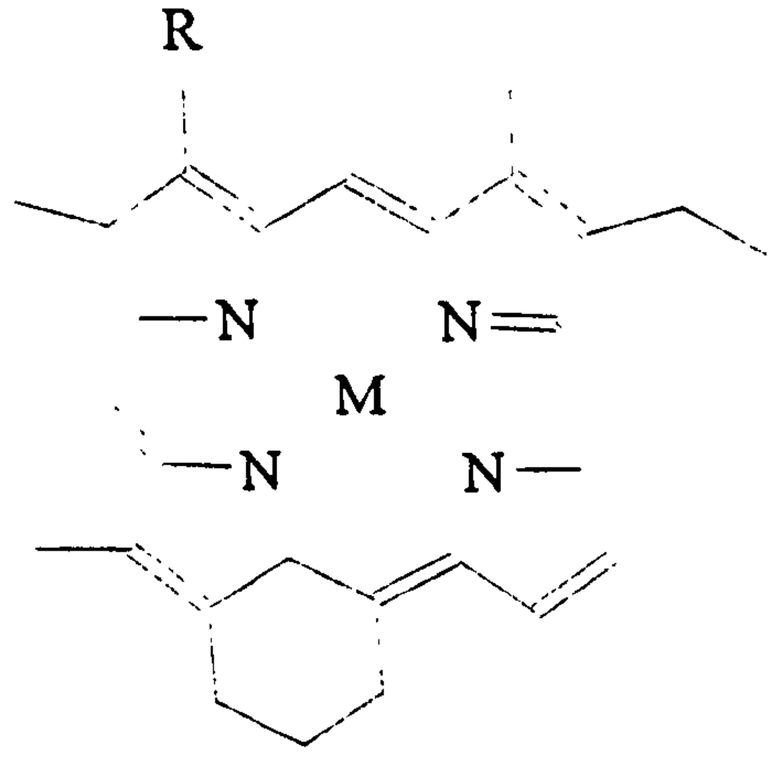

R = Et, Me, H

Figure 2.10 Metal containing species that have been positively identified in oil.

M refers to metal, Me = -CH_3 and Et = -CH_2CH_3.

The effect that these metal contaminants have on the product stream from the FCCU are well known,[58-62] but what is less certain is the mechanism by which these metals react with the zeolite to bring about these changes.

Vanadium together with nickel are found in the greatest concentration within crude oil.[63] Nickel, and to a lesser extent vanadium, promote the increased production of hydrogen and coke at the expense of the more useful and profitable gasoline products. Table 2.3 illustrates the effect that increasing metal levels has upon product yield distributions.[59]

Metals	Metal levels /ppm		
Nickel	180	570	2500
Vanadium	100	1930	3600
Iron	3700	3400	8100
Product	Relative product yield distributions		
Dry Gas /mass%	5.8	6.6	7.1
Coke /mass%	2.4	3.1	7.3
Gasoline /vol%	61.0	59.0	54.0

Table 2.3 The effect of increasing metal levels upon the relative product yield distributions.

Vanadium in addition, however, also reacts with the zeolite in such a way that it destroys the crystalline structure. Rather than affecting product selectivities, this reaction lowers the activity of the catalyst. Wormsbecher and co-workers[61] showed that the surface area of a laboratory-prepared FCC decreased on treatment with vanadium; for example a steam-treated FCC with no vanadium present had a surface area of 191 m^2g^{-1} while a similarly prepared sample, but with 0.5 mass% vanadium present, had a much smaller surface area of 51 m^2g^{-1}. Surface area is a direct probe of the amount of crystalline zeolite-Y present in an FCC sample. If deposition of vanadium is allowed to continue unchecked complete loss of activity is the final result.

At present to control the metal levels to which FCC particles are exposed at an economical level, and to maintain product yields and selectivities out of the FCCU, the refiner daily removes a quantity of spent catalyst and makes up the difference with fresh catalyst. The extent of the make-up rate dictates the average metal loading on a catalyst. Make up rates of between 1-3% (by mass) of the total catalyst inventory are typical and depend both on the specific formulation of the FCC and the technical details of the FCCU. Make-up levels much greater than 3% would render the FCCU uneconomical.

Clearly for an effective metal-tolerant catalyst to be designed it is necessary to have a much greater understanding of the chemical and physical nature of metal-FCC interactions. It is

also reasonable to suggest that investigations of simpler systems, such as the zeolite catalyst itself, are of direct relevance to this complex problem.

2.2.1 Depòsition of Vanadium

It is important to have an overview of what is currently known concerning the deposition of vanadium on to catalyst samples (both commercially and in the laboratory) and this will be the focus of this section. Details of the chemical state and distribution through the FCC particle will also be discussed.

As was stated earlier vanadium is found in crude oil as organometallic compounds such as porphyrins and naphthenates,[54-57] (Figure 2.10). Saraceno and co-workers,[64] using electron paramagnetic resonance (EPR), have shown that vanadium is present in the +4 oxidation state, in the form of VO^{2+} organometallic compounds, for several distillates, residues and crudes. Vanadium, in a commercial FCCU, is deposited on to the catalyst during the cracking reaction in the riser cracker and at this stage will still probably be present as VO^{2+}. Anderson and co-workers,[65] via EPR studies, have confirmed that for laboratory-prepared samples of europium-exchanged zeolite-Y (Eu-Y) that vanadyl cations introduced from vanadyl naphthenate are stabilised as octahedral VO^{2+}. The VO^{2+} cations were found to be stable even after calcination at 540°C.[65]

Vanadyl naphthenate is widely used by several workers as a model compound for the artificial impregnation of vanadium on to catalyst samples. Mitchell[6] has suggested that this material dissolved in benzene provides a realistic method for impregnation of catalyst samples. A particularly important result was that the hydrothermal treatment of laboratory-prepared samples was found to give results comparable with catalysts deactivated in a commercial FCCU.

It is generally thought that the hydrothermal oxidising atmosphere of the regenerator part of the FCCU causes the oxidation of vanadium to V(V) species.[66] For example Anderson and co-workers,[65] found that VO^{2+} cations stabilised on Eu-Y were almost completely converted to V(V) species upon hydrothermal treatment; this has also been observed by

other workers.[67-69] It is believed that it is in the regenerator part of the FCCU where the destructive vanadium chemistry occurs. Clearly the nature of the V(V) species present is important and is possibly the key to the mechanism by which the vanadium destroys the zeolite lattice. This is discussed in more detail in Section 2.2.2.

The initial 'contamination' of FCC particles with vanadium (and other metals) has been studied by several groups. Wormsbecher and co-workers[61] working with a laboratory-prepared FCC containing 10%, by mass, zeolite demonstrated, using a vanadium electron microprobe profile, that vanadium is initially deposited onto the surface of an FCC particle. This still remained the case even after calcination at 760°C. Steaming the sample, however, produced an even distribution of vanadium throughout the FCC particle. This result is significant in that it indicates the importance of steam in the redistribution of vanadium.

Metal profiles across FCC particles which have been hydrothermally treated have also been studied by Nishimura and co-workers[70] by means of electron probe X-ray microanalysis (EPMA). Vanadium profiles were determined on two types of FCC: firstly an RE-Y FCC and secondly an H-Y FCC. The results showed two distinct types of behaviour depending upon the zeolite present in the FCC particle. The vanadium profile of the H-Y FCC mirrored that found by Wormsbecher and co-workers,[61] that is, an even distribution of vanadium throughout the FCC particle after hydrothermal treatment. The results for the RE-Y FCC were quite different, with the vanadium distribution mirroring the lanthanum distribution profile throughout the FCC particle. This was found to be the case even in the presence of differing amounts of residual sodium. This result can be interpreted in terms of an affinity of vanadium for lanthanum (and other rare earths) and, subsequently, has formed the basis for mechanistic explanations of the vanadium-induced destruction of the zeolite structure (Section 2.2.2). Vanadium distributions have been studied by other workers and similar results have been reported.[55,71-73]

Maselli and Peters[72] have reported interesting differences in the vanadium profiles of FCC particles containing identical zeolite components, but differing matrix components. Two FCC samples were prepared, one with an RE-Y zeolite together with an inert matrix of clay

and silica binder, and the other with identical RE-Y zeolite but with a high surface area catalytically active silica/alumina matrix binder. The vanadium profile of the FCC particles containing the inert matrix mirrored that of the lanthanum distribution profile and is similar to that reported by Nishimura and co-workers.[70] The distribution of vanadium in the FCC particle with the catalytically active matrix was uniform and similar to that observed for RE free zeolites. It seems that the high surface area matrix results in the even distribution of vanadium throughout the FCC particle even in the presence of RE-Y type zeolites. No explanation for this behaviour was presented by Maselli and Peters[72] but vanadium tolerance benefits have been reported by Speronello and Reagon[74] as a result of increasing the surface area of the matrix.

The vanadium profiles for FCC particles reported above[55,70-72] refer to laboratory-prepared FCCs which have been artificially impregnated with vanadium according to the Mitchell[6] method. Similar studies have also been reported for commercial samples. Kugler and Leta,[73] using secondary ion mass spectrometry (SIMS), determined vanadium distributions on samples removed from FCCUs. This also provided an opportunity for vanadium distributions to be observed as a function of time in the FCCU. Since the samples originated from working FCCUs then, due to the daily make-up rates, there was a distribution of particle ages. Some particles would have been in the FCCU for only a day, whereas others may have been present for durations as long as six months. The age of the particle was determined according to its nickel loading; this is an adequate guide to the age of particle due to the low mobility of nickel once deposited. Results on samples that contained only RE-Y, clay and binder were in good agreement with those for similar laboratory-prepared samples; that is the vanadium distribution mirrored that of the rare earths. However, on FCCs which contained an alumina matrix the picture was quite different; the vanadium distribution was found to be in good agreement with the distribution of the alumina particles in the FCC. This clearly suggested a preference of vanadium for alumina. It was noted, however, that for the older particles in the samples studied, the vanadium was also found on the zeolitic component of the FCC. Occelli and Stencel[75] have reported the vanadium passivation effects of boehmite, a naturally hydrated

form of aluminium oxide with the general formula γ-AlO(OH). This is discussed in more detail in Section 2.2.3.

To return to the work of Kugler and Leta,[73] they also found that there was very little correlation between the nickel and vanadium loadings in all of the samples they examined. They observed similar vanadium loadings on FCC particles that had been in the FCCU for at least fifteen months, compared with those that had been there for considerably less time. This provides strong evidence that inter-particle movement of vanadium must be occurring at FCCU operating conditions.

Vanadium migration under hydrothermal conditions has been investigated by Occelli.[76] A mixture of sepiolite (a hydrated magnesium silicate with the general formula $Mg_2Si_3O_8.2H_2O$) and FCC were hydrothermally treated. Prior to mixing only one of the components was loaded with vanadium. The results clearly indicated that particle to particle transport of vanadium was possible under hydrothermal conditions. Interestingly, high mobility of vanadium under FCCU conditions lends further weight to the active vanadium species being in the +5 oxidation state. The melting temperature of lower oxidation state vanadium compounds are in considerable excess of the temperatures to be found in a typical FCCU, as the examples in Table 2.4 confirm.

Oxide	Vanadium oxidation state	Melting temperature /°C
V_2O_5	+5	658
VO_2	+4	1640
V_2O_3	+3	1970

Table 2.4 The melting temperatures and oxidation state of some common vanadium oxides.[63]

2.2.2 Proposed Mechanisms of Vanadium Attack

An overview of the mechanisms, including current proposals, that have been put forward to account for the vanadium-induced destruction of the zeolite component is given below.

When vanadium supported on solids is exposed to water various complex hydrolysis-condensation-polymerisation reactions occur.[66,77] The nature of the poly-ions formed and their degree of protonation, is dependent on a number of factors including vanadium concentration, surface composition and liquid pH. Figure 2.11 summarises the various vanadate species that can be formed as a function of pH and total vanadium concentration.

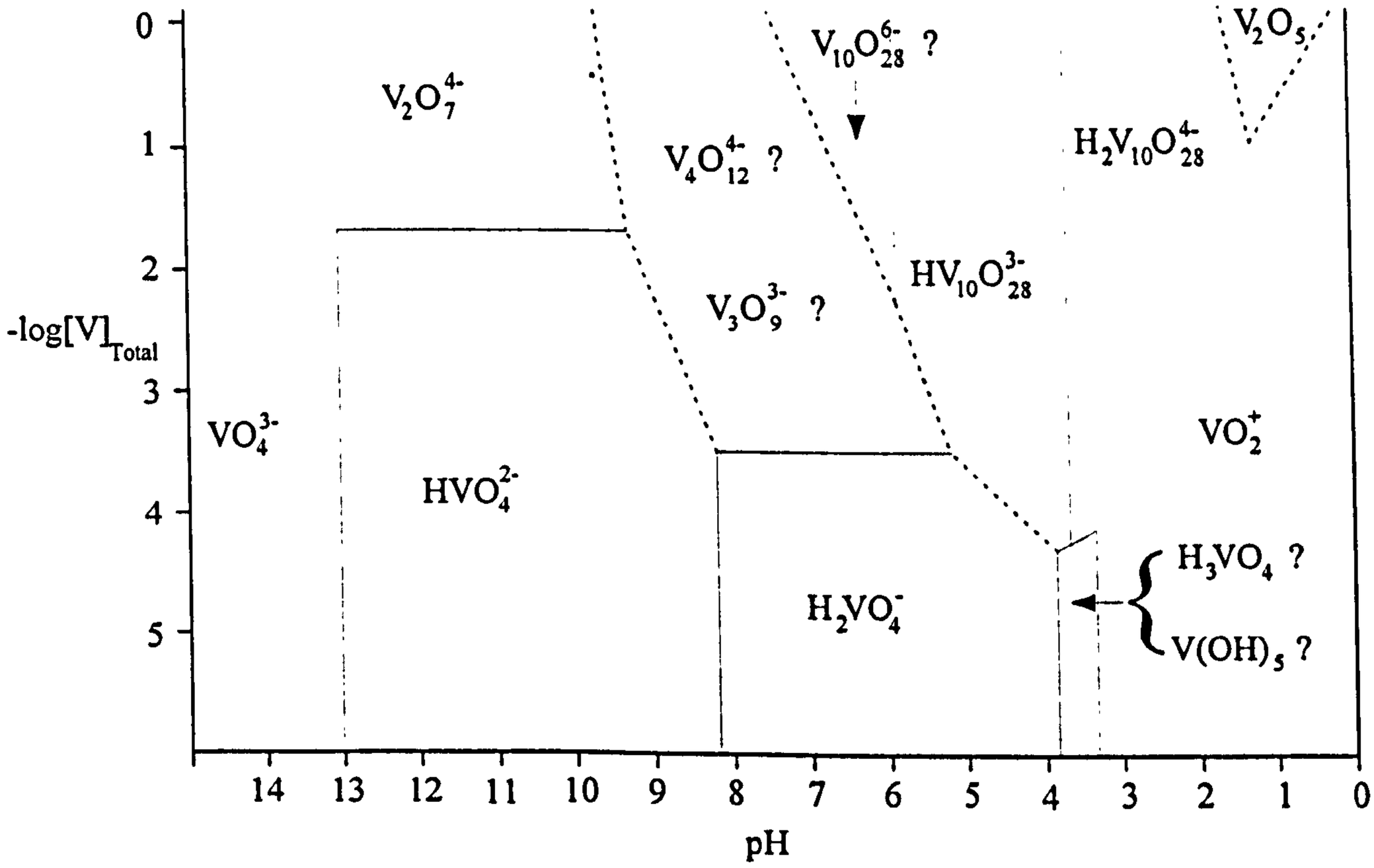

Figure 2.11 Phase diagram showing the approximate conditions of pH and total vanadium concentration under which a given species would be the major solute component of a vanadate solution at 25°C. Demarcations about which there is considerable doubt are represented by broken lines.

It is believed that similar chemistry will affect the nature of vanadium compounds formed when a support loaded with vanadium is exposed to steam. Indeed Occelli[66] observed an array of vanadium ions when calcined, vanadium-loaded catalysts were exposed to water. In general, it is known that the destruction of a zeolite due to vanadium increases with amount of vanadium and rising temperature; it is also greatly accelerated when the zeolite is heated in the presence of steam.[66] Vanadium level, temperature and steaming conditions

are, therefore, three important factors that can be investigated to obtain a better understanding of vanadium-zeolite interactions under FCCU conditions.

Work presented by Meisenheimer[58] demonstrated the importance of the chemical state of a metal contaminant towards the deactivation of an FCC. He postulated that the mechanism of attack was due to the combination of metal contaminants with the zeolite to form silicate or aluminosilicate compounds, although no evidence for such compounds was given. The mechanism proposed by Meisenheimer was not widely accepted by other workers, but his evidence for the importance of the chemical state of the metal contaminants is widely recognised, with V(V) species believed to be the active vanadium species.

Pompe and co-workers[78] suggested that RE-Y zeolites were destabilised by vanadium due to the formation of a eutectic compound. A systematic study of V_2O_5/RE-Y mixtures was undertaken using differential thermal analysis (DTA) and X-ray diffraction (XRD). It was found that melting occurred well below the melting temperature of V_2O_5, indicating that a reaction could occur between zeolite and V_2O_5, before V_2O_5 itself melts. Characterisation of the mixtures by XRD showed that, in addition to V_2O_5 and zeolite-Y, new diffraction peaks due to an $REVO_4$ phase were present. The conclusion was reached that V_2O_5 attacks the rare earth component of the zeolite-Y forming a low melting RE-vanadate phase. It was also suggested that the incorporation of sodium would further lower the melting temperature of the eutectic. Vanadate formation requires more oxygen per RE than can be supplied by V_2O_5 alone, and so the following reaction scheme was suggested:

$$\text{"2 Z(O)}_{1.5}\text{RE"} + V_2O_5 \longrightarrow 2\ REVO_4 \qquad (2.1)$$

In this scheme the 'extra' oxygen needed for reaction comes from the zeolite lattice (represented by Z); thus vanadate formation leads to the destruction of the zeolite framework. The importance of RE_2O_3-V_2O_5 eutectics has also been proposed by other workers.[79,80] Upson and co-workers[79], via DTA, showed that V_2O_5 reacts with RE-Y to form a eutectic compound with a melting temperature of 630°C. They concluded that at regenerator conditions vanadium would migrate to the zeolite to form a eutectic which on melting would destroy the zeolite crystalline structure.

The formation of RE_2O_3-V_2O_5 eutectic compounds during the regeneration process, however, has been placed in some doubt by Wormsbecher and co-workers.[61] If an RE_2O_3-V_2O_5 eutectic lowers the melting temperature of the zeolite, resulting in destruction of the crystalline lattice on melting, then this process would be expected to occur during dry air calcination. A series of experiments on identical catalysts, with and without vanadium present, were carried out in which calcination took place in dry air and in the presence of steam. It was shown that only samples that were hydrothermally treated showed any loss of catalytic activity. It was thus concluded, in contradiction to other workers, that eutectic formation was not important in the mechanism by which vanadium destroyed the zeolite crystal structure. Clearly in this work the presence of steam was a significant feature. Indeed it has been shown that vanadium levels of 5 mass% are needed before destruction of a zeolite is observed in dry air[66] and this is far in excess of that found in a typical FCC particle. It has also been reported[81-85] that solid state ion-exchange has been successful with zeolite/V_2O_5 mixtures with no loss of crystallinity following calcination in dry air.

As well as demonstrating the importance of steam in the overall mechanism of zeolite destruction, Wormsbecher and co-workers[61] also demonstrated that the vanadium species present were volatile. Evidence for this came from a series of experiments in which V_2O_5 was held in a crucible below a zeolite sample: Figure 2.12 illustrates the experimental arrangement.

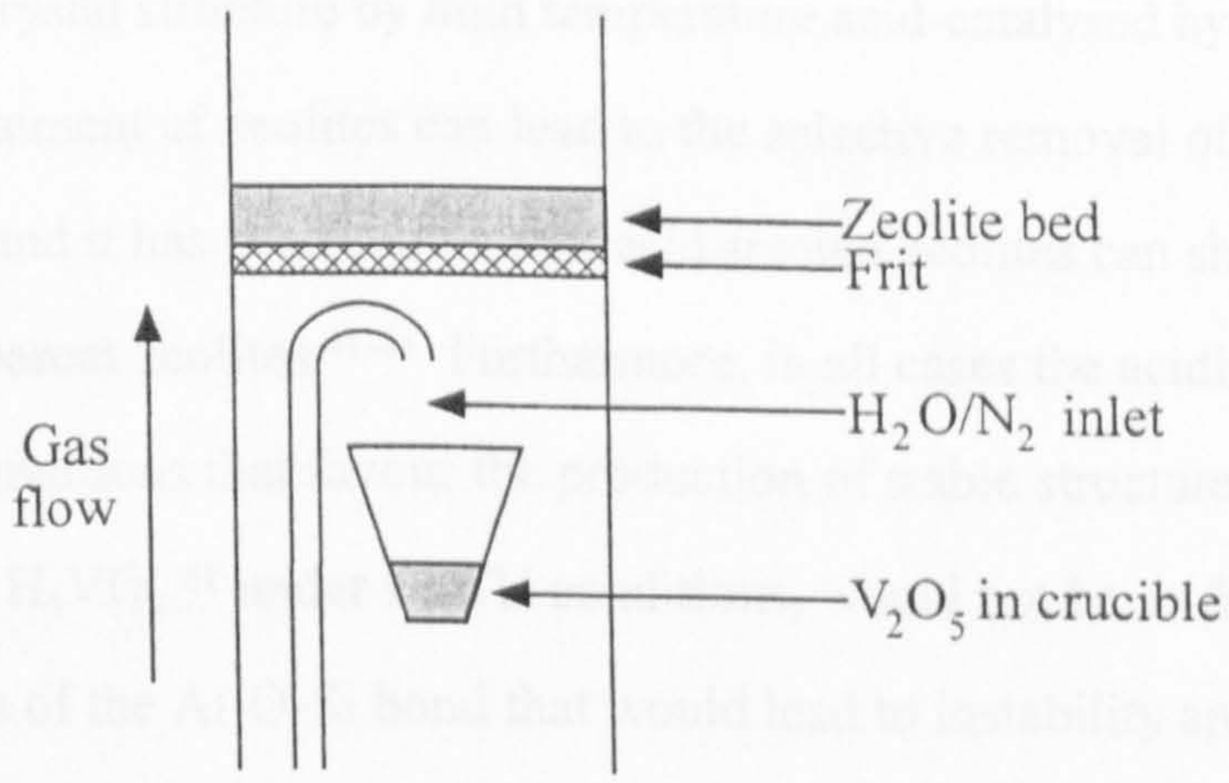

Figure 2.12 Schematic diagram showing the experimental arrangement of 'flowing tube reactor' used for exposure experiments to demonstrate the volatility of vanadium species.

Hydrothermal treatment showed enhanced destruction of the zeolite crystalline structure in these circumstances. This enhanced destruction could only result from one, or several, volatile vanadium species being carried from the crucible by the steam/nitrogen carrier gas to the zeolite. Two possible (volatile) vanadium compounds were suggested to be present as a result of the V_2O_5/H_2O reaction as indicated in the following reactions:

$$V_2O_{5\,(s)} + H_2O_{\,(g)} \rightleftharpoons 2\,VO_2(OH)_{\,(g)} \qquad (2.2)$$

$$V_2O_{5\,(s)} + 3\,H_2O_{\,(g)} \rightleftharpoons 2\,VO(OH)_{3\,(g)} \qquad (2.3)$$

Reaction 2.3 was considered more probable because of the higher, and more favourable, co-ordination of vanadium. Thermochemical evidence has also been reported by Yannopoulos[86] for the presence of $VO(OH)_3$ due to the reaction between V_2O_5 and H_2O at elevated temperatures. Figure 2.13 shows the reported structure of the gaseous vanadium oxide trihydroxide.

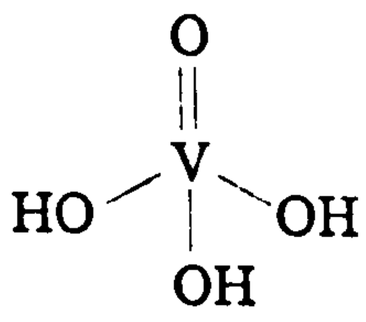

Figure 2.13 The structure of $VO(OH)_3$.

It was concluded that $VO(OH)_3$ would be a strong acid, by analogy with phosphoric acid, and so $VO(OH)_3$ was referred to as vanadic acid with the formula H_3VO_4. H_3VO_4 would destroy the zeolite crystal structure by high temperature acid-catalysed hydrolysis. However, acidic treatment of zeolites can lead to the selective removal of aluminium from the zeolite lattice[87] and it has been shown that acid-treated zeolites can show enhanced stability over their parent zeolites.[41-44] Furthermore, in all cases the acidic treatment was carried out under conditions that favour the production of stable structures. Presumably acidic attack due to H_3VO_4,[61] under FCCU conditions, would not be so favourable and it would be hydrolysis of the Al-O-Si bond that would lead to instability and destruction. In this case a vanadium-aluminate phase would be expected to be present. The formation of $AlVO_4$ has been reported by Gallezot and co-workers[88] in US-Y zeolites; but only under mild hydrothermal conditions. At temperatures lower than 650°C they concluded that

V_2O_5 would react with extra-framework aluminium to form $AlVO_4$. Above 650°C evidence for $AlVO_4$ could not be found. This is consistent with the work of Occelli and Stencel[75] who showed that unsupported $AlVO_4$ started to decompose at 650°C, and decomposition to V_2O_5 and Al_2O_3 was complete at 780°C. It has been subsequently suggested that $AlVO_4$ is not important in the mechanism of zeolite destruction because of its instability at temperatures greater than 650°C.[75]

Assuming that the mechanism proposed by Wormsbecher and co-workers[61] for the destruction of zeolite crystal structure is correct, that is destruction due to the hydrolysis of Al-O-Si bonds, then this would go some way to explaining the additional stability seen for dealuminated zeolites. Zeolites with low Si/Al ratios (high aluminium content) when attacked by vanadium (H_3VO_4) would have many lattice defects (vacancies in the lattice were aluminium has been removed) and often in close proximity to one another. The presence of so many defects would lead to a rapid collapse of the zeolite lattice. For zeolites with high Si/Al ratios (low aluminium content) then the number of such defects would be lower and statistically not so close together. This could make self-annealing of the zeolite more efficient (replacement of removed Al with Si) and the result would be greater stability.

Pine[89] working with a variety of zeolites with differing Si/Al ratios and silicalite (an aluminium-free zeolite), questioned whether Al-O tetrahedra were the place of vanadium attack. He found that the rates of destruction of two zeolites with differing Si/Al ratios, were essentially the same. This is contrary to what might be expected from the simple argument that if the aluminium site is the place of attack, then the more sites present, the greater the rate of destruction. Pine also showed that hydrothermal treatment of silicalite in the presence of vanadium also lead to destruction of the crystal structure, suggesting that attack on Si-O-Si bonds can also occur. Overall he concluded that the site of attack is more probably Si-OH terminal bonds. Pine[89] also gave evidence that the presence of rare earths in a zeolite lattice does not influence vanadium tolerance, but just changes the base tolerance of the zeolite to steam attack. This last statement seems to suggest that RE-Y and H-Y zeolites would have similar tolerances to vanadium. However this is contradicted by a simple experiment by Gallezot and co-workers.[88] A physical mixture of La-Y and US-Y

were simultaneously loaded with vanadium and hydrothermally treated. The results showed that the La-Y zeolite was markedly less stable than US-Y under identical conditions. Evidence will also be presented later in this thesis (Chapter 5) which shows that as RE levels increase then the tolerance to vanadium decreases. Gallezot and co-workers[88] also suggested that RE-containing zeolites and RE-free zeolites are probably destroyed by different mechanisms. This is probably true, at least initially, in view of the affiliation of vanadium to rare earths as described in Section 2.2.1.

Gallezot and co-workers[88] carried out a series of experiments on an RE-free US-Y zeolite. Half of this zeolite was extracted with acid to remove all the extra-framework aluminium and under hydrothermal treatment in the presence of vanadium this portion was shown to be the least stable. Reaction schemes (Figure 2.14(a) and (b)) were put forward to account for the observed behaviour of the two zeolitic forms.

It was concluded that additional stability could be achieved due to the presence of extra-framework aluminium. Vanadium is stabilised as $AlVO_4$ at temperatures below 650°C but is released at temperatures ~ 650°C to continue the destruction of the zeolite. Both reaction schemes are essentially the same, although in the absence of aluminium, mullite cannot be formed.. Gravette and co-workers[90] have shown that V_2O_5 is capable of dissolving silica, and cristobalite can precipitate from the melt. Interestingly vanadium was found in the crystallites of mullite. In this context other workers[66,91,92] have shown that vanadium is capable of being incorporated into the mullite crystal structure, and indeed vanadium is known to act as a mineralising agent lowering the temperature of mullite formation by more than 400°C. However, there is general agreement that vanadium levels incorporated into the mullite structure are low and so the majority of vanadium is free to continue the destruction of the zeolite.

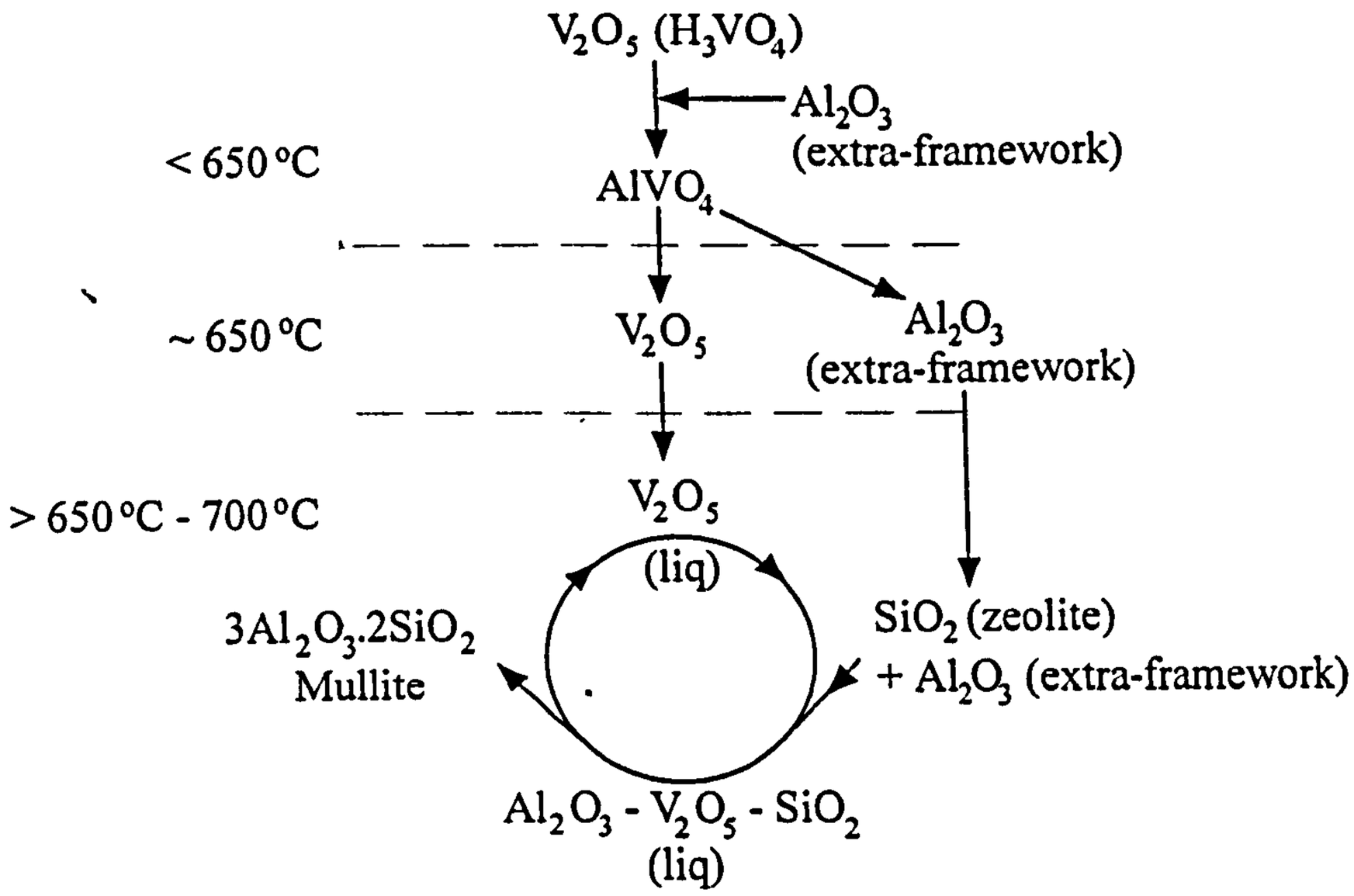

Figure 2.14(a) The proposed reaction scheme for the destruction of US-Y by vanadium.

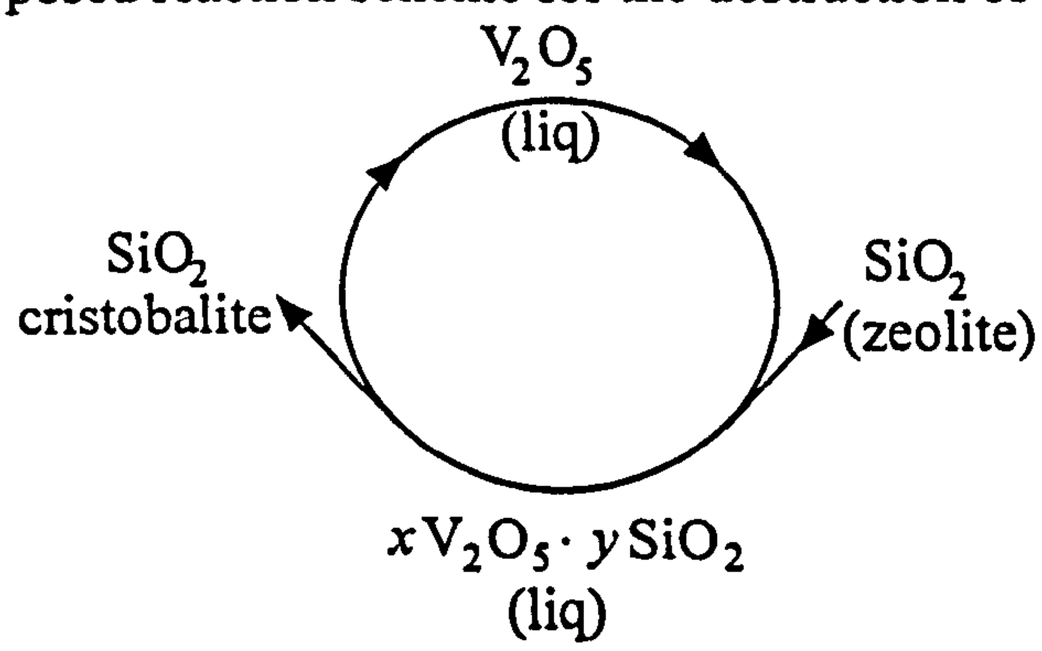

Figure 2.14(b) The proposed reaction scheme for the destruction of acid leached US-Y by vanadium.

Maugé and co-workers,[93] working with highly exchanged lanthanum zeolites (La-Y), observed the formation of $LaVO_4$ on hydrothermal treated samples in the presence of vanadium. The formation of $LaVO_4$ was also observed on samples that were calcined in dry air under relatively mild (600°C) conditions. The observation of vanadate formation is consistent with the work of Pompe and co-workers.[78] It can be recalled that these workers suggested that the extra oxygen needed for vanadate formation would originate in the zeolite lattice, which in turn would lead to the destruction of the zeolite. Maugé and co-workers[93], however, dismissed this mechanism in favour of the destruction being due to removal of the stabilising La-O(H)-La linkages across sodalite cages; in this case extra oxygen would come from the extra-framework oxygen present in these linkages. Rare

earth complexes are thought to give RE-exchanged-zeolites added thermal stability.[20,24,37] Removal of these stabilising linkages would lead to thermal instability and increased destruction of the zeolite crystalline structure.

Other authors (including work in this thesis) have observed $REVO_4$ species.[66,69,82] Anderson and co-workers[69] reported the formation of $EuVO_4$ when working with europium-exchanged zeolites. Occelli[66] reported $CeVO_4$ formation on RE-Y zeolites and proposed the reaction scheme given below (Equation 2.4) which mirrors proposals put forward by Maugé and co-workers.[93] .

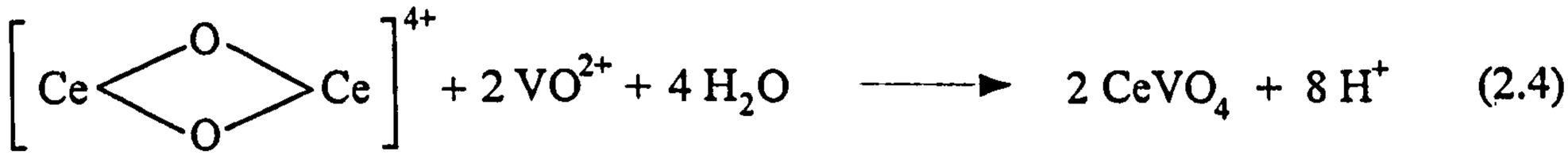

$$\left[Ce \begin{array}{c} O \\ \diagup \diagdown \\ O \end{array} Ce \right]^{4+} + 2\,VO^{2+} + 4\,H_2O \longrightarrow 2\,CeVO_4 + 8\,H^+ \qquad (2.4)$$

Occelli[66] also suggested that destabilisation could be further enhanced by the removal of other counter-ions , for example Na^+, due to vanadate formation.

In summary, a number of suggestions have been put forward to account for the mechanism of destruction of the zeolite component of an FCC due to the presence of vanadium. The problem is undoubtedly complex and it seems fair to state that there is no final agreement on a mechanism in the open literature. However, it may well be necessary to develop two distinct mechanisms, one for RE-Y zeolites and one for RE-free zeolites. A mechanism for RE-Y zeolites will most likely involve the formation of $REVO_4$, but it must be commented that it has been suggested[61] that $REVO_4$ formation is only a by-product of another mechanism and is only produced *after* the zeolite lattice has been destroyed. A mechanism for the destruction of RE-free zeolites must account for the relatively facile formation of mullite.

2.2.3 Passivation of Metal Contaminants

As an understanding of metal-contaminant/zeolite interactions has developed, then so have more informed efforts been directed at preventing these interactions occurring. A number of methods have been put forward for the passivation of metal contaminants, although only

a few have been widely used by the petroleum industry to date. This section provides a brief review of some of the main approaches in this commercially sensitive area.

The effects of nickel, like vanadium, on an FCC have been widely investigated. It has been found that increased production of hydrogen and coke as a result of nickel/zeolite interactions can be successfully lowered by the introduction of antimony into the FCCU.[94]

Passivation of vanadium compounds has not been so successful. Pragmatically vanadium/zeolite interactions can be controlled and maintained at acceptable levels by increasing the make-up rates and prudent FCC and FCCU design, but it is inevitable that a more metal-tolerant FCC is required.

Research into the production of more metal-tolerant catalysts has not been restricted to the zeolite component of the FCC. As indicated earlier in the review, Speronello and Reagon[74] have reported that increasing the surface area of the matrix has a marked effect on the FCC tolerance to vanadium.

Wormsbecher and co-workers[61] suggested that basic oxides such as alkaline earths (for example MgO) should be added to the FCC. This was based on their proposed mechanism of attack involving acidic H_3VO_4. Results of tests involving a 20% by mass MgO mix with catalyst clearly showed increased activity and selectivity in the presence of vanadium.

In general, the addition of compounds to an FCC results in a dual-function cracking catalyst (DFCC). The role of the additive in the DFCC is to inhibit vanadium/zeolite interactions by selectively sorbing vanadium and passivating its destructive effect. The relative ease with which vanadium can migrate at FCCU conditions is well known (Section 2.2.1), so any additive must react with vanadium in such a way as to prevent its migration back to the zeolite component of the FCC (Figure 2.15). Overall the 'DFCC approach' seems to be accepted as having the best potential for vanadium passivation.

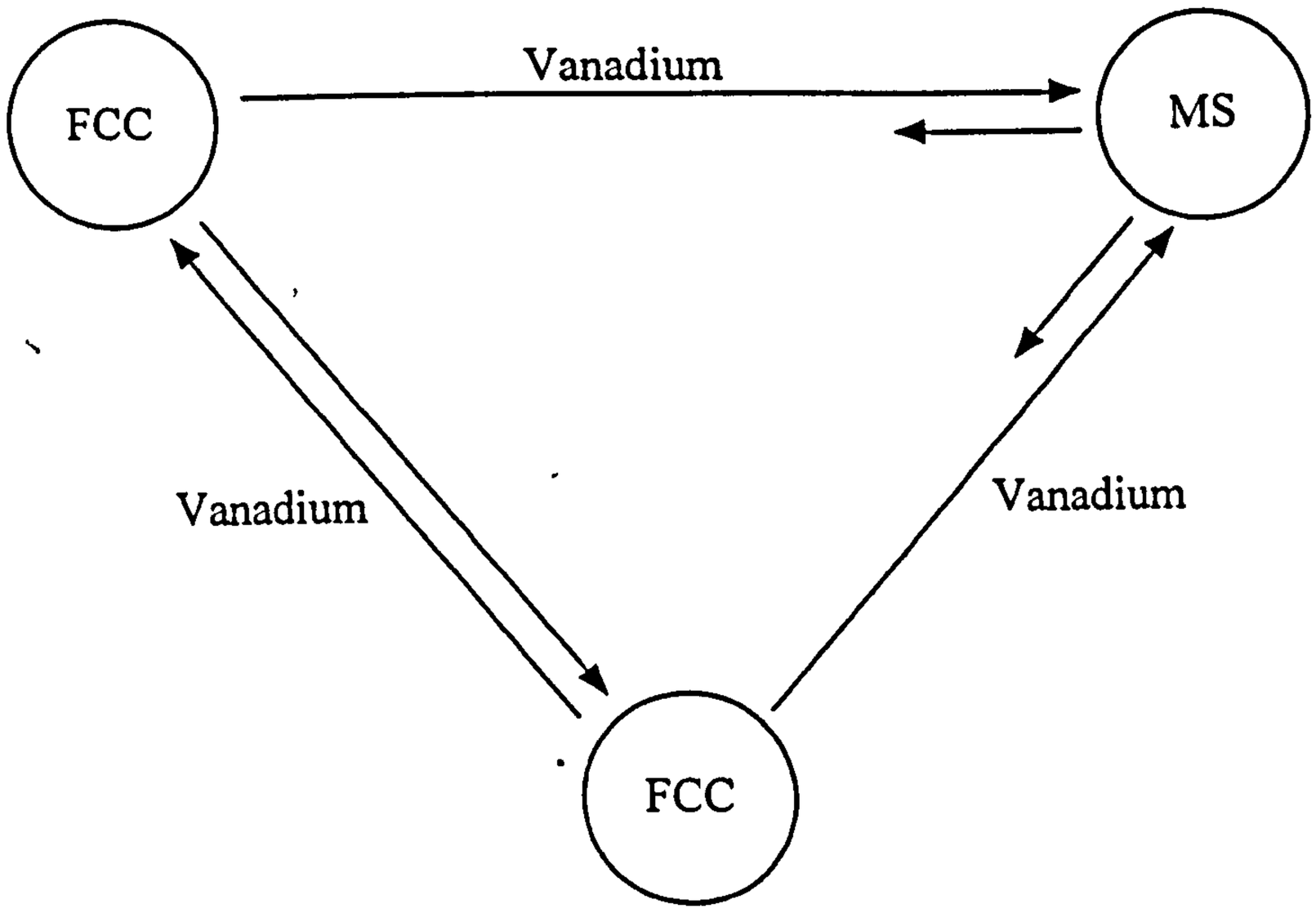

Figure 2.15 Diagram illustrating the necessary properties of an effective metal scavenger (MS).

Upon the addition of a metal trap an immediate loss of activity is observed due to the dilution of catalyst inventory. With time, and as metal levels build in the FCCU, the activity of the DFCC exceeds that of the FCC alone. The cross-over point (the point at which the DFCC becomes more active than the FCC alone) is dependent on the gas/oil composition, feed metal levels, zeolite concentration and type in the host FCC, and on the properties of the metal trap.[66,76] In addition to the necessary vanadium passivation properties, any metal trap must also have similar physical properties to the FCC particle; that is it must have similar density so effective mixing of the two can be maintained in the FCCU. Furthermore the metal scavenger must be stable enough to withstand the variety of harsh conditions in the FCCU and it must be strong enough to withstand the many impacts with the FCCU walls and other FCC particles.[61]

Occelli and Stencel[75] investigated the addition of boehmite (γ-AlO(OH)) to FCCs. Vanadium transport experiments confirmed that vanadium readily migrated from the surface of the FCC to the boehmite additive, but migration from boehmite to the FCC was negligible. Catalyst activity and selectivity tests on the DFCC confirmed the effectiveness of boehmite as a metal scavenger. It was noted, however, that at high metal loadings

(5 mass% V) the surface area of the boehmite reduced significantly and the vanadium/boehmite support collapsed to give V_2O_5 and γ-alumina. The loss of surface area was accompanied by a decrease in metal scavenging properties. These results are consistent with those of Speronello and Reagon.[74]

Many other additives have also been suggested, and patented, as being effective vanadium scavengers. These include calcium titanates,[95] strontium titanate,[96] strontium carbonate,[97] sacrificial zeolites,[98] sepiolite,[76,99] anionic clays[100] and mixtures of rare earths.[101]

Vanadium passivators can also be introduced into the FCCU deposited on FCC particles rather than as a dilutant additive as in a DFCC. For example, Anderson and co-workers[65] demonstrated that tin compounds deposited on the surface of a europium-exchanged zeolite-Y mediate the effect of vanadium. Tin was introduced to the surface of the zeolite as tetraphenyltin dissolved in toluene, in a manner similar to the Mitchell method.[6] It was found that the tin and vanadium complexed and so it was concluded that this reduced vanadium-zeolite interactions. The order of deposition (tin followed by vanadium, or vanadium followed by tin) was not important, but it was noted that excess tin was to be avoided since this promoted the formation of $EuVO_4$, with a consequent loss of zeolite crystallinity. In the work reported in this thesis we have observed the retention of zeolite crystallinity on FCC samples loaded with RE-containing compounds prior to vanadium loading and hydrothermal treatment (Chapter 5).

An alternative approach to extending the life of an FCC has been reported.[102] Rather than the addition of metal passivators, the contaminant metals themselves are removed from the surface of equilibrium FCCs. Elvin[102] reported results which showed that catalytic activity can be partially restored after the removal of vanadium and other contaminant metals. It was concluded that there were two types of vanadium present. The first resulted in the permanent destruction of the zeolite, while the second caused blocking of the zeolite pores. This blocking of pores prevents access of the hydrocarbons to the active sites which in turn lowers the activity of the zeolite. Removal of these blockages restores access and activity to the zeolite.

References

1 J.S. Magee, *Molecular Sieves II*, ACS Symposium Series 40, J.R. Katzer, Ed., 1977, ACS, Washington, D.C., 650.

2 J.N. Miale, N.Y. Chen and P.B. Weisz, *J. Catal.*, 1966, **6**, 278.

3 J.S. Magee and J.J. Blazek, *Zeolite Chemistry and Catalysis*, ACS Monograph 171, J.A. Rabo, Ed., 1976, ACS, Washington, D.C., 615.

4 B.W. Wojciechowski and A. Corma, *Catalytic Cracking Catalysts, Chemistry and Kinetics*, 1986, Marcel Dekker Inc., New York.

5 C.J. Groenenboom, *Zeolites as Catalysts, Sorbents and Detergent Builders*, H.G. Karge and J. Weitkamp. Ed., 1989, Elsvier, 645.

6 B.R. Mitchell, *Ind. Eng. Chem. Prod. Res. Dev.*, 1980, **19**, 209.

7 F.G. Ciapetta and D.S. Henderson, *Oil Gas J.*, 1967, **65**, 88.

8 J.A. Montgomery and S.W. Letzsch, *Oil Gas J.*, 1971, **69**, 60.

9 J.V. Smith, *Zeolite Chemistry and Catalysis*, ACS Monograph 171, J.A. Rabo, Ed., 1976, ACS, Washington, D.C., 3.

10 J.R. Sohn, S.J. DeCanio, J.H. Lunsford and D.J. O'Donnel, *Zeolites*, 1986, **6**, 225.

11 B.W. Breck, **U.S. Patent No. 3, 130, 007**, 1964.

12 P.K. Maher, E.W. Alders and C.V. McDaniel, **U.S. Patent No. 3, 671, 191**, 1972.

13 E. Roland, *Zeolites as Catalysts, Sorbents and Detergent Builders*, H.G. Karge and J. Weitkamp. Ed., 1989, Elsvier, 645.

14 V.P. Shiralkar and S.B. Kulkarni, *J. Thermal Anal.*, 1982, **25**, 399.

15 A. Dyer, *Thermochimica. Acta.*, 1987, **110**, 521.

16 E. Trif, D. Strugarc, I Ivan, R. Russu, G. Gheorgue and A. Nicula, *Studia. Univ. Babes-Bolyal. Physica. XXXIII*, 1988, **1**, 79.

17 D.B. Hawkins, *Mat. Res. Bull.*,1967, **2**, 1021.

18 L.V.C. Rees, *Ann. Rep. Prog. Chem.*, 1970, **67**, 191.

19 J.W. Ward, *J. Catal.*, 1970, **18**, 348.

20 H. Bremer, W. Mörke, R. Schödel and F. Vogt, *Moleculer Sieves*, Advan. Chem. Ser. 121, W.H. Meier and J.B. Uytterhoeven, Ed., 1973, ACS. Washington, D.C., 249.

21 J. Ràkoczy and B. Sulikowski, *Polish J. Chem.*, 1980, **54**, 71.

22 R.P. Townsend, *Stud. Surf. Sci. Catal.*, 1986, **28**, 273.

23 K.R. Franklin, R.P. Townsend, S.J. Whelan and C.J. Adams, *Stud. Surf. Sci. Catal.*, 1986, **28**, 289.

24 F. Maugé, P. Gallezot, J-C. Courcelle, P. Engelhard and J. Grosmangin, *Zeolites*, 1986, **6**, 261.

25 L.V.C. Rees and T. Zuyi, *Zeolites*, 1986, **6**, 201.

26 H. Uyama, Y. Kanzaki and O. Matsumoto, *Mat. Res. Bull.*,1987, **22**, 157.

27 B.L. Khusid, G.D. Chukin, C. Gullyev and B.K. Nefedov, *Kinetics and Catalysis*, 1987, **28**, 823.

28 B. Fahlke, W. Wieker and S.P. Shdanov, *Proc. VIth Int. Symp. Heterogeneous Catalysis Part 2*, Sofia, 1987, 298.

29 R.L. Martins, A.C.B. Leite, Y.L. Lam and S.T. de Costa, *Thermochimica. Acta.*, 1988, **135**, 397.

30 C.Y. Li and L.V.C. Rees, *Reactive Polymers*, 1988, **7**, 89.

31 A. Dyer, *Inorg. Ion Exch. Chem. Anal.*, 1991, 33.

32 W.P.J.H. Jacobs, J.H.M.C. van Wolput and R.A. van Santen, *Zeolites*, 1993, **13**, 170.

33 S.F. Garcia and P.B. Weisz, *J. Catal.*, 1993, **144**, 109.

34 R. Kumar, W-C. Cheng, K. Rajagopalan, A.W. Peters and P Basu, *J. Catal.*, 1993, **143**, 549.

35 E. Trif, D. Strugarc, I Ivan, R. Russu, G. Gheorgue and A. Nicula, *J. Thermal Anal.*, 1994, **41**, 871.

36 H. Klein, H. Fuess and M. Hunger, *J. Chem. Soc. Faraday Trans.*, 1995, **91**, 1813.

37 J.V. Smith, J.M. Bennet and E.M. Flanigen, *Nature*, 1967, **215**, 241.

38 C.V. McDaniel and P.K. Maher, *Zeolite Chemistry and Catalysis*, ACS Monograph 171, J.A. Rabo, Ed., 1976, ACS, Washington, D.C., 285.

39 P.K. Maher and C.V. McDaniel, **U.S. Patent No. 3, 402, 996,** 1968.

40 R.M. Barrer and M.B. Makki, *Can. J. Chem.*, 1964, **42**, 1481.

41 G.T. Kerr, *J. Phys. Chem.*, 1968, **72**, 1385.

42 G.T. Kerr, *J. Phys. Chem.*, 1968, **72**, 2594.

43 G.T. Kerr, *J. Phys. Chem.*, 1969, **73**, 2780.

44 G.T. Kerr, *Adv. Chem. Ser.*,1973, **121**, 219.

45 D.W. Breck and G.W. Skeels, *Molecular Sieves II*, ACS Symposium Series 40, J.R. Katzer, Ed., 1977, Washington, D.C., 271.

46 P. Fejes, I. Kiricsi, I. Hannus and GY. Schöbel, *Stud. Surf. Sci. Catal.*, 1984, **24**, 263.

47 I. Dékany, F. Szántó and H.K. Beyer, *Stud. Surf. Sci. Catal.*, 1984, **24**, 385.

48 J. Scherzer, *Catalytic Materials*, ACS Symposium Series, Washington, D.C., 1984, 157.

49 J.W. Roelofsen, H. Mathies, R.L. de Groot, P.C.M. van Woerkom and H. Anga Gaur, *Stud. Surf. Sci. Catal.*, 1986, **28**, 337.

50 A.T. Steel and E. Dooryhee, *Zeolites*, 1993, **13**, 336.

51 H.K. Beyer, I.M. Belenykaja, F. Hange, M. Tielen, P.J. Grobet and P.A. Jacobs, *J. Chem. Soc. Faraday Trans. 1*, 1985, **81**, 2889.

52 P. Jacobs and J.B. Uytterhoeven, *J. Catal.*, 1971, **22**, 193.

53 P. Gallezot, R. Beaumont and D. Barthomeut, *J. Phys. Chem.*, 1974, **78**, 1550.

54 D.A. Skinner, *Ind. Eng. Chem.*, 1952, **44**, 1159.

55 S. Jaras, *App. Catal.*, 1982, **2**, 207.

56 R.H. Fish, J.J. Komlenic, *Anal. Chem.*, 1984, **56**, 510.

57 P. Sundararaman, *Anal. Chem.*, 1985, **57**, 2204.

58 R.G. Meisenheimer, *J. Catal.*, 1962, **1**, 356.

59 R.N. Cimbalo, R.L. Foster and S.J. Wachtel, *Oil Gas J.*, 1972, 112.

60 R.E. Ritter, L. Rheume, W.A. Welsh and J.S. Magee, *Oil Gas J.*, 1981, 103.

61 R.F. Wormsbecher, A.W. Peters and J.M. Maselli, *J. Catal.*, 1986, **100**, 130.

62 M. Torrealba, M.R. Goldwasser, G. Perot and M. Guisnet, *Appl. Catal. A: Rev.*, 1992, **90**, 35.

63 M.L. Occelli, *Fluid Catalytic Cracking II: Concepts in Design*, ACS Symposium Series 212, M.L. Occelli, Ed., 1991, ACS, Washington, D.C., 343.

64 A.J. Saveceno, D.T. Fanale and N.D. Coggeshal, *Anal. Chem.*, 1961, **33**, 500.

65 M.W. Anderson, M.L. Occelli and S.L. Suib, *J. Catal.*, 1990, **122**, 374.

66 M.L. Occelli, *Catal. Rev.-Sci. Eng.* 1991, **33**, 241.

67 M.L. Occelli, D. Psaras and S.L. Suib, *J. Catal.*, 1985, **96**, 363.

68 G.L. Woolery, A.A. Chin, G.W. Kirter and A.M. Huss, *Fluid Catalytic Cracking: Role in Modern Refining*, ACS Symposium Series 35, M.L. Occelli, Ed., 1989, ACS, Washington, D.C., 215.

69 M.W. Anderson, M.L. Occelli and S.L. Suib, *J. Catal.*, 1989, **118**, 31.

70 Y. Nishimura, T. Masuda, G. Sato and S. Egashira, *S. Prepr. Div. Pet. Chem. Soc.*, 1982, **28**, 707.

71 T. Masuda, M. Ogata, T. Ida, K. Takakura and Y. Nishimura, *J. Japan. Pet. Inst.*, 1983, **26**, 344.

72 J.A. Maselli and A.W. Peters, *Catal. Rev. Sci. Eng.*, 1984, **26**, 525.

73 E.L. Kugler and D.P. Leta, *J. Catal.*, 1988, **109**, 387.

74 B.K. Speronello and W.J. Reagan, *Oil Gas J.*, 1984, 139.

75 M.L. Occelli and J.M. Stencel, *Zeolites: Facts, Figures, Future Part B*, P.A. Jacobs and R.A. van Santen, Ed., Elsevier, 1989, 1311.

76 M.L. Occelli, *ACS Symposium Series 375*, 1989, 162.

77 M.T. Pope and B.W. Dale, *Q. Rev. (London)*, 1968, **22**, 527.

78 R. Pompe, S. Järås and N-G. Vannerberg, *Appl. Catal.*, 1984, **13**, 171.

79 L. Upson, S. Järås and I. Dalin, *Oil Gas J.*, 1982, 135.

80 J.E. Otterstedt, S.B. Gevert, S.G. Järås and P.G. Menon, *Appl. Catal.* 1986, **22**, 159.

81 M. Huang, S. Shan, C. Yuan, Y. Li and Q. Wang, *Zeolites*, 1990, **10**, 772.

82 C. Marchal, J. Thoret, M. Gruia, C. Dorémieux-Morin and J. Fraissard, *Fluid Catalytic Cracking II: Concepts in Design*, ACS Symposium series 212, M.L. Occelli, Ed., 1991, ACS, Washington, D.C., 343.

83 M. Petráš and B. Wichterlová, *J. Phys. Chem.*, 1992, **96**, 1805.

84 J. Thoret, C. Marchal, C. Dorémieux-Morin, P.P. Man, M. Gruia and J. Fraissard, *Zeolites*, 1993, **13**, 269.

85 J. Thoret, P.P. Man and J. Fraissard, *J. Chem. Soc. Faraday Trans.*, 1995, **96**, 1037.

86 L.N. Yannopoulos, *J. Phys. Chem.*, 1968, **72**, 3293.

87 C. V. McDaniel and P.K. Maher, *Zeolite Chemistry and Catalysis*, ACS Monograph 171, J.A. Rabo, Ed., 1976, ACS, Washington, D.C., 285.

88 P. Gallezot, B. Feron, M. Bourgogne and Ph. Engelhard, *Zeolites: Facts, Figures, Future Part B*, P.A. Jacobs and R.A. van Santen, Ed., Elsevier, 1989, 1281.

89 L.A. Pine *J. Catal.*, 1990, **125**, 514.

90 N.C. Gravette, D. Barham and L.R. Barrett, *Trans. Brit. Ceram. Soc.*, 1986, **65**, 199.

91 G.Y. Meng and R.A. Haggins, *Mat. Res. Bull.*, 1983, **18**, 581.

92 M.L. Occelli and J.M. Stencel, *Zeolites as Catalysts, Sorbents and Detergent Builders*, H.G. Kerge and J. Weitkamp, Ed., 1989, Elsvier, 127.

93 F. Maugé, J.C. Courrcelle, Ph. Engelhard, P. Gallezot and J. Grosmangin, *Proceedings 7th International Zeolite Conference*, Y. Murakami, A. Iijima and J.W. Ward, Ed., 1986, **28**, 803.

94 D.L. Mckay, **U.S. Patent No. 4, 153, 536**, 1979.

95 B.R. Mitchell and K. Vogel, **U.S. Patent No. 4, 451, 355**, 1985.

96 D.J. Rawlence, K. Gosling, L.H. Staal and A.P. Chapple, *Preparation of Catalysts V*, G. Pomcelet, P.A. Jacobs, P. Grange and B. Delmon, Ed., Elsevier, 1991, 407.

97 E.L. Kugler, **U.S. Patent No. 4, 944, 864**, 1990.

98 W.P. Hettinger, *Fluid Catalytic Cracking: Role in Modern Refining*, ACS Symposium Series 375, M.L. Occelli, Ed., 1989, ACS, Washington, D.C., 308.

99 T.I. de Jong, **U.S. Patent No. 4, 519, 897**, 1985.

100 E.H. van Brockoven, **U.S. Patent No. 4, 946, 581**, 1990.

101 R. Kumar, **U.S. Patent No. 5, 194, 413**, 1993.

102 F.J. Elvin, *Oil Gas J.*, 1987, 42.

Chapter 3

Characterisation of Samples

3 Characterisation of Samples

Three major techniques have been used for sample characterisation in this work; these are powder X-ray diffraction (XRD), surface area determination and magic-angle-spinning nuclear magnetic resonance (MAS NMR) spectroscopy. It should be noted that surface area measurements were carried out only for those samples for which significant changes were expected; that is for those containing zeolite-Y.

This chapter provides an outline description of each of the three techniques including a technical summary of the apparatus used. Details of particular experimental procedures are given and, where relevant, these are illustrated with specific examples taken from results which are to be discussed in more detail in later chapters.

3.1 X-ray Diffraction

Powder XRD is a very well established technique for the characterisation of solid samples and, as such, it has been used extensively in the present work. In general it has been used to monitor the behaviour of known crystalline phases including an assessment of the extent of crystallinity and, in addition and where appropriate, to identify the emergence of new phases as a function of sample treatment. An important further application has been in the investigation of changes of the unit cell constant for zeolite-Y as a function of the treatment of samples containing this zeolite.

3.1.1 Background

X-ray diffraction can be used to study the properties and structure of crystalline solids, and a number of detailed accounts of the technique are available (see, for example, references 1-6). This section provides a brief description of the technique, together with an account of some of the important properties of X-rays and crystalline solids that permit the diffraction phenomenon to be observed.

In 1912 Laue first demonstrated the ability of crystalline solids to diffract X-rays. His experiment confirmed that X-rays had the same properties as electromagnetic radiation and that crystals had an ordered array of atoms.

Properties of X-rays

X-rays were first discovered in 1895 by Röentgen and were so called as their properties were unknown at that time. Today it is known that X-rays are electromagnetic radiation of the same nature as light, but of very much smaller wavelength. X-rays are found between gamma rays and ultraviolet light in the electromagnetic spectrum and have wavelengths in the range 0.001-1 nm. X-rays that are used for diffraction purposes have wavelengths between, approximately, 0.05-0.25 nm. X-rays, like all electromagnetic radiation, have an electric field vector (**E**) and magnetic field vector (**H**) normal to the direction of propagation, as well as being normal to one another.

It is the electric field vector that interacts with the electrons of the atom (ion) in a crystal such that X-rays are scattered in all directions, and it will be only this component of the wave that will be considered further (the scattering of X-rays by atoms in a crystal will be discussed later in this section). The electric field vector has an oscillating behaviour as it travels out in the z direction with velocity c. This can be described by the expression

$$E = E_0 \sin 2\pi\nu \left(t - \frac{z}{c} \right) \tag{3.1}$$

where E_0 is the amplitude and ν the frequency. This expression describes the behaviour with time (t) at a fixed value of z or, alternatively, the behaviour with position (z) at a fixed value of time.

The wave picture of X-ray radiation allows a relatively simple description of the manner in which different waves can interact. Any two waves with identical wavelengths (λ) which are in phase (their electric field vectors have the same magnitude and direction at the same instant in time at any point z measured along the direction of propagation of the wave), or differ in phase by a whole number of wavelengths, will reinforce one another. This type of

interference is called constructive interference. If waves are out of phase then destructive interference occurs. Any two waves (with identical wavelengths) that differ in phase by $\lambda/2$ completely annul one another. It is constructive and destructive interference which are intrinsic to the diffraction process.

In general constructive and destructive interference is observed for all types of electromagnetic radiation. For example, if visible light (with fixed λ and ν) is passed through a diffraction grating (consisting of equally spaced lines) then equally spaced spots can be observed, but only if the spacing between the lines etched on the diffraction grating is of the same order of magnitude as the wavelength of the incident light (Figure 3.1). The dark spots result from destructive interference.

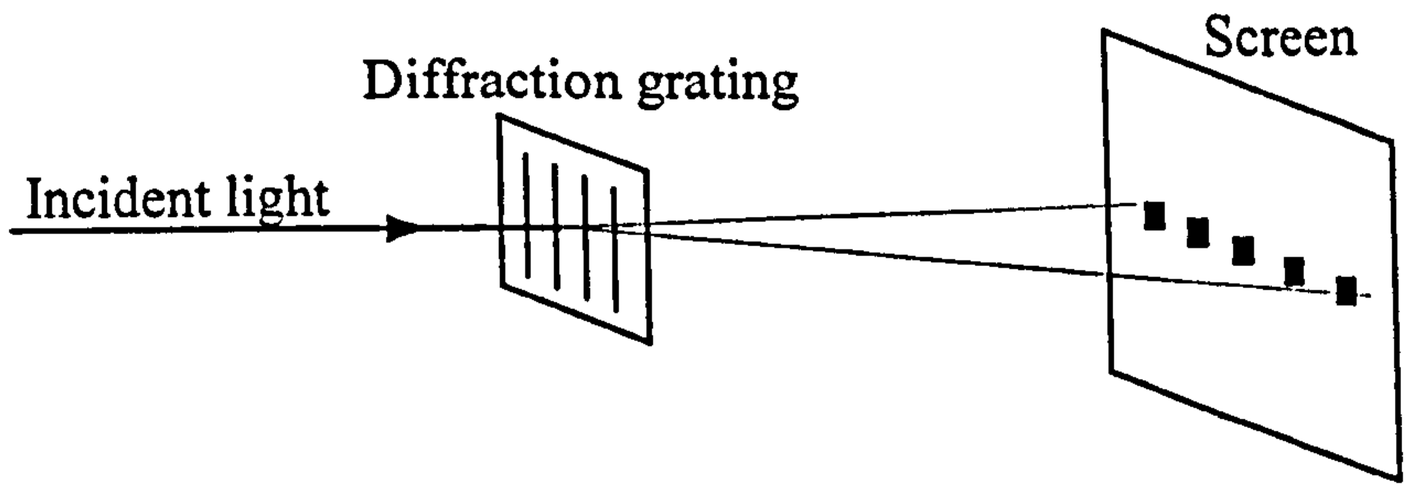

Figure 3.1 Schematic view of constructive and destructive interference.

Diffraction of X-rays by crystalline solids is essentially similar in nature. However the crystal acts as a three-dimensional diffraction grating and irradiation is now with X-rays. X-rays are used because their wavelengths are of the same order of magnitude as interatomic distances in crystalline solids.

X-rays are produced when any electrically-charged particle of sufficient kinetic energy is rapidly decelerated. High energy electrons are typically used for this purpose. Today, X-rays are usually produced in an X-ray tube, this contains a source of electrons and two metal electrodes. The high voltage maintained across the electrodes (tens of thousands of volts) rapidly draws electrons to the anode, or target, which they strike with very high velocity. X-rays are produced at the point of impact and radiate in all directions. X-rays of a range of wavelengths are produced (continuous radiation or Bremstrahlung) and the variation of intensity with wavelength is dependent on the accelerating voltage. However, above a certain accelerating voltage a characteristic spectrum is produced, superimposed on

the continuous radiation. This spectrum depends on the nature of the target metal, as shown in Figure 3.2, and does not change with an increase in accelerating voltage.

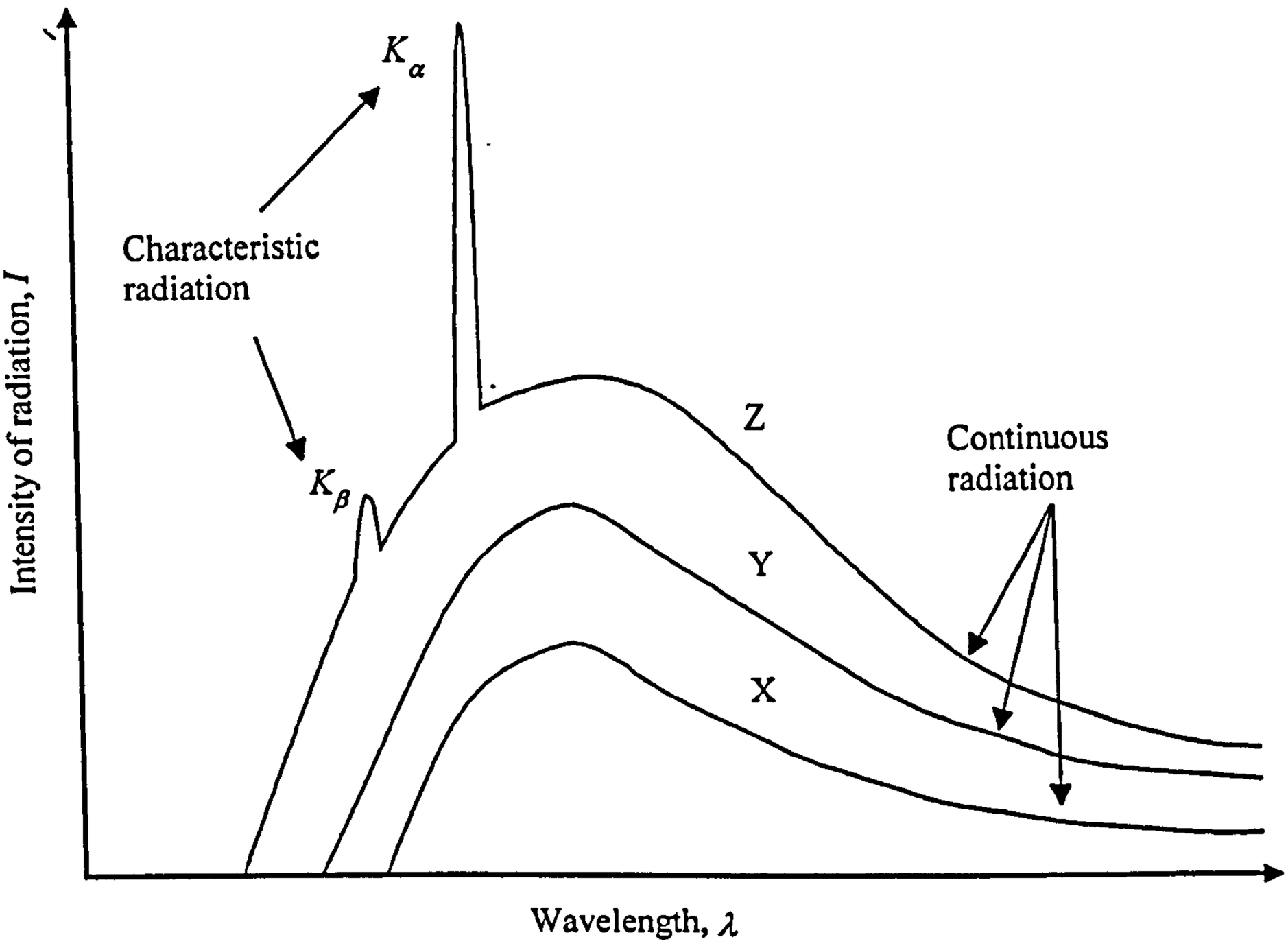

Figure 3.2 Graph illustrating the variation of intensity, I, with wavelength, λ, for the continuous, as well as characteristic, radiation formed when the accelerating voltage is increased. The accelerating voltages are X, Y and Z where X < Y < Z. K_α and K_β represent the characteristic radiation.

A continuous band of radiation is produced because the incident electrons are not all decelerated in the same way. Some electrons will be stopped with one impact and so will give up there energy at once. Others are only deviated by the atoms of the target, and successively lose fractions of there total energy. The characteristic radiation is produced due to the interaction of the incident high-energy electrons with electrons in the core shells of the target metal. If in a collision an electron is ejected from the K shell of a target metal atom then this atom is left in an excited state. Electrons from higher shells (L, M,...) will fall into this vacancy in the K shell, releasing excess energy in the process, and the atom is

once again in its normal energy state. The excess energy is emitted in the form of radiation of a definite wavelength and is, in fact, the characteristic K_α , K_β radiation. The overall process is shown schematically in Figure 3.3.

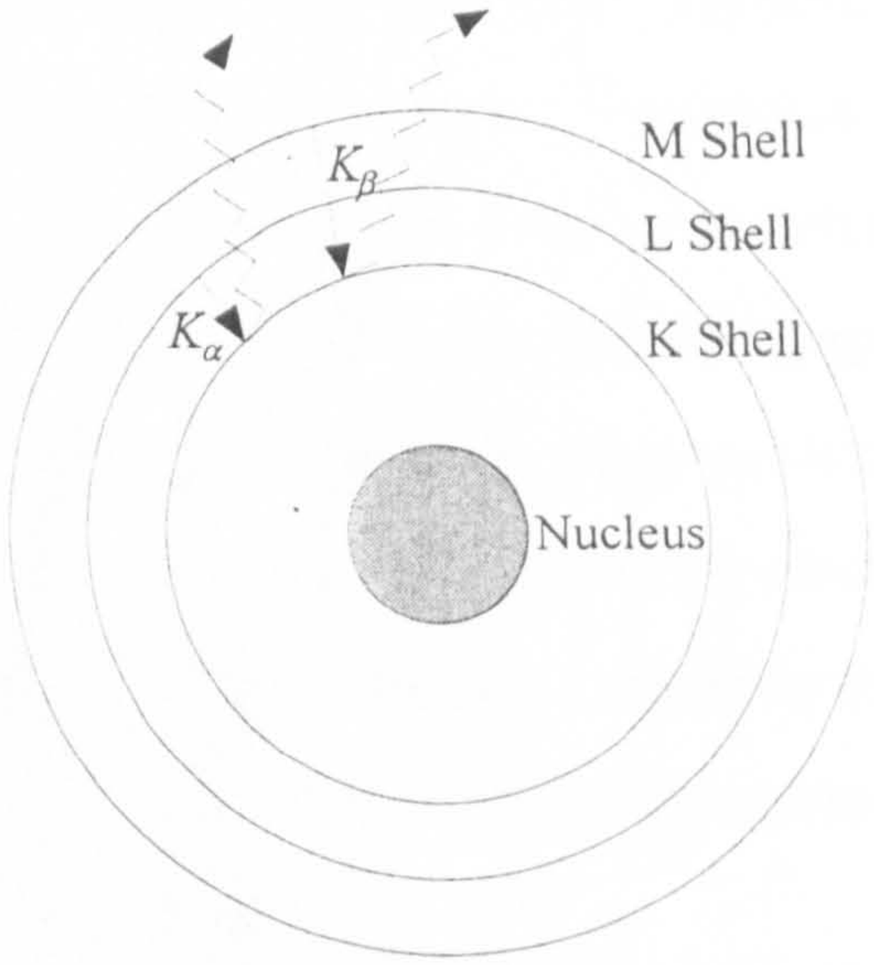

Figure 3.3 The mechanism by which K_α and K_β radiation is formed.

Table 3.1 gives the characteristic wavelengths (in both Å and nm) for copper, a metal target used frequently in X-ray tubes.

Radiation type	Transition	Wavelength /nm	Wavelength /Å
$K_{\alpha 1}$	$2p \rightarrow 1s$	0.15405	1.54050
$K_{\alpha 2}$	$2p \rightarrow 1s$	0.154434	1.54434
K_β	$3p \rightarrow 1s$	0.139217	1.39217

Table 3.1 The characteristic wavelengths, K_α and K_β , for copper metal.

It can be seen from Table 3.1 that K_α is in fact a doublet. This is due to two different total angular momentum states of the 2p electron. Diffraction due to Cu $K_{\alpha 1}$ and $K_{\alpha 2}$ irradiation can be seen in an XRD pattern, becoming more resolved as the diffraction angle increases.

If a K_α X-ray source is required then X-ray filters are used. Nickel is used as a filter for copper K_β , and most of the continuous radiation, because it absorbs X-rays. It is not 100% efficient, but essentially Cu K_α X-ray radiation is produced.

The basic diffraction condition

As was stated earlier it is the interaction of the X-ray electric field vector with electrons of atoms that is responsible for the scattering of X-rays. In general an electric field exerts a force on any charged particle, such as an electron. Thus, the oscillating field of an X-ray beam will set any electron it encounters into oscillatory motion about its mean position. This electron will be continuously accelerating and decelerating during its motion and, therefore, will emit an electromagnetic wave (the X-ray gun is an example of this, rapidly decelerating electrons producing X-rays). In this sense, an electron is said to scatter X-rays and the scattered beam is simply the beam radiated by the electron under the action of the incident beam. The scattered beam has the same frequency and phase as the incident beam and is said to be coherent with it.

As atoms scatter incident X-rays in all directions, then in some directions the scattered beams will be completely in phase and so reinforce each other to form a diffracted beam. A diffracted beam may be defined as a beam composed of a large number of scattered rays mutually reinforcing one another.

The Bragg law of X-ray diffraction describes the condition necessary for a set of crystalline planes to diffract an incident X-ray beam. It can be derived from Figure 3.4.

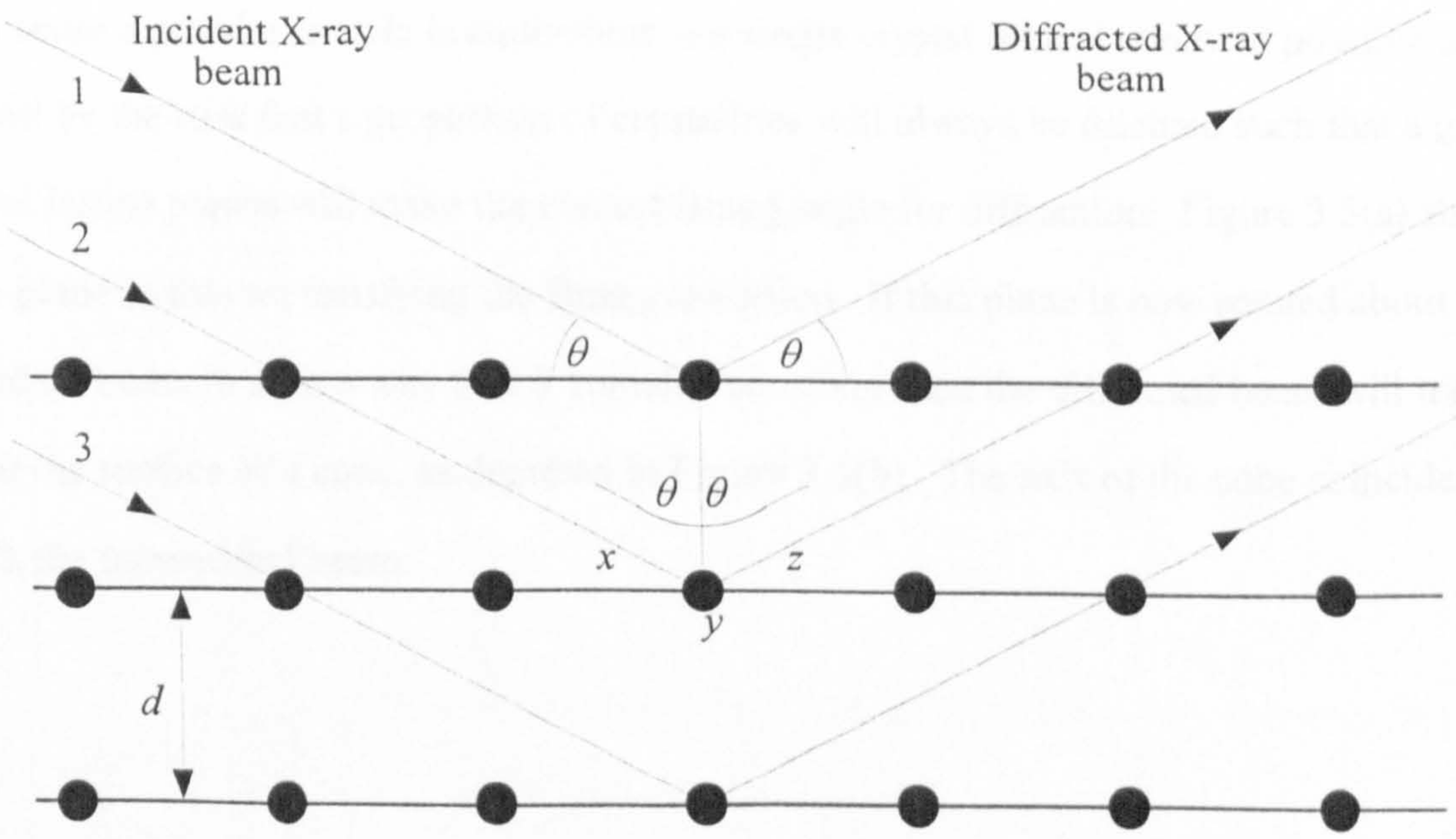

Figure 3.4 Schematic representation of the diffraction of an X-ray beam (1,2,3) incident at an angle θ to parallel planes of spacing d.

It can be seen that the path difference between incident beams 1 and 2 is $xy + yz$. However, xy and yz are both, individually, equal to $d\sin\theta$. It follows that the path difference between the two beams is given by Equation 3.2.

$$xy + yz = 2d\sin\theta \tag{3.2}$$

Since the condition for diffraction requires the diffracted beams to be in phase, or differ in phase by an integral number of wavelengths, then for diffraction to be observed Equation 3.3 must be satisfied

$$xy + yz = n\lambda \tag{3.3}$$

where λ is the wavelength of the X-rays and n is an integer. Combining Equations 3.2 and 3.3 gives the diffraction condition.

$$n\lambda = 2d\sin\theta \tag{3.4}$$

This is the Bragg law where n is the order of diffraction and θ is known as the Bragg angle.

The simple model in Figure 3.4 can be extended to single crystals as well as polycrystalline, or powder, systems; here only the latter will be considered. A powder is defined as a collection of randomly oriented small crystallites. Within a powder sample, all possible orientations of all planes with respect to the incident beam will be present. In this sense a powder sample is equivalent to a single crystal rotated about all possible axes. It will be the case that a proportion of crystallites will always be oriented such that a given set of lattice planes will make the correct Bragg angle for diffraction. Figure 3.5(a) shows one plane in this set satisfying the Bragg condition. If this plane is now rotated about the incident beam in such a way that θ remains constant, then the diffracted beam will travel over the surface of a cone, as depicted in Figure 3.5(b). The axis of the cone coincides with the transmitted beam.

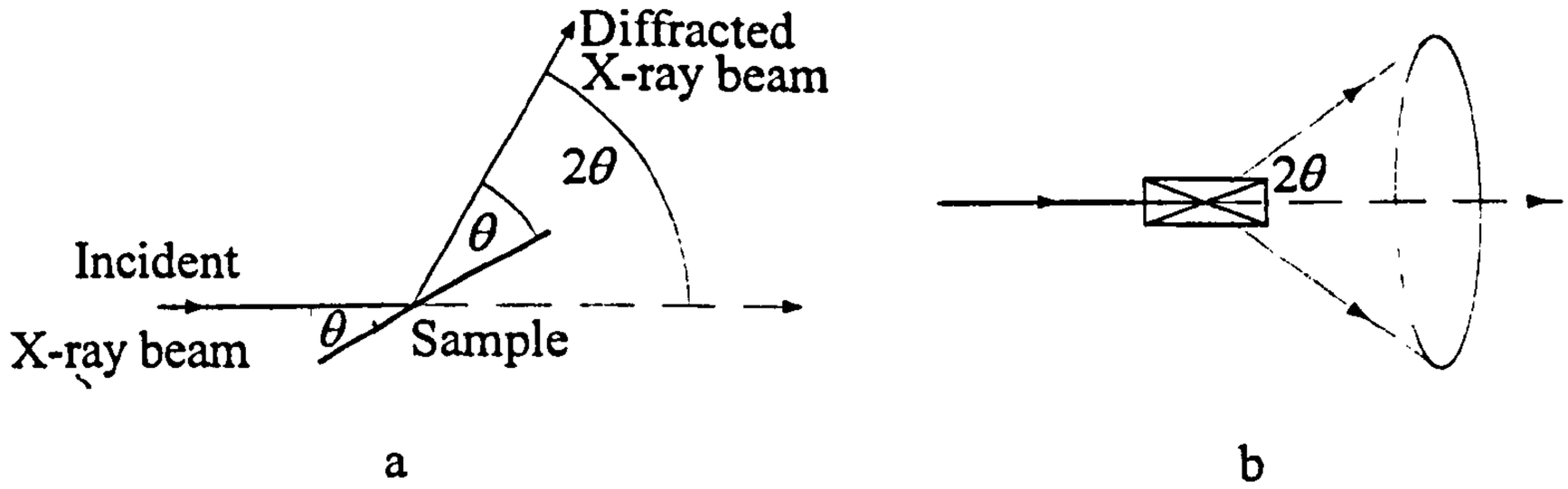

Figure 3.5 Diagram showing (a) the Bragg condition for one set of lattice planes, and (b) the formation of a diffraction cone due to the same plane from a number of randomly oriented crystallites.

It follows that a separate diffraction cone will be formed for each set of differently-spaced lattice planes. Diffracted X-rays from sets of planes of spacing d_1 generate a cone of semi-apex $2\theta_1$, planes of spacing d_2 generate a cone of angle $2\theta_2$ and so on, as displayed in Figure 3.6. The pattern of concentric rings resulting from the diffracted cones can be recorded, for example, by placing a photographic film in a circle about the sample: in this way angles of $0° < 2\theta < 180°$ can be measured. More modern methods of recording powder XRD patterns will be described in due course.

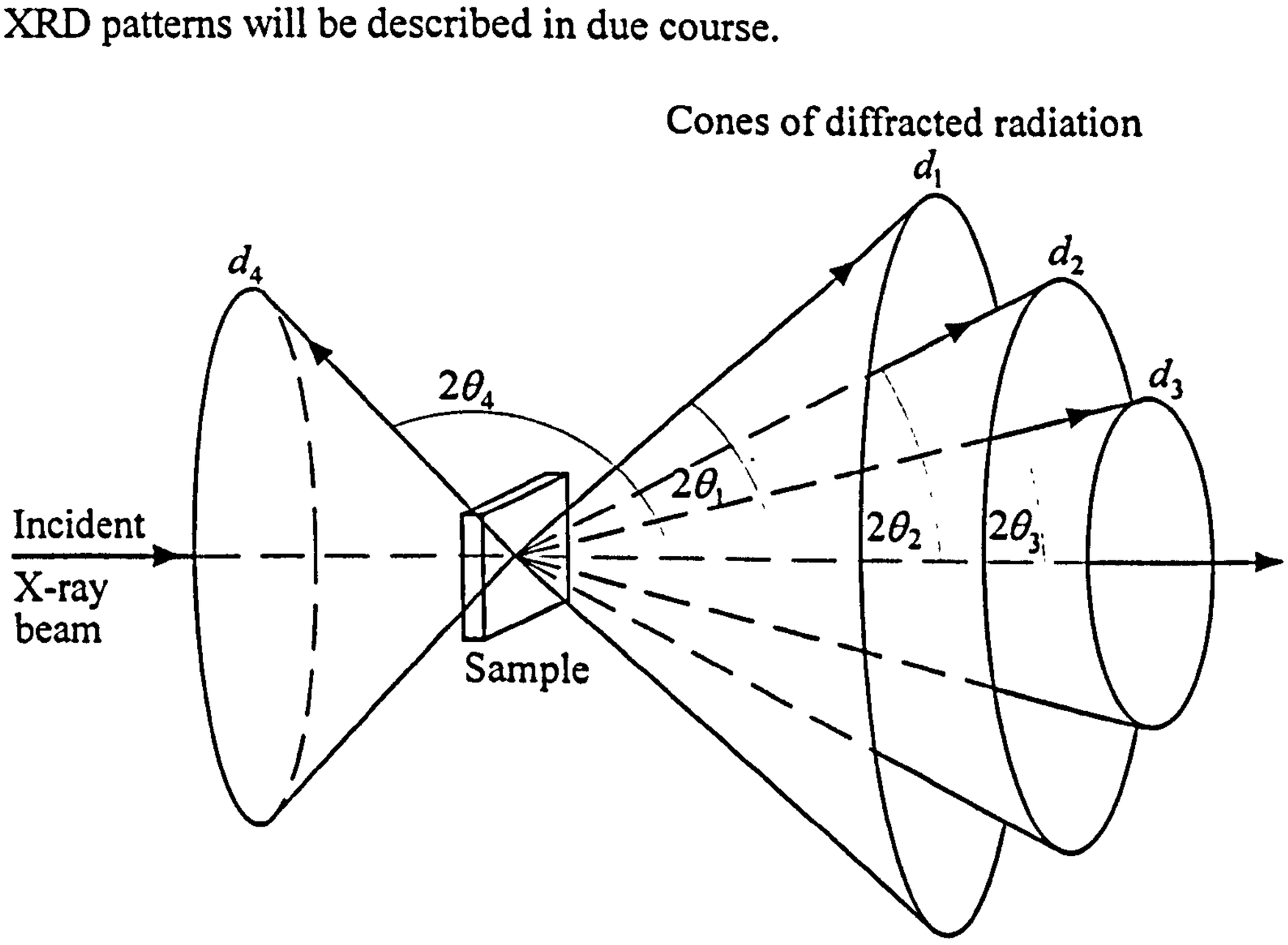

Figure 3.6 Diagram showing the formation of diffraction cones for a powder sample.

Crystals and crystal structure

Crystals are constructed from repeating blocks which build up in three dimensional space. The smallest unique building block is called the unit cell. There are seven possible different-shaped unit cells which can pack to fill three-dimensional space; these give the seven possible different crystal systems, each with different symmetry elements as summarised in Table 3.2. In the table the dimensions of the unit cells are denoted by a, b and c, and the corresponding angles by α, β and γ. Collectively a, b, c, α, β and γ are known as the lattice constants for a unit cell.

If the sites of atoms (ions) in a crystal structure are represented by points, then the array of points forms a three-dimensional lattice. The unit cell is the smallest (unique) regular figure by which continuous replication generates the entire lattice. Unit cells can contain lattice points in different arrangements. A unit cell with lattice points only at the corners is primitive (P), a cell which has a lattice point in the centre is body-centred (I), one which has lattice points in the centres of all the faces is face-centred (F), and one which has lattice points in the centre of two opposite faces is face-centred (A, B or C). Combining the possible crystal systems with the possible types of lattice gives the Bravais lattice of the structure; there are only 14 possible Bravais lattices. Table 3.2 summarises the Bravais lattices associated with the seven different crystal systems and, as an example, the Bravais lattices for the orthorhombic crystal system are illustrated in Figure 3.7. It should be noted that zeolite-Y has a cubic unit cell.[7]

Crystal system	Shape of crystal system	Axial lengths and angles	Bravais lattice	Lattice symbol
Cubic	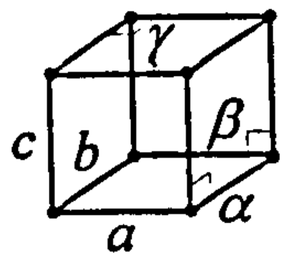	$a = b = c$ $\alpha = \beta = \gamma = 90°$	Simple Body-centred Face-centred	P I F
Tetragonal	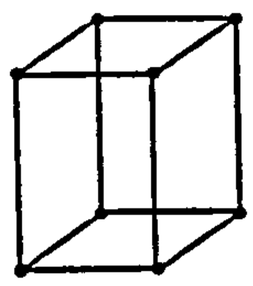	$a = b \neq c$ $\alpha = \beta = \gamma = 90°$	Simple Body-centred	P I
Orthorhombic	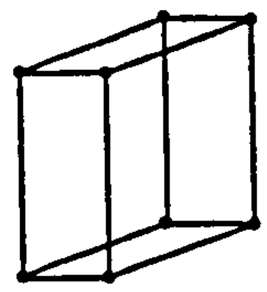	$a \neq b \neq c$ $\alpha = \beta = \gamma = 90°$	Simple Body-centred Base-centred Face-centred	P I C F
Rhombohedral or Trigonal	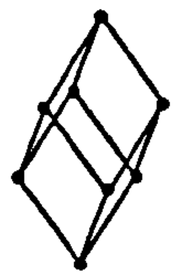	$a = b = c$ $\alpha = \beta = \gamma \neq 90°$	Simple	P
Hexagonal	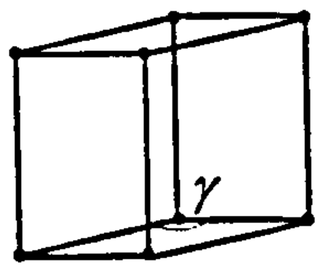	$a = b \neq c$ $\alpha = \beta = 90°$, $\gamma = 120°$	Simple	P
Monoclinic	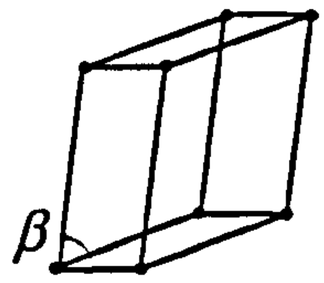	$a \neq b \neq c$ $\alpha = \gamma = 90° \neq \beta$	Simple Base-centred	P C
Triclinic	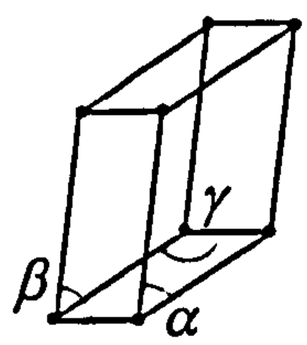	$a \neq b \neq c$ $\alpha \neq \beta \neq \gamma \neq 90°$	Simple	P

Table 3.2 The seven possible crystal systems and the fourteen Bravais lattices associated with these crystal systems.

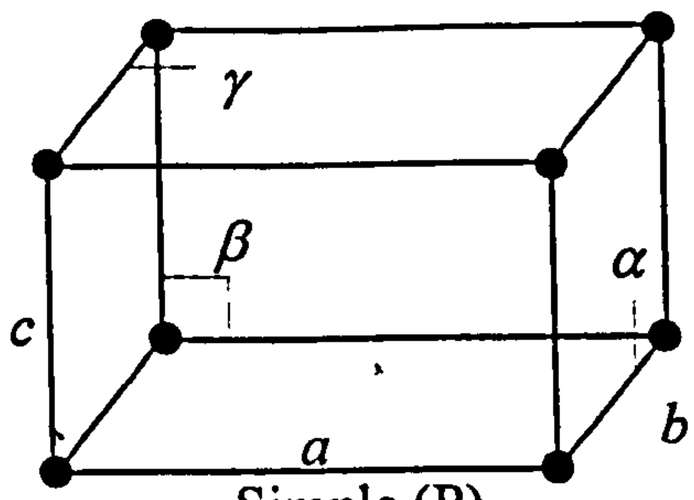

Simple (P)

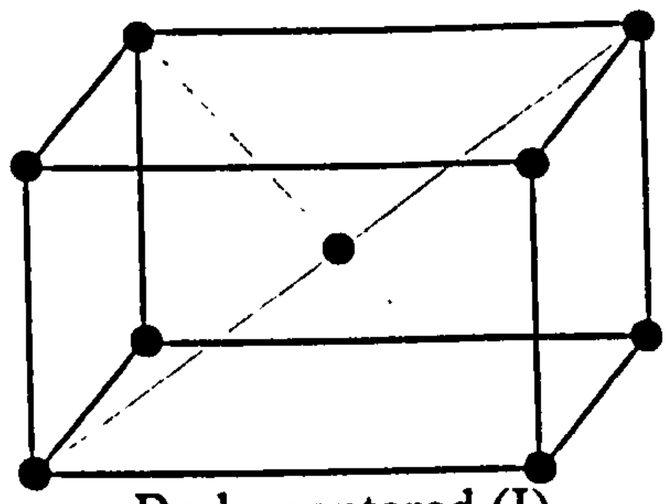

Body-centered (I)

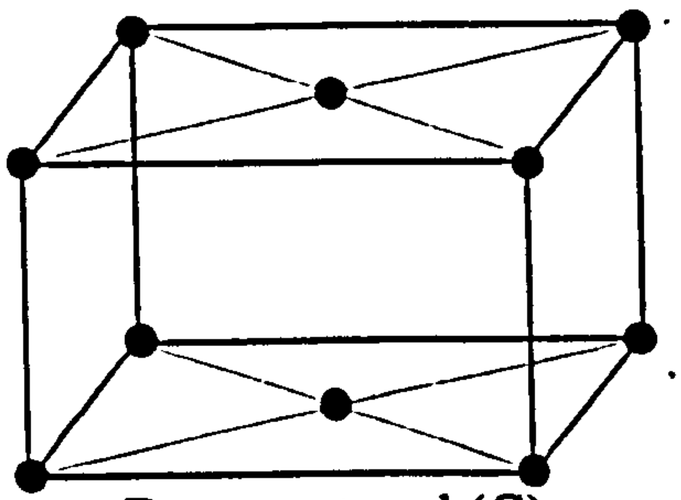

Base-centered (C)

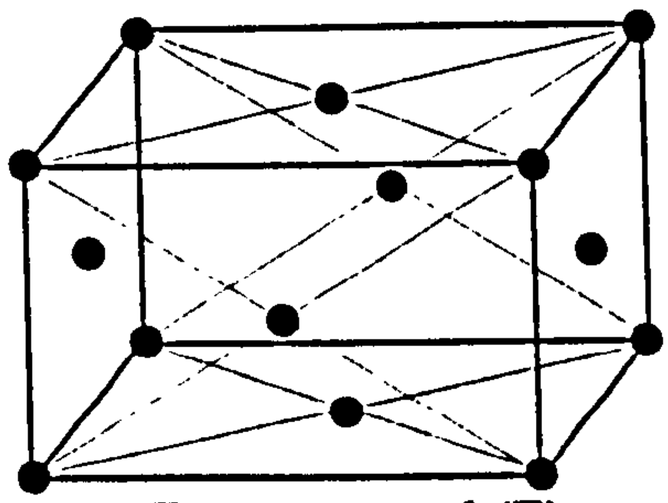

Face-centered (F)

Figure 3.7 Diagram illustrating the four Bravais lattices associated with the orthorhombic crystal system ($a \neq b \neq c$, $\alpha = \beta = \gamma = 90°$).

Crystalline planes and diffraction

A English crystallographer Miller devised a system for identifying and labelling planes of atoms in a crystal. The Miller index, as it is known, describes a plane of atoms within a crystal and this plane will be, in principle, responsible for a particular diffracted X-ray beam. Miller indices are defined as the reciprocals of the fractional intercepts which a given plane makes with the crystallographic axes within a unit cell. Miller indices of a general plane are denoted (hkl), and this plane makes fractional intercepts $1/h$, $1/k$, $1/l$ with the crystallographic axes. In terms of the lattice constants a, b, c then the actual intercepts are a/h, b/k, c/l. Figure 3.8 illustrates two different Miller indices for a cubic unit cell.

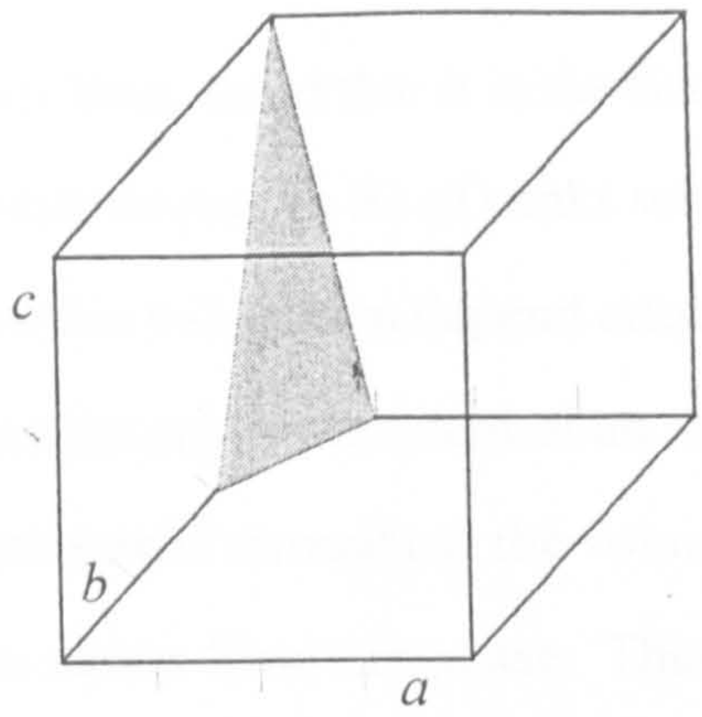

Miller index (431)

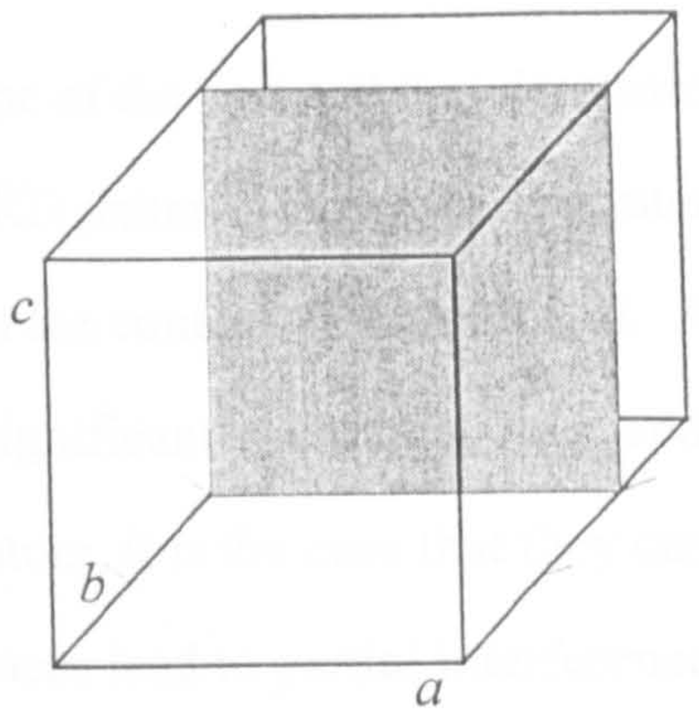

Miller index (030)

Figure 3.8 Diagram illustrating the labelling of two different planes in a cubic unit cell.

Miller indices are used in XRD to relate particular sets of crystalline planes to diffraction peaks. Each Bragg angle θ, for a given diffraction peak with Miller index (*hkl*), can be used to calculate an interplanar spacing, *d*. The spacing of different planes d_{hkl}, depends only on the crystal system and the lattice dimensions. As a consequence, two crystals having the same type, and dimension, of unit cell will give the same XRD pattern.

In more detail, the interplanar spacing d_{hkl}, measured at right angles to a given set of planes, is a function of (*hkl*) and the lattice constants $(a,b,c,\alpha,\beta,\gamma)$; the exact relation depends on the crystal system involved. For a cubic system, the relationship is relatively straightforward,

$$d_{hkl} = \frac{a}{\sqrt{h^2 + k^2 + l^2}} \tag{3.5}$$

Examples of the calculation of the unit cell constant for the cubic system of zeolite-Y will be given in Section 3.1.3. Expressions for d_{hkl} for other systems are more complex but are tabulated in the literature.[5]

A key step in the analysis of an XRD pattern is indexing, that is the designation of specific diffraction peaks to (*hkl*) planes. This can be achieved manually, or via computer software, but often the process is not trivial: a full description is given in the literature.[2] Once a pattern is indexed it is possible to calculate interplanar spacings and, in turn, use these to refine the lattice constants.

It has already been stated that it is the size and shape of the unit cell that determines the positions (with respect to θ) of peaks within an XRD pattern. However, the intensities of the peaks within this pattern depend critically upon the content of the unit cell. As electrons are the only component of an atom that significantly scatter X-rays, and as electrons are spread throughout the volume of an atom, it is the case that they cannot be expected to scatter X-rays in phase. These differences lead to partial interference and, as a consequence, a decrease in the scattering amplitude for an atom. The scattering efficiency of an atom for X-rays is described by the atomic scattering factor (*f*), also known as the form factor. The atomic scattering factor is largely dependent upon the number of electrons in an atom; that is it is roughly proportional to the atomic number. For a unit cell containing several atoms the intensity of the diffraction peak for a given plane (*hkl*) depends upon both the positions within the unit cell, and the scattering factors, of these atoms. Overall this is reflected in the structure factor F_{hkl} for the unit cell. Other factors that also affect the intensities of diffraction peaks are (i) the multiplicity factor, which accounts for different planes within the crystal system having the same interplanar spacing; (ii) the Lorentz-polarisation factor, which account for polarisation effects in the X-ray scattering process; (iii) the absorption factor, which accounts for the absorption of X-rays by the sample; and (iv) the temperature factor which accounts for the thermal vibrations of atoms within the unit cell.

In qualitative terms an XRD pattern is a fingerprint of a crystal and can be used to identify its chemical nature. This can be achieved by reference to published XRD charts[8] or, more efficiently, by searching appropriate computer data bases. XRD charts are generally organised so that the three most intense peaks are listed first, followed by other peaks in the pattern (typically 6). The charts are searched by matching the three most intense XRD peaks for the recorded XRD pattern with the published data. Computer searches using data bases are similar, but the relative intensities of various peaks can also be matched. This results in a more accurate match of sample with standard. A CD-ROM data base (Joint Committee on Powder Diffraction Standards, JCPDS, version 2.11a, PDF-2, database sets 1-40, 1990) has been used extensively in the work in this thesis.

Powder diffraction methods

One method of recording an XRD powder pattern is to use a Debye-Scherrer camera. A typical arrangement is shown schematically in Figure 3.9

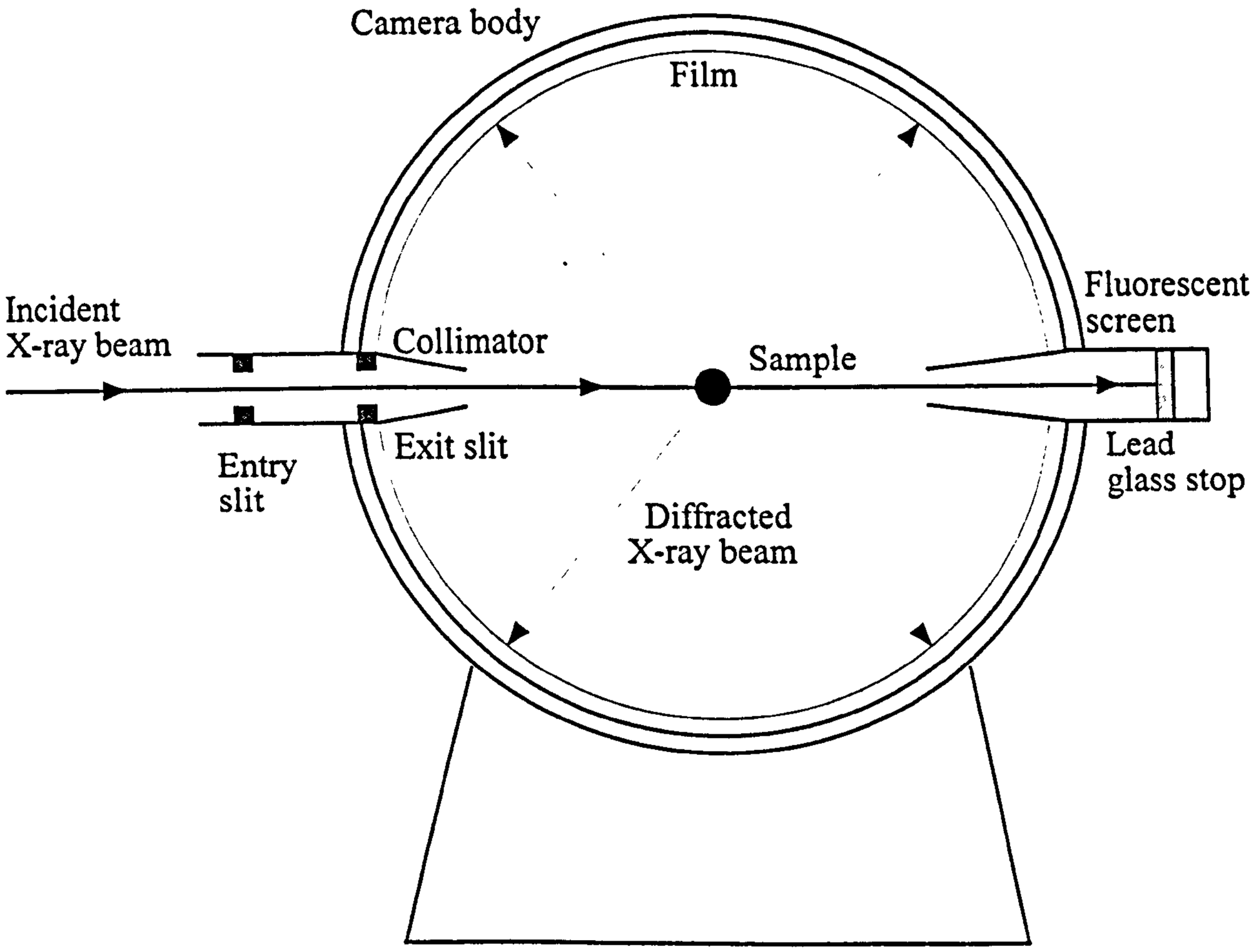

Figure 3.9 Schematic representation of a Debye-Scherrer camera arrangement for recording XRD powder patterns.

The Debye-Scherrer camera consists of a light-tight cylindrical chamber into which the X-ray beam is admitted via a collimator arrangement. The powder specimen is prepared in the form of a narrow cylinder, either by coating it on a gummed glass fibre, or enclosing it in a capillary tube. The sample is rotated about the axis of the cylinder in order to compensate for any preferred orientations of the crystallites and so effectively ensure that the crystallites are distributed at random with respect to the incoming beam. The pattern is recorded using photographic film held on the interior of the cylindrical chamber. The diffracted X-ray cones are recorded as arcs on the film, as shown in Figure 3.10.

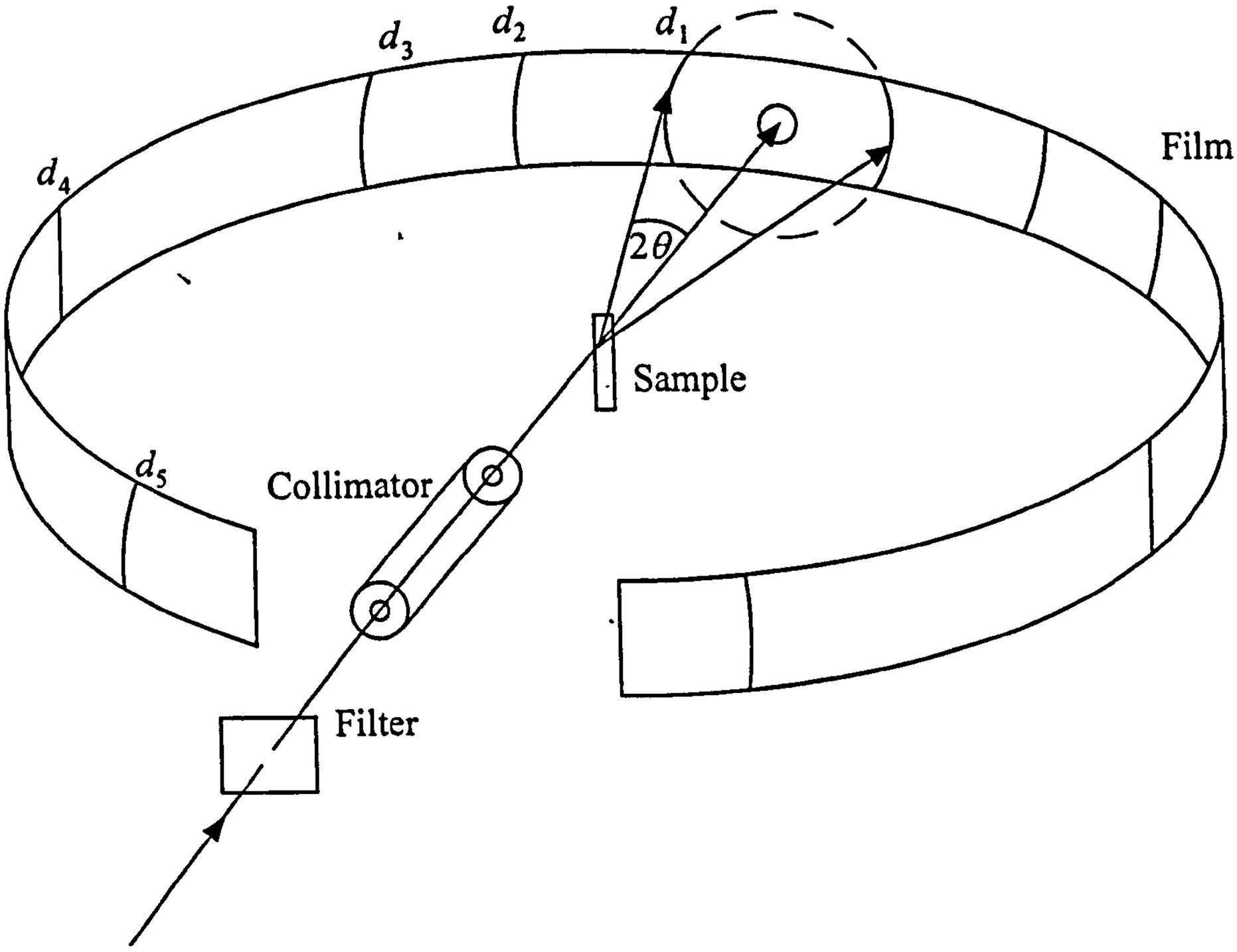

Figure 3.10 Diagram showing the recording of X-ray cones by the Debye-Scherrer method.

The diffraction angle (2θ) for each of the diffracted cones can be calculated from the diameter of the cone, that is,

$$2\theta = \frac{AB}{R} \tag{3.6}$$

where 2θ is the cone angle (in radians), AB is the diameter of the cone of the diffracted X-rays, and R is the radius of the film.

Today most XRD patterns are recorded on a computer-controlled diffractometer. Figure 3.11 shows a schematic representation of a typical modern diffractometer.

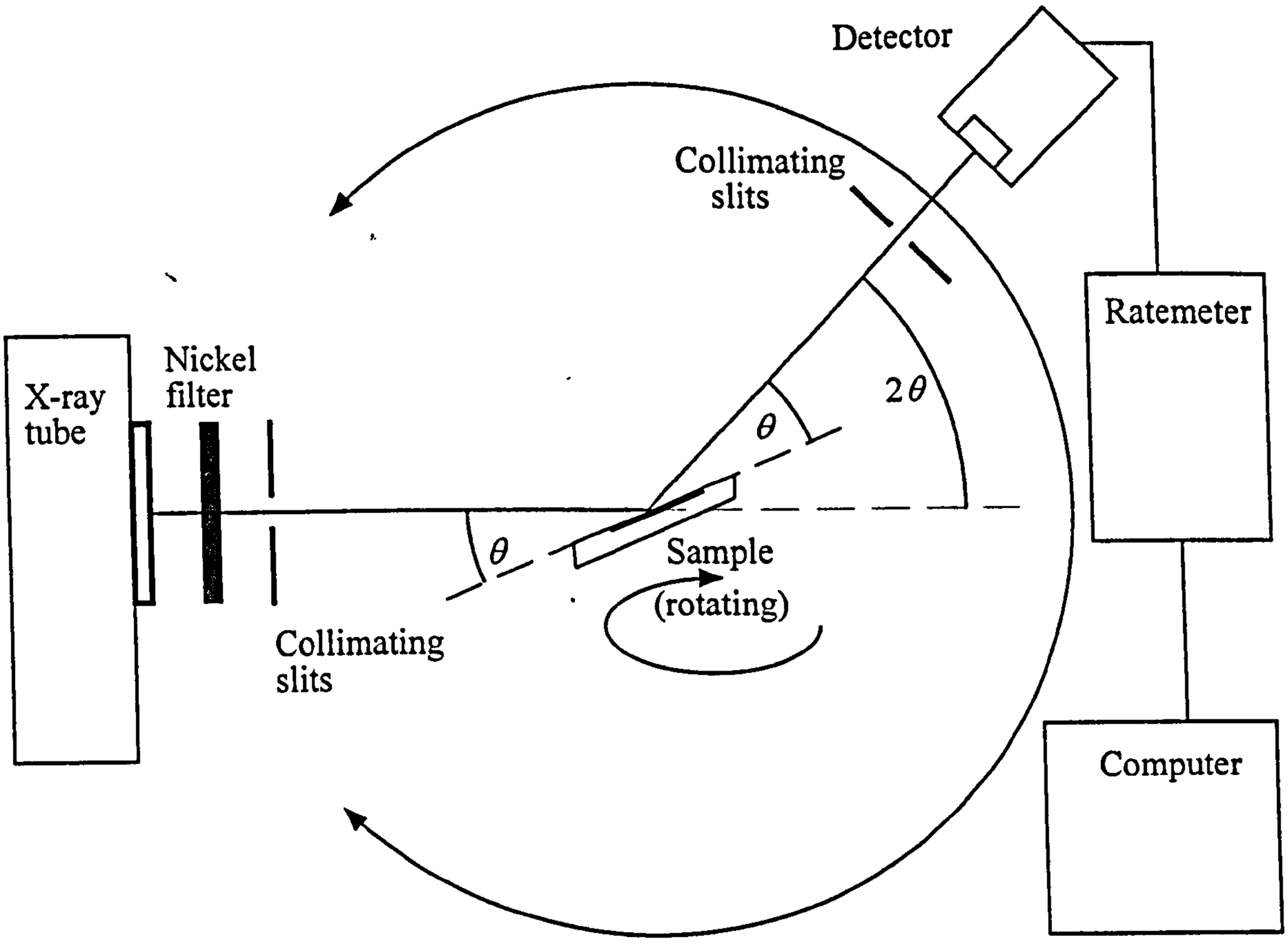

Figure 3.11 Schematic representation of a modern powder X-ray diffractometer.

Again the sample, usually formed on a flat plate, is rotated at a constant rate (in a plane normal to the paper). The sample is also rotated (in the plane of the paper) through θ (the Bragg angle) and the detector is rotated simultaneously through 2θ. In this way only diffracted cones with the correct Bragg angle are recorded.

The detector converts the X-rays into electric pulses, and the number of pulses per unit time is proportional to the intensity of the diffracted X-ray beam. In this way an XRD pattern is recorded in the form of intensity versus 2θ. Modern diffractometers are interfaced directly to computers and the XRD pattern is stored digitally.

3.1.2 Instrumentation

All X-ray diffraction patterns presented in this thesis were recorded on a Siemens D5000 diffractometer. The diffractometer is linked directly to a Dell 386 personal computer equipped with DIFFRAC.AT (version 3.1) software for storing and displaying recorded data. As already indicated a CD-ROM data base was available.

The diffractometer produces X-rays via a copper metal target using an X-ray tube incorporating a tungsten filament with a current of 30 milliamps; the electron acceleration voltage was 30 kilovolts. X-rays leave the X-ray tube via a beryllium window, and are collimated using a slit of 2 mm. A nickel filter removes the K_β, and most of the continuous X-ray radiation, to produce an almost pure K_α X-ray beam.

A scintillation detector is used to record the diffracted X-ray beam; this was equipped with three collimating slits of 2 mm, 0.2 mm and 6 mm, in that order.

3.1.3 Experimental Procedure

All samples were prepared for X-ray diffraction in the same way, however, different programs for running the X-ray diffractometer were used depending upon sample type.

Sample preparation

Samples were carefully loaded into standard sample holders and a glass slide was used to ensure that the surface of the sample was as flat as possible. Samples that contained zeolite-Y, (that is zeolite-Y powder or FCC samples), were first spiked with a silicon standard (National Bureau of Standards, 640b) before loading; approximately 4% by mass was used. Samples which were spiked were shaken vigorously, using a flask shaker, to ensure good mixing. The silicon spike was used so that accurate measurements of unit cell constants could be made, as described in more detail later.

The same sample holder was used for every sample studied throughout the course of this work, therefore, within any class of sample (model zeolite-Y, FCC samples etc.) it is reasonable to expect that approximately the same mass of samples was used.

Diffractometer settings

In the main only two different types of diffractometer setting were used and these were determined by the type of sample to be investigated. Diffractometer settings relate to how

the sample and detector are moved during the collection of data, that is the step angle and the speed.

For FCCs, which were ~60 μm particles, effective packing of the sample holder was difficult, and hence the diffractometer was set into continuous scan mode at a rate of 0.02° per second between angles of 5-70° in 2θ. Continuous scan was used, as opposed to step scan, to prevent jarring and hence stop the movement of the sample within the sample holder. All other samples, which were fine powders, the diffractometer was set to step scan at 0.02° per second between angles of 5-70° in 2θ.

All scans were approximately one hour in length.

Unit cell constant determination

Two different methods were used for the determination of the unit cell constants for zeolite-Y containing samples. For neat zeolite-Y powder samples, the unit cell constants were determined as averages of three peaks, in the diffraction patterns. The (440), (533) and (642) peaks at approximately 20°, 23.5° and 27.5°, respectively, in 2θ were used. These peaks were chosen as they remain relatively strong, and well resolved, even after deactivation treatments. For FCC samples the unit cell constant was determined from a single peak in the XRD pattern. The (533) peak at approximately 23.5° in 2θ was used. Only one peak was used because the XRD pattern of clay particles present in the FCC samples had a masking effect on the (440) and (642) peaks of zeolite-Y even for relatively mild deactivation treatments.

To determine a unit cell constant for a zeolite-Y containing sample, the following procedure was used. For the silicon standard (unit cell constant 5.430940±0.000035 Å) the (111), (220) and (311) diffraction peaks were chosen as calibration peaks. For a given spiked diffraction pattern the recorded positions in 2θ of these peaks were fed into a calibration program. This program determines a quadratic equation (as a function of 2θ) which has parameters which best translate the observed 2θ positions of the silicon calibration peaks to those of their calculated positions. This equation is then used to

correct all other peaks of interest in the XRD pattern. In this way corrected 2θ positions for zeolite-Y peaks can then be used to compute a reliable unit cell constant. An example of this procedure is described below using the diffraction pattern shown in Figure 3.12.

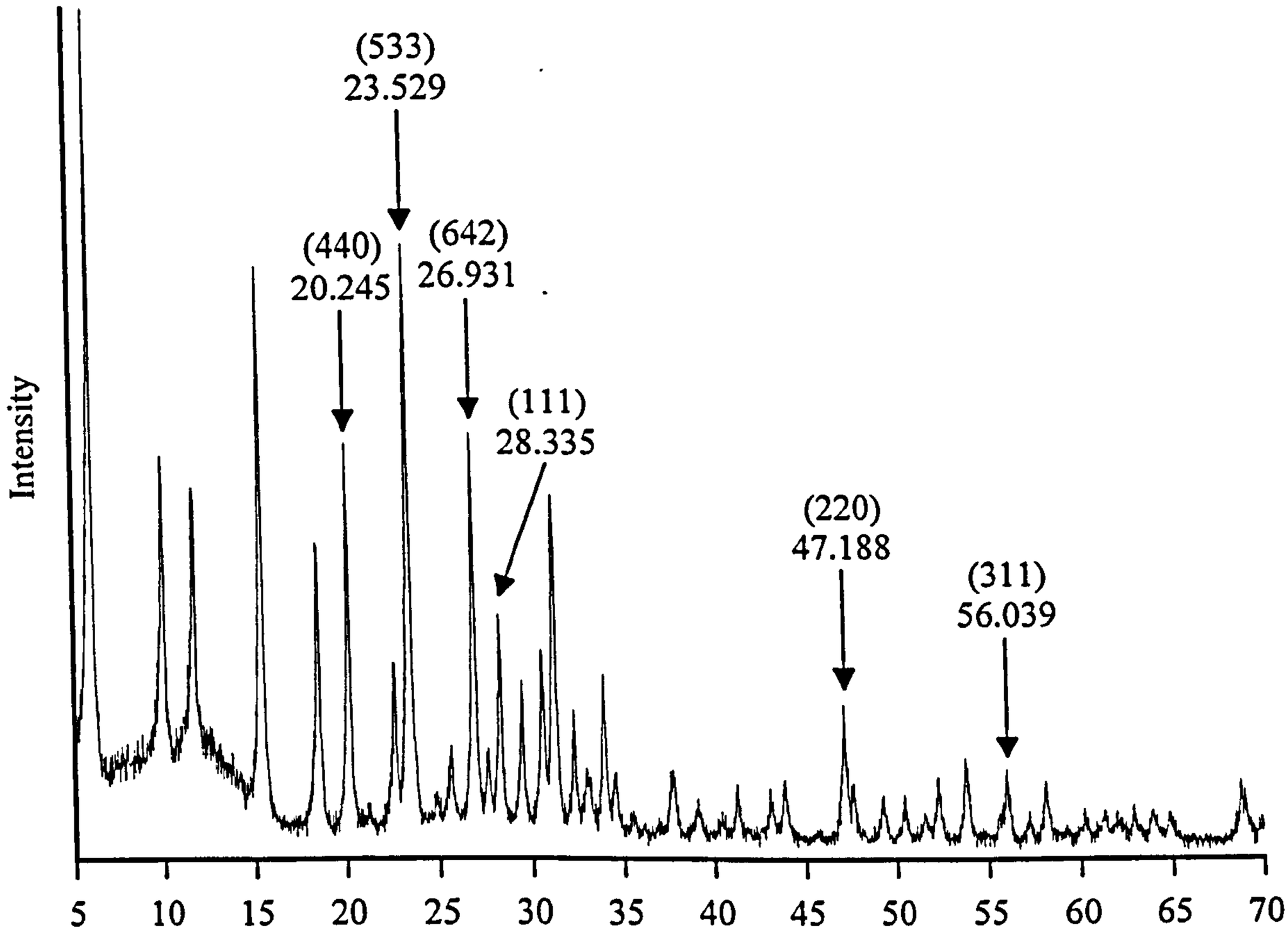

Figure 3.12 X-ray diffraction pattern recorded for a powder sample of untreated ammonium exchanged zeolite-Y (NH_4-Y), spiked with a silicon standard.

The observed positions of the silicon calibration peaks when fed into the calibration program, generated the following quadratic equation:

$$\text{Correction} = -0.0957 + (0.0113 \times 2\theta) - (0.0001 \times (2\theta)^2) \qquad (3.7)$$

Table 3.3 gives the positions (in 2θ) of the observed silicon calibration peaks, compared with their calculated values.

Peak	Observed position in 2θ	Calculated position in 2θ
(111)	28.335	28.443
(220)	47.188	47.304
(311)	56.039	56.122

Table 3.3 The observed and calculated positions in 2θ for silicon calibration peaks.

Equation 3.7 is then used to correct the selected zeolite-Y peaks, with the results shown in Table 3.4.

Peak	Observed position in 2θ	Corrected position in 2θ
(440)	20.245	20.337
(533)	23.529	23.644
(642)	26.931	27.067

Table 3.4 The observed and corrected positions in 2θ for selected zeolite-Y peaks.

It is the corrected peaks that are used in determining the unit cell constant. For example, for the (440) peak at 20.337° in 2θ,

$$1.5406 = 2d_{(440)} \sin\left(\frac{20.337}{2}\right) \tag{3.8}$$

so that

$$d_{(440)} = 4.363 \text{ Å}$$

Table 3.5 gives the computed unit cell constants (using Equations 3.4 and 3.5) determined from the corrected 2θ positions for the (440), (533) and (642) peaks.

Peak	Unit cell constant /Å
(440)	24.682
(533)	24.656
(642)	24.633

Table 3.5 The unit cell constants computed using Equations 3.4 and 3.5 for the corrected zeolite-Y peaks.

The unit cell constant is taken as the average value of the three determinations, it is 24.657 ±0.02 Å.

The method used for FCC samples was the same except that only the (533) peak was used in the determination of the unit cell constant.

Errors and reproducibility

The reproducibility in the determination of the unit cell constant from a diffraction pattern was investigated in order to gain information on any systematic errors, together with any errors which may result from sample packing procedures. In one set of experiments a zeolite-Y/silicon spike sample was prepared and the unit cell constant determined in each of ten consecutive runs. The same sample was used for each run, but the sample was reloaded into the sample holder on each occasion. The standard deviation for the measurements was then determined and found to be ±0.035 Å. A similar experimental procedure was used for an FCC type sample and the standard deviation was found to be slightly larger at ± 0.04 Å. This may be due to the fact that the FCC sample contains less zeolite-Y.

The standard deviations quoted for the experiments above are larger than the errors determined from single runs and the differences may be taken to reflect 'errors in reproducibility'. In this thesis, therefore, the errors quoted in the determination of unit cell constants will be typically the order of ± 0.035 Å for zeolite-Y powder samples and ± 0.04 Å for FCC type samples.

Presentation of X-ray diffraction patterns

Throughout the course of this work it has been of direct relevance to compare XRD patterns for differently treated samples. This allows differences to be easily observed, for example changes in amounts of phases present (different peak intensities) as well as the loss, or emergence, of new phases. Clearly in order to do this the patterns must have common intensity scales. In this thesis patterns which are to be compared are found on the same figure, and they all have the same intensity scale. In general, patterns have been offset to make comparisons easy. For example, Figure 5.1 in Section 5 of this thesis shows four XRD patterns related to studies of commercial FCC catalysts. Each of the four patterns, offset for convenience, are on the same intensity scale so it is possible to compare peak heights (strictly area under the peaks) as a guide to the relative amounts of the various components present. It must be noted, however, that although these four XRD patterns can be compared amongst themselves, they cannot be directly compared with any other XRD patterns in subsequent figures since the intensity scales may differ. Where it has been necessary to compare patterns from two different figures, a new figure has been constructed or the figures have been produced with the same intensity scale. Where two, or more, figures have the same intensity scale, allowing comparison across figures, this will always be indicated in the text (notably Section 5.3).

3.2 Surface Area Determination

Surface area measurements have proved a useful tool in the quantitative characterisation of zeolite samples of all types. Zeolite samples have a very large surface area due to their complex pore structure; for example, the surface area of a fresh zeolite-Y powder sample can be as high as 800 m^2g^{-1}. Severe treatment of zeolite samples under hydrothermal conditions can reduce the surface area to ~20-40 m^2g^{-1} and this indicates complete loss of zeolitic material. In general, therefore, monitoring the extent of loss of surface area can be directly used as a measure of how stable a zeolite sample is to a given set of sample conditions.

This section provides a brief introduction to the principles underlying surface area measurement, together with an outline of the experimental procedures and instrumentation necessary for obtaining the surface area of a sample of interest.

3.2.1 Background

There are two distinct ways in which a gas (adsorbate) can interact with a solid (adsorbent). The nature of these interactions depends upon both the adsorbate gas and the surface of the adsorbent solid, and can be described as either chemical adsorption or physical adsorption. Chemical adsorption involves the formation of chemical bonds between the adsorbate and the surface atoms of the adsorbent solid. Chemical adsorption is thus a very specific interaction and is therefore limited to monolayer coverage. Physical adsorption relates to the physical adsorption of an adsorbate gas on the surface of the adsorbent by weak attractive van der Waals forces. This type of adsorption is not specific and can be used for the determination of the total surface area of a solid.

The total surface area of any sample can be determined by monitoring the physical adsorption of an inert gas onto the surface of that sample. In this context the total surface area refers to not only contributions from the external surface but also any internal pores; for instance the surface area of fresh zeolites is high due to contributions to the total surface area from the complex internal pore structure. If the condition where a complete layer of adsorbed gas, averaging one molecule thick, can be achieved, and the area per molecule for the adsorbed gas is known, then the quantity of adsorbed gas can be used to directly calculate the surface area.

The most widely used method for the determination of total surface area was developed by Brunauer, Emmett and Teller,[9] the so called BET method. The theory is based on a kinetic model of the adsorption/desorption processes that occur during physical adsorption, as presented by Langmuir.[10] The BET model extends the adsorption of a gas to multilayer

adsorption, where less strongly adsorbed layers tend to develop on top of the initially adsorbed monolayer. The most convenient form of the BET equation is given by

$$\frac{p/p_o}{n(1-p/p_o)} = \frac{1}{n_m c} + \frac{(c-1)}{n_m c}\frac{p}{p_o} \tag{3.9}$$

where n is the quantity of gas (mol) adsorbed by the sample at an equilibrium pressure p, p_o is the vapour pressure of the adsorbate gas in the condensed state at the adsorption temperature, n_m is the quantity of gas (mol) adsorbed at the monolayer capacity of the solid and c is a constant related to the net heat of adsorption of the adsorbate. The derivation of the BET equation, and the assumptions made in the model, will not be presented here but can be found in the literature.[11]

The BET equation is generally valid and linear for p/p_o values in the range 0.05-0.35,[12] although for zeolite systems this range is reduced to 0.01-0.25.[13] A plot of $(p/p_o)/(n(1-p/p_o))$ against p/p_o in the latter range gives a straight line with slope (s) and intercept (i), where:

$$s = \frac{(c-1)}{n_m c} \qquad i = \frac{1}{n_m c}$$

Solution of these two simultaneous equations gives the value of n_m

$$n_m = \frac{1}{s+i} \tag{3.10}$$

The monolayer capacity of a solid (n_m) is defined as the amount of adsorbate which can be accommodated within a completely filled single monolayer on the surface of the solid.[11] Therefore the total surface area, A, of a given mass of solid is given by

$$A = n_m a_m L \tag{3.11}$$

where a_m is the average area (measured in m^2) occupied by a molecule of adsorbate in the monolayer and L is the Avogadro constant. For practical purposes, the specific surface area of a sample is often quoted and this is given by

$$A = \frac{n_m a_m L}{m} \tag{3.12}$$

where m is the mass of sample. Specific surface area is typically measured in m^2g^{-1}.

The most commonly used adsorbate is dinitrogen (N_2) gas at 77K; the average area occupied by a molecule of dinitrogen in the monolayer, a_m, is 16.2×10^{-20} m^2.[12,13] Dinitrogen adsorption was used in the present work for the determination of the specific surface areas of samples.

3.2.2 Instrumentation

Surface area measurements were made on equipment which was constructed, partly for the purpose of the work in this thesis, from commercially available components. Figure 3.13 shows a schematic diagram of the apparatus.

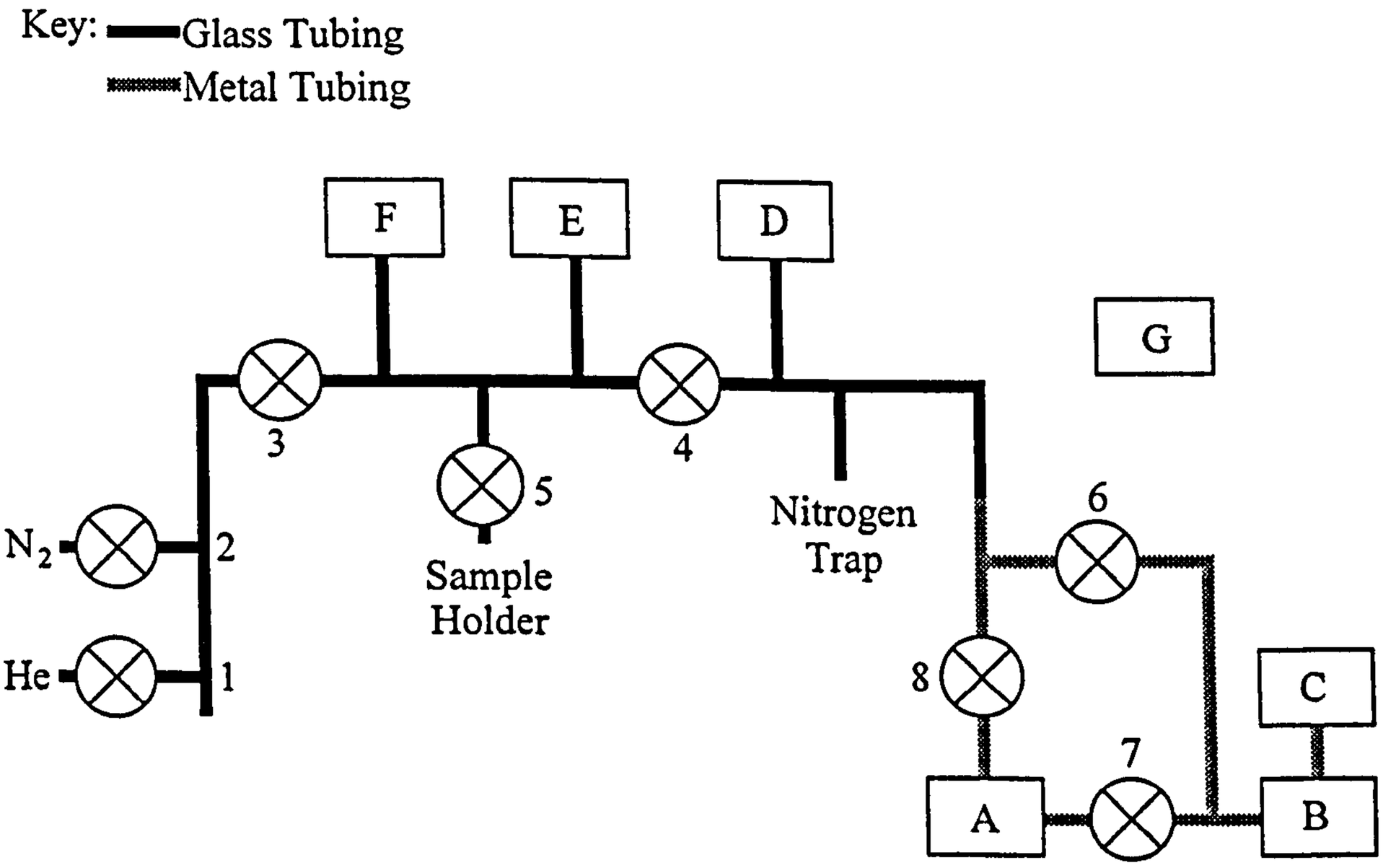

Figure 3.13 Schematic diagram showing the apparatus used for surface area measurements of zeolite samples. The main components, all of which are Edwards, are as follows: (A) is an air-cooled diffusion pump (model E050-60), (B) is a two-stage rotary pump (model E2M2), (C) is an active pirani gauge: range 100-10^{-3} mBar (model APG-M-NW16AL), (D) is an inverted magnetron gauge: range 10^{-3}-10^{-8} mBar (model AIM-S-NW25), (E) is a barocel capacitance barometer: range 0-1000 mBar (model 600AB), (F) is a barocel capacitance barometer: range 0-10 mBar (model 600AB) and (G) is an active gauge controller (model RS232CM VER). The taps 1-5 are Youngs PTFE 10mm screw valves and 6-8 are Edwards speedivalves.

The vacuum line was made of Pyrex glass and metal tubing. The sample is contained in a Pyrex sample holder and is clipped to the system using a ball and socket joint with a silicone "O" ring. A sinter is placed above the sample holder to prevent sample loss during evacuation. The system is evacuated by an air-cooled diffusion pump backed up with a two stage rotary pump, together these allowed pressures of 10^{-5} torr to be easily reached.

Two special features of the equipment are as follows. First, each gas inlet is fitted with a mini regulator (not shown in Figure 3.13) which prevents pressures of greater than one atmosphere being admitted into the apparatus. This is to prevent excessive pressure build up in the system and the risk of explosion. Second, the air-cooled diffusion pump is fitted with a trip switch which cuts off the power in the event of fan failure. This prevents the diffusion pump from over heating.

Apparatus Calibration

As the vacuum line was newly constructed, determination of the dosing volume was necessary. The dosing volume is defined as the volume (measured in cm^3) entrapped by the valves 3, 4, and 5 and is denoted as V_d. This is shown more clearly in Figure 3.14, which also defines other volumes that are important in the determination of the dosing volume. It is important that the dosing volume is known accurately since this value is used in the determination of surface area.

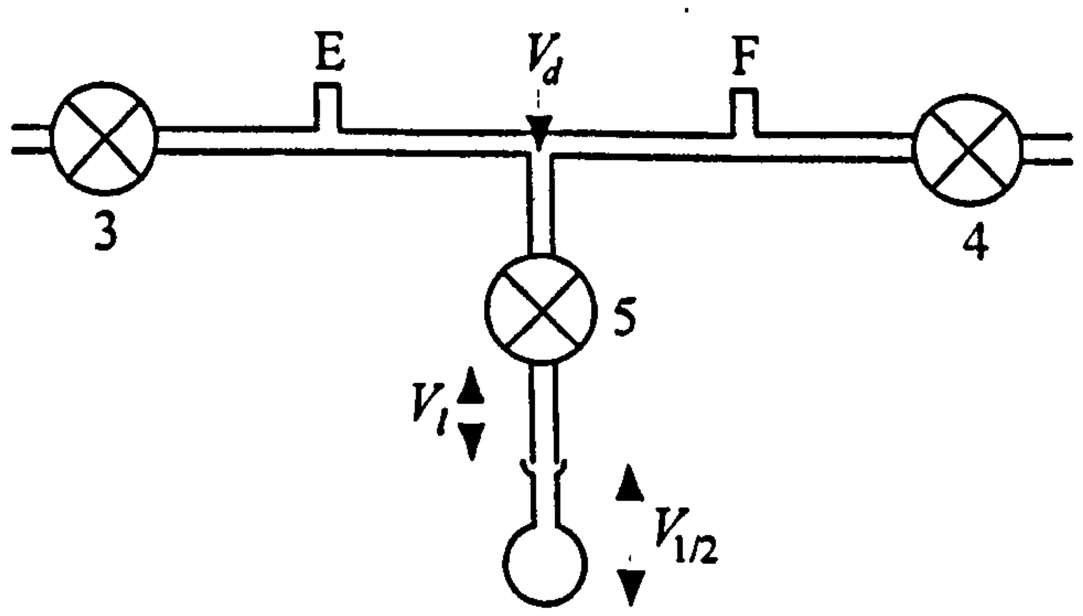

Figure 3.14 Schematic diagram showing the dosing volume for the surface area apparatus. V_d is the dosing volume. V_l is the volume between valve 5 and the sample holder connector. $V_{1/2}$ is the volume of sample holders 1 and 2, respectively, where $V_1 \neq V_2$.

Given the ideal gas law, for this system, it can be shown that:

$$\frac{p_{d(i)}V_d}{T_{d(i)}} = \frac{p_{e(i)}\left(V_d + V_{(i)} + V_l\right)}{T_{e(i)}} \tag{3.13}$$

The individual parameters in this equation, with their typical units, are defined as follows, p_d is the initial pressure in the dosing volume (torr), p_e is the final pressure when gas is admitted into sample holder 1/2 (torr), T_d is the temperature of gas in the dosing volume (K), T_e is the temperature of the gas when admitted into sample holder 1/2 (K), V_d is the dosing volume (cm^3), V is the volume of sample holder 1/2 (cm^3), V_l is the volume between valve 5 and the sample holder connector (cm^3) and i denotes the particular sample holder (1/2).

Assuming $T_{d1} = T_{d2} = T_{e1} = T_{e2} = T$, and rearranging the two equations generated from Equation 3.13 for sample holders 1 and 2, it can be shown that:

$$V_d = V_1 - V_2\left(\frac{p_{e1}p_{e2}}{p_{d1}p_{e2} - p_{d2}p_{e1}}\right) \tag{3.14}$$

The values of p_d and p_e, as defined above, can easily be obtained experimentally. The volumes of the sample holders (V_1 and V_2) are found by determining the mass of deionised water required to completely fill them. For the present work V_1 and V_2 were determined to be 60.9847±0.0419 cm^3 and 13.1263±0.0226 cm^3, respectively.

V_d was subsequently determined to be 57.70±0.26 cm^3 by admitting a known pressure of nitrogen into the dosing volume (recorded as $p_{d(i)}$) and monitoring the pressure decrease when the gas was admitted into sample holder (i) (recorded as $p_{e(i)}$). This process was repeated several times for each sample holder with increasing values of p_d.

3.2.3 Experimental Procedure

The American standard test method D 4365,[13] which is designed specifically for the determination of the surface area of the zeolite component of a fluid cracking catalyst, was followed. A brief summary of the procedure is as follows. The sample to be studied (approximately 0.05 grams) was loaded into a sample holder and connected to the surface

area apparatus which was then slowly evacuated. Under reduced pressure, the sample was degassed (removal of adsorbed material from the surface of the sample) by heating the sample gradually to 300°C at a rate of 1.7°C min^{-1}: degassing was considered complete when a pressure of 6.5×10^{-5} torr could be maintained at 300°C. Following this operation the furnace was removed and the sample was allowed to cool to room temperature. The dead-space was then determined using helium gas at 77K. The dead-space is defined as the quantity of gas within the sample tube, including the gas below valve 5 (Figure 3.13), when the tube is immersed in liquid nitrogen to the proper depth (any depth which ensures complete immersion of sample in liquid nitrogen, this level is then used for the remainder of the experiment). Determining the volume below valve 5 under experimental conditions in this way takes into account the volume occupied by the sample. Dead-space determination was routinely recorded three times, between pressures of 500-600 torr, and an average of these values was used in the surface area calculations. Dead-spaces values of approximately 0.035 cm^3 $Torr^{-1}$ were typical.

After the dead-space determination the system was re-evacuated. When this operation was complete the sample tube was again immersed in liquid nitrogen to the appropriate level. A known amount of nitrogen was admitted into the dosing volume and the pressure was recorded. The nitrogen was then admitted to the sample and the reduced pressure was recorded when equilibrium was reached; this was taken as the point when the pressure did not fall for a period of five minutes. This process was repeated with increasing amounts of nitrogen gas.

For each surface area determination a total of 6-8 experimental data points were typically recorded. Any given experiment was repeated if at least four of these data points did not lie in the linear region of the BET plot. The use of four data points in the linear region was considered to be a good balance between single point and full multi-point analysis. Curve fitting was achieved by the least squares fitting method, and linear regions with R values less than 0.9999 were discarded and the experiment repeated.

The BET method employed here leads to a measurement of the total surface area of the sample under study. In addition, careful manipulation of the experimental data can lead to the so-called t-area.[13] The t-area is specific to components of the sample that are non-zeolitic; this in turn leads to the specific surface area of the zeolite component of a fluid cracking catalyst. This can be very useful for samples that typically are only composed of 20% zeolite. Most of the surface area data in the present work relates to just the zeolite component of the fluid cracking catalyst and as a consequence only the BET area is relevant. However, it is worth noting that as some of the zeolite is degraded in these samples a 'non-zeolite' component will be present. In principal this can lead to an error in the determination of the total surface area of the zeolite sample via the BET method. Complete destruction of various zeolite samples led to materials with specific surface areas of less than $25 m^2 g^{-1}$. Systematic errors in the determination of specific surface areas for processed zeolite samples can thus be taken to be relatively small.

For commercial fluid cracking catalyst where the zeolite content is the order of 20% by mass, the BET area and t-area were determined elsewhere (B.P. Oil International, Sunbury). When the samples were subject to different treatments, it was assumed that the t-area would remain constant, this again will lead to only a minimal increase in experimental error.

Experimental Error and Reproducibility

In general, the error involved in the measurement of the total surface area of any given sample has been estimated at ±10%.[11] This value takes into account both the errors due to assumptions inherent in the BET model, and the errors arising due to experimental procedure. The latter were determined as a result of a project in the United Kingdom,[14] involving thirteen laboratories all well experienced in the field. The project was designed to establish a bank of substances that would serve as surface area standards. The differences between the various laboratories were traced to a number of experimental factors including: imperfect control of the conditions of degassing (time, temperature, and

final pressure); variation in temperature of the sample during the experiment; inadequate monitoring of the saturation vapour pressure; purity of nitrogen; and leaks in the apparatus.

In order to check the reproducibility of the surface area apparatus used in the present work a standard sample was studied. This was a graphitized carbon black (National Physics Laboratory, No. M11-02) which was one of the surface area standards recommended by the project mentioned above.[14] The specific surface area, determined by nitrogen adsorption, was quoted to be 71.3±2.7 m^2g^{-1}.

The surface area of this standard was determined a total of ten times using a fresh sample for each experiment. A value of 69.8±0.4 m^2g^{-1} was found. It can be seen that this value is very similar to that quoted, and well within the limits of experimental error.

As a further test of the surface area apparatus used in the present work, the surface area of a commercial zeolite-Y sample was obtained. The surface area of this sample also was determined elsewhere (B.P. Oil International, Sunbury) and found to be 203m^2g^{-1}. Figure 3.15 gives the BET plot for this sample.

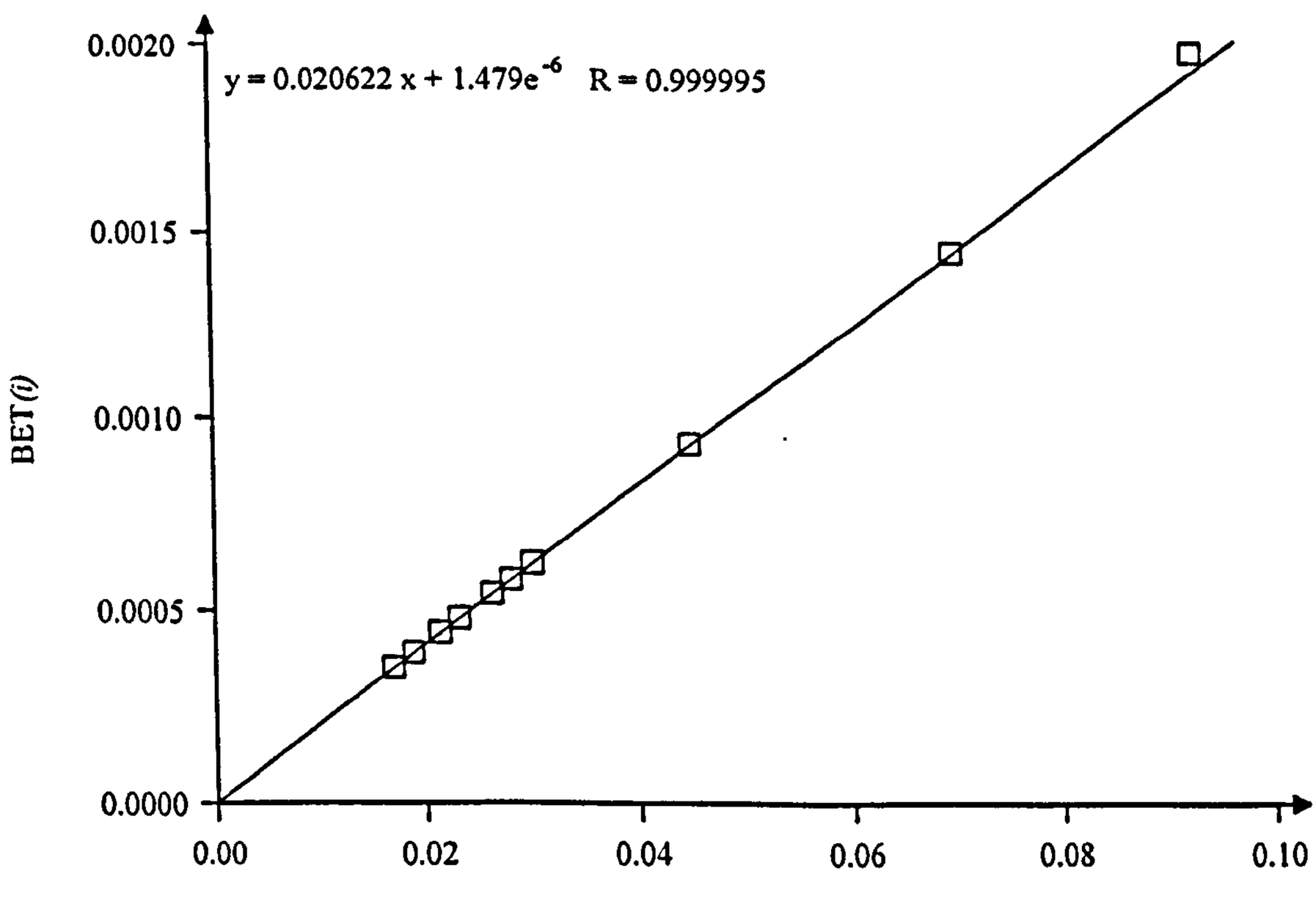

Figure 3.15 Graph showing BET plot for untreated commercial zeolite-Y sample. BET(i) = ($X(i)/V_a(i)$)(1/(1-$X(i)$)), where $V_a(i)$ is the amount of gas adsorbed by the sample and $X(i)$ is the relative pressure.

Given that $s = 0.020622$ and $i = 1.479e^{-6}$ (Section 3.2.1) it can be calculated that the total surface area of this sample is $211 m^2 g^{-1}$. This value again compares very well with that determined elsewhere, and a difference of only 4% is well within the limits of experimental error.

The errors quoted for a specific surface area measurement in the present work will be ±10%. However, the error determined from the variation of the linear region of the BET plot can be as low as $\pm 1 m^2 g^{-1}$.

3.3 Magic-Angle-Spinning Nuclear Magnetic Resonance Spectroscopy

Many of the samples studied in this work have been investigated by magic-angle-spinning (MAS) nuclear magnetic resonance (NMR) spectroscopy. In the main ^{27}Al and ^{51}V MAS NMR studies have been the most fruitful. ^{27}Al MAS NMR has proved important in the determination of aluminium environments after severe treatment of model zeolite-Y samples; the reaction products are amorphous and as a result XRD is of little help. ^{51}V MAS NMR has been used for the characterisation of vanadium compounds and has been particularly useful with samples that contain low (<1 mass%) levels of this element since these levels could not be detected using XRD.

This section gives a theoretical description of the MAS NMR technique, the experimental methods used, and a description of the spectrometer, including software, used for the collection of data.

3.3.1 Background

The major applications of NMR spectroscopy are to the liquid and solution state for which well defined, high-resolution, spectra can be obtained. These spectra provide a wealth of chemical information. In contrast, the NMR spectra of solids are generally broad, and poorly resolved, so that only limited information can be abstracted. However, MAS NMR spectroscopy provides a means of obtaining high-resolution spectra for solids and, as a consequence, has established itself as a major technique in solid state studies of a wide

range of materials. This section provides a background to the technique starting from the basic principles of NMR spectroscopy. Detailed descriptions of the NMR technique (including MAS NMR) can be found in the literature.[15-19]

Basic NMR concepts

The total angular momentum, **P**, of any isolated particle cannot take an arbitrary magnitude but has discrete values; angular momentum is said to be quantised. In general, the magnitude of **P** can be specified in terms of a quantum number, R, by means of Equation 3.15

$$P = \hbar[R(R+1)]^{1/2} \tag{3.15}$$

where $\hbar$ is $h/2\pi$ and h is Planck's constant. R is either integral or half-integral.

The angular momentum associated with NMR is that of nuclear spin, it is the transition between nuclear spin energy levels that gives rise to the NMR phenomenon.

The property of spin was first suggested by Pauli in 1924 as a means of explaining splittings in atomic spectra. These splittings demonstrated that elements, and isotopes of elements, possess different spin angular momentum. These differences, though difficult to explain, result from the specific composition and structure of the nucleus. The proton and neutron have a nuclear spin quantum number of $I = ½$. With nuclei other than the proton, the spin angular momenta couple within the nucleus to give an observed total. In general, nuclear spin quantum numbers can take on values of zero, half-integral or integral.

Equation 3.15 now takes the form

$$P = \hbar[I(I+1)]^{1/2} \tag{3.16}$$

Nuclei with $I = 0$ are NMR inactive and those with $I > ½$ possess an electric quadrupole moment. The nuclear spin quantum numbers of various nuclei, including those involved in this work, are given in Table 3.6.[15]

Nuclei	Natural abundance /%	I	Resonance frequency[a] /MHz	γ /10^7 radT^{-1}s^{-1}
^{1}H	99.985	$\frac{1}{2}$	399.985	26.7520
^{13}C	1.108	$\frac{1}{2}$	100.533	6.7282
^{17}O	0.037	$\frac{5}{2}$	54.210	-3.6279
^{19}F	100	$\frac{1}{2}$	376.142	25.181
^{27}Al	100	$\frac{5}{2}$	104.169	6.9760
^{29}Si	4.70	$\frac{1}{2}$	79.426	-5.3188
^{31}P	100	$\frac{1}{2}$	161.858	10.841
^{51}V	99.76	$\frac{7}{2}$	105.075	7.0453
^{139}La	99.911	$\frac{7}{2}$	56.473	3.801

[a] The resonance frequency is calculated for a magnetic field of 9.395T.[15]

Table 3.6 The spin properties of some NMR active nuclei where γ is the magnetogyric ratio of the given nucleus, this constant is discussed in further detail later in this section.

In terms of classical electromagnetism it is known that a circulating charge in a magnetic field has an associated magnetic moment. In the particular case of nuclei that possess spin angular momentum, this magnetic moment can be expressed by

$$\mu = \gamma \mathbf{P} \tag{3.17}$$

where μ is the magnetic moment. The quantity γ is the magnetogyric ratio of the nucleus (Table 3.6); it is defined as the ratio of the magnetic moment to the angular momentum. It follows that (c.f. Equation 3.16) the magnitude of the nuclear magnetic moment is,

$$\mu = \gamma \hbar [I(I+1)]^{1/2} \tag{3.18}$$

In a magnetic field, the energy of an isolated nucleus is no longer independent of its orientation. If the field, **B**, is applied along the z direction, then the magnetic

moment will have an interaction energy given classically by

$$E = -\mu.\mathbf{B} = -\mu_z B \tag{3.19}$$

where μ_z is the component of μ in the z direction. This component can be expressed by,

$$\mu_z = \gamma \hbar m_I \tag{3.20}$$

where m_I is the magnetic quantum number and it follows that,

$$E = -\gamma \hbar m_I B \tag{3.21}$$

The magnetic quantum number can take on $(2I+1)$ values and this corresponds to $(2I+1)$ non-degenerate energy levels. Figure 3.16 illustrates the nuclear spin energy level diagram for an $I = 3/2$ nucleus and adjacent energy levels are separated by $|\gamma \hbar B|$.

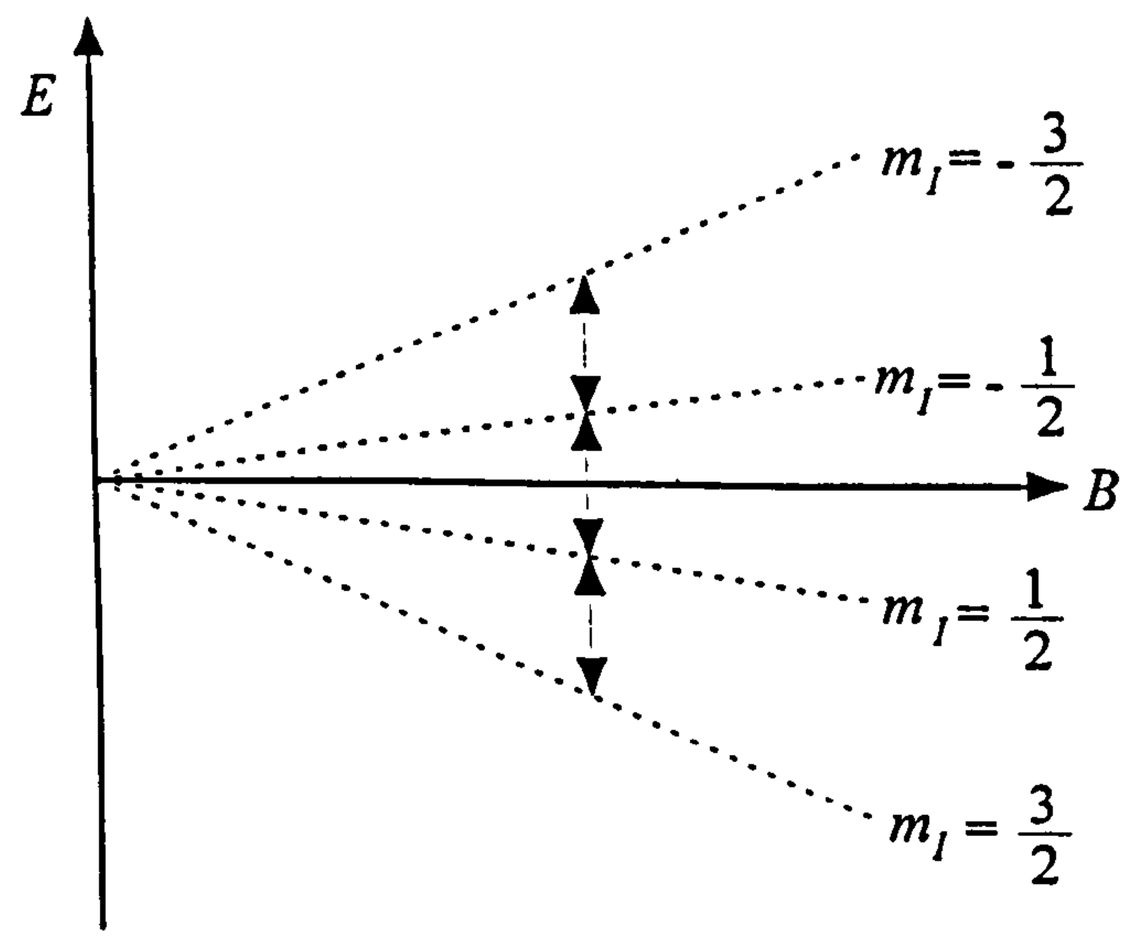

Figure 3.16 Nuclear spin energy level diagram for an isolated spin $I = 3/2$ nucleus with a positive value for the magnetogyric ratio, plotted as a function of the magnitude of the applied magnetic field in the z direction. The transitions obeying the selection rule $\Delta m_I = \pm 1$ for a given value of B are indicated.

Transitions between adjacent magnetic energy levels can be induced by the use of appropriate electromagnetic radiation and the energy difference, ΔE, between these levels can be expressed as $h\nu$, where ν is the frequency of the electromagnetic radiation.

Thus for NMR transitions for an isolated nucleus

$$\nu = \left| \left(\frac{\gamma}{2\pi} \right) B \Delta m_I \right| \tag{3.22}$$

Since transitions are governed by the selection rule $\Delta m_I = \pm 1$ then this equation simplifies to

$$\nu = \left| \frac{\gamma}{2\pi} \right| B \tag{3.23}$$

and this is the basic NMR resonance condition.

It is worth noting that an alternative approach to the description of the behaviour of an isolated magnetic moment in an applied magnetic field is often found to be useful. This is usually referred to as the 'classical picture'. In this model, the isolated magnetic moment precesses about the applied magnetic field. This is known as Larmor precession and is shown in Figure 3.17. The Larmor precession frequency can be shown to be exactly the same as that for the basic NMR resonance condition, Equation 3.23.

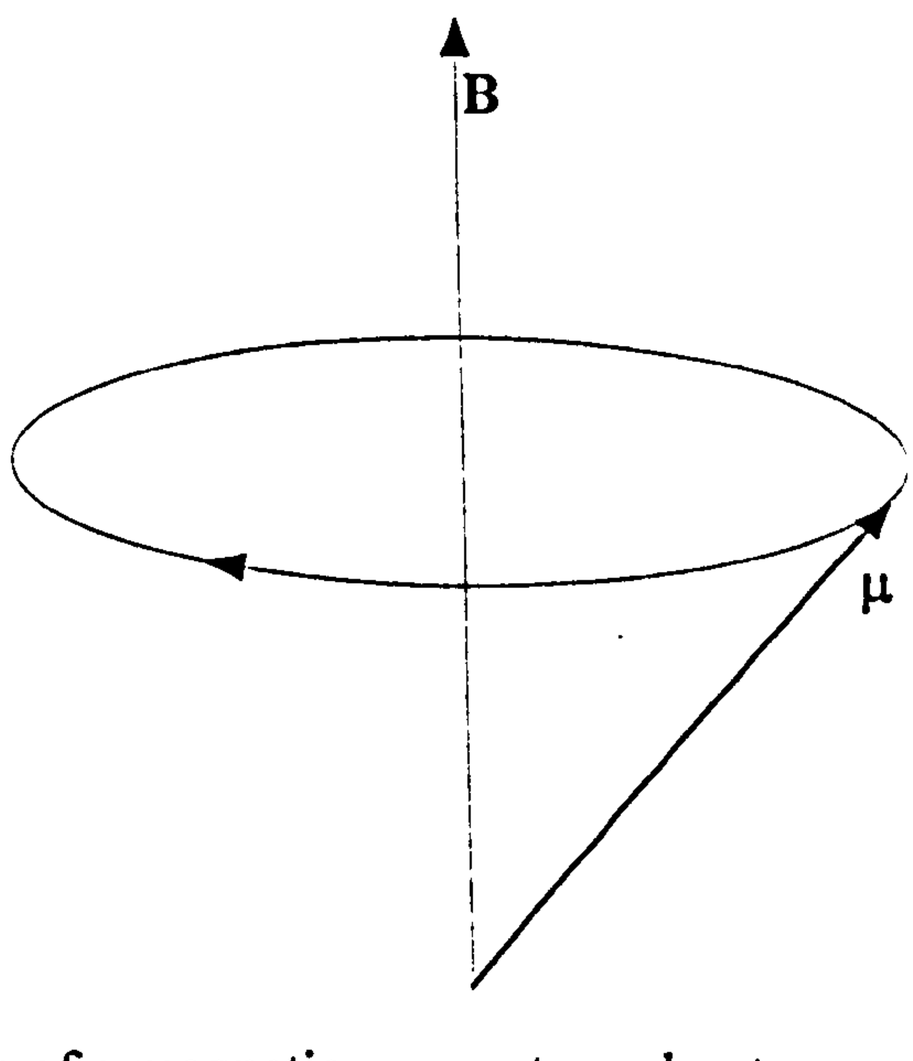

Figure 3.17 Precession of a magnetic moment, μ, about an applied magnetic field **B**.

So far the discussion has focussed on the behaviour of isolated nuclear spins. In practice, however, nuclei are far from isolated and this has distinct consequences for NMR spectra. In particular nuclei are surrounded by electrons and this has two major effects: (1) a shielding (or screening) of a nucleus by the surrounding electrons from the full influence of

the applied magnetic field and (2) a coupling between nuclei 'transmitted' via the electrons of intervening chemical bonds: this is referred to as 'spin-spin coupling'.

The shielding of a nucleus from the applied magnetic field, now labelled B_0, by electrons is taken into account by introducing an effective field, B, which represents the field experienced by the nucleus. It can be expressed as

$$B = B_0(1-\sigma) \tag{3.24}$$

where σ is the shielding constant: it is dimensionless and usually quoted in ppm. The more general form of the resonance condition now becomes

$$\nu_j = \left|\frac{\gamma}{2\pi}\right| B_0(1-\sigma_j) \tag{3.25}$$

where ν_j and σ_j refer to the Larmor frequency and shielding constant, respectively, for a given nucleus j.

It is the dependence of the resonance frequency on the shielding constant that is one of the most powerful features of NMR spectroscopy. In many cases, particularly for organic molecules, this allows the position of a resonance line in an NMR spectrum to be directly related to the chemical environment of the nucleus of interest. In this sense the NMR technique is of great importance in the determination of chemical structure.

NMR spectroscopy in solids

NMR spectra of solids often have linewidths of the order of kHz, whereas high-resolution spectra of liquid, or solution, samples can be recorded with linewidths significantly less than 1 Hz. As an example, Figure 3.18 compares the solution and solid-state ^{13}C NMR spectra of adamantane.

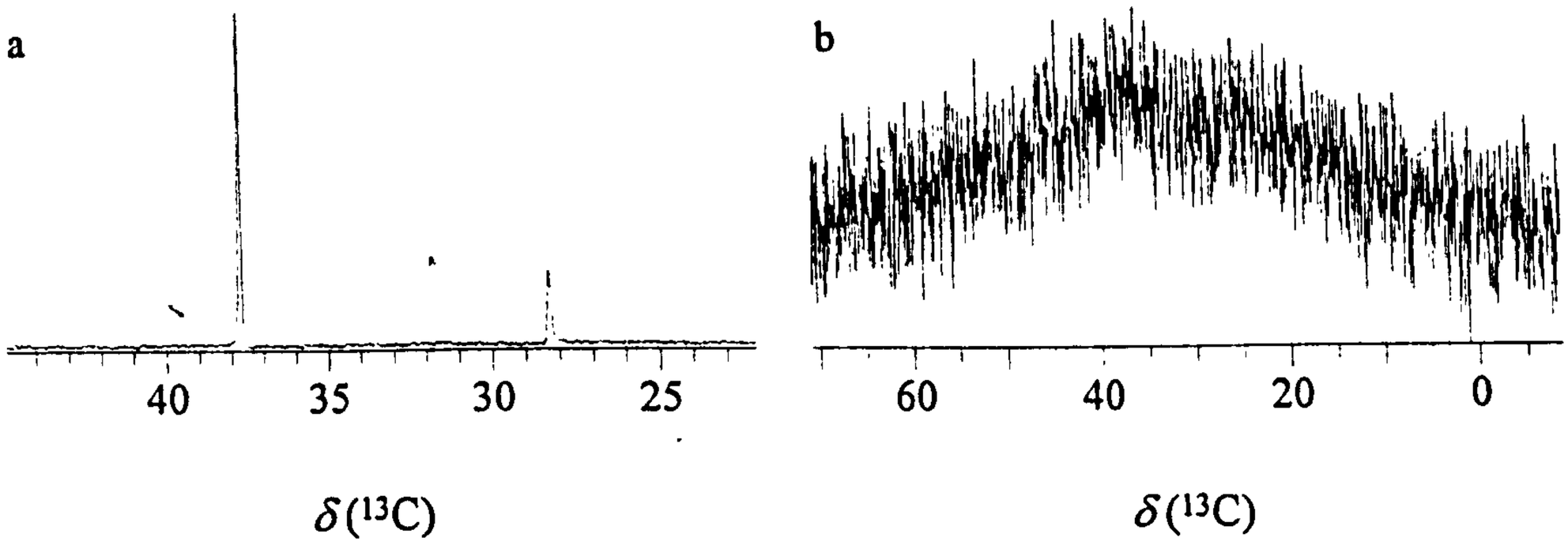

Figure 3.18 (a) The solution ^{13}C-{^{1}H} NMR spectrum of adamantane dissolved in $CDCl_3$, pulse delay = 2.5 s, pulse width = 5 μs, number of scans 40. (b) The ^{13}C NMR spectrum (with no proton decoupling) of solid adamantane, pulse delay = 10 s, pulse width = 4 μs, number of scans 100.

The structure of adamantane ($C_{10}H_{16}$) has two chemically inequivalent carbon sites, which are clearly evident in the solution spectrum (Figure 3.18(a)). The solid spectrum (Figure 3.18(b)) is markedly different consisting of a single unresolved broad line with a half-width of the order of 2 kHz.

This broadening of the solid-state spectrum is due to both magnetic dipole-dipole interactions and chemical shielding anisotropy. In the solution state these interactions are averaged to zero by the rapid tumbling of the adamantane molecules and, therefore, do not contribute to the observed NMR frequency spectrum.

3.3.2 Magnetic dipole-dipole interactions

The NMR resonance frequency of a nucleus present in a solid sample depends upon the magnetic field at its particular position. Besides the external magnetic field applied along the laboratory z direction, there are also local internal fields due to the presence of neighbouring nuclei in the sample. The exact resonance frequency depends upon the contribution of these local fields. At a given nucleus the local field, B_{loc}, measured in the z direction, due to the presence of a neighbouring nucleus with spin $I \neq 0$ and magnetic

moment μ can be expressed as,

$$B_{loc} \sim \pm \frac{\mu}{r^3}\left(3\cos^2\theta - 1\right) \tag{3.26}$$

where r is the distance between neighbouring nuclei and θ is the angle between r and the z direction. This is illustrated in Figure 3.19 for two nuclei labelled A and B.

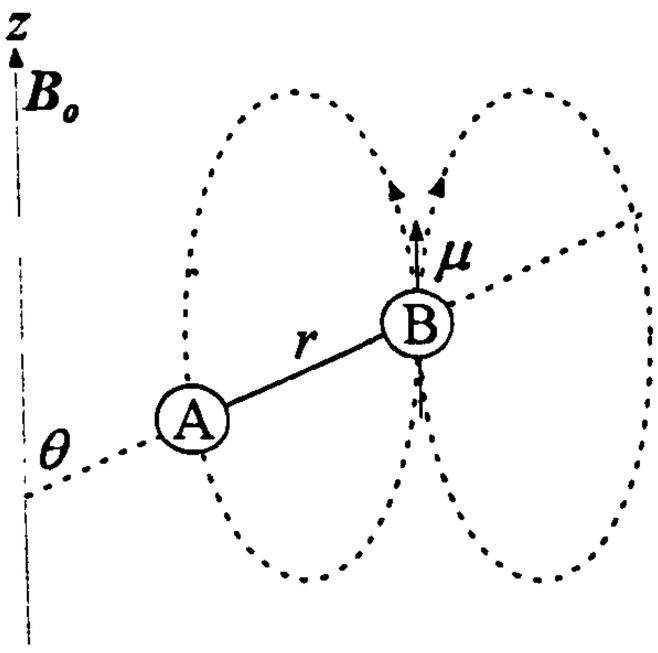

Figure 3.19 The local magnetic field experienced by A as a result of nucleus B with magnetic moment μ.

It can be readily envisaged that for any pair of nuclei in a polycrystalline solid sample all possible values of θ will simultaneously exist. Furthermore, a given nucleus will experience many different pairwise interactions. Overall this will result in broadening of the resonance line. As the local fields generated by nearest neighbours can be of the order of 10^{-4} T, linewidths can be of the order of kHz. As already indicated the linewidth at half-height for the solid adamantane spectrum shown in Figure 3.18(b) is of the order of 2 kHz. The line broadening is referred to as being due to magnetic dipole-dipole interactions.

Magnetic dipolar interactions in liquid or solution systems are affected by the rapid tumbling motion of the molecules. On the time scale of this tumbling motion, the value of θ for a given pair of nuclei sweeps through all values and as a result the $(3\cos^2\theta\text{-}1)$ term in Equation 3.26 averages to zero; in this case the contribution of the magnetic dipole-dipole interaction to the linewidth of the NMR spectrum effectively vanishes. Overall this results in linewidths for solution spectra having linewidths of the order of Hz, or less.

An effective means of removing the line broadening due to anisotropic magnetic dipole-dipole interactions is by a double resonance experiment. This involves the decoupling of neighbouring nuclei: the magnetic dipole-dipole interactions are reduced via a reduction of the effective magnetic moment, μ. Taking adamantane as an example, the line broadening due to magnetic dipole-dipole interactions observed for the ^{13}C NMR spectra (Figure 3.18(b)) can be reduced by decoupling the protons. This is achieved by applying a decoupling radio-frequency field of appropriate strength at the ^{1}H NMR resonance frequency.

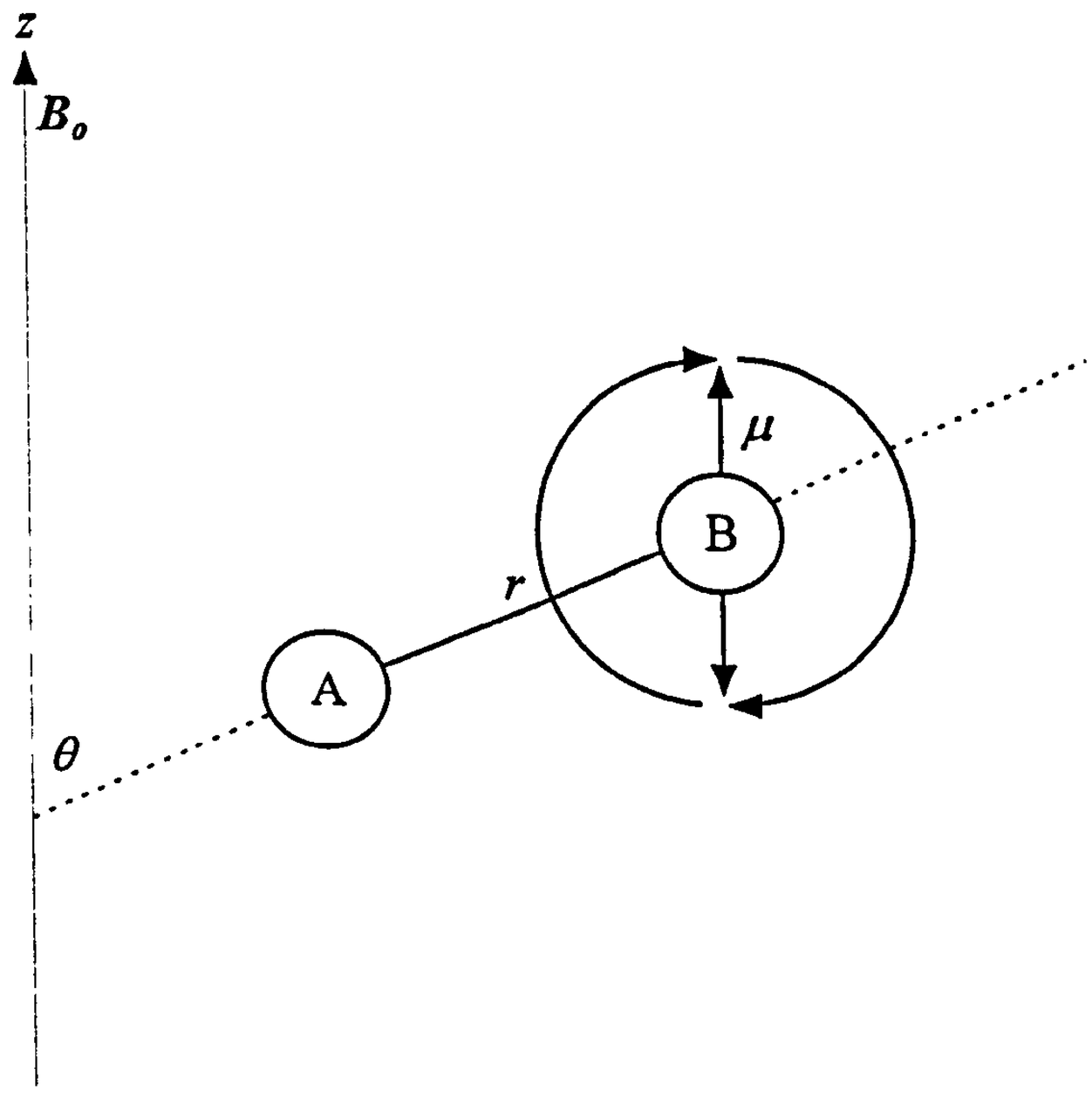

Figure 3.20 Schematic view of the effect of high-power decoupling on the magnetic moment of nucleus B.

If carbon is represented by nucleus A and hydrogen by nucleus B, the high-power decoupling forces the ^{1}H magnetic moment to undergo spin flips (Figure 3.20). This can effectively average the magnetic moment to zero and the magnetic dipole-dipole interactions are removed. Experimentally the approach is similar to decoupling in solution-state NMR, but higher decoupling power is required in solids to overcome the relatively large magnetic dipole-dipole interactions.

The effect of high-power decoupling can be seen in Figure 3.21. The ^{13}C high-power ^{1}H decoupled NMR spectra for adamantane gives rise to two single resonances each with linewidths of the order 0.2 kHz. However, comparison of this spectrum with that obtained for the solution (Figure 3.18(a)) shows that the individual lines are still relatively broad. The remaining line broadening is predominantly due to chemical shielding anisotropy.

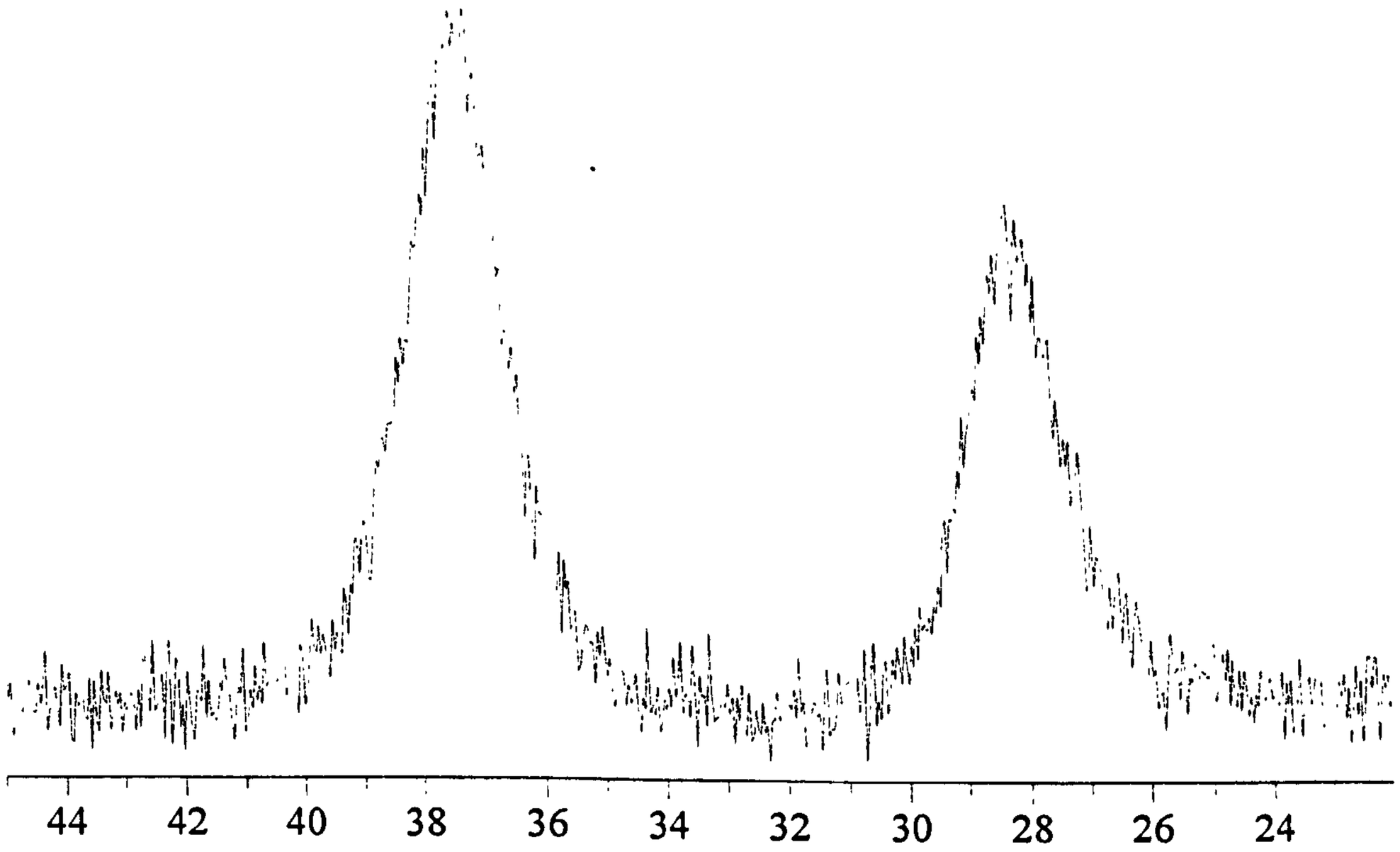

Figure 3.21 Effect of high-power proton decoupling on a solid sample of adamantane observed at 100.533 MHz, using a broad ^{1}H decoupling channel (~8 kHz, 1.9×10^{-4} T). Spectrum referenced to TMS, pulse delay = 10 s, pulse width = 4μs, and number of scans = 30.

3.3.3 Chemical shielding anisotropy

The magnitude of the chemical shielding constant σ (Equation 3.24) for a particular nucleus in a solid sample will depend upon the orientation of the nuclear environment with respect to the applied magnetic field. For polycrystalline, or amorphous, samples all possible orientations will be possible and this will lead to a spread of chemical shift values for magnetically equivalent nuclei, and hence broad resonance lines. In a similar manner to

magnetic dipole-dipole interactions, the chemical shield anisotropy contribution to the NMR linewidth in solution is averaged to zero by the rapid tumbling motions of the molecules.

The broadening effects of chemical shielding anisotropy can be overcome by magic-angle-spinning NMR (MAS NMR). This technique involves the rapid (several kHz) spinning of the solid sample at an angle of 54.7° relative to the applied magnetic field (z direction). Under these conditions the chemical shielding anisotropic effects are reduced or, depending upon the spinning speed, completely removed. Magnetic dipolar contributions are also similarly affected. Figure 3.22 shows the geometric relationships important in MAS NMR.

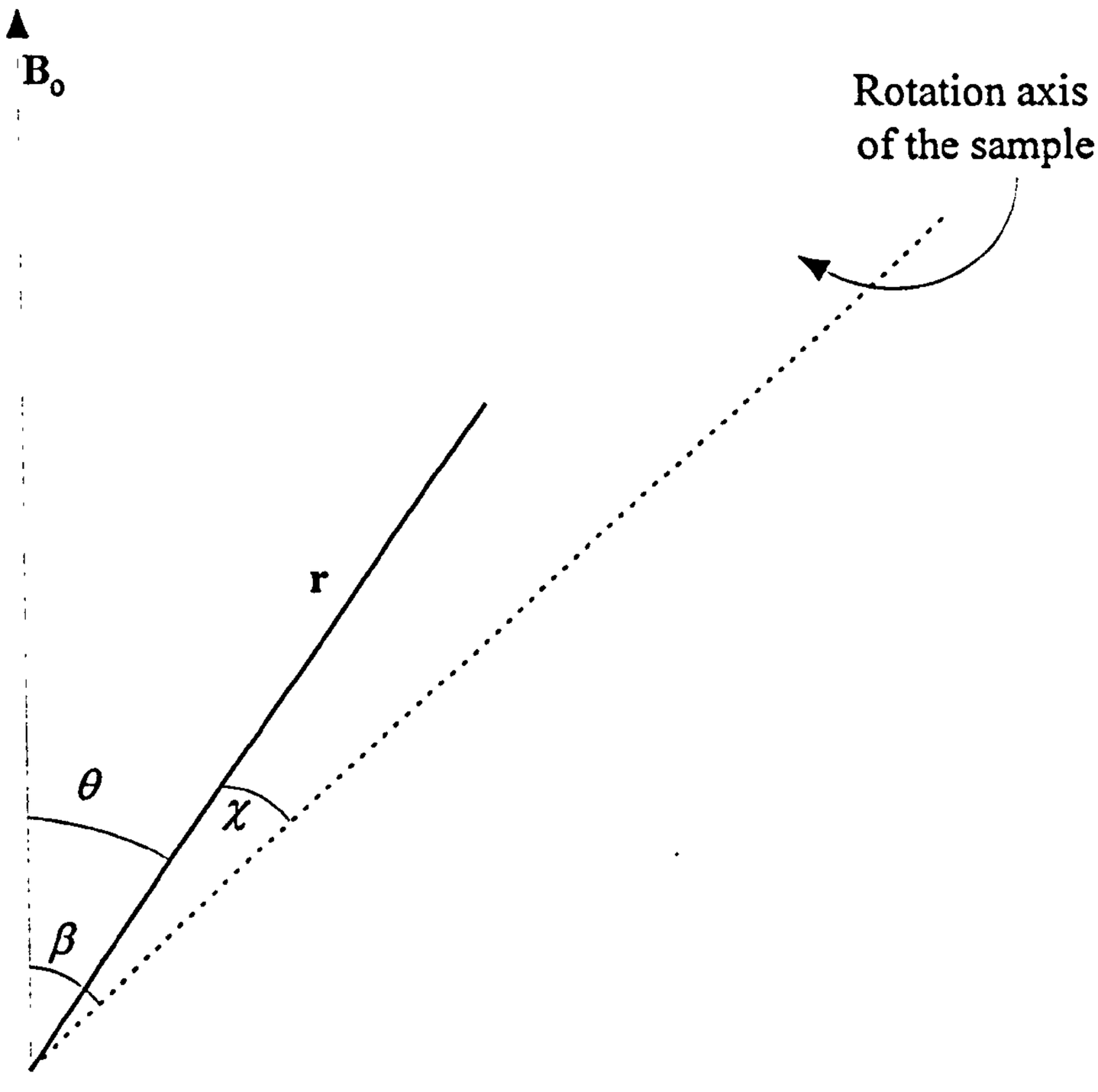

Figure 3.22 Geometric relationships important in the MAS NMR technique. Further details are given in the text.

In general for an interaction depending on $(3\cos^2\theta - 1)$, the time average of this quantity over the conical path taken by the vector **r** is given by

$$\langle 3\cos^2\theta - 1 \rangle = \tfrac{1}{2}(3\cos^2\beta - 1)(3\cos^2\chi - 1) \qquad (3.27)$$

The angle χ will take on all possible values in a polycrystalline, or amorphous, sample. However, in the special case that β is 54.7° the time average in Equation 3.27 reduces to zero and anisotropic interactions are effectively removed from the observed spectrum. The angle β is 54.7° and is referred to as the magic-angle. An important condition for this method of line-narrowing to be applicable is that the frequency of sample spinning must be significantly greater than the frequency spread due to the anisotropic interactions. Currently spinning frequencies of up to 20 kHz are available with commercial state-of-the-art MAS NMR probes.

The effect of a MAS NMR experiment (no ^{1}H decoupling) can be seen by comparing Figure 3.23 with Figure 3.18(b), the spectra presented have been recorded under the same conditions (that is the same pulse delay and pulse width) but the former sample was spun at 7 kHz at an angle of 54.7° to the applied magnetic field.

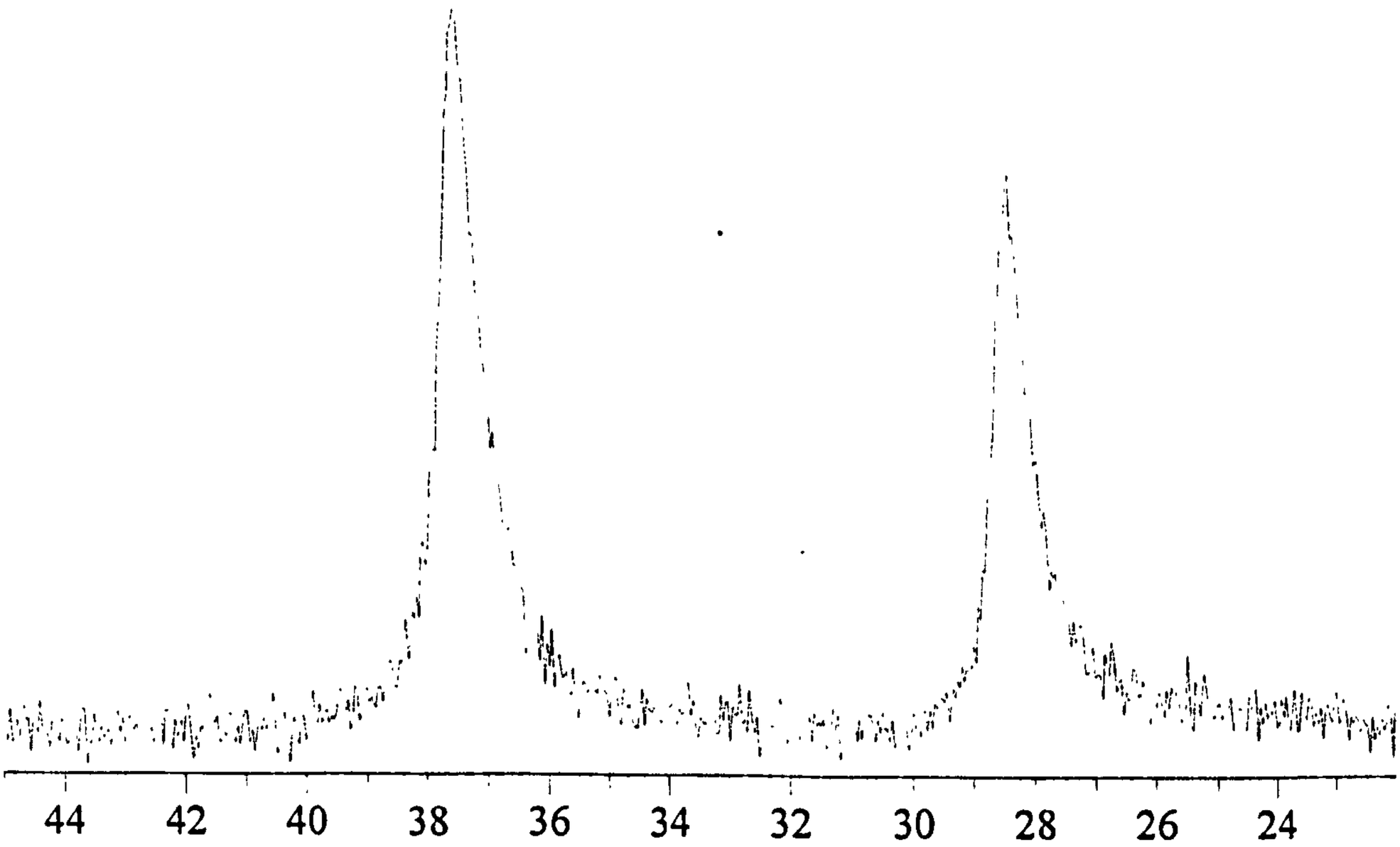

Figure 3.23 MAS NMR spectra of solid adamantane, with no ^{1}H decoupling, recorded at 100.533 MHz, sample spun at a frequency of ~ 7 kHz at an angle of 54.7° to the applied magnetic field. Spectrum referenced to TMS, pulse delay = 10 s, pulse width = 4μs, and number of scans = 30.

It can be seen again that the spectrum has resolved into two lines, as would be expected for the two inequivalent carbons present in adamantane. However, the linewidths are still significantly broader than those observed for the solution spectrum of adamantane (Figure 3.18(a)). The broadening is due to the effects of incomplete averaging of magnetic dipole-dipole interactions.

The spectra shown in Figures 3.21 and 3.23 can be significantly improved by coupling the MAS NMR experiment with ^{1}H high-power decoupling (Figure 3.24). The results are dramatic, it can be seen that the linewidths at half peak height are the order of 5 Hz, which becomes comparable with those observed for solution NMR.

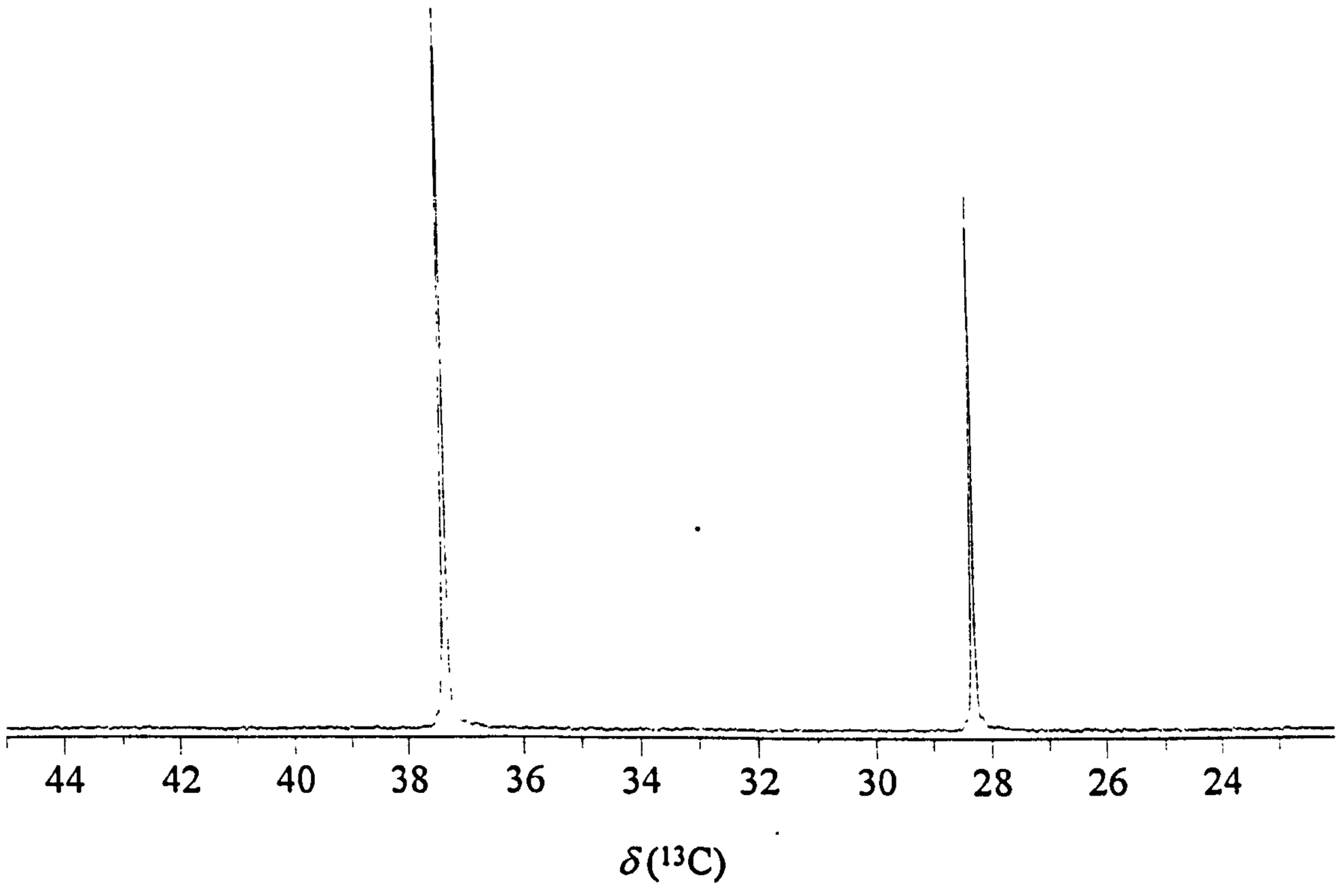

Figure 3.24 A solid adamantane sample recorded at 100.533 MHz, using a broad-band ^{1}H decoupling channel (~ 8 kHz, 1.9×10^{-4} T). Spectrum referenced to TMS, pulse delay = 10 s, pulse width = 4 μs, spinning frequency ~ 7 kHz, and number of scans = 30.

A further refinement is to introduce cross-polorisation (CP/MAS), but this technique is not relevant for the samples considered in this thesis.

3.3.4 Instrumentation

All MAS NMR spectra were recorded on a JEOL JNM-EX400 FT NMR instrument equipped with a JEOL EX Solid NMR facility coupled with a Doty Scientific Inc. MAS NMR probe (5 mm, high speed (14 kHz), double-tuned, multinuclear, CP/MAS). The probe had a ^{1}H decoupling field strength of a maximum of 60 kHz (1.4×10^{-3} T) at 400 MHz. The 5 mm rotors were made of silicon nitride and were fitted with vespal caps. A compressed air system was used for the sample spinning. The probe had two air inlets, one for bearing gas which prevents the rotor colliding with the side of the stator and the other as a drive to spin the rotor. Rotor speeds of 14 kHz were attainable with this system although typically samples were spun in the range of 7 to 10 kHz.

NMR signal data was transferred to a PC (Dell, P133c) for processing using the Bruker WIN-NMR software (version 950901.1).

3.3.5 Experimental Procedure

All samples were prepared for MAS NMR experiments using the same procedure. The acquisition parameters used for the collection of data varied depending upon sample type.

Sample preparation

Before any sample was loaded into an NMR rotor it was ground into a fine powder. It was found that fine powders, carefully packed, ensured even spinning of the rotor, particularly at high frequencies. Sample packing was achieved using accurately machined plastic tools. A small amount of any given sample was carefully placed in the rotor and compacted using a plastic ram. This procedure was continued until the rotor was full. When full, using another plastic tool, a portion of the sample was removed to the depth of the vespal cap and the second cap was then fitted.

Manipulation of data

In general all MAS NMR spectra were processed in a similar manner. Typically, a given free induction decay (FID) was suitably apodized, in the main using exponential filters, before Fourier transforming (FT) and subsequent phasing. For samples with only minimal amounts of the resonant nucleus present, and hence poor signal-to-noise ratios, significant broadening was caused by exponential filtering. However, since the aim was to observe a signal, rather than quantify the lineshape, this was taken as acceptable. An example in a particularly demanding case is shown in Figure 3.25. The extent of artificial broadening of signals will be noted where relevant in subsequent discussions.

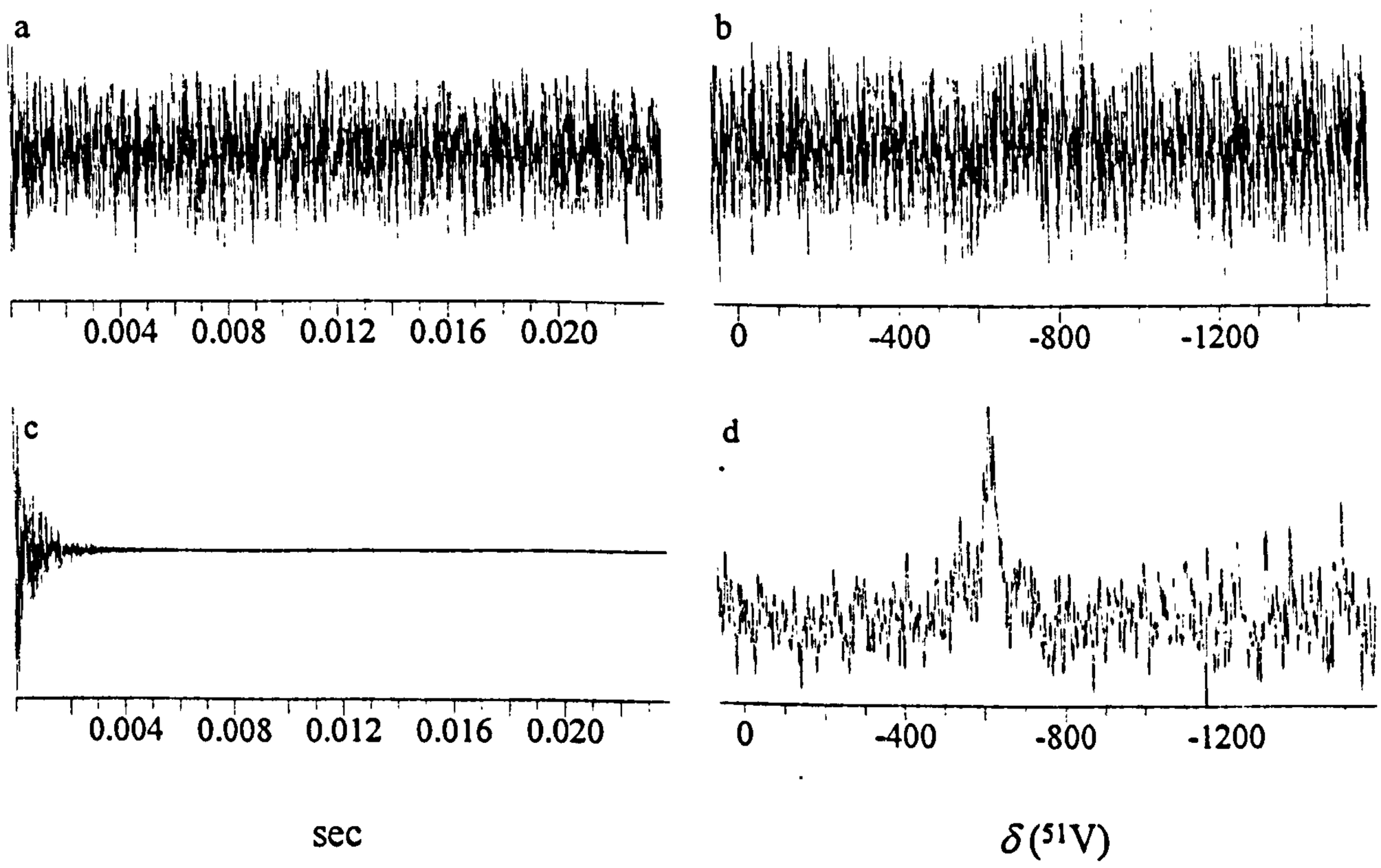

Figure 3.25 ^{51}V MAS NMR spectra observed at 105.075 MHz for a sample of α-alumina support material loaded with 1 mass% vanadium and 11.0 mass% lanthanum. External reference liquid $VOCl_3$, pulse delay = 1 s, pulse width = 2 μs, spinning frequency ~ 7 kHz, and number of scans = 62 000. (a) FID as collected, (b) FT of FID presented in (a), (c) FID after exponential filtering, and (d) FT of FID presented in (c).

^{51}V MAS NMR methods

^{51}V is a quadrupolar nucleus with nuclear spin $I = 7/2$ and natural abundance of 99.76%. Potentially it is a good nucleus for NMR study since its sensitivity, relative to that for ^{13}C, is 2.15×10^3. Typically in work in this thesis ^{51}V MAS NMR spectra were found to have central linewidths of the order 1 kHz, or less. All ^{51}V MAS NMR spectra were recorded at 105.075 MHz with reference to an external sample of liquid $VOCl_3$; $\delta(^{51}V) = 0\pm2$ ppm. MAS NMR acquisition parameters were chosen so as to make full use of the available spectrometer time. A short pulse delay (1 s) was used to increase the total number of scans recorded for each spectrum in a given time period. This was particularly important with samples that contained 1 mass% vanadium, or less. With these samples, at least 15 hours spectrometer time was required to obtain spectra with acceptable signal to noise ratios. Figures 3.26(a) and (b) show the ^{51}V MAS NMR spectra recorded for polycrystalline lanthanum vanadium oxide ($LaVO_4$) at two different pulse delays: 1 s and 5 s respectively. In both experiments a $\pi/2$ pulse (3.25 μs) was used and the number of scans was fixed at 200. Both spectra are very similar and lineshape analysis (via WIN-FIT) of the central peak gave essentially identical results in both cases. It is reasonable to conclude that there are no significant saturation effects using short pulse delays of 1 s. On the basis of this result it was generally assumed that ^{51}V spin-lattice relaxation time (T_1) would be reasonably short for the material considered in this thesis. (Experimental studies on various different samples indicated that this was the case.)

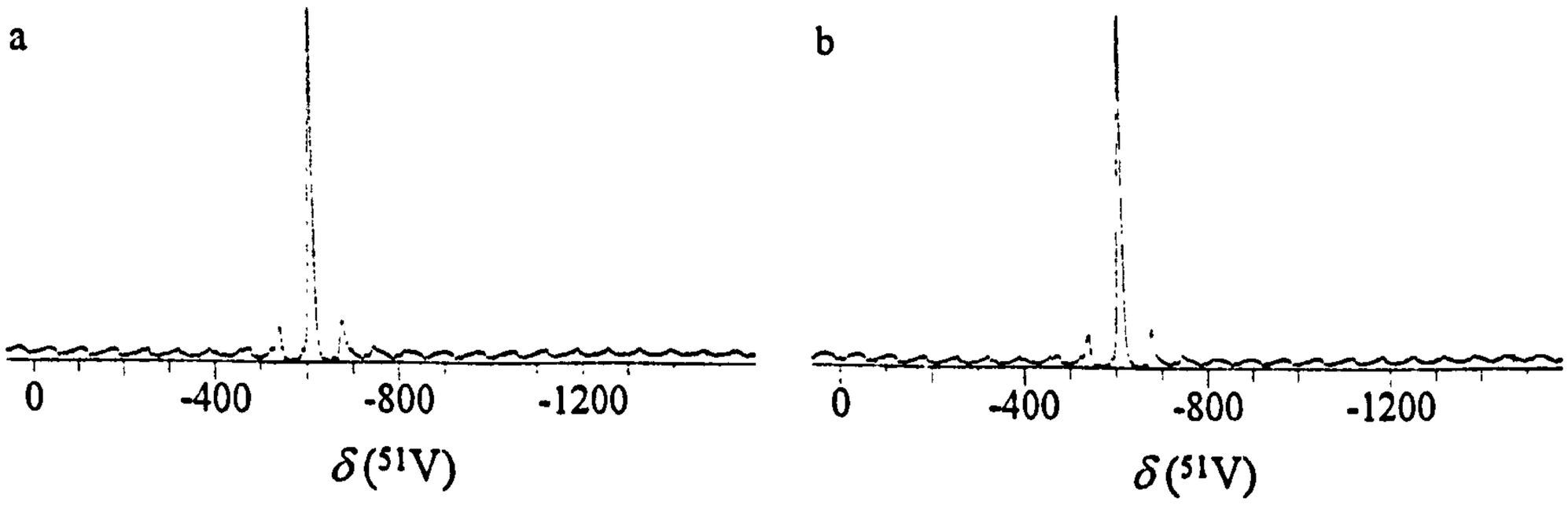

Figure 3.26 ^{51}V MAS NMR spectra for polycrystalline $LaVO_4$ recorded at 105.075 MHz. (a) pulse delay = 1 s, $\delta(^{51}V) = 611 \pm 5$ ppm and (b) pulse delay = 5 s, $\delta(^{51}V) = 611 \pm 5$ ppm. For both spectra the external reference was liquid $VOCl_3$, pulse width = 3.25 μs, number of scans = 200, and spinning frequency ~ 7.5 kHz.

^{51}V MAS NMR spectra were recorded with pulse widths of 2 μs. It is well known, however, that lineshapes in MAS NMR spectra for half-integer quadrupolar nuclei can be influenced by pulse duration.[20] Figures 3.27 (a)-(d) show the effect of pulse duration on the ^{51}V MAS NMR spectra of polycrystalline $LaVO_4$: the $\pi/2$ duration was found to be 3.25 μs.

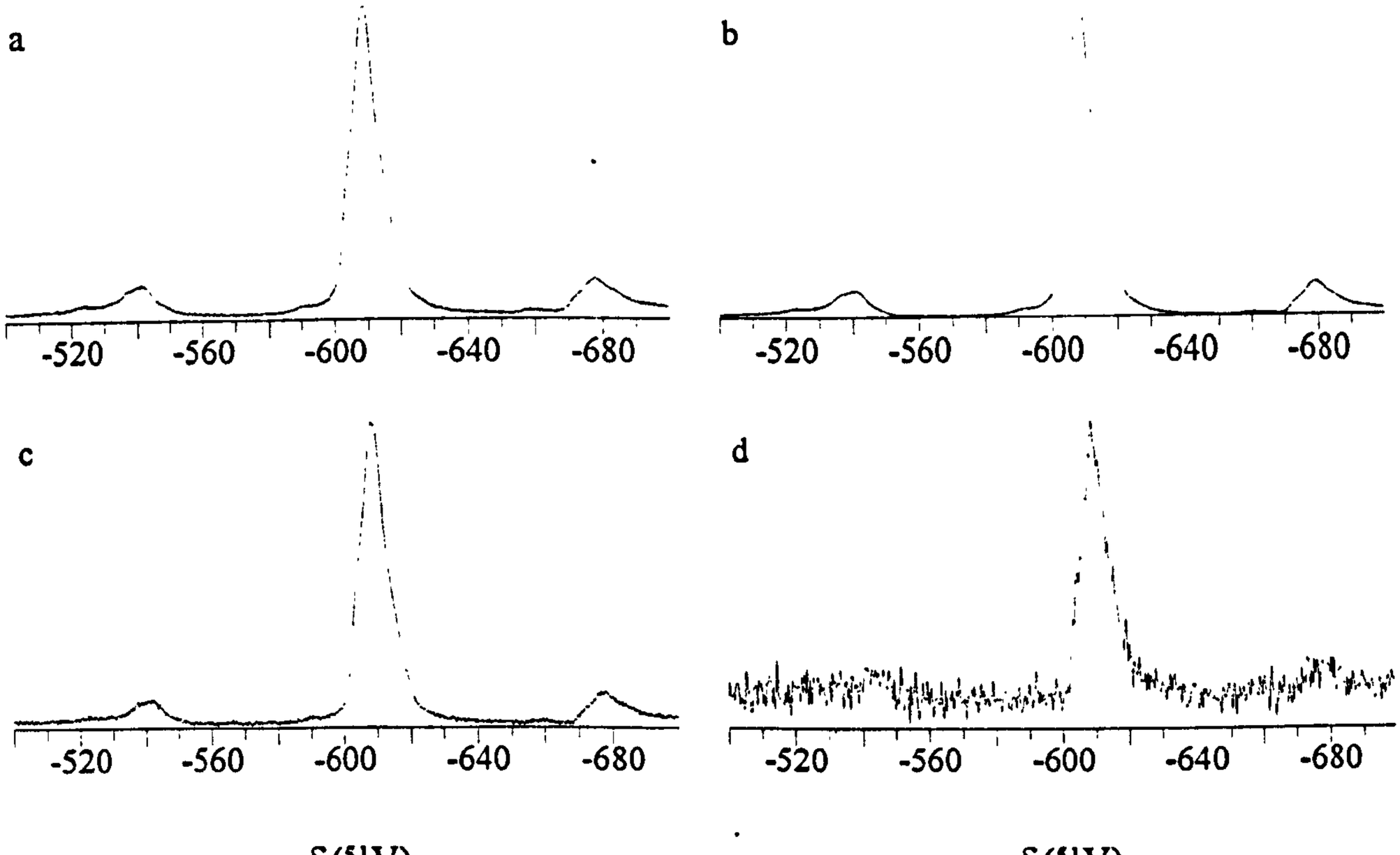

Figure 3.27 ^{51}V MAS NMR spectra of polycrystalline $LaVO_4$ at 105.075 MHz as a function of pulse duration. (a) pulse width = 3.25 μs, number of scans = 200, δ(^{51}V) = 611 ± 5 ppm, (b) pulse width = 2 μs, number of scans = 1 000, δ(^{51}V) = 611 ± 5 ppm, (c) pulse width = 0.81 μs, number of scans = 1 000, δ(^{51}V) = 611 ± 5 ppm, and (d) pulse width = 0.54 μs, number of scans = 3 000, δ(^{51}V) = 611 ± 5 ppm. In all cases the external reference was liquid $VOCl_3$, pulse delay = 1 s, and spinning frequency ~ 7.5 kHz.

The decrease in signal-to-noise as the pulse width is shortened can be clearly seen by comparing spectra (a) and (d) (Figure 3.27). In particular, spectrum (d), recorded with a pulse width of 0.54 μs, has a significantly poorer signal-to-noise ratio over that of spectrum (a), recorded at 3.25 μs, despite having some 2 800 more scans.

Line shape analysis of spectra (a), (b) and (c) indicated that as the pulse width was increased then quadrupolar broadening effects also increased. Ideally, a short pulse duration should be employed to minimise these effects. However, with the majority of the samples studied in this work this was detrimental to gaining a reasonable signal-to-noise ratio. A pulse width of 2 μs was selected as a compromise, balancing the effects of increasing spectral linewidth with increasing pulse width, with the signal-to-noise reduction observed with collecting data at shorter pulse widths.

^{27}AL MAS NMR methods

^{27}Al is a quadrupolar nucleus with a nuclear spin $I = 5/2$ and a natural abundance of 100%. It has a high sensitivity (1.17×10^2) relative to that for ^{13}C and has been studied widely using MAS NMR techniques.[21]

In the present work all spectra were recorded at 104.169 MHz using a pulse delay of 1 s and a pulse width of 2 μs. The number of scans varied with sample and available spectrometer time. An external reference of an aqueous solution of aluminium nitrate (0.1 mol dm^{-3}) was used. As previously discussed for ^{51}V MAS NMR the spectral acquisition parameters were selected to give acceptable signal-to-noise ratio without causing significant distortion.

^{139}La MAS NMR methods

^{139}La has a sensitivity relative to ^{13}C of 3.4×10^2, and has a natural abundance of 99.911%. It is a quadrupolar nucleus with nuclear spin $I = 7/2$. The ^{139}La NMR spectrum measured in the MAS NMR probe, for an aqueous solution of $LaCl_3$ (0.1 mol dm^{-3}) is shown in Figure 3.28. As expected, there is a sharp single resonance. ^{139}La MAS NMR spectra for the various lanthanum containing materials prepared in this thesis, as well as a sample of lanthanum oxide, La_2O_3, could not be observed. This was despite an intensive investigation in which spectral acquisition parameters were changed in a systematic manner.[22] A zeolite-Y sample, containing 8.6 mass% ion-exchanged lanthanum, was also

sent to the EPSRC Solid State NMR Service at Durham University: again no spectrum was observed. It is unclear why the central ½ ↔ -½ quadrupole transition cannot be recorded: this is an area for further work.

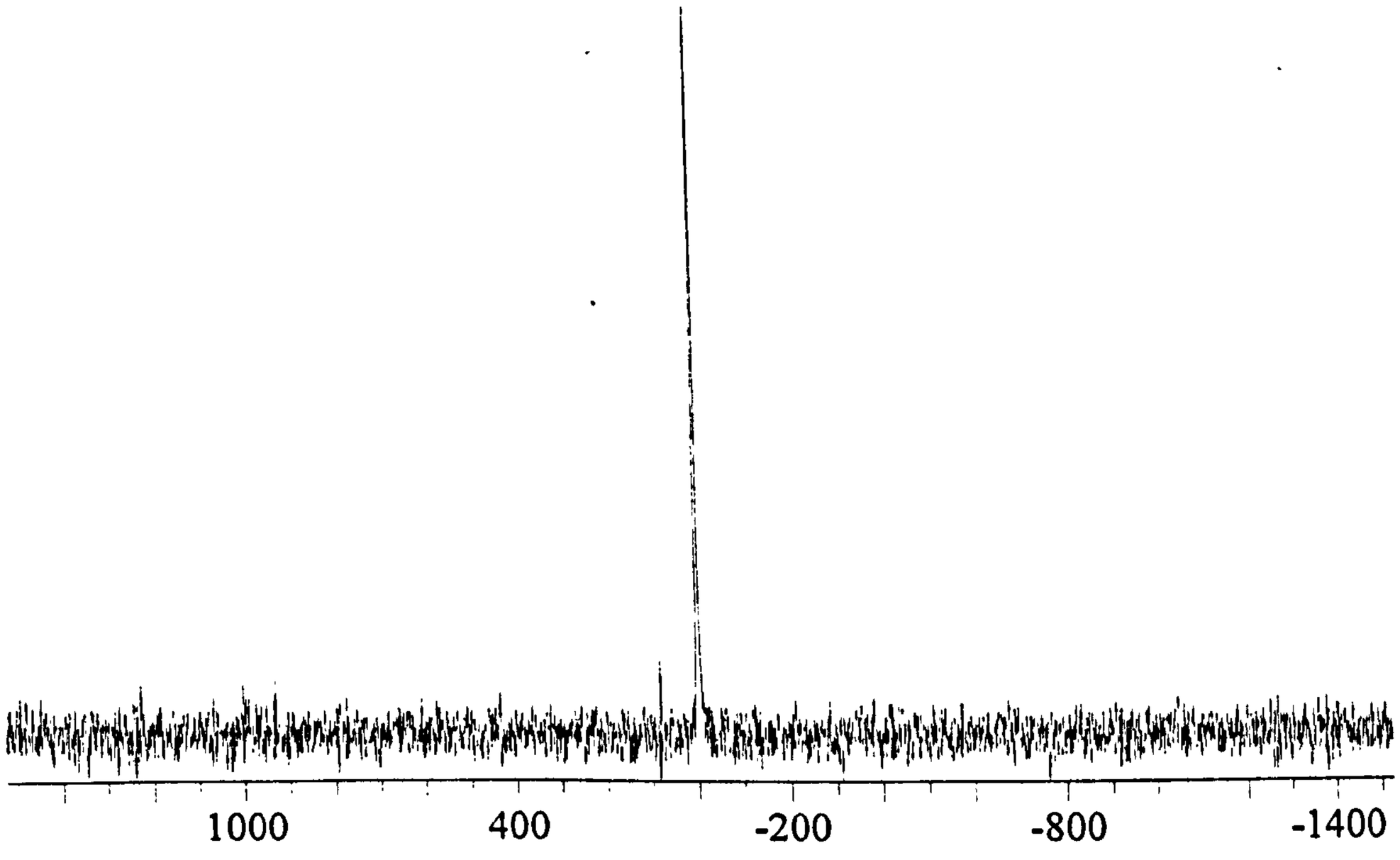

Figure 3.28 ^{139}La NMR spectrum observed at.56.473 MHz in the MAS NMR probe for an aqueous solution of $LaCl_3$, pulse delay = 10 s, pulse width = 4 μs, and number of scans = 100.

Errors and reproducibility

The errors associated with any resonance line in the MAS NMR spectra in this thesis are quoted as half the width of the resonance line at half height. For spectra which have a poor signal to noise, for example those in Figure 3.26, no error is quoted. In this case the presence of a resonance is taken to be the most critical feature. Similarly no error will be quoted where the half width at half height could not be determined due to significant overlap of neighbouring peaks.

References

1 H.P. Klug and L.E. Alexander, *X-ray Diffraction Procedures for Polycrystalline and Amorphous Materials*, 1954, John Wiley & Sons Inc., New York, London, Sidney.

2 L.V. Azároff and M.J. Buerger, *The Powder Method in X-ray Crystallography*, 1958, McGraw-Hill. New York, Toronto, London.

3 J.W. Jeffery, *Methods in X-ray Crystrallography*, 1971, Academic Press, London.

4 J. Wormald, *Diffraction Methods*, 1973, Clarendon Press, Oxford.

5 B.D. Cullity, *Elements in X-ray Diffraction*, (2nd edn), 1978, Addison-Wesley Publishing Co. Inc., London.

6 C.Whiston, *X-ray Methods*, 1987, John Wiley & Sons Inc., Great Britain.

7 B.W. Wojciechowski and A. Corma, *Catalytic Cracking Catalysts, Chemistry and Kinetics*, 1986, Marcel Dekker Inc., New York.

8 *Powder Diffraction File*: *Search Manual*, Joint Committee on Powder Diffraction Standards, Publication SMA-26, Pennsylvania USA, 1976.

9 S. Brunauer, P.M. Emmett and E. Teller, *J. Amer. Chem. Soc.*, 1938, **60**, 309.

10 I. Langmuir, *J. Amer. Chem. Soc.*, 1916, **38**, 2221.

11 S.J. Gregg and K.S.W. Sing, *Adsorption, Surface Area and Porosity*, (2nd edn), 1982, Academic Press, London.

12 **BS 4359 : Part 1**, *Determination of the Specific Area of Powders*, 1984.

13 **D 4365**, *Standard Test Method for Determining Zeolite Area of a Catalyst*, 1985.

14 D.H. Everett, G.D. Parfitt, K.S.W. Sing and R. Wilson, *J. Appl. Chem. Biotechnol.*, 1974, **24**, 199.

15 R.K. Harris, Nuclear Magnetic Resonance Spectroscopy, Longman Group UK Limited, 1986.

16 J.C. Davis, *Advanced Physical Chemistry*, Roland, New York, 1965.

17 E. Lippmaa, M. Mägi, A. Samoson, G. Englehardt, and A.R. Grimmer, *J. Am. Chem. Soc.*, 1980, **102**, 4889.

18 D. Müller, W. Gessner, H.J. Behrens, and G. Scheler, *Chem. Phys. Lett.*, 1981, **79**, 59.

19 A. Samoson, E. Kundla and E. Lippmaa, *J. Magn. Reson.*, 1982, **49**, 350.

20 M.E. Smith, *Appl. Magn. Reson.*, 1993, **4**, 1.

21 G. Engelhardt and D. Michel, *High-Resolution Solid-State NMR of Silicates and Zeolites*, John Wiley and Sons, Chichester, 1987.

22 R. Dupree, M.H. Lewis and M.E. Smith, *J. Am. Chem. Soc.*, 1989, **111**, 5125.

Chapter 4

Sample Preparation and Treatment

4 Sample Preparation and Treatment

This section gives a detailed description of the procedures used for the preparation of the samples in this work. An account is also given of the methods and apparatus used to treat these samples under a variety of conditions that compare with those in a commercial FCCU.

4.1 Introduction

Two distinct types of zeolite-Y based sample have been investigated in this work. One series of samples was based on commercial FCCs (donated by B.P. Oil International, Sunbury) and was used as provided. These samples were artificially contaminated with vanadium and were subjected to various controlled steam treating regimes. The other series of samples were based upon well characterised zeolite-Y itself. These samples can be treated as a model series since, in particular, they allow rare earth (RE)-vanadium-zeolite-Y chemistry to be investigated in the absence of the various amorphous materials present in commercial FCCs. This model series was subjected to the same type of steam treatment as the commercial series of catalysts. It should be noted, however, that a wider range of RE ion-exchange levels was investigated for the model zeolite-Y samples than that typical of the commercial materials.

For completeness in the work support materials typically found in commercial FCCs were also investigated. Attention was focussed on RE-vanadium interactions in the presence of these materials. This work was also complemented by more general studies of the chemistry between RE and vanadium-containing compounds.

In general all samples were subject to a variety of controlled reaction conditions. These conditions were selected in order to gain information relevant to the destruction of the zeolite-Y lattice by vanadium under commercial conditions. Experimental conditions were used which allowed the evaluation of: increasing temperature, increasing RE ion-exchange levels within the zeolite lattice, increasing vanadium levels, the effect of differing partial pressures of steam and the effect of steaming atmosphere. Nitrogen was substituted for air

so the effect of external oxygen sources could also be evaluated. The apparatus used for these experiments was designed to simulate commercial regenerator conditions on a laboratory scale and was similar to that described by other workers in the field.[1,2]

An important conclusion reached from the various studies was that the presence of 'free lanthanum' (or other RE) on the surface of a zeolite-Y based catalyst should provide protection against destruction by vanadium contamination. Preparative methods were thus developed to introduce lanthanum and cerium on to the surface of zeolite-Y based catalyst particles.

4.2 Commercial and Model Zeolite-Y Based Samples

The commercial FCC samples, which had increasing RE ion-exchange levels, were received in their final form. The compositional details of the catalysts (denoted as alpha-52, alpha-54 and alpha-56) are given in Table 4.1. It should be noted that all three catalyst samples contained the same type of amorphous clay particle and aluminosilicate binder. All three forms of the catalyst contained approximately 20-25 mass% zeolite.

Sample	RE_2O_3 /mass%
Alpha-52	0.61
Alpha-54	1.12
Alpha-56	2.73

Table 4.1 RE loadings for the commercial FCC forms of zeolite-Y based samples. The data was supplied by B.P. Oil International, Sunbury. The data is expressed in terms of RE_2O_3 due to the mixed nature of RE ions found within commercial samples.

Zeolite-Y powder was obtained[3] in an ammonium exchanged form, NH_4-Y. This zeolite had residual sodium levels of 0.024 mass%, measured in terms of Na_2O, and a silicon/aluminium ratio (SiO_2/Al_2O_3) of 3.01.

Ion-exchange procedure to prepare model zeolite-Y samples with differing RE (lanthanum) loadings

For the model RE-exchanged zeolite-Y samples, lanthanum was selected as the RE. Single element RE ion-exchange was used in order to keep the model system as simple as possible. It can be recalled (Section 2.1.1) that RE ion-exchange within commercial samples is achieved with a mixed RE source. The use of lanthanum for single element ion-exchange has been adopted by many workers in this field[2,4] and has similar effects on the stability of the zeolite-Y lattice as does ion-exchange with multiple REs. The use of single element ion-exchange also helps significantly with the detection of new RE phases during analysis. The levels employed here are near the limits of detection of both X-ray diffraction (XRD) and magic-angle-spinning nuclear magnetic resonance (MAS NMR), decreasing the concentration of RE-based phases by the use of multiple REs would further hamper the detection of new phases.

The ion-exchange procedure is summarised in Figure 4.1 (over the page) and is based upon that used by other workers.[4,5] Overall the procedure involves the partial exchange of NH_4^+ counter-ions present in the ammonium-exchanged zeolite-Y with La^{3+} counter-ions.

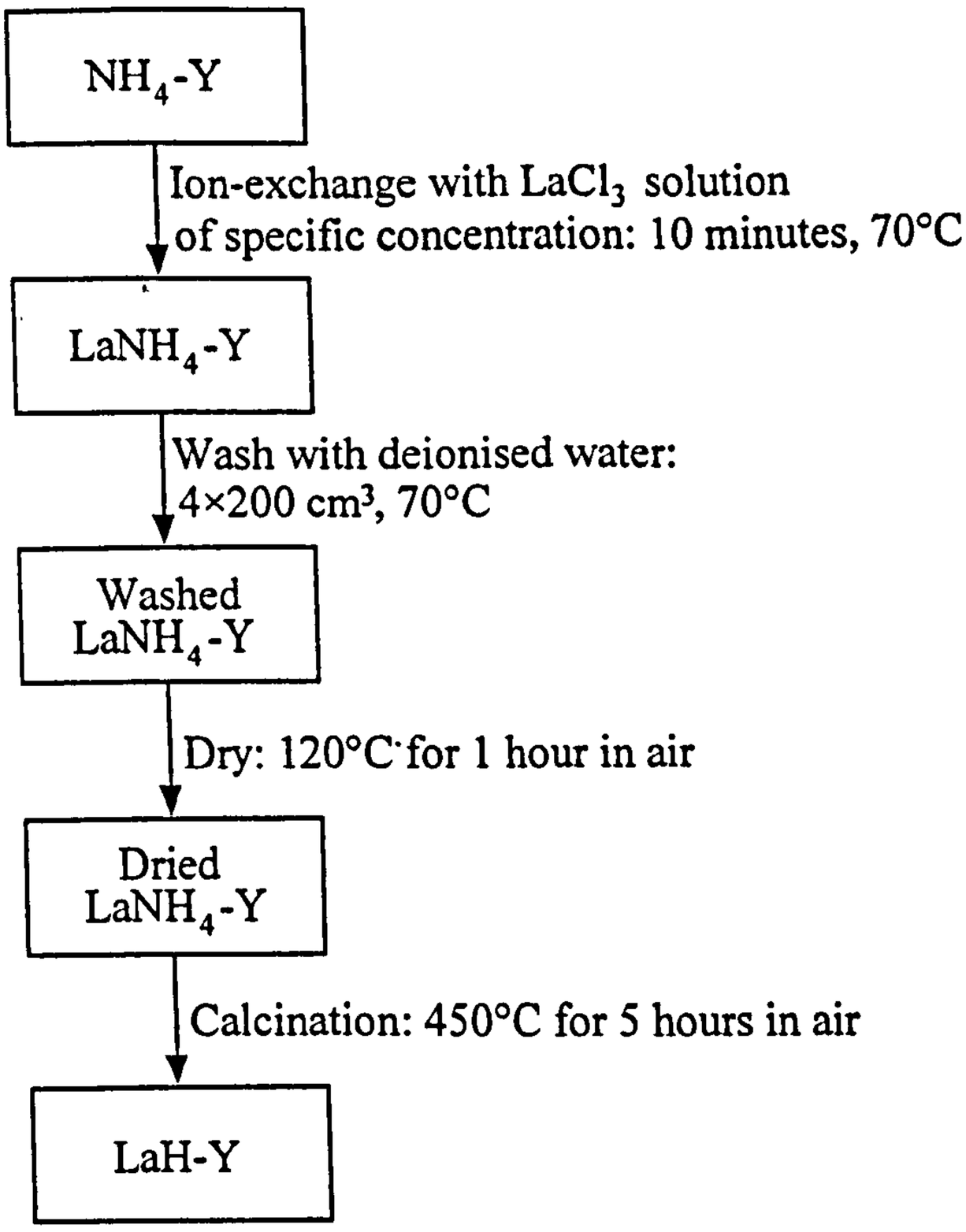

Figure 4.1 Schematic diagram summarising the ion-exchange procedure for zeolite-Y.

A lanthanum trichloride heptahydrate ($LaCl_3.7H_2O$, Aldrich, 99.999%) solution was prepared in 200 cm³ of deionised water. The concentration of this solution was calculated on the basis that complete exchange of lanthanum cations into the zeolite would take place during the ion-exchange procedure. This assumption was verified by subsequent analysis (see later). The $LaCl_3$ solution was heated to a constant temperature of 70°C. To the hot solution was added the NH_4-Y zeolite (typically 20 g) and the slurry was stirred for a further 10 minutes. After this period the slurry was filtered and washed with hot (70°C) deionised water (200 cm³). The washing step was to ensure complete removal of NH_4^+ and Cl^- ions from the zeolite surface. The wash water was tested for Cl^- ions with silver nitrate solution. Washing was repeated with deionised water (200 cm³, 70°C) until no Cl^- could be detected: typically 4 washes were found to be sufficient to remove all traces of Cl^-. The zeolite was then dried at 120°C for 1 hour in air before being calcined at 450°C for 5 hours in air. This final calcination step promotes the breakdown of any remaining NH_4^+, leaving H^+ and evolving ammonia gas. The zeolite is now in the LaH-Y form.

Samples that required no lanthanum ion-exchange were simply treated in accordance with the last two steps in Figure 4.1 to leave the zeolite in the H-Y form.

It should be noted that the following notation will be used for describing zeolite-Y based samples throughout the remainder of this thesis. H-Y will represent zeolite-Y samples that have had no partial ion-exchange of lanthanum into their lattice. X.XLaH-Y will represent samples with a partial lanthanum exchange level of X.X mass%.

The target values for lanthanum-exchanged zeolite-Y samples were 1.5, 2.5, 5.0 and 8.0 mass%. Lanthanum elemental analysis (Medac LTD) of the target 2.5 mass% sample was carried out in some detail. Two separate samples were analysed by X-ray fluorescence methods (XRF, 8-10 g of sample per analysis) and a third by inductively-coupled plasma emission spectroscopy single element analysis (ICP, 0.5-1 g of sample per analysis). These techniques gave an average value close to 2.6 mass% lanthanum confirming that complete ion-exchange of lanthanum had been achieved in the preparative procedure. The 8.0 mass% target sample was analysed by ICP alone and again gave a value (8.6 mass%) close to that expected for complete lanthanum exchange. On the basis of these analyses the 1.5% and 5.0 mass% target samples (for which only limited amounts were available) were not analysed directly. However strong indirect evidence was obtained that these samples incorporated the target amount of lanthanum. For example, Figure 4.2 shows the surface area variation as a function of lanthanum ion-exchange level for a zeolite-Y sample steam treated at 800°C, without any vanadium contamination. The plot shows a smooth increase in surface area as a function of increasing ion-exchange level. This behaviour is exactly that to be expected since it is known that the incorporation of lanthanum into zeolite-Y results in increased thermal and hydrothermal stability of the zeolite.[4,5]

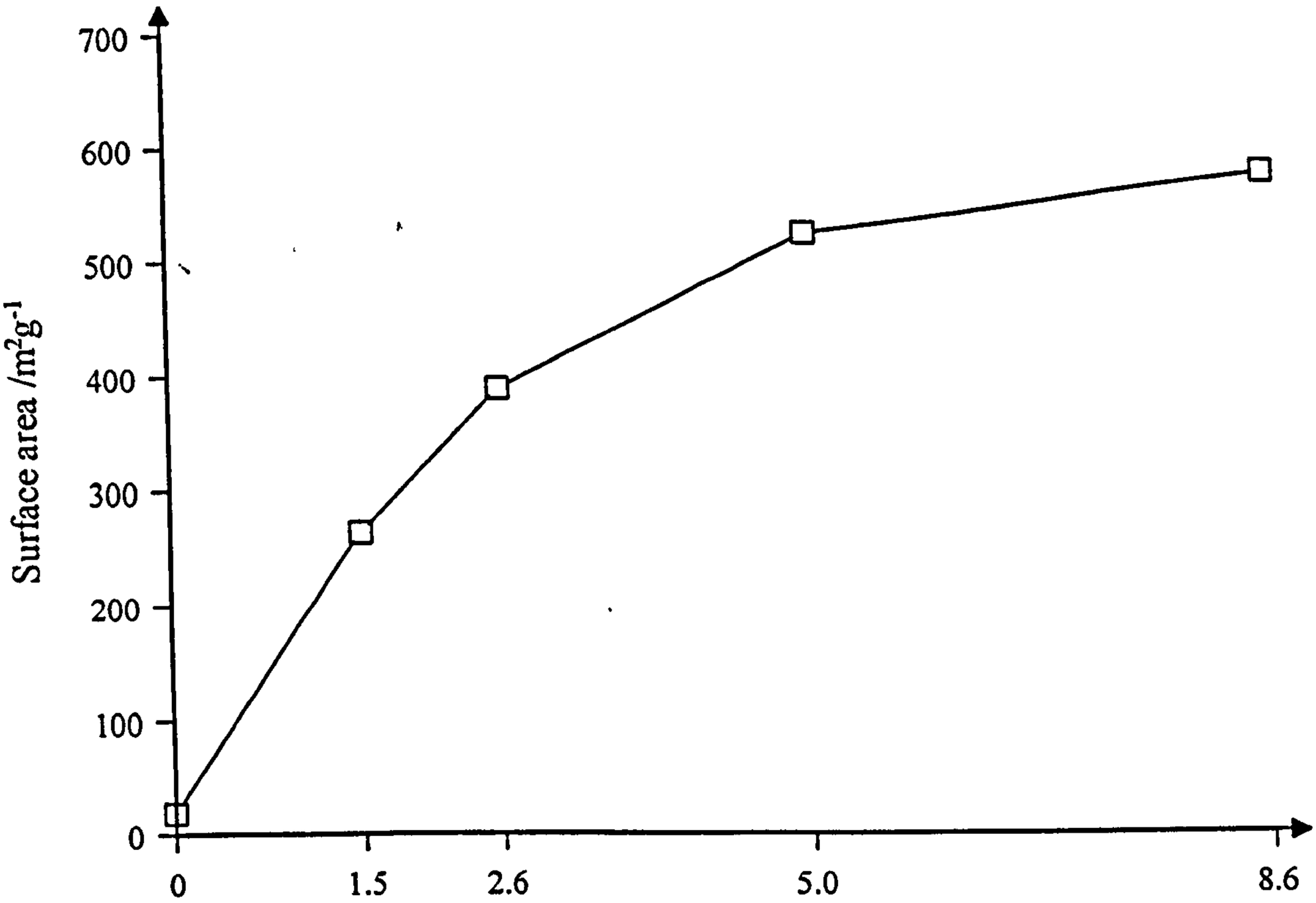

Figure 4.2 Variation in surface area as a function of increasing lanthanum ion-exchange level for a zeolite-Y sample steam treated at 800°C, without any vanadium contamination.

Vanadium deposition

Commercial and model zeolite-Y based samples were artificially contaminated with vanadium using vanadyl naphthenate 3% (that is 3%, by mass, vanadium). The general procedure was based upon the Mitchell method[1] which is recognised as an effective method for the deposition of vanadium contaminants onto the surfaces of zeolite-Y based catalysts. Other methods are available but are not considered in the present work.

Vanadyl naphthenate 3% is a dark green/black viscous liquid which is formed from a range of naphthenic acids and has a boiling temperature range of 300-450°C. The general formula of naphthenic acids is $R(CH_2)_nCOOH$, where R represents one, or several, rings.[1,6] Figure 4.3 gives the structure of the simplest naphthenic acid with n=1 (cyclopentane acetic acid).

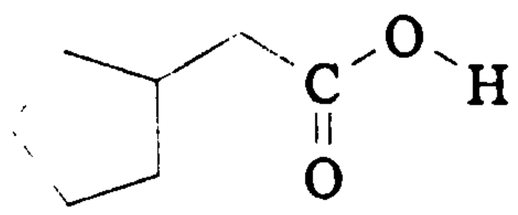

Figure 4.3 Structure of the naphthenic acid, cyclopentane acetic acid.

A typical procedure for the vanadium contamination of a zeolite-Y based sample was as follows. A known amount (typically 10 g) of sample was weighed into a round-bottomed flask (250 cm^3). To it was added an accurately weighed amount (dependent upon the desired final vanadium loading) of vanadium naphthenate 3% (supplied by B.P. Oil International, Sunbury) dissolved in toluene (Aldrich, 99.8+%). The mixture was then attached to a rotary evaporator (no vacuum) and allowed to mix for 10 minutes. After this period the vacuum was applied and the solvent consequently removed. It was assumed that all of the vanadium was deposited: in view of the boiling range of the vanadyl naphthenate 3% used it is unlikely that any vanadium would escape during the rotary evaporation procedure. When thoroughly dry the sample was calcined at 300°C for 3 hours in air to remove any traces of remaining solvent (samples, with no vanadium loading, which were to be used in comparative experiments, were always calcined under the same conditions).

The vanadium contamination levels used for the commercial FCC catalysts were in the range 0 to 4000 ppm. This range is consistent with that expected in a commercial FCCU. It should be recognised, however, that the zeolite-Y component of a commercial catalyst comprises only 20-25% of its total mass. Thus, if all of the vanadium is assumed to be associated with this component, then the vanadium contamination level at the zeolite is effectively increased by a factor of between 4 and 5. There is strong evidence that this is the case. Wormsbecher and co-workers[2] have shown that the vanadium distribution in a composite catalyst following hydrothermal treatment closely resembles that of the zeolite-Y distribution. Furthermore, similar observations have been made by other workers,[7-9] in particular for samples derived from working FCCUs.[10] On this basis the upper range for vanadium contamination for the model zeolite-Y based samples was extended to 20 000 ppm.

For the commercial samples, vanadium contamination at a level of 4000 ppm was such that any vanadium compounds formed were all well below the detection limits of powder XRD and close to the detection limits of the ^{51}V MAS NMR experiment. Table 4.2 provides a summary of all the samples that were prepared.

Zeolite-Y based sample	Vanadium loading /ppm
H-Y	0, 5000
1.5LaH-Y	0, 1000, 3000, 5000
2.6LaH-Y	0, 1000, 3000, 5000, 10 000, 20 000
5.0LaH-Y	0, 5000, 10 000
8.6LaH-Y	0, 5000, 10 000, 15 000
Alpha-52	0, 2000, 4000
Alpha-54	0, 2000, 4000
Alpha-56	0, 2000, 4000

Table 4.2 The vanadium levels used for all forms of zeolite-Y based samples.

Steam treatment

Details of the various steam treatments that were applied to the samples summarised in Table 4.2 are given in Table 4.3. Full details of the apparatus, and the methods used, for steam treatment are given later in Section 4.5.

Surface deposition of rare earths

The procedure for introducing 'free rare earths' onto the surfaces of catalyst particles was developed only for the commercial FCCs. Just two REs were used, that is lanthanum and cerium. The overall procedure was designed to minimise any ion-exchange of deposited RE into the zeolite lattice. A fixed vanadium loading of 10 000 ppm was selected for these samples. This magnitude of loading would cause severe damage to commercial FCCs and thus provides a critical test of any zeolite-Y protection strategy.

Sample	Vanadium loading /ppm	Steaming temperature /°C	Water vaporised /cm^3	Steam/gas ratio /% steam	Steaming atmosphere
H-Y	0, 5000	750, 800	0, 60	80	Air
1.5LaH-Y	0, 1000, 3000, 5000	750, 800	60	40, 80	Air
2.6LaH-Y	0, 1000, 3000, 5000	750, 800	0, 60	40	Air
	0, 1000, 3000, 5000	750, 800	60	80	Air
	10 000, 20 000	800	60	40, 80	Air
	5000	800	60	0, 50, 60, 70, 80, 100	Air
	10 000	800	60	0, 40, 50, 60	Air
	0, 5000	800	60	80	Nitrogen
5.0La-H-Y	0, 5000, 10 000	750, 800	60	80	Air, Nitrogen
8.6LaH-Y	0, 5000, 10 000, 15 000	750, 800	60	80	Air, Nitrogen
Alpha-52	0, 2000, 4000	788, 816	60	80	Air
Alpha-54	0, 2000, 4000	788, 816	60	80	Air
Alpha-56	0, 2000, 4000	788, 816	60	80	Air

Table 4.3 Summary of steaming experiments performed on zeolite-Y based samples.

A known amount (typically 10 g) of FCC sample was added to a round-bottomed flask (250 cm^3). A RE solution in deionised water (2-4 cm^3) was accurately prepared and added to this flask. Solutions were prepared which had either a ten-fold ($LaCl_3$, $La(NO_3)_3$ and $CeCl_3$) or twenty-fold molar excess ($LaCl_3$) of free RE to vanadium. That is for every vanadium present in the FCC either 10 or 20 REs were introduced to the surface. The mixture was quickly attached to a rotary evaporator and the solution was allowed to mix for several seconds. After this period the vacuum was applied and the water was rapidly removed. The total contact time of RE solution and FCC did not exceed 1 minute.

A summary of the samples prepared, based on alpha-56, and their subsequent treatment is given in Table 4.4.

RE loading /100 000 ppm, and source	Vanadium loading /ppm	Steaming temperature /°C	Steaming atmosphere
0, $LaCl_3$	0, 10 000	750, 800	Air
1.0, $LaCl_3$	0, 10 000	750, 800	Air, Nitrogen
2.0, $LaCl_3$	10 000	750, 800	Air
1.0, $La(NO_3)_3$	10 000	750, 800	Air
1.0, $CeCl_3$	10 000	750, 800	Air

Table 4.4 Summary of steaming experiments performed on RE surface-loaded alpha-56.

4.3 Rare Earth-Vanadium Samples Based upon Support Materials

A series of RE-vanadium reactions were carried out in the presence of support materials; silica and α-alumina were selected as being typical. Lanthanum was deposited on both of the materials before subsequent vanadium deposition followed by steam treatment. The level of vanadium deposition was considerably higher than that used for the catalyst samples to aid the detection of new phases by both MAS NMR and XRD.

Wormsbecher and co-workers[2] have suggested that RE-vanadium interactions only occur after the collapse of the zeolite-Y lattice, rather than these interactions being important in the mechanism of zeolite-Y lattice collapse as suggested by others.[11,12] A series of samples was thus prepared from a commercial FCC (alpha-54) which had been completely destroyed by extreme thermal treatment.

Silica and alumina support materials

Before deposition of vanadium, the support samples were first loaded with lanthanum. The same lanthanum deposition procedure for both the silica (quartz, Aldrich, 99.8%) and the α-alumina (corundum, Aldrich, 99.8%) was used. A given amount of support material (40 g) was dried at 110°C for 24 hours in air, and then placed into a 400 cm^3 beaker. To it was added a known amount of lanthanum trichloride heptahydrate ($LaCl_3.7H_2O$, Aldrich, 99.999%) dissolved in deionised water (100 cm^3) The mixture was stirred, using a mechanical stirrer, for 24 hours at room temperature. After this period the water was removed by calcination at 110°C for 24 hours in air, the resulting pellet was reground. XRF analysis confirmed 11.0 mass% deposited upon the α-alumina support material and 9.5 mass% deposited upon the surface of the silica support material.

Samples that required no lanthanum deposition were dried under the same conditions.

Vanadium deposition (1.0 mass%) was carried out using vanadyl naphthenate 3% as already described. Table 4.5 provides further details.

Lanthanum loading /mass%	Vanadium loading /mass%	Steaming temperature /°C	Water vaporised /cm^3	Steam/gas ratio /% steam	Steaming atmosphere
0	0, 1.0	800	0, 60	80	Air, Nitrogen
~ 10.0	0, 1.0	750, 800	0, 60	80	Air, Nitrogen

Table 4.5 Summary of the lanthanum and vanadium loadings used for the both the silica and α-alumina support samples, together with a summary of the steaming conditions used in the steam treatment of these samples.

A 'completely degraded' FCC sample

The collapse of the FCC sample (alpha-54) was achieved by severe heat treatment for a prolonged period, that is calcining in air at 1400°C for 48 hours. Vanadium deposition was carried out in the same manner as described previously. Table 4.6 provides further details.

Vanadium loading /mass%	Steaming temperature /°C	Water vaporised /cm^3	Steam/gas ratio /% steam	Steaming atmosphere
0	800	0, 60	80	Air, Nitrogen
1.0	750, 800	0, 60	80	Air, Nitrogen

Table 4.6 Summary of the vanadium loading and steaming conditions performed on 'completely degraded' alpha-54.

4.4 General RE-vanadium Chemistry

The reactions between a number of RE (lanthanum and cerium) and vanadium compounds were investigated. These are summarised in Table 4.7. Vanadium (V) oxide (V_2O_5, Aldrich, 99.99%) was selected because the vanadium is present in the +5 oxidation state and may be one of the active vanadium compounds responsible for the destruction of the zeolite lattice.[13-15] Vanadyl phthalocyanine ($VON_8C_{32}H_{16}$, Eastman Organic Chemicals) was chosen because the vanadium is co-ordinated in a manner that may be typical of its situation in crude oil (Figure 4.4). In this case it is interesting to compare the results with those obtained from vanadyl naphthenate 3%.

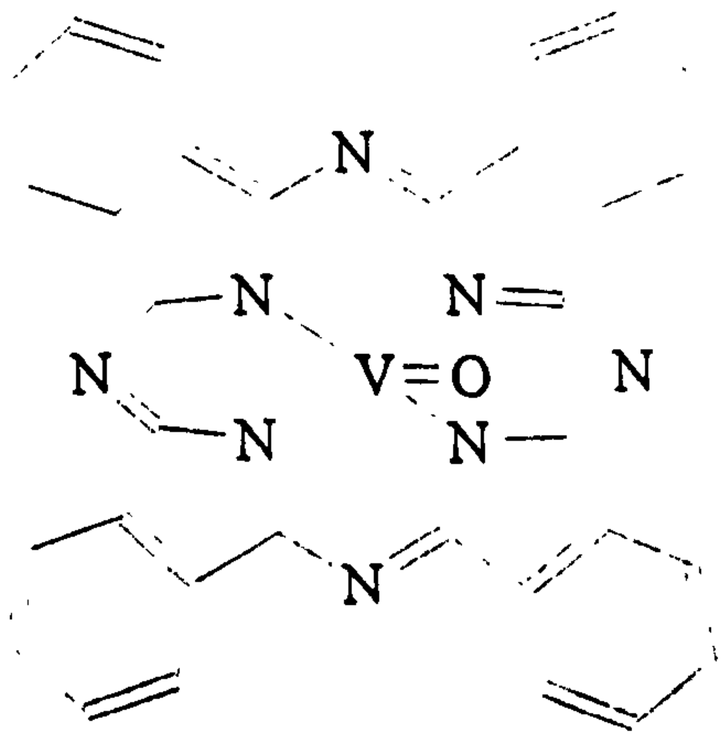

Figure 4.4 The structure of vanadyl phthalocyanine.

Vanadium compound	RE compound
Vanadyl naphthenate 3%	$LaCl_3.7H_20$
	$La(NO_3)_3.6H_2O$
	La_2O_3
	$CeCl_3.7H_2O$
Vanadium (V) oxide	$LaCl_3.7H_20$
Vanadyl phthalocyanine	$LaCl_3.7H_20$

Table 4.7 Summary of the reaction mixtures.

The apparatus used for reactions between vanadium and RE containing compounds is shown schematically in Figure 4.5. There are two major components: a high temperature (1400°C) horizontal tube furnace (Heraeus, work tube length 32 cm, work tube diameter 40 mm) and a quartz work tube (length 750 mm, external diameter 34 mm, internal diameter 31 mm).

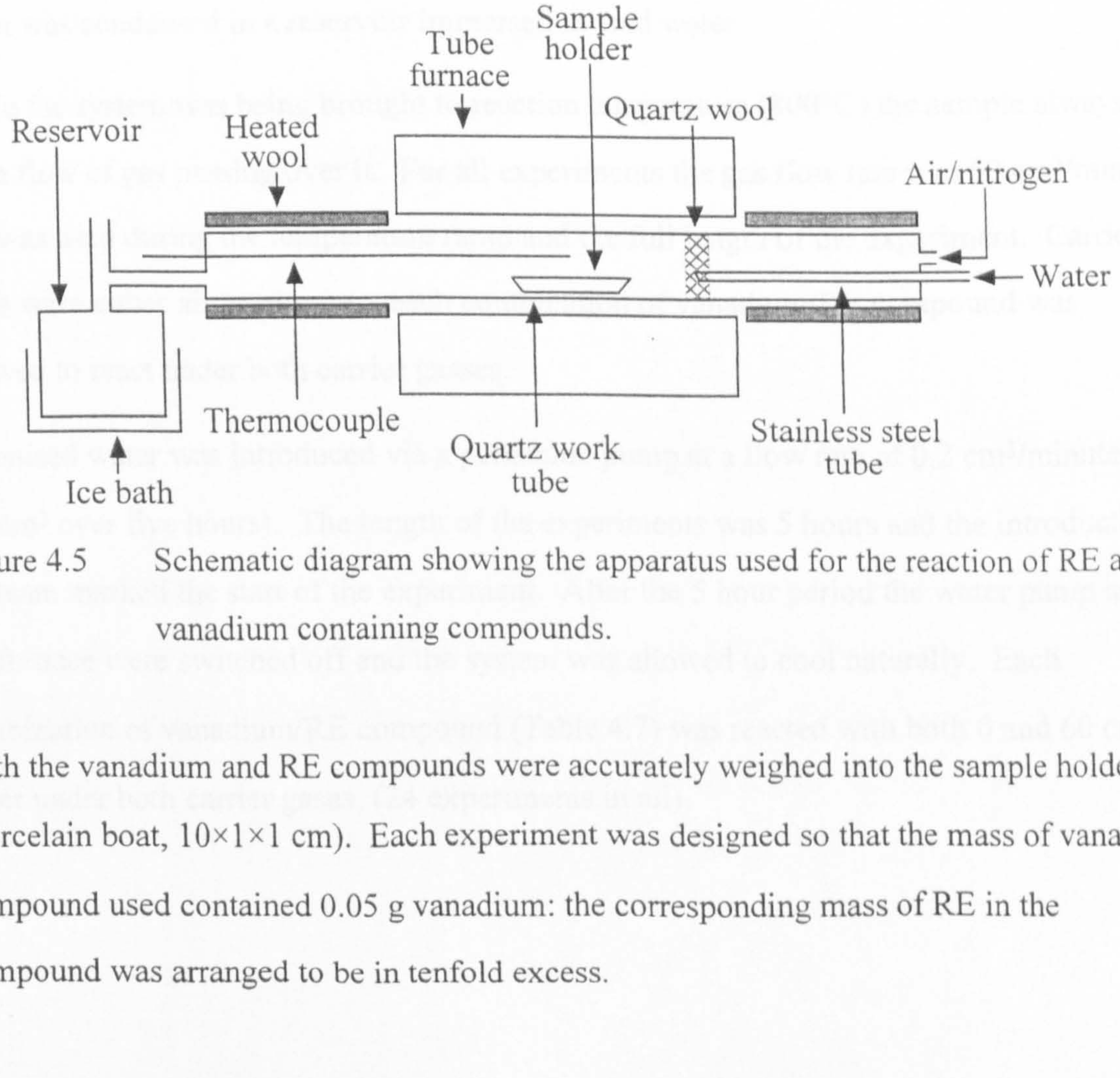

Figure 4.5 Schematic diagram showing the apparatus used for the reaction of RE and vanadium containing compounds.

Both the vanadium and RE compounds were accurately weighed into the sample holder (porcelain boat, 10×1×1 cm). Each experiment was designed so that the mass of vanadium compound used contained 0.05 g vanadium: the corresponding mass of RE in the compound was arranged to be in tenfold excess.

The temperature was controlled using a thermostat, equipped with only a set temperature function, this allowed the temperature to be controlled to ±4°C. All experiments were carried out at 800°C. A significant temperature drop (8-12°C) was observed between the furnace elements and the centre of the quartz work tube so an external thermocouple (type K, nickel/chromium), positioned above the sample, was used to adjust the final target temperature. Experimental conditions, as far as possible, were kept identical to those for a typical steaming experiment using the vertical tube furnace (Section 4.5). As the thermostat had no ramp-rate; temperature control was achieved manually, an approximate ramp rate of 200°C/hour was used with the temperature being increased 100°C every ½hour. When the system had reached the target temperature, the temperature at the centre of the quartz work tube was monitored and carefully increased to the target temperature. The system was then left to equilibrate for a further hour.

For experiments that required steam passing over the sample, the heated wool (Figure 4.5) was maintained at 110°C for the length of the experiment. This was to prevent the condensation of steam on the cooler parts of the quartz work tube outside the furnace. The steam was condensed in a reservoir immersed in iced water.

While the system was being brought to reaction temperature (800°C) the sample always had a flow of gas passing over it. For all experiments the gas flow rate was 60 cm^3/minute, this was used during the temperature ramp and the full length of the experiment. Carrier gases were either air or nitrogen, each combination of vanadium/RE compound was allowed to react under both carrier gasses.

Deionised water was introduced via a peristaltic pump at a flow rate of 0.2 cm^3/minute (60 cm^3 over five hours). The length of the experiments was 5 hours and the introduction of steam marked the start of the experiment. After the 5 hour period the water pump and the furnace were switched off and the system was allowed to cool naturally. Each combination of vanadium/RE compound (Table 4.7) was reacted with both 0 and 60 cm^3 of water under both carrier gases, (24 experiments in all).

Preparation of lanthanum vanadium (V) oxide

Throughout the course of this work the formation of lanthanum vanadium (V) oxide ($LaVO_4$) has been observed for many classes of sample after treatment under varying conditions. Production of phase pure vanadate, therefore, was important so that thorough characterisation, by both XRD and ^{51}V MAS NMR, could be achieved. In addition samples of this vanadate could be exposed to the same conditions of steam and temperature as used for the zeolite-Y based samples.

The method of vanadate formation was loosely based on methods found in the literature:[16-20]

$$La_2O_3 + V_2O_5 \longrightarrow 2\,LaVO_4 \qquad (4.1)$$

The following experimental procedure was used. Equivalent molar quantities (0.002 mol) of the lanthanum oxide and vanadium oxide were accurately weighed and intimately mixed. The mixture was carefully transferred to a quartz ampoule, the ampoule was evacuated and sealed under vacuum. The ampoule was then placed in a tempered steel container which would contain the reactants in the event of ampoule failure. The steel container was placed in a conventional oven and heated to 1400°C at 20°C/minute. The mixture was heated at 1400°C for 48 hours, after this time the mixture was allowed to cool naturally to room temperature.

4.5 Steam Treatment

Steam treatment is very important for the samples investigated in this thesis, that is all modified forms of zeolite-Y, FCC samples, (including samples loaded with La^{3+} ions and those destroyed by high temperature reaction), and those based on silica and α-alumina support materials. In all cases the steam treatment was designed to be similar to industrial practice, in particular commercial regenerator conditions (c.f. Section 2.1).

A vertical tube furnace with controllable air and water flow rates was designed to mimic the conditions that an FCC would experience in the regenerator part of an FCCU. A schematic diagram of the furnace is shown in Figure 4.6. It consists of two major components; a quartz work tube (length 750 mm, external diameter 34 mm, internal diameter 31 mm) and a high temperature (1400°C) vertical tube furnace (Carbolite, work tube length 600 mm, work tube diameter 68 mm).

The temperature was controlled using a Eurotherm thermostat (model 808) which was equipped with ramp and dwell facilities which allowed temperature control to ±1°C. A ramp rate of 3.35°C/minute (200°C/hour) was used for all samples. Final temperatures were either 750 or 800°C at the sample. Due to the temperature drop that exists from the furnace elements to the centre of the furnace work tube an external thermocouple (type K, nickel/chromium) was positioned at the centre of the sample. The Eurotherm was adjusted so the temperature of the sample was constant at the target temperature: a temperature drop of 6-12°C was typical. When the target temperature had been reached the system was allowed to stand at this temperature for 1 hour; this was to ensure that the system had reached equilibrium. After this period the sample was kept at the target temperature for a further 5 hours, this was the time duration of all steam treatment experiments. After 5 hours the temperature was allowed to cool naturally.

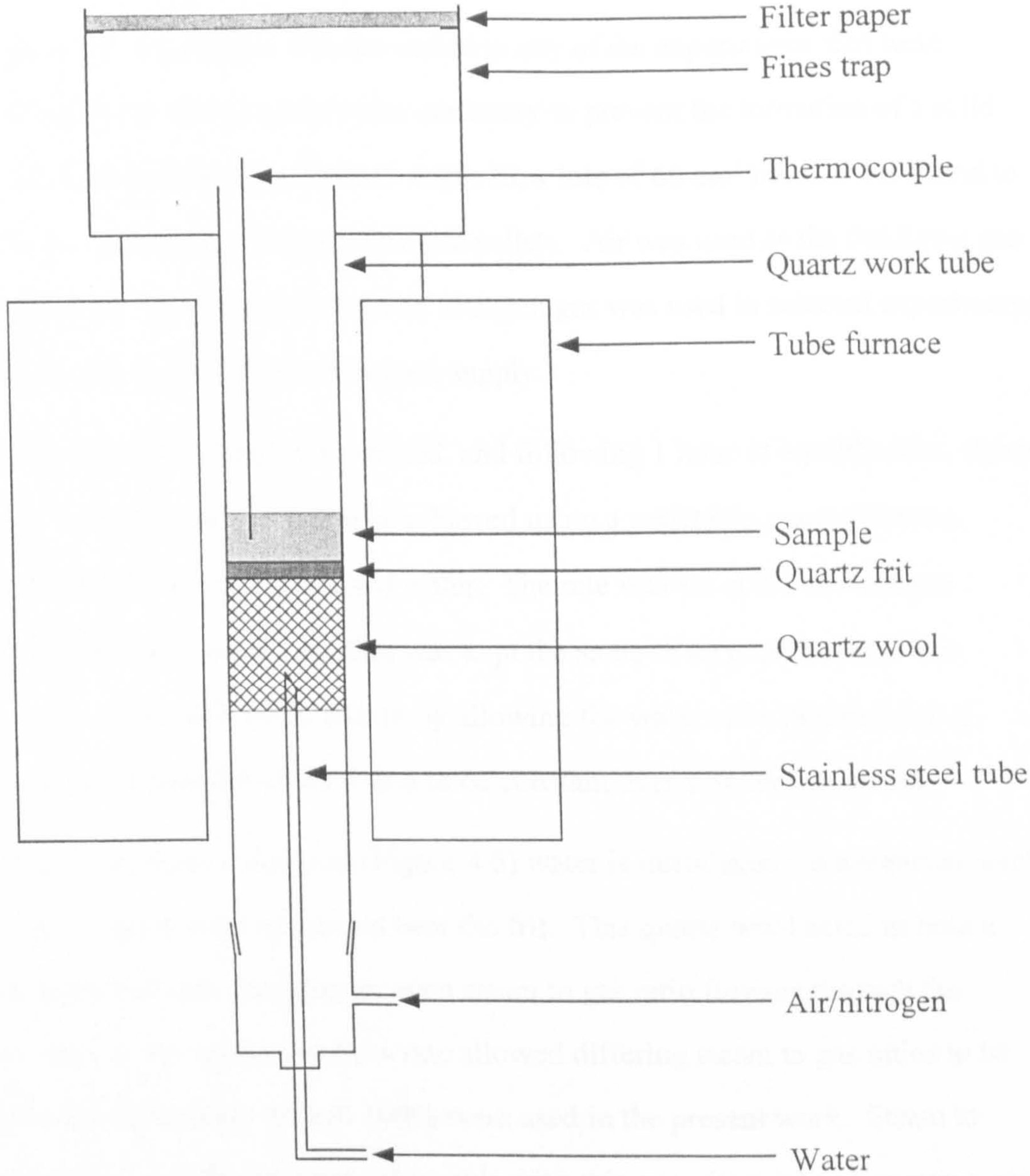

Figure 4.6 Schematic diagram showing the vertical tube furnace design for the steam deactivation of samples.

In a typical experiment 2 g of sample was poured into the quartz work tube; the tube was gently tapped to ensure that all of the sample reached the quartz frit. This mass of sample gave an average sample depth of 0.5 cm. The thermocouple was inserted into the work tube to a depth of roughly 0.25 cm from the surface of the quartz frit and the fines trap was placed over the top of the tube. The purpose of this trap was to collect any small particles that escaped by convection. The quartz work tube was then placed carefully within the tube furnace and positioned so that the sample was at the centre point; this was to ensure an even and constant heat supply to the sample. Whilst the sample was being raised to the target temperature (750°C or 800°C) it was fluidised with a flow of gas

(60 cm^3/minute): this rate of flow was not varied in any of the experiments that were undertaken. Fluidisation of the sample was necessary to prevent the formation of a solid pellet during the length of the experiment. A gas flow rate of 60 cm^3/minute was found to be sufficient to prevent the formation of sample pellets. Air was used as the fluidising gas in 'standard' steaming experiments, however, nitrogen gas was used in selected experiments to investigate the effect of a restricted oxygen supply.

After the target temperature had been reached, and following 1 hour of equilibration, steam was introduced into the system. This was achieved using a peristaltic pump (Watson Marlow, Model 101U) fed with deionised water. The rate was set at 0.2 cm^3/minute (60 cm^3 over a period of 5 hours) and this was kept the same in all experiments. The peristaltic pump was checked every month by allowing the water to be pumped into a measuring cylinder. Water flow was found to be constant over a 36 month period.

As indicated in the schematic diagram (Figure 4.6) water is introduced via a stainless steel tube embedded in quartz wool at the end near the frit. This quartz wool acted as both a vaporiser and a gas diffuser, ensuring an even steam to gas ratio flowing through the sample. Variation of the carrier gas flow rate allowed differing steam to gas ratios to be used; typically values between 40 and 100% were used in the present work. Steam to carrier gas ratios below 40% were not achievable with this experimental arrangement, since the relatively high carrier gas flow rates needed for these ratios would carry the sample out of the furnace system and hence cause significant loss of sample. After five hours the flow of water was stopped and this marked the end of the experiment. As already indicated the furnace was then allowed to cool naturally. When at room temperature, the sample was removed from the quartz tube by suction.

A carrier gas flow of 60 cm^3/minute and a water flow of 0.2 cm^3/minute gave a steam to gas ratio of 80%, that is for every 100 litres of gas that passed the quartz frit 80 litres would be steam. This was the standard steaming experiment ratio. During experiments which required a different ratio this was achieved by changing the carrier gas flow rate while the water flow rate remained constant at 0.2 cm^3/minute. For example if a 40% steam to gas ratio was required a carrier gas flow rate of 400 cm^3/minute was used. For experiments

that required a 0% steam to gas ratio (simple calcination) then the water pump was disconnected from the apparatus, the carrier gas flow rate was, in these circumstances, maintained at 60 cm^3/minute for the length of the experiment. When a 100% steam atmosphere was required the carrier gas was stopped upon the introduction of water, however during the temperature ramp and the 1 hour equilibrium period the carrier gas flow rate was maintained at 60 cm^3/minute. The fluidised bed was maintained by the passage of steam through the sample. This was confirmed by the samples remaining in a powdered form.

4.6 Reproducibility of Treatment Experiments

As already stated four samples have been prepared, and treated, which contain differing levels of lanthanum ion-exchanged into the zeolite-Y lattice (1.5LaH-Y, 2.6LaH-Y, 5.0LaH-Y, and 8.6LaH-Y). With the exception of the 2.6LaH-Y samples, the zeolites were prepared in a single batch, and this batch was used throughout for subsequent treatment experiments. As will be made clear later in this thesis a lanthanum loading in the region of 2 to 3 mass% is of particular interest and so several batches of 2.6LaH-Y were prepared. A specific investigation was undertaken to test the reproducibility of a given set of reaction conditions for these batches.

Two batches of 2.6LaH-Y were prepared and treated. Samples from both batches were contaminated with 0, 3000 and 5000 ppm vanadium and steam treated at 800°C for 5 hours, with an 80% steam to air ratio. Table 4.8 gives the specific unit cell constant and surface area measurements obtained for these samples. Other batches of 2.6LaH-Y gave results which showed similar trends and values of surface area, and unit cell constant, within the same range. The results in the table thus represent the full experimental range for the various batches of 2.6LaH-Y.

Steaming conditions	Vanadium loading /ppm	Batch 1 Unit cell constant /Å (±0.035Å)	Batch 1 Surface area /m^2g^{-1} (±10%)	Batch 2 Unit cell constant /Å (±0.035Å)	Batch 2 Surface area /m^2g^{-1} (±10%)
800/5/80/AIR	0	24.227	398	24.187	329
	3000	24.231	346	24.238	288
	5000	24.252	245	24.243	195

Table 4.8 Unit cell constant and surface area data obtained for different batches of 2.6LaH-Y steam treated as indicated.

The surface area measurements do show differences, but it is interesting to note that the changes in surface area as the vanadium loading is increased are very similar between the two batches. In this sense the trend in changes of surface area of the samples prepared from the two batches are within the overall error associated with surface area measurements. The samples are subject to a fairly complex treatment procedure and it could be that particle size is one factor, coupled with some non-uniformity in the heating and steaming procedures, that gives rise to the observed differences between the two batches. It is worth noting that investigations into how steam to carrier gas ratios affect the overall system (Section 5.2.2) have shown that a steam to carrier gas ratio of 80 % steam, for a 2.6LaH-Y sample loaded with 5000 ppm vanadium, is a particularly sensitive region and relatively large decreases in surface area are observed as the steam to carrier gas ratio is increased from 70 to 80 % steam (Figure 4.7, reproduced from Figure 5.18(a) Section 5.2.2). It would therefore only require a small deviation in steam to carrier gas ratio for a relatively large change in surface area to be observed. The comparison in Table 4.8 therefore relates to sensitive experimental conditions.

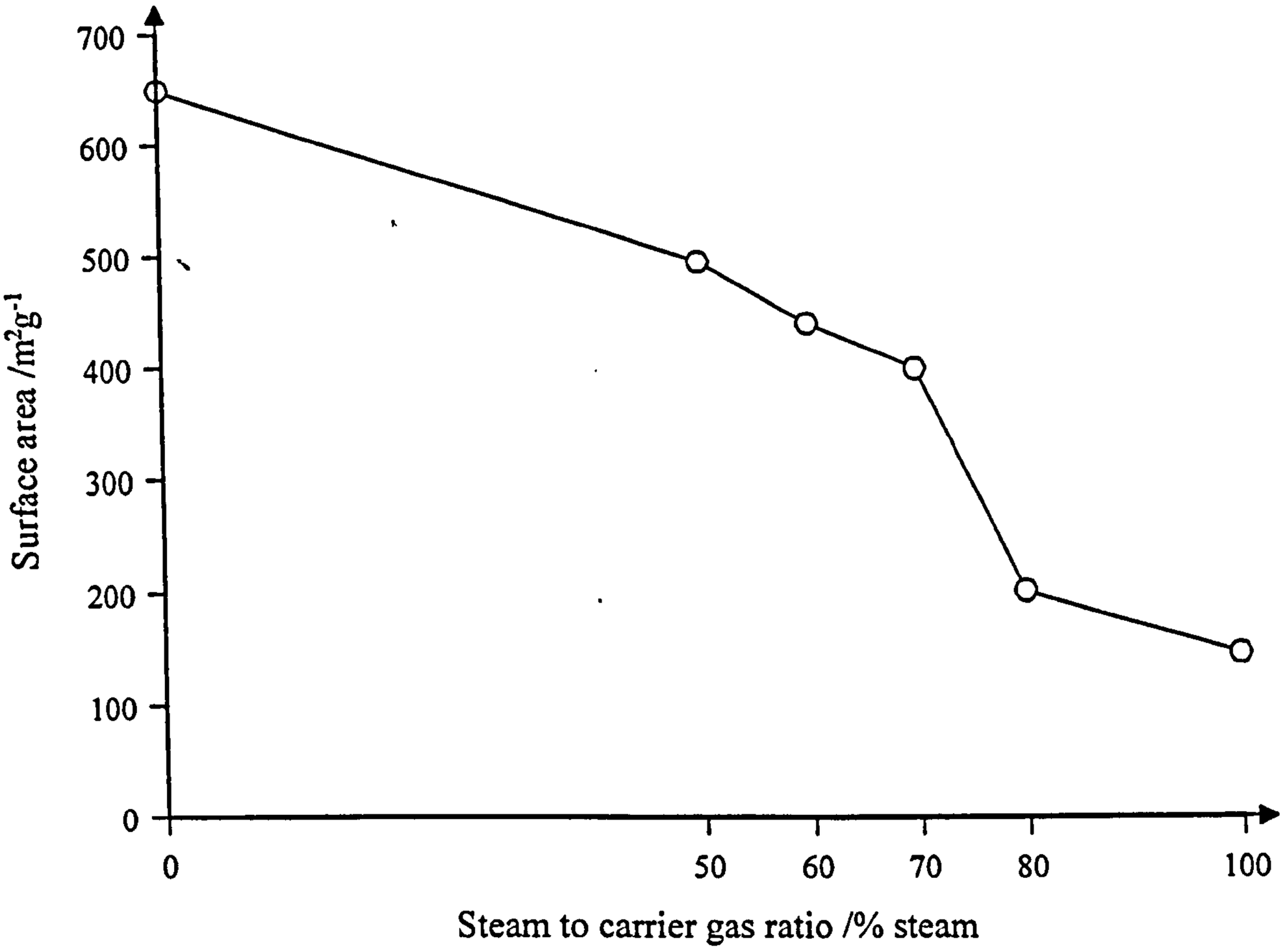

Figure 4.7 Variation in surface area as the steam to carrier gas ratio is increased for a sample of 2.6LaH-Y treated at 800°C in the presence of 5000 ppm vanadium. Graph reproduced from Section 5.2.2, Figure 5.18(a).

Finally, it can be seen from Table 4.8 that the unit cell constant data for the two batches of sample, within the limits of experimental error, are identical and both show a trend of small increases as the vanadium loading is increased.

References

1 B.R. Mitchell, *Ind. Eng. Chem. Prod. Res. Dev.*, 1980, **19**, 209.

2 R.F. Wormsbecher, A.W. Peters and J.M. Maselli, *J. Catal.*, 1986, **100**, 130.

3 Kindly denoted by Dr. F. Berry, Open University.

4 F. Maugé, P. Gallezot, J-C. Courcelle, P. Engelhard and J. Grosmangin, *Zeolites*, 1986, **6**, 261.

5 H. Bremer, W. Mörke, R. Schödel and F. Vogt, *Moleculer Sieves*, Advan. Chem. Ser. 121, W.H. Meier and J.B. Uytterhoeven, Ed., 1973, ACS. Washington, D.C., 249.

6 S. Jaras, *App. Catal.*, 1982, **2**, 207.

7 Y. Nishimura, T. Masuda, G. Sato and S. Egashira, *S. Prepr. Div. Pet. Chem. Soc.*, 1982, **28**, 707.

8 T. Masuda, M. Ogata, T. Ida, K. Takakura and Y. Nishimura, *J. Japan. Pet. Inst.*, 1983, **26**, 344.

9 J.A. Maselli and A.W. Peters, *Catal. Rev. Sci. Eng.*, 1984, **26**, 525.

10 E.L. Kugler and D.P. Leta, *J. Catal.*, 1988, **109**, 387.

11 F. Maugé, J.C. Courrcelle, Ph. Engelhard, P. Gallezot and J. Grosmangin, *Proceedings 7th International Zeolite Conference*, Y. Murakami, A. Iijima and J.W. Ward, Ed., 1986, **28**, 803.

12 M.L. Occeli, *Catal. Rev.-Sci. Eng.* 1991, **33**, 241.

13 L. Upson, S. Järås and I. Dalin, *Oil Gas J.*, 1982, 135.

14 R. Pompe, S. Järås and N-G. Vannerberg, *Appl. Catal.*, 1984, **13**, 171.

15 J.E. Otterstedt, S.B. Gevert, S.G. Järås and P.G. Menon, *Appl. Catal.* 1986, **22**, 159.

16 R. Pankajavalli and O.M. Sreedharan, *Materials Lett.*, 1995, **24**, 247.

17 Y. Kimishima, M. Takahashi, K. Okada, H. Ishikawa and Y. Ichiyanagi, *J. Magnetism and Magnetic Materials*, 1995, **140-144**, 1185.

18 J. Kikuchi, H. Yasuoka, Y. Kokubo and Y. Ueda, *J. Physical Soc. Japan*, 1994, **63**, 3577.

19 G. Ranga Rao and D.D. Sarma, *Mod. Phys. Lett. B*, 1990, **4**, 277.

20 B.C. Tofeild and W.R. Scott, *J. Solid State chem.*, 1974, **10**, 183.

Chapter 5

Results and Discussion

5 Results and Discussion

This section describes the results of X-ray diffraction (XRD), surface area measurement and magic-angle-spinning nuclear magnetic resonance (MAS NMR) investigations into the various classes of sample studied in this work. At this stage the discussion of the results will be mainly confined to a given class of sample although, where appropriate, specific points will be emphasised that are common to all classes of sample. A more general discussion, framed in the context of the overall aims of the work and based upon all of the results, will form the main focus of the next chapter (Chapter 6).

The arrangement of this chapter is as follows. Sections 5.1 and 5.2 describe the results of general investigations of the behaviour of FCC and model zeolite-Y based samples, respectively, under a range of pretreatment and reaction conditions. These studies are extended for both types of sample in Section 5.3. Section 5.4 considers the behaviour of lanthanum-and/or vanadium-doped silica and α -alumina support materials. To compliment these studies results are also reported for the matrix/clay component of a typical FCC as well as for a 'completely degraded' FCC sample. The final section reports on a series of experiments which were designed to investigate rare earth/vanadium chemistry under conditions similar to those used for the treatment of FCC and model zeolite-Y samples.

It is useful to note that for the remainder of this thesis experimental conditions will be given in the following shorthand format. A steam treatment reaction that was performed at 800°C for 5 hours using air as a carrier gas will be denoted 800/5/80/AIR, where 800 specifies reaction temperature in degrees Celsius, 5 specifies the duration of the experiment in hours, 80 denotes that an 80% steam to air ratio was used over the duration of the experiment and AIR signifies that the experiment was performed using air as a carrier gas. Similarly, 750/5/0/N_2, indicates that the reaction was calcined at 750°C for 5 hours under a nitrogen atmosphere. In this work the standard duration of an experiment is 5 hours and standard steam treatment relates to an 80% steam to air ratio.

5.1 Commercial Fluid Cracking Catalysts

As was discussed in Section 4.2, a series of FCC samples were prepared and subjected to various reaction conditions using laboratory facilities at B.P. Oil International Laboratories (Sunbury). Three different FCC samples were investigated which contained differing levels of ion-exchanged rare earth (RE). The samples were artificially contaminated with vanadium and steam treated at 788°C and 816°C using air as a carrier gas. This series of experiments allowed three important parameters to be investigated, the effect of increasing RE ion-exchange, the effect of increasing vanadium contamination, and the effect of increasing temperature.

5.1.1 Fluid Cracking Catalyst without Steam Treatment

Figure 5.1 shows the XRD patterns recorded for the three untreated FCC samples, (alpha-52, alpha-54 and alpha-56). The pattern recorded for the matrix/clay component of the FCC samples is also shown in the figure for comparison. For the FCC samples (Figure 5.1 (b), (c), and (d)) the zeolite-Y diffraction peaks can clearly be seen superimposed on the XRD pattern of the matrix/clay component.

The computed unit cell constants for the three FCC samples are given in Table 5.1. The table also includes the RE ion-exchange levels and the results of surface area measurements.

Sample	RE_2O_3 /mass%	Unit cell constant /Å (± 0.04 Å)	Surface area /m^2g^{-1} (±10%)
Alpha-52	0.61	24.55	201
Alpha-54	1.12	24.58	200
Alpha-56	2.73	24.64	203

Table 5.1 Computed unit cell constants, RE ion-exchange levels and surface area data for untreated FCC samples.

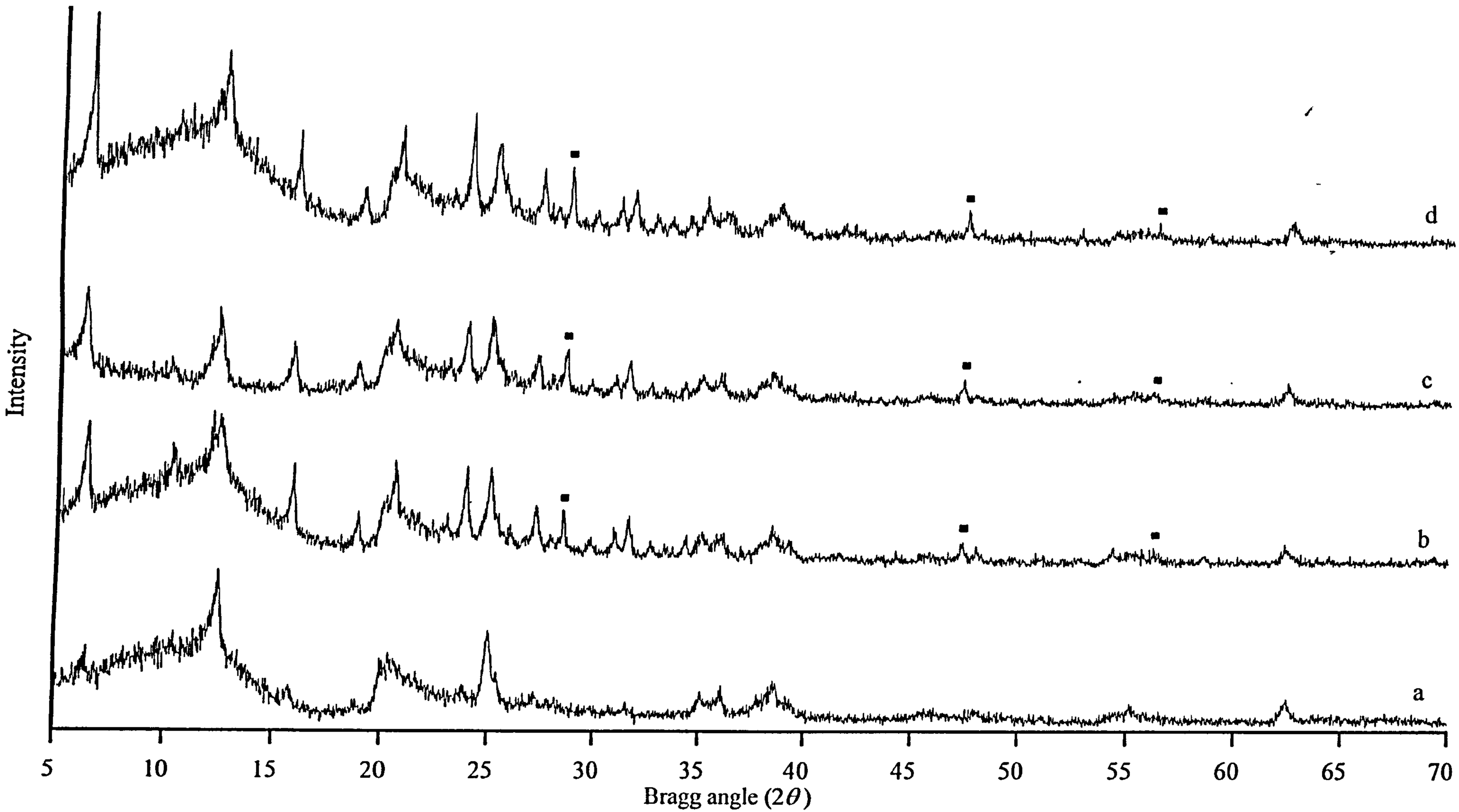

Figure 5.1 XRD patterns recorded for (a) untreated matrix/clay component of FCC, (b) untreated alpha-52, (c) untreated alpha-54, and (d) untreated alpha-56. ■ labels the diffraction peaks for the silicon standard.

The increase in unit cell constant as the RE ion-exchange level is increased is to be expected as the lattice has to expand to incorporate the RE ions. This effect has been reported by other workers, for example Roelofsen and co-workers[1] observed an increase in unit cell constant from 24.69±0.02 Å to 24.74±0.02 Å upon ion-exchange with a mixture of RE ions. The surface area measurements (determined by B.P. Oil International, Sunbury) for the three FCC samples are similar and reflect the fact that all three samples have comparable zeolite-Y crystallinity. This observation is consistent with the form of the XRD patterns recorded for the samples (Figure 5.1).

The XRD patterns for the three FCC samples contaminated with 0, 2000, and 4000 ppm vanadium were found to be similar to those recorded for the uncontaminated samples. In view of the relatively low vanadium levels this result was not surprising (the detection limits for powder XRD are of the order of 4 mass%).

5.1.2 Steam Treatment of Fluid Cracking Catalysts

FCC samples were separately steam treated at 788°C and 816°C using air as a carrier gas. The surface area measurements and the unit cell constants, determined from the XRD patterns, following the steam treatment experiments are given in Table 5.2. The surface area and unit cell constant data for the untreated FCC samples are also included in the table for comparison. In some cases unit cell constant data could not be determined because there was insufficient crystalline material remaining, after steam treatment, for accurate determination.

The steam treatment results are also shown graphically in Figures 5.2 and 5.3. Figure 5.2 shows the experimental data plotted as a function of RE ion-exchange level, in terms of both surface area ((a), (c) and (e)) and unit cell constant ((b), (d) and (f)). Figure 5.3 shows the experimental data plotted as a function of vanadium contamination, in terms of surface area ((a), (c) and (e)) and unit cell constant ((b), (d) and (f)). ^{51}V MAS NMR spectra could not be recorded for any of the samples because the vanadium concentrations were below the detection limits of the NMR experiment. ^{27}Al MAS NMR spectra were not recorded due to the complex nature of the composite catalyst. The matrix/clay component, which

makes up approximately 80 mass% of the composite catalyst, contains aluminium and resonances from this component mask those due to the zeolite-Y component of the catalyst.

Sample	Reaction conditions	Vanadium loading /ppm	Unit cell constant /Å (± 0.04 Å)	Surface area /m^2g^{-1} (±10%)
Alpha-52	Untreated	Untreated	24.55	201
	788/5/80/AIR	0	24.28	151
		. 2000	24.26	126
		4000	-	79
	816/5/80/AIR	0	24.25	125
		2000	24.24	92
		4000	-	35
Alpha-54	Untreated	Untreated	24.58	200
	788/5/80/AIR	0	24.32	163
		2000	24.27	118
		4000	24.28	77
	816/5/80/AIR	0	24.28	134
		2000	24.28	68
		4000	-	38
Alpha-56	Untreated	Untreated	24.64	203
	788/5/80/AIR	0	24.37	170
		2000	24.34	134
		4000	24.32	89
	816/5/80/AIR	0	24.31	143
		2000	24.30	87
		4000	-	41

Table 5.2 Unit cell constants and surface area measurements for three commercial FCC samples following steam treatment. Vacancies appear in the unit cell constant columns due to insufficient crystalline material remaining, after steam treatment, for accurate determination.

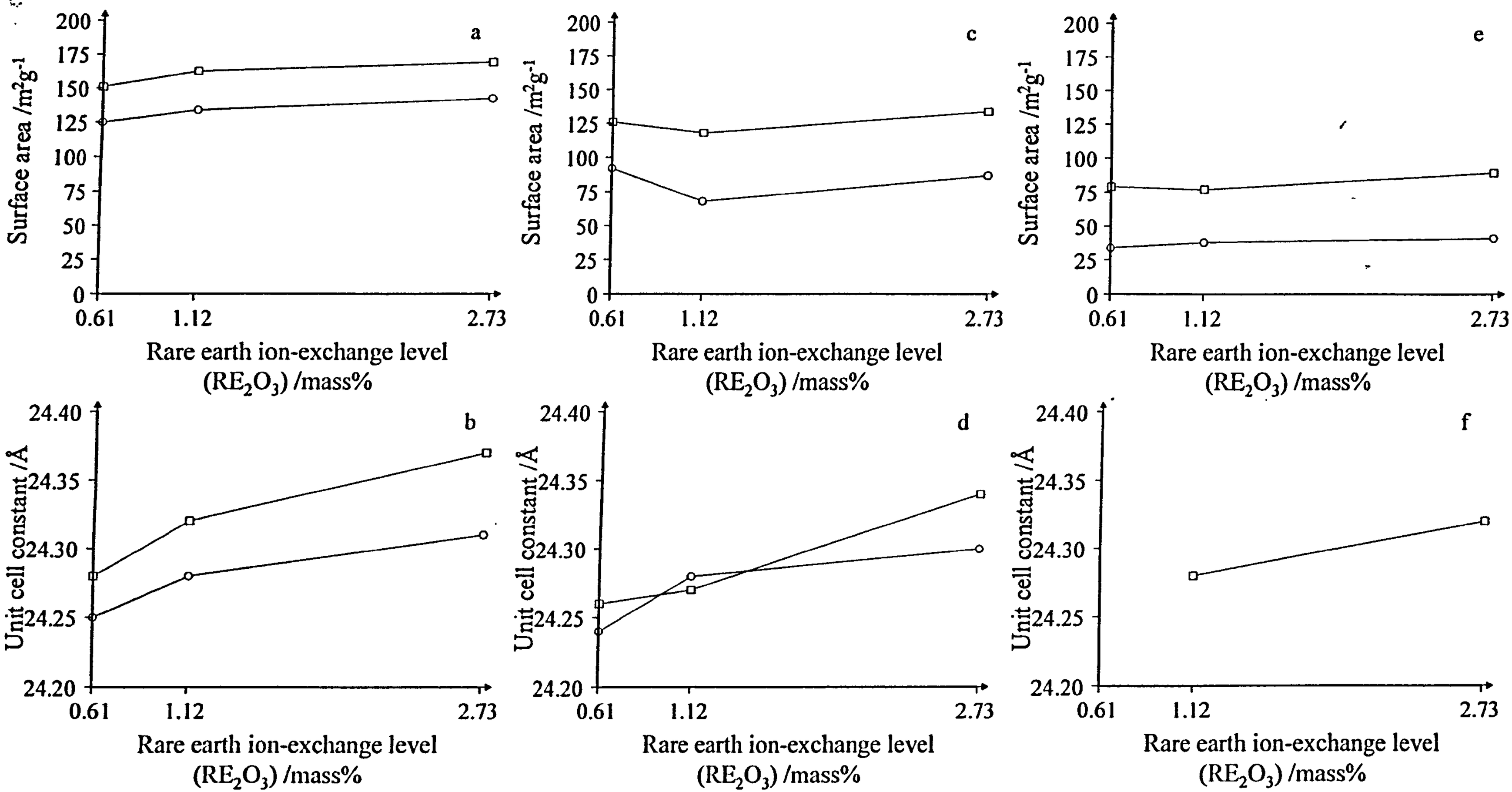

Figure 5.2 Steam treatment data presented in Table 5.2. □ represents steam treatment at 788°C, and ○ represents steam treatment at 816°C. (a) and (b) represent data for FCC samples free from vanadium contamination, (c) and (d) represent data for FCC samples contaminated with 2000 ppm vanadium, and (e) and (f) represent data for FCC samples contaminated with 4000 ppm vanadium. The lines in the figures have no significance other than as a guide to the general trends.

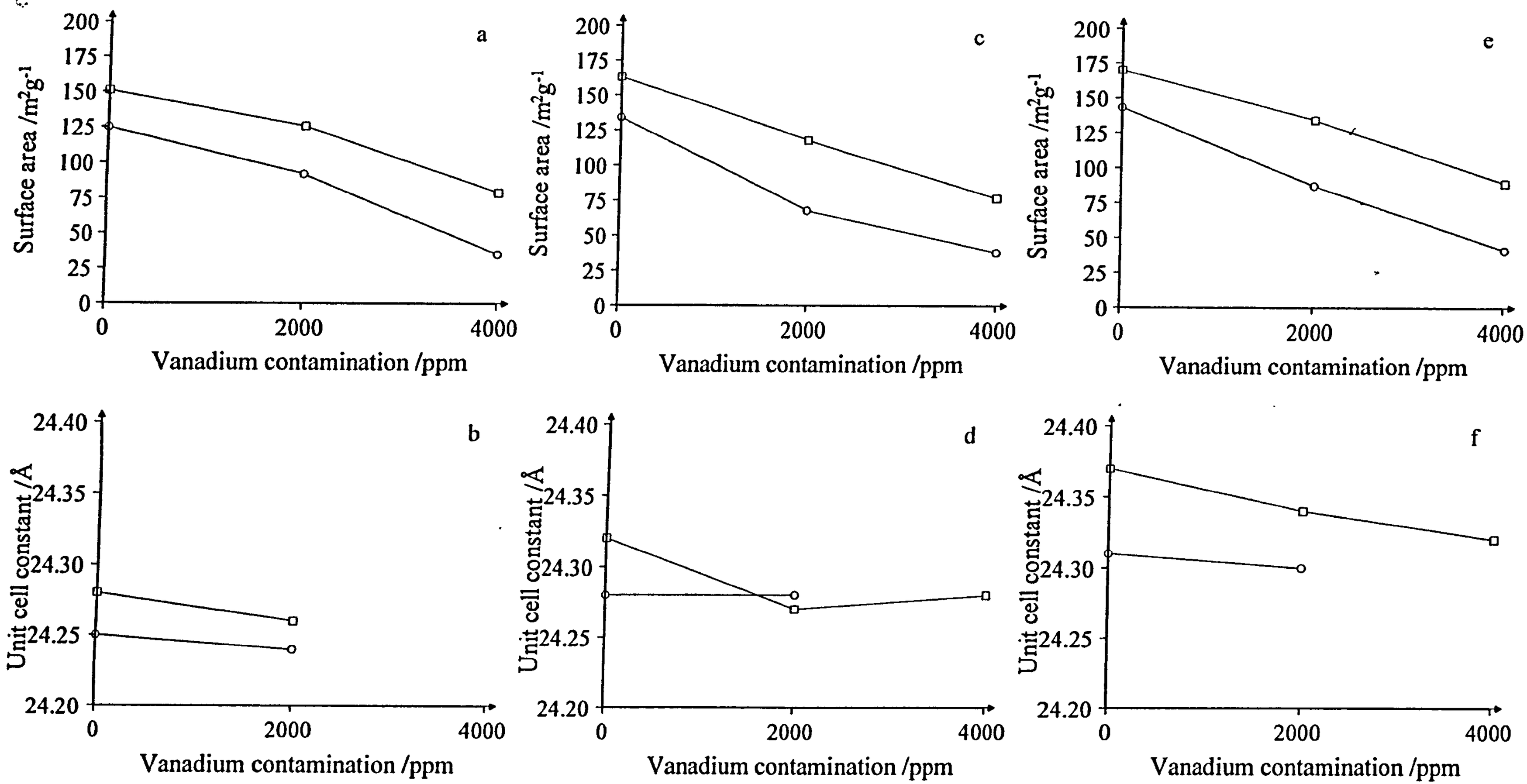

Figure 5.3 Steam treatment data presented in Table 5.2. □ represents steam treatment at 788°C, and O represents steam treatment at 816°C. (a) and (b) represent data for alpha-52, (c) and (d) represent data for alpha-54, and (e) and (f) represent data for alpha-56. The lines in the figures have no significance other than as a guide to the general trends.

It can be seen from the information presented in Table 5.2 that steam treatment of the FCC samples results in a decrease in surface area and unit cell constant. The degree of the changes observed, as illustrated in the figures, depend upon vanadium concentration, together with temperature and the RE ion-exchange levels. Overall the results illustrate the significant effect that steam treatment has on the FCC samples, even in the absence of vanadium contaminants. This general behaviour is consistent with that reported by other workers.[2,3] For example, Maugé and co-workers[2] found that steam treatment of a highly lanthanum ion-exchanged sample (17.4 mass% lanthanum) resulted in a change in unit cell constant from 24.73Å to 24.59Å, and this was accompanied with a 78% reduction in zeolite-Y crystallinity. A fuller understanding of the effect of steam treatment in the absence of vanadium contaminants is necessary if the combined effect of vanadium contamination and steam treatment is to be fully investigated.

Effect of increasing rare earth ion-exchange levels

Figure 5.4 shows the XRD patterns recorded for the three FCC samples ((a) alpha-52, (b) alpha-54, and (c) alpha-56) free from vanadium contamination and steam treated at 816°C for 5 hours using air as a carrier gas. It can be seen that as the RE ion-exchange level increases then the loss of zeolite-Y crystallinity decreases. This can be illustrated, for example, by considering the diffraction peak at $2\theta = 24°$ which has the index (533). The relative intensity of this peak tends to show small increases with increasing RE concentration. In qualitative terms this indicates that there is increasing retention of zeolite-Y crystallinity. This indicates that the amount of RE present determines the resistance of zeolite-Y to loss of crystallinity via hydrothermal treatment. This conclusion is also borne out by the surface area measurements (Figure 5.2(a)) for which small increases in surface area are observed, at both 788°C and 816°C, as the RE concentration increases.

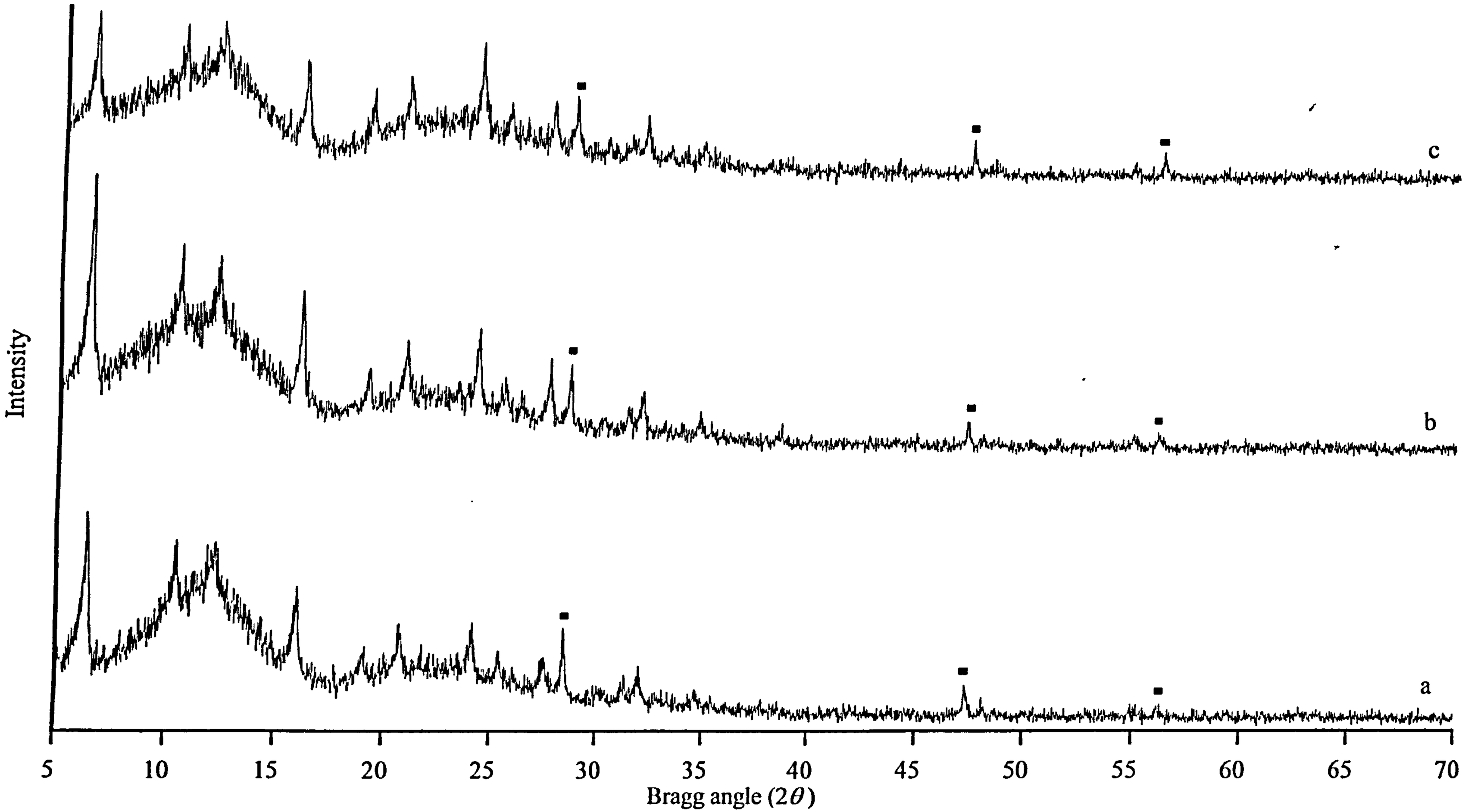

Figure 5.4 XRD patterns recorded for FCC samples free from vanadium contamination, and steam treated at 816°C for 5 hours using air as a carrier gas. (a) alpha-52, (b) alpha-54, and (c) alpha-56. ■ labels the diffraction peaks for the silicon standard.

Steam treatment in the presence of vanadium reveals the same general trends (Figure 5.2 (c) and (e)). However, there are exceptions observed when alpha-54 is steam treated since decreases in surface area are observed over equivalent steam-treated alpha-52 samples. The general trend is re-established when the results for alpha-56 are considered, with the observed surface areas being greater than those for alpha-54 and alpha-52. Clearly the relationship between RE ion-exchange level, vanadium contamination and temperature can be variable in FCCs and this probably depends on the details of the batch and preparation of these industrial materials. Blockage of pore structure could influence the effect of vanadium and also effect surface area measurement.

With regard to unit cell constant changes, as the RE ion-exchange levels are increased, the picture is more uniform. It can be seen from Figure 5.2 ((b), (d) and (f)) that, in all cases, as the RE ion-exchange levels are increased then the observed unit cell constant tends to increase. However, the observed increases do vary across vanadium loadings and temperatures. It must be noted that the observed changes are relatively small and in most cases within the limits of experimental reproducibility for this type of sample.

Effect of increasing vanadium contamination

The three XRD patterns for alpha-56 steam treated at 816°C for 5 hours, using air as a carrier gas, with increasing vanadium loadings are given in Figure 5.5: that is, alpha-56 free from vanadium contamination (a), contaminated with 2000 ppm vanadium (b) and contaminated with 4000 ppm vanadium (c). It can be seen that as the vanadium loading is increased there is a general reduction in the intensity of the diffraction peaks due to the zeolite-Y component. This indicates that as the vanadium loading is increased then there is a concomitant loss of zeolite-Y crystallinity.

The increased destruction to the zeolite-Y lattice as the vanadium loading is increased is also reflected in the surface area data obtained. It can be seen from Figure 5.3 ((a), (c) and (e)) that as the vanadium contamination is increased then the measured surface area decreases.

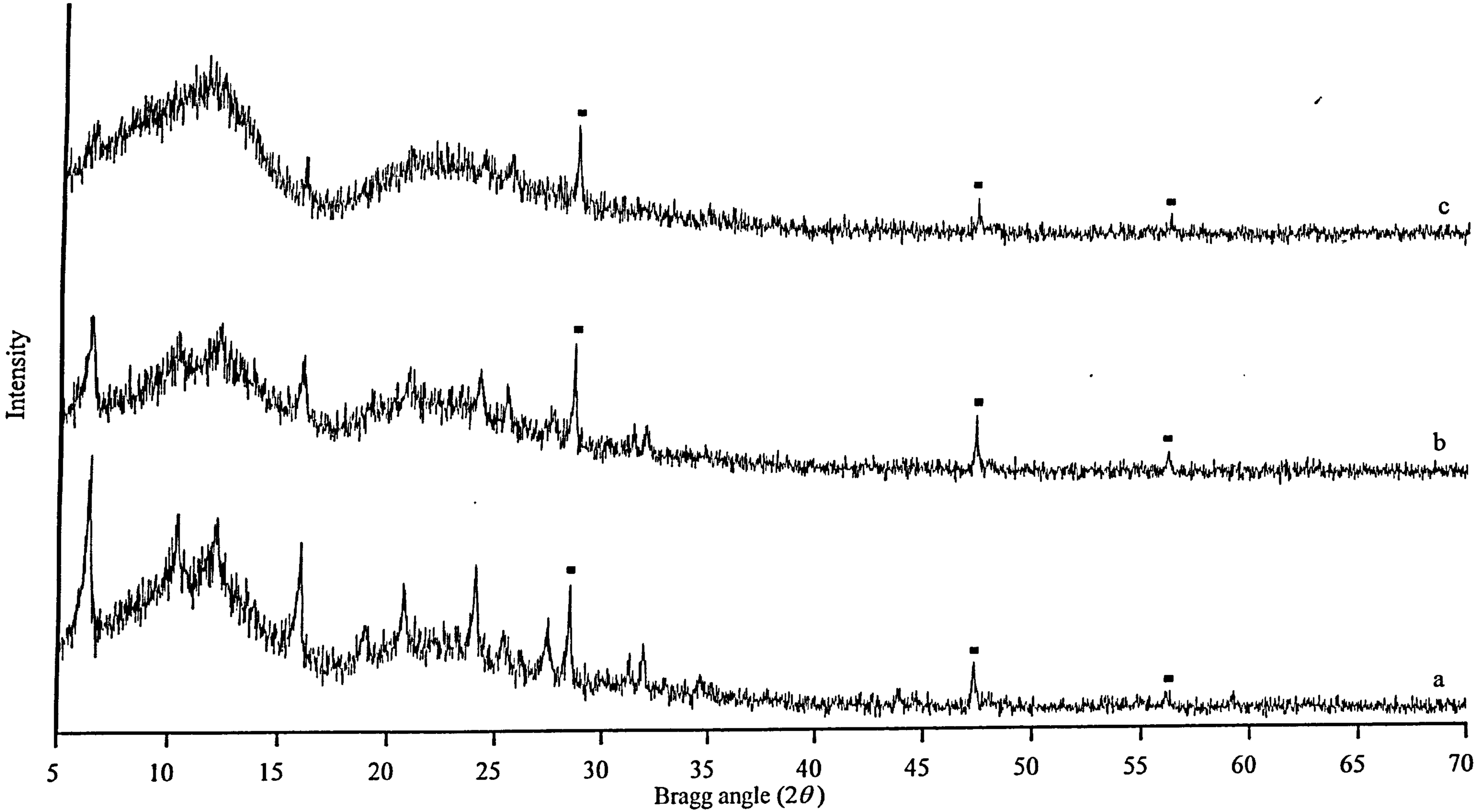

Figure 5.5 XRD patterns recorded for alpha-56 steam treated at 816°C for 5 hours, using air as a carrier gas, contaminated with (a) 0 ppm vanadium, (b) 2000 ppm vanadium, and (c) 4000 ppm vanadium. ■ labels the diffraction peaks for the silicon standard.

There is also a general trend that as the vanadium loading is increased, then the observed unit cell constant falls (Figure 5.3 ((b), (d) and (f)). This is true in all cases except for alpha-54 steam treated at 788°C. However, the observed reductions are small and within the limits of experimental error.

Effect of increasing temperature

Figure 5.6 shows the XRD patterns for two samples of alpha-56, contaminated with 4000 ppm vanadium, steam treated for 5 hours, using air as a carrier gas, at both 788°C (a) and 816°C (b). It can be seen that as the temperature is increased there is a general reduction in the intensity of the diffraction peaks due to the zeolite-Y component. This is a clear indication that as the treatment temperature is increased then the loss of zeolite-Y crystallinity also increases.

This observation is also mirrored in the surface area results. It can be seen from Figures 5.2 and 5.3 ((a), (c) and (e)) that as the reaction temperature is increased from 788°C to 816°C, in all cases, there is an additional decrease in the surface area. This is true regardless of the RE ion-exchange level (Figure 5.2 (a), (c) and (e)) and vanadium contamination (Figure 5.3 (a), (c) and (e)).

It is also noticeable from Figures 5.2 and 5.3 ((b), (d) and (f)) that, as the temperature is increased from 788°C to 816°C, there is an additional decrease in the unit cell constant (this is true for all samples with the exception of alpha-54 contaminated with 2000 ppm vanadium (Figure 5.2 and 5.3 (d))). The observed changes, however, are relatively small.

5.1.3 Summary

The results for the three commercial FCCs indicate that increasing the vanadium contamination results in increased loss of zeolite-Y crystallinity at temperatures of 788°C and 816°C. The loss of crystallinity is also accompanied by a trend to smaller unit cell constants; although the changes between individual samples are within the limits of experimental reproducibility.

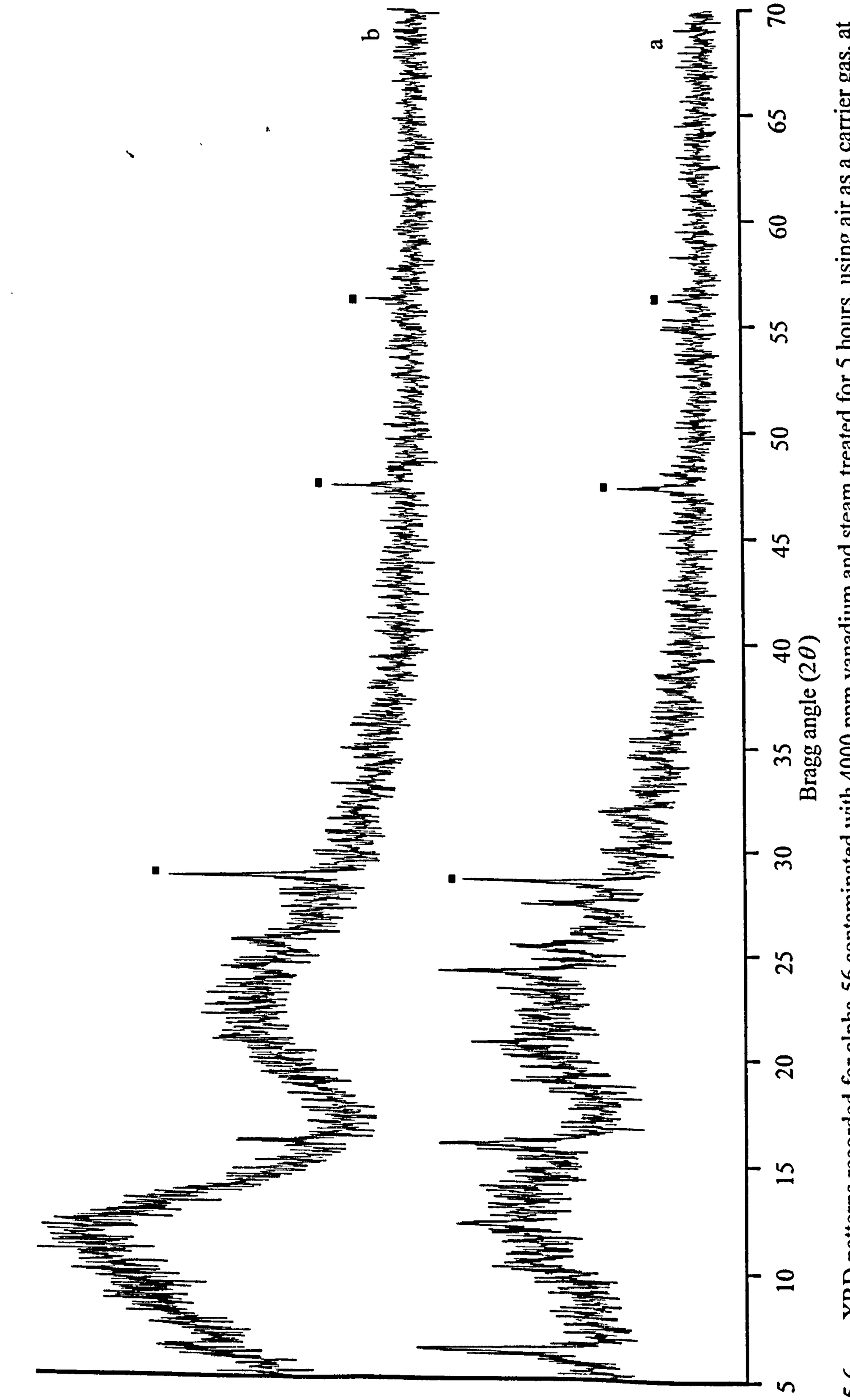

Figure 5.6 XRD patterns recorded for alpha-56 contaminated with 4000 ppm vanadium and steam treated for 5 hours, using air as a carrier gas, at (a) 788°C, and (b) 816°C. ■ labels the diffraction peaks for the silicon standard.

It has also been demonstrated that increasing the reaction temperature results in increased destruction to the zeolite-Y lattice. This is true regardless of the RE ion-exchange levels or the vanadium loading. A trend to a smaller unit cell constant was also observed as the reaction temperature was increased. In general, increasing the RE ion-exchange level increases the resistance of the zeolite-Y component of the catalyst to loss of crystallinity.

Overall the results obtained for the three commercial FCC catalysts are consistent with the types of behaviour that have been reported by other workers and, in particular, illustrate factors that are important in influencing the loss of zeolite-Y crystallinity. The commercial materials, however, are complex mixtures and to gain a better understanding of these factors it is appropriate to investigate the individual components in more detail.

5.2 Model Zeolite-Y Samples

The investigations carried out for the model series of samples based on zeolite-Y can be divided, for convenience, into two strands. To begin with, the effects of increasing lanthanum (RE) and vanadium concentrations, as well as temperature, are considered. The results are compared directly with those from the study of the commercial FCC series of samples, although the range of lanthanum ion-exchange level in the model series is greater. The second strand focusses on the variation of experimental conditions. In particular, experiments were performed under a nitrogen, rather than air, atmosphere and with steaming ratios other than the standard value of 80 %. The key aim of all these experiments was to gain insight into the factors that cause the loss of zeolite-Y crystallinity in the presence of vanadium.

MAS NMR spectroscopy offers particular advantages in characterising the model series of samples compared to commercial FCCs. For example, ^{27}Al MAS NMR spectra are not complicated due to the presence of additional signals due to non-zeolitic materials. ^{51}V MAS NMR is also sensitive enough to probe zeolite-Y/vanadium chemistry directly. It should be recalled (Section 4.2) that relatively low vanadium levels are required to simulate FCCU conditions. However, given that the zeolite-Y component of a typical FCC makes up only 20% by mass of the catalyst, and that all the vanadium present is associated

with the zeolite-Y, then it is realistic to investigate much higher vanadium loadings for the model series of samples. Furthermore with the model systems used in this work RE ion-exchange has been achieved using a specific RE ion (lanthanum). In contrast commercial FCCs use a mixture of REs for ion-exchange and so detection of ^{51}V MAS NMR signals would be complicated due to the possibility of several related vanadium compounds being formed with different RE ions. These different compounds will have different chemical shifts and probably different distributions of MAS sideband intensities.

5.2.1 The Effect of Lanthanum and Vanadium

Five zeolite-Y samples were investigated which had increasing levels of lanthanum ion-exchange (Section 4.2 and Table 4.2). These samples were subsequently contaminated with vanadium, calcined and steam treated (details of the apparatus and methods used for the treatment of samples can be found in Section 4.5).

5.2.1.1 Samples without Steam Treatment

Figure 5.7 shows the XRD patterns recorded for the five model samples. It can be seen that each of the five XRD patterns are similar, with only a small movement of peaks indicating changes in unit cell constant. The computed unit cell constants and surface area measurements are presented in Table 5.3. These values are similar to those found in the literature although direct comparison depends critically on the exact nature of the zeolite: for example, the extent of ion-exchange, the ion-exchange procedure employed and, most importantly, the silicon/aluminium ratio. As found with the commercial FCC samples (Section 5.1.1), increasing lanthanum (RE) ion-exchange results in a trend towards a larger unit cell constant. The diffraction patterns indicate that all five samples are highly crystalline and this is consistent with the high surface areas recorded in Table 5.3.

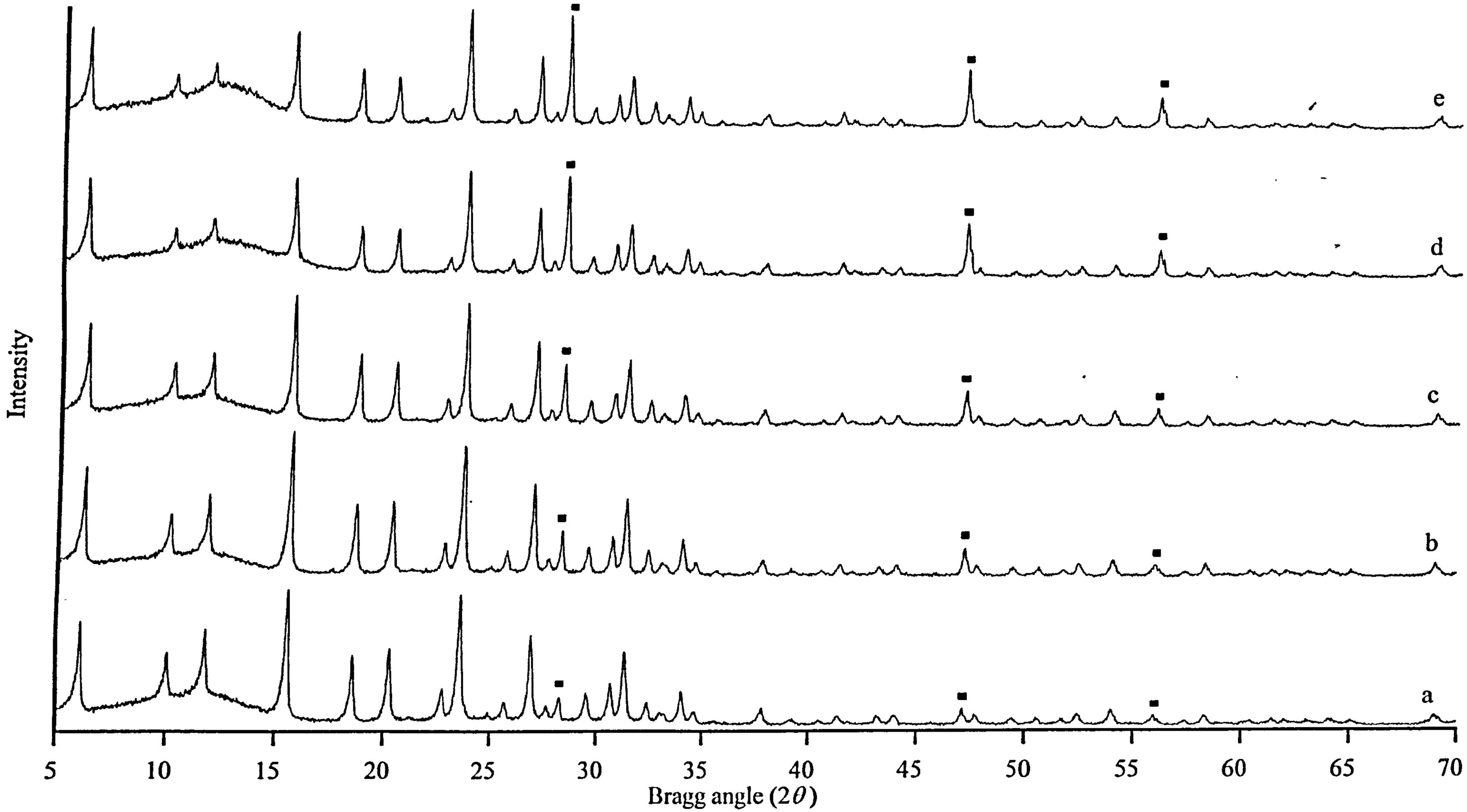

Figure 5.7 XRD patterns recorded for zeolite-Y samples with increasing lanthanum ion-exchange level, (a) H-Y, (b) 1.5LaH-Y, (c) 2.6LaH-Y, (d) 5.0LaH-Y and (e) 8.6LaH-Y. ■ labels the diffraction peaks for the silicon standard.

Sample	Unit cell constant /Å (±0.035Å)	Surface area /m^2g^{-1} (±10%)
H-Y	24.591	787
1.5LaH-Y	24.603	805
2.6LaH-Y	24.636	783
5.0LaH-Y	24.637	787
8.6LaH-Y	24.654	784

Table 5.3 Unit cell constant and surface area data obtained for zeolite-Y samples containing differing levels of lanthanum.

Figure 5.8 shows the ^{27}Al MAS NMR spectra recorded for (a) untreated NH_4-Y and (b) untreated 8.6LaH-Y. In qualitative terms the spectra are similar to one another.

The well-resolved resonance at $\delta(^{27}Al) = 60 \pm 4$ ppm in the spectrum for NH_4-Y can be assigned to tetrahedral framework aluminium. The two lower frequency resonances, that is the broad unresolved resonance in the region of $\delta(^{27}Al) = 30$ ppm and a low-intensity resonance at $\delta(^{27}Al) = 0$ ppm are due to non-framework aluminium.[4-15] The presence of non-framework aluminium is typical of an NH_4-Y zeolite that has undergone extensive ion-exchange to reduce the sodium level.[4] (The residual sodium level in the present sample is 0.024 mass%, expressed in terms of Na_2O). The detailed preparative history of the sample used in the present work was not available but it is likely that multiple ion-exchange with fresh NH_4^+ solutions will have been used at elevated temperatures (70-100°C). It is also known that an intermediate calcination step (200-600°C) is useful since it promotes rearrangement of ions within the zeolite-Y lattice and so makes more of the Na^+ ions accessible to exchange with NH_4^+.[16] Such a calcination step would also give rise to non-framework aluminium as, for example, demonstrated in the work of Klein and co-workers.[4]

There is general agreement in the literature that the resonance centred at $\delta(^{27}Al) = 0$ ppm is due to a octahedrally co-ordinated non-framework species. Klinowski and co-workers[15] suggested that the main species is present as $[Al(H_2O)_6]^{3+}$ in cationic positions and this

suggestion has been accepted by other workers.[4-14] Two possible explanations have been put forward for the nature of the non-framework aluminium which gives rise to a broad resonance in the region of $\delta(^{27}Al) = 30$ ppm. Gilson and co-workers[8] proposed that this aluminium species was due to the presence of penta co-ordinate aluminium on the basis of a comparison with similarly co-ordinated aluminium in the mineral andalusite. By contrast Samoson and co-workers[10] suggested that this resonance was due to a highly distorted tetrahedral species. This is an area which remains to be resolved.

The ^{27}Al MAS NMR spectrum of untreated 8.6LaH-Y (Figure 5.8(b)), as already indicated, shows similar features to that of the parent untreated NH_4-Y sample. The general form of the spectrum is also similar to that reported by Klein and co-workers[4] for a partially exchanged lanthanum/sodium zeolite-Y (LaNa-Y) which was calcined at 350°C for 24 hours. A more detailed comparison of the ^{27}Al MAS NMR spectrum with that for untreated NH_4-Y shows that there is a relative increase in the amount of non-framework aluminium.

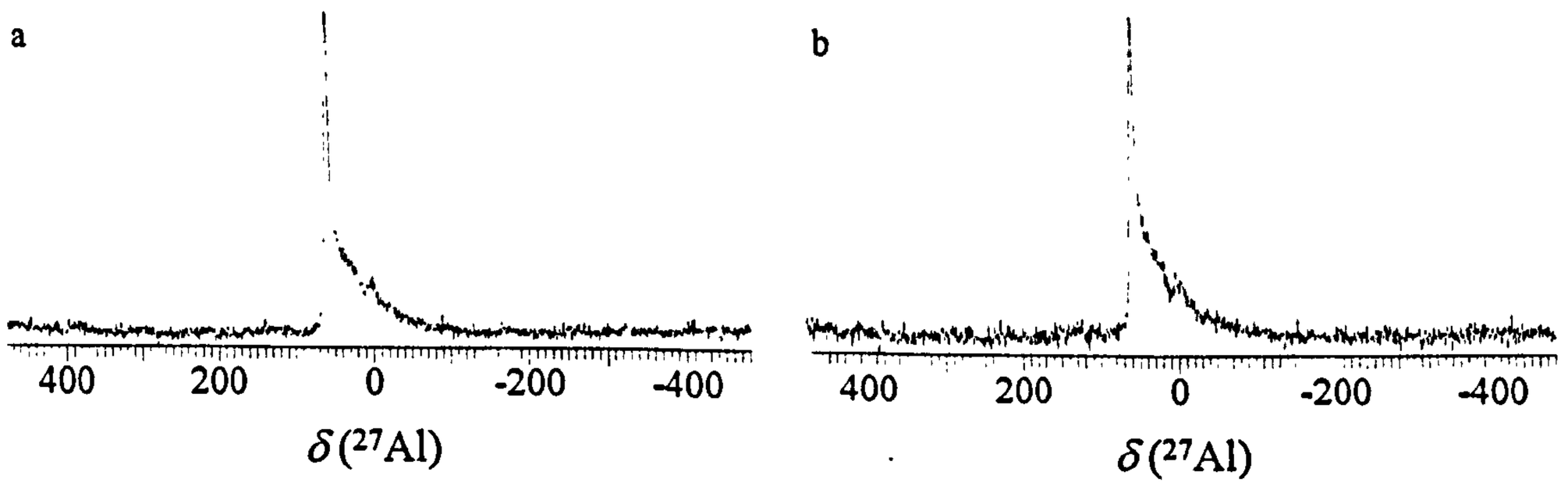

Figure 5.8 ^{27}Al MAS NMR spectra observed at 104.169 MHz for (a) an untreated sample of NH_4-Y, number of scans = 10 000 and $\delta(^{27}Al) = 60\pm4$ ppm, and (b) untreated 8.6LaH-Y, number of scans = 15 000 and $\delta(^{27}Al) = 60\pm5$ ppm. For both spectra the external reference was a 0.1 mol dm^{-3} aqueous solution of $[Al(H_2O)_6]^{3+}$, pulse delay = 1 s, pulse width = 2 μs, and spinning frequency ~ 8 kHz.

No ^{27}Al MAS NMR spectra were recorded for the other lanthanum-loaded samples. This was due to limited access to the NMR spectrometer. However, it is reasonable to assume

that ion-exchange with lower levels of lanthanum would have a similar effect on the zeolite-Y lattice, that is small increases in non-framework aluminium at the expense of framework aluminium. This assumption is supported by the XRD data (Figure 5.7, Table 5.3) which shows that all samples have comparable crystallinity. Relatively large reductions in unit cell constant would be expected[12] if extensive extraction of aluminium from the zeolite-Y lattice had occurred.

XRD patterns recorded for samples contaminated with vanadium did not show any deviation, in terms of crystallinity, from the patterns recorded for the untreated lanthanum ion-exchanged samples (Figure 5.7). Table 5.4 gives the computed unit cell constants for these samples; within experimental error no distinct trends are observed except in the case of the H-Y and 1.5LaH-Y samples which are discussed in more detail shortly. Surface area measurements were not carried out on these samples since, being unsteamed, there was the possibility of introducing vanadium contamination into the surface area apparatus.

Sample	Vanadium loading /ppm	Unit cell constant /Å (±0.035Å)
H-Y	0	24.591
	5000	24.531
1.5LaH-Y	0	24.603
	1000	24.556
	3000	24.573
	5000	24.588
2.6LaH-Y	0	24.636
	1000	24.627
	3000	24.605
	5000	24.663
5.0LaH-Y	0	24.637
	5000	24.661
	10 000	24.653
8.6LaH-Y	0	24.654
	5000	24.669
	10 000	24.683
	15 000	24.710

Table 5.4 Computed unit cell constants for vanadium-contaminated zeolite-Y with differing levels of lanthanum ion-exchange.

The ^{27}Al MAS NMR spectra recorded for the 8.6LaH-Y sample contaminated with (a) 0 ppm vanadium, (b) 5000 ppm vanadium, (c)10 000 ppm vanadium, and (d) 15 000 ppm vanadium are given in Figure 5.9.

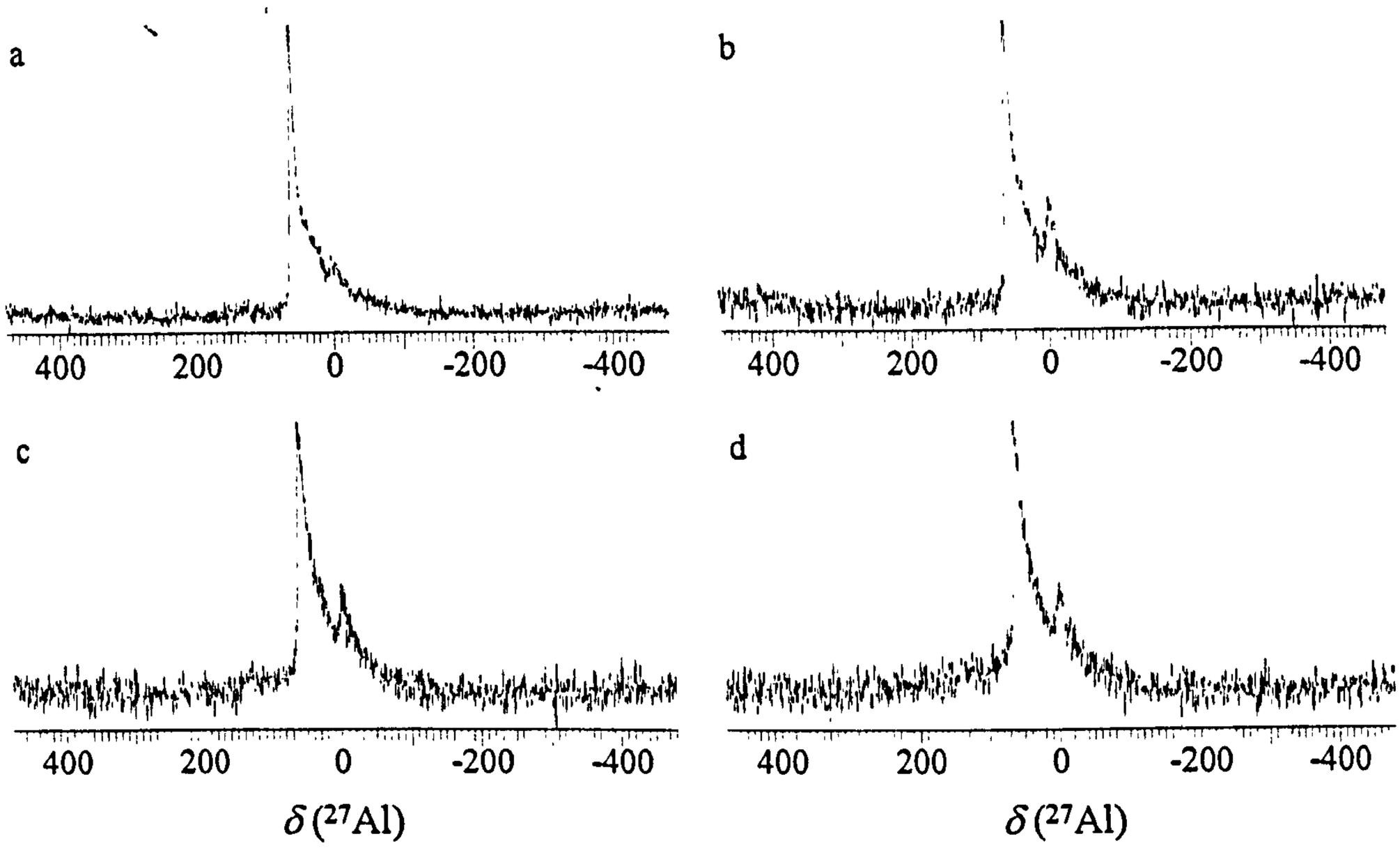

Figure 5.9 ^{27}Al MAS NMR spectra observed at 104.169 MHz for 8.6LaH-Y contaminated with (a) 0 ppm vanadium, number of scans = 15 000, and $\delta(^{27}Al) = 60\pm5$ ppm, (b) 5000 ppm vanadium, number of scans = 15 000 and $\delta(^{27}Al) = 58\pm8$ ppm, (c) 10 000 ppm vanadium, number of scans = 14 000 and $\delta(^{27}Al) = 58\pm10$ ppm and (d) 15 000 ppm vanadium, number of scans = 6000 and $\delta(^{27}Al) = 57\pm10$ ppm. For all spectra the external reference was a 0.1 mol dm^{-3} aqueous solution of $[Al(H_2O)_6]^{3+}$, pulse delay = 1 s, pulse width = 2 μs, and spinning frequency ~ 8 kHz.

The spectra show that contamination with vanadium results in an increase in the resonance centred at $\delta(^{27}Al) = 0$ ppm. This resonance, as already indicated, can be attributed to non-framework octahedral aluminium sites.[4-15] One possibility, therefore, is that vanadium, even under the relatively mild preparation conditions (Section 4.2), promotes increased production of non-framework aluminium sites. It can also be noted that there is also an increase in the halfwidth of the framework aluminium resonance centred at $\delta(^{27}Al) \sim 60$ ppm which is consistent, as for example reported by Klinowski and co-workers,[12] with a change from framework to non-framework aluminium.

A decrease in framework aluminium sites would be expected to be accompanied by a decrease in the unit cell constant. Klinowski and co-workers[12] demonstrated in studies of the dealumination of zeolite-Y by both hydrothermal treatment and treatment with silicon tetrachloride (Section 2.1.1) that a decrease in unit cell constant occurred as a result of the removal of framework aluminium. The results presented in Table 5.4 for the H-Y and 1.5LaH-Y samples show a similar, but small, trend, however this is not the case as the lanthanum loading increases further. There is thus not definitive evidence that contamination with vanadium in the absence of steam treatment, can lead to dealumination. It could also be possible that vanadium interacts with non-framework aluminium species that are already present and in some way promotes the formation of octahedral aluminium species. This is an area for further work.

5.2.1.2 Samples with Steam Treatment

Steam treatment was carried out at 750°C and 800°C for five hours using air as a carrier gas. Table 5.5 gives the computed unit cell constants and surface area measurements obtained from this series of experiments. In general, and as observed for the commercial FCC samples, steam treatment results in a loss of zeolite-Y crystallinity. The extent of this loss depends upon the lanthanum ion-exchange level, the vanadium contamination and the temperature of treatment.

Effect of increasing lanthanum ion-exchange levels

Figure 5.10 shows the XRD patterns recorded for five zeolite-Y samples ion-exchanged with differing levels of lanthanum. The samples were contaminated with 5000 ppm vanadium and steam treated at 800°C for 5 hours using air as a carrier gas. The XRD patterns show that as the lanthanum ion-exchange level is increased, then the amount of crystalline material remaining in these samples also increases. This is consistent with the expectation that increasing the lanthanum ion-exchange level increases the resistance of the zeolite-Y lattice to destruction.

Sample	Reaction conditions	Vanadium loading /ppm	Unit cell constant /Å (± 0.035 Å)	Surface area /m^2g^{-1} (± 10%)
H-Y	Untreated	Untreated	24.591	787
	750/5/80/AIR	0	-	27
		5000	-	81
	800/5/80/AIR	0	-	18
		5000	-	22
1.5LaH-Y	Untreated	Untreated	24.603	805
	750/5/80/AIR	0	24.215	436
		1000	24.226	405
		3000	24.242	370
		5000	24.264	357
	800/5/80/AIR	0	-	263
		1000	-	103
		3000	-	108
		5000	-	109
2.6LaH-Y	Untreated	Untreated	24.636	783
	750/5/80/AIR	0	24.291	504
		1000	24.307	540
		3000	24.267	510
		5000	24.274	473
	800/5/80/AIR	0	24.208	389
		1000	24.217	401
		3000	24.200	346
		5000	24.267	245
5.0LaH-Y	Untreated	Untreated	24.637	787
	750/5/80/AIR	0	24.378	610
		5000	24.369	520
		10 000	24.308	386
	800/5/80/AIR	0	24.269	523
		5000	24.249	330
		10 000	-	96
8.6LaH-Y	Untreated	Untreated	24.654	784
	750/5/80/AIR	0	24.431	646
		5000	24.375	535
		10 000	24.366	420
		15 000	24.287	207
	800/5/80/AIR	0	24.382	574
		5000	24.276	373
		10 000	-	112
		15 000	-	20

Table 5.5 Computed unit cell constants and surface area measurements for steam treated model zeolite-Y samples. Omissions appear in the unit cell constant data due to insufficient crystalline material remaining, after treatment, for accurate determination.

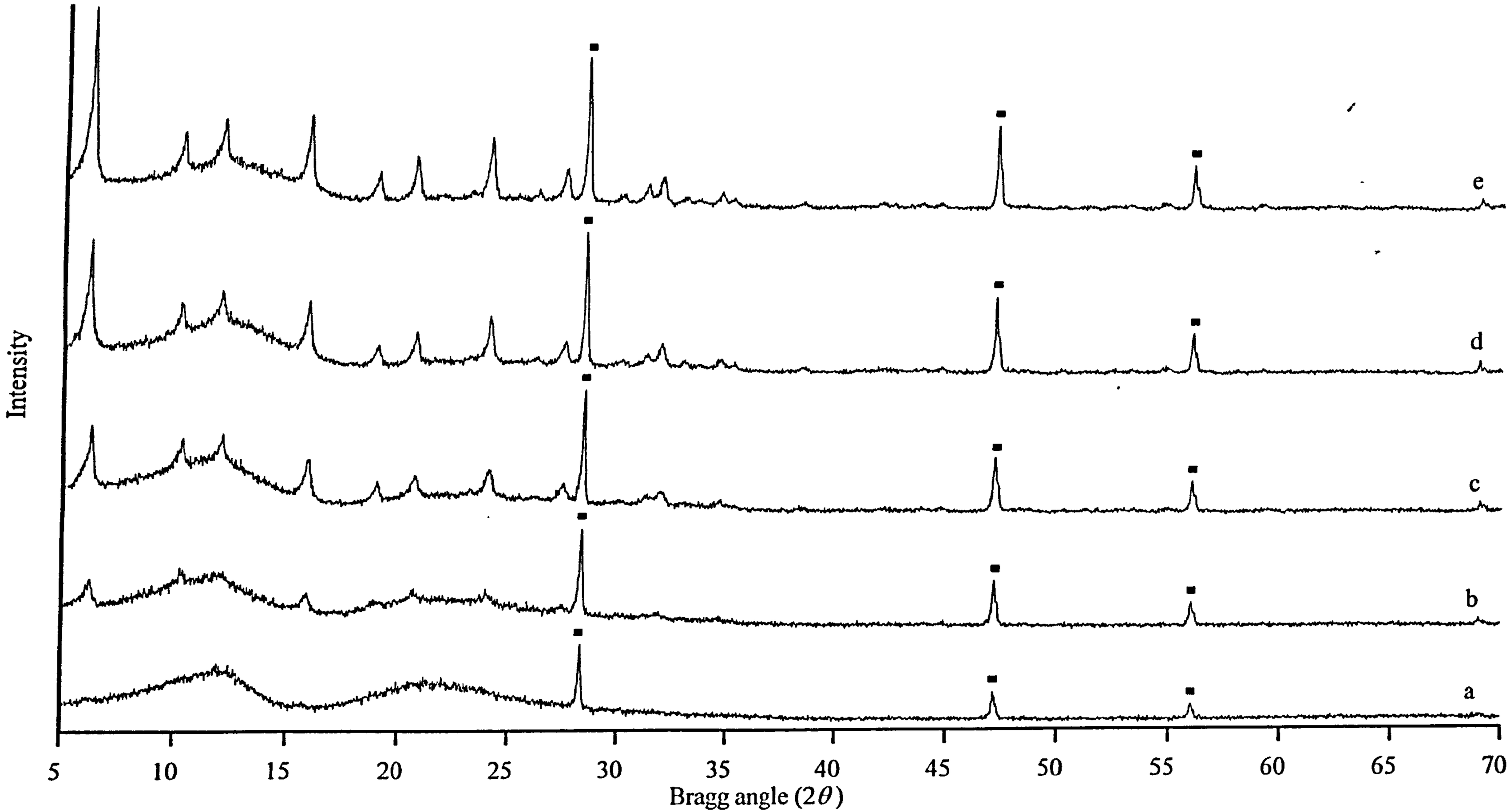

Figure 5.10 XRD patterns recorded for five zeolite-Y samples contaminated with 5000 ppm vanadium and steam treated at 800°C for 5 hours using air as a carrier gas, (a) H-Y, (b) 1.5LaH-Y, (c) 2.6LaH-Y, (d) 5.0LaH-Y and (e) 8.6LaH-Y. ■ labels the diffraction peaks for the silicon standard.

Figure 5.11 shows, in graphical form, the results of the steam treatment of samples with differing lanthanum ion-exchange levels at vanadium loadings of zero ((a) and (b)) and 5000 ppm ((c) and (d)) vanadium, in terms of the behaviour of both surface area ((a) and (c)) and unit cell constant ((b) and (d)). From graphs (a) and (c) it can be seen that as the lanthanum ion-exchange level increases then so does the amount of crystalline material remaining within these samples (increasing surface area); this is consistent with the XRD results (Figure 5.10). From the shape of the curves it can be seen that, at both reaction temperatures and with vanadium present or not, there is a sharper increase in the zeolite-Y resistance to destruction as the lanthanum ion-exchange level is increased from 0 to *ca.* 3.0 mass% lanthanum, than there is as the lanthanum ion-exchange level is further increased. This suggests, for any given set of reaction conditions (steaming temperature, vanadium loading), that there is an optimum lanthanum ion-exchange level, above which there is relatively little further benefit to be gained in promoting stability of the zeolite-Y lattice.

The same general trend for the surface area to increase as the lanthanum ion-exchange level increases is also observed for the other vanadium loadings as can be confirmed in Table 5.5. For example, for samples that have been contaminated with 1000 ppm vanadium and steam treated at 750°C it can be seen that the surface area increases from 405 m^2g^{-1}, for the 1.5LaH-Y sample, to 540 m^2g^{-1} for the 2.6LaH-Y sample.

From the unit cell constant data presented in Figure 5.11 (b) it can be seen that as the lanthanum ion-exchange level increases then so does the observed unit cell constant. This general behaviour is less pronounced in the presence of 5000 ppm vanadium (Figure 5.11 (d)) and for steam treatment at 800°C there is, within experimental error, no increase in unit cell constant. For samples contaminated with 10 000 ppm vanadium and steam treated at 750°C it can be seen, from Table 5.5, that the unit cell constants: 24.308 ± 0.035 Å for the 5.0LaH-Y sample and 24.366 ± 0.035 Å for the 8.6LaH-Y sample are similar, within experimental error.

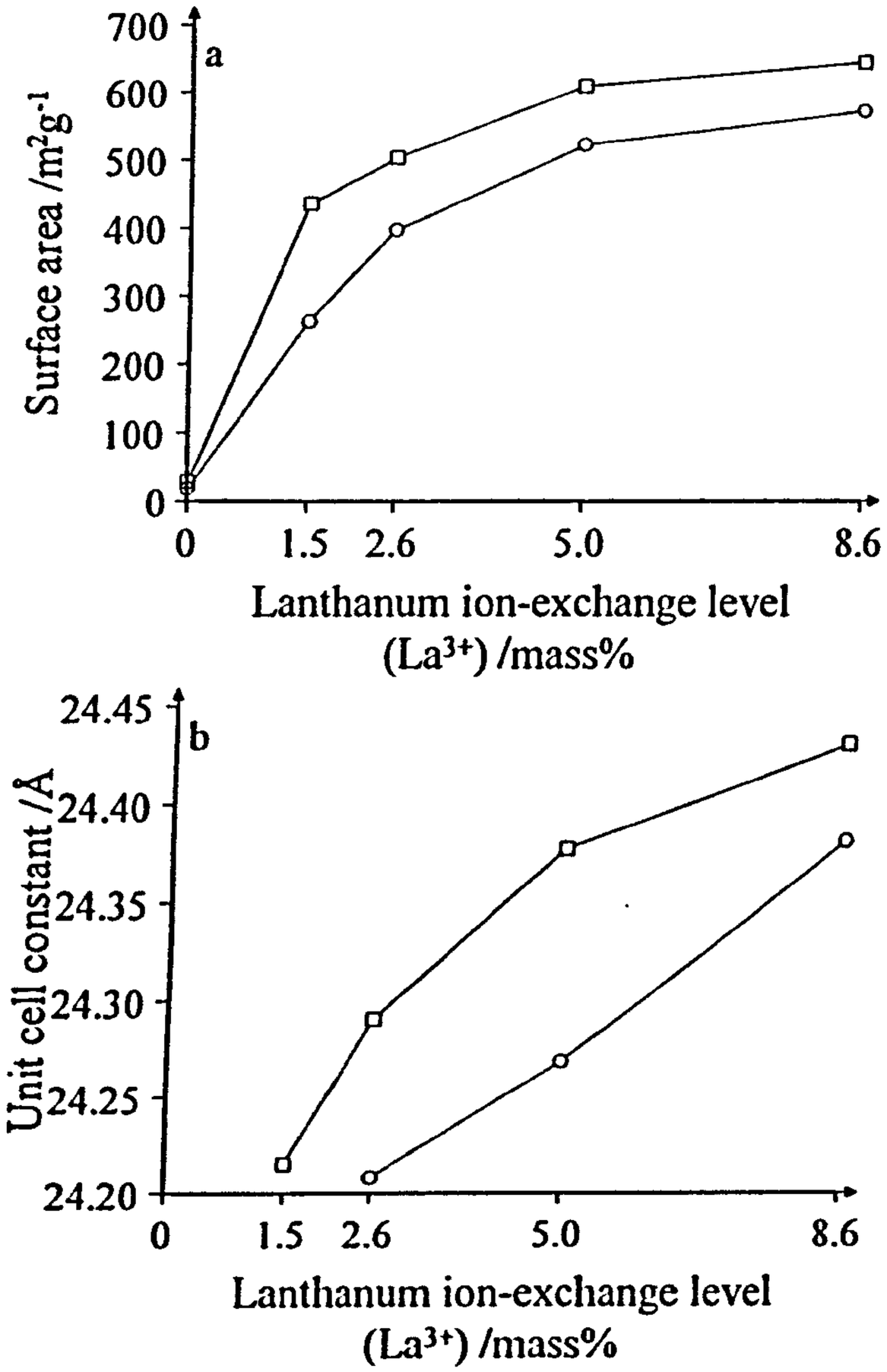

Figure 5.11 Steam treatment data presented in Table 5.5. □ represents steam treatment at 750°C, and O represents steam treatment at 800°C. Plots (a) and (b) represent results for zeolite-Y samples free from vanadium contamination, and (c) and (d) represent results for zeolite-Y samples contaminated with 5000 ppm vanadium. The lines in the figures have no significance other than as a guide to the general trends.

The ^{27}Al MAS NMR spectra recorded for zeolite-Y samples contaminated with 0 and 5000 ppm vanadium, and steam treated at 750°C for 5 hours using air as a carrier gas, are given in Figure 5.12. All of the spectra were subject to filtering through an exponential window prior to Fourier transformation, in order to improve the signal to noise ratio (Section 3.3.3). Spectra (a), (c), (e), (g) and (i) (first column) are for samples which are vanadium free, spectra (b), (d), (f), (h) and (j) (second column) are for samples contaminated with 5000 ppm vanadium. Spectra (a) and (b) are for H-Y samples, (c) and (d) for 1.5LaH-Y samples, (e) and (f) for 2.6LaH-Y samples, (g) and (h) for 5.0LaH-Y samples, and (i) and (j) for 8.6LaH-Y samples; that is, moving down a column of spectra shows the effect of increasing lanthanum ion-exchange level and moving across shows the effect of introducing 5000 ppm vanadium.

One immediate feature of all these spectra is the change in the relative intensities of the framework and non-framework aluminium. This is particularly evident with lanthanum ion-exchange levels below 2.6 mass% lanthanum where non-framework aluminium species are dominant. Similar observations have been made by other workers following steam treatment of zeolite-Y based samples.[5,6,8-10,12,15] It is generally found, as in the present work, that the extent of the framework to non-framework ratio depends upon the steaming conditions (reaction temperature, duration of experiment and steam to carrier gas ratio), the specific characteristics of the zeolite-Y used (Si/Al ratio, residual sodium level, type and concentration of balancing ions) and the vanadium loading. In addition to the resonances discussed previously (δ(^{27}Al) ~ 60, 30, 0 ppm) it can be seen that there is also a very broad resonance which spans some 400-500 ppm; this resonance is most evident in the spectra of the lower lanthanum ion-exchanged samples. Klinowski and co-workers[12] assigned this broad signal to the presence of a polymeric aluminium species. For such species it can be anticipated that the aluminium will be in low symmetry environments and consequently there will be a wide range of electric field gradients leading to a distribution of quadrupole interactions for the aluminium nucleus. It is worth noting at this stage that in addition to the four resonances observed here other workers[6,9] have found evidence for additional resonances in the ^{27}Al MAS NMR spectrum after hydrothermal treatment. Notably a

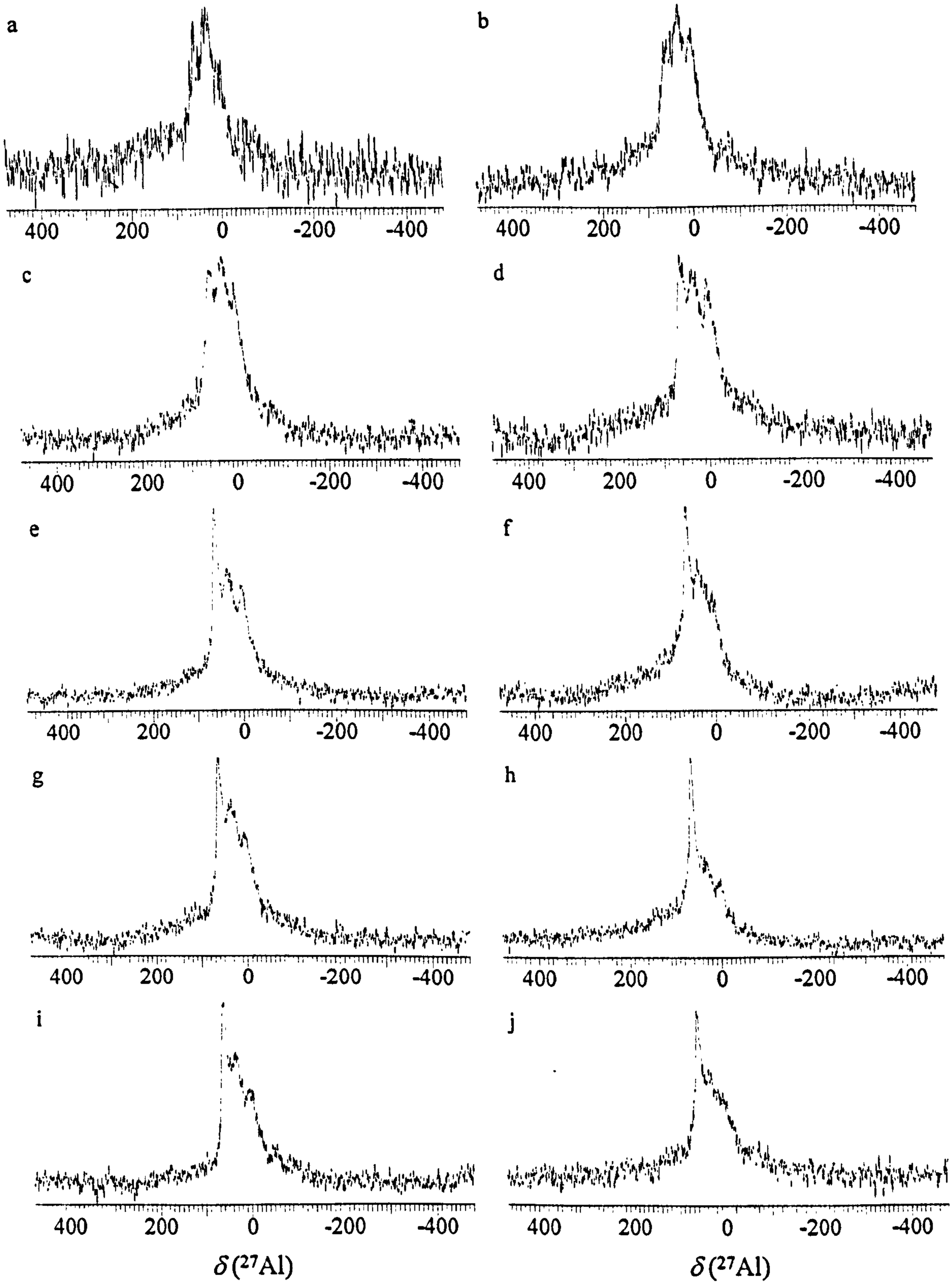

Figure 5.12 ^{27}Al MAS NMR spectra observed at 104.169 MHz; all spectra were filtered through an exponential window prior to Fourier transformation. For all spectra the external reference was a 0.1 mol dm^{-3} aqueous solution of $[Al(H_2O)_6]^{3+}$, pulse delay = 1 s, pulse width = 2 μs, spinning frequency ~ 8 kHz, number of scans = 10 000, except for (a) = 15 000 scans and (i) and (j) = 6000 scans. Samples steam treated at 750°C for 5 hours using air as a carrier gas with (a), (c), (e), (g) and (i) vanadium free and (b), (d), (f), (h) and (j) contaminated with 5000 ppm vanadium. (a) and (b) represent spectra for H-Y samples, (c) and (d) 1.5LaH-Y, (e) and (f) 2.6LaH-Y, (g) and (h) 5.0LaH-Y, and (i) and (j) 8.6LaH-Y.

resonance centred at $\delta(^{27}Al) \sim 50$ ppm and resonances in the range $\delta(^{27}Al) \sim 0$-4 ppm. Grobet and co-workers[6] found that the resonance centred at $\delta(^{27}Al) \sim 50$ ppm was formed under relatively mild hydrothermal conditions for which extraction of aluminium from the zeolite-Y lattice was not favoured. Under hydrothermal conditions that favoured removal of aluminium from the zeolite-Y lattice the resonance was not present but instead a resonance at $\delta(^{27}Al) \sim 30$ ppm was observed. The resonance was assigned to tetrahedral aluminium similar to that observed in amorphous silica-alumina. Freude and co-workers[9] also assigned the resonance to tetrahedral aluminium, but in a different environment, namely AlOOH associated with two framework oxygens. Grobet and co-workers[6] assigned the resonances in the range $\delta(^{27}Al) \sim 0$-4 ppm to six co-ordinate aluminium in some polymeric form.

Returning to Figure 5.12, it can be seen, moving down either of the columns of spectra, that as the lanthanum ion-exchange level increases then so does the relative amount of framework aluminium present within each sample; that is an increase in the relative intensity of the resonance centred at $\delta(^{27}Al) \sim 60$ ppm. This is consistent with the XRD and surface area measurements which confirm that increasing the lanthanum ion-exchange level increases the amount of crystalline material present within each sample. It can also be noted that the observed increase in unit cell constant with increasing lanthanum ion-exchange level is also indicative of an increase in the relative amount of framework aluminium.

Effect of increasing vanadium contamination

The effect of increased vanadium loading is most clearly observed for high lanthanum ion-exchanged samples where greater amounts of vanadium can be added. Figure 5.13 gives the XRD patterns for the series of 8.6LaH-Y samples steam treated at 800°C for 5 hours using air as a carrier gas and contaminated with 0, 5000, 10 000 and 15 000 ppm vanadium. It can be seen that as the vanadium concentration is increased then the amount of crystalline material falls. This happens to such an extent that at 15 000 ppm vanadium no crystalline zeolitic material remains. The low intensity diffraction peaks that can be

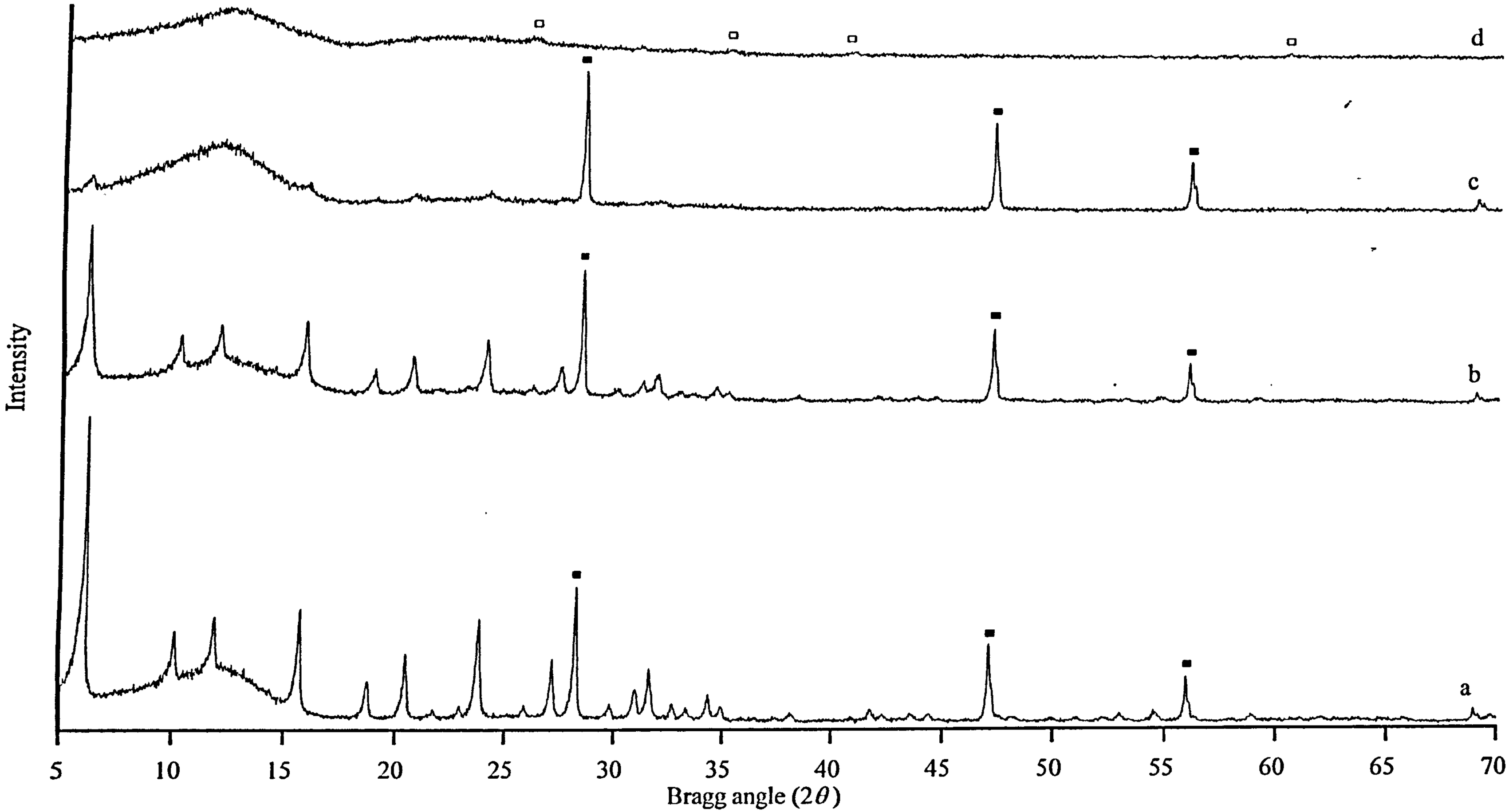

Figure 5.13 XRD patterns recorded for 8.6LaH-Y steam treated at 800°C for 5 hours using air as a carrier gas (a) 0 ppm vanadium, (b) 5000 ppm vanadium, (c) 10 000 ppm vanadium and (d) 15 000 ppm vanadium. ■ labels the diffraction peaks for the silicon standard and □ labels diffraction peaks due to mullite.

seen in this XRD pattern (Figure 5.13 (d)) at 26, 35, 41 and 60.5°, in 2θ (peaks labelled □) are due to the formation of mullite. Mullite is an aluminosilicate which can have a range of compositions from $Al_6Si_2O_{13}$ to $Al_4Si_2O_{10}$. It can be regarded as a disordered phase of aluminium silicate intermediate between the ordered phases of sillimanate (Al_2SiO_5) and andalusite (Al_2SiO_5).[17] The formation of mullite from severely treated zeolite-Y has been reported by Gallezot and co-workers.[18] Other workers[6,19-20] have shown that vanadium can be incorporated into the mullite lattice and it is known to act as a mineralising agent lowering the formation temperature of mullite by more than 400°C.

The change in zeolite-Y crystallinity as the vanadium concentration is increased can also be followed via surface area measurements. Figure 5.14 shows the surface area measurements for the lanthanum ion-exchanged samples plotted as a function of vanadium loading. Figure 5.14 (a), for the H-Y sample, illustrates how unstable the zeolite-Y lattice is without the presence of lanthanum ions. Treatment of this sample, at both reaction temperatures, with and without vanadium, results in the complete loss of all zeolitic material. The small increase in surface area when the sample is steam treated in the presence of vanadium, is most likely due to recrystallisation of amorphous material. The 1.5LaH-Y (b) and 5.0LaH-Y (d) samples show similar trends to those already discussed for the 8.6LaH-Y (e) sample; that is, increasing the vanadium loading increases the loss of zeolite-Y crystallinity. For the 2.6LaH-Y (c) sample the same is true for steam treatment at 800°C, however, at 750°C there is a small increase in surface area at 1000 and 3000 ppm vanadium compared to the vanadium free sample. The reason for this behaviour is not clear although it is interesting to note that at this lanthanum ion-exchange level, the measurements of surface area is particularly sensitive to experimental conditions (Chapter 4). It can also be noted that even at 5000 ppm vanadium the reduction in surface area, compared to the vanadium free sample, is only small.

The changes in unit cell constant for the steam-treated samples can be compared using Figure 5.15. Unit cell constants could not be obtained from the essentially amorphous XRD patterns for the H-Y samples. Contrasting results are observed, depending upon the lanthanum ion-exchange level. For the 1.5LaH-Y (a) sample it can be seen that as the vanadium loading is increased there is a trend for the unit cell constant to also increase.

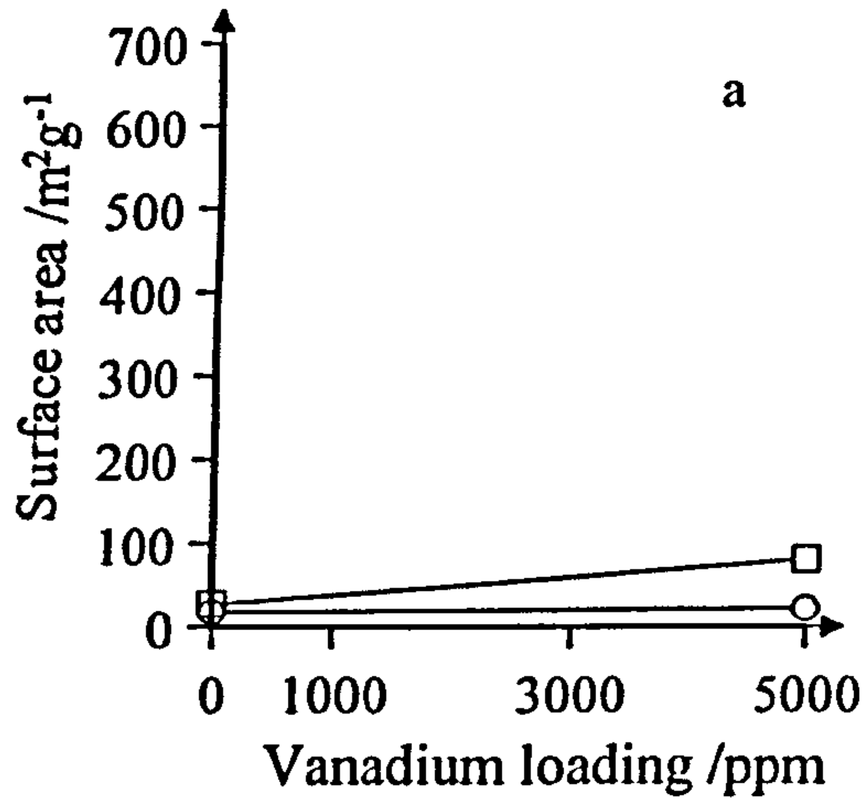

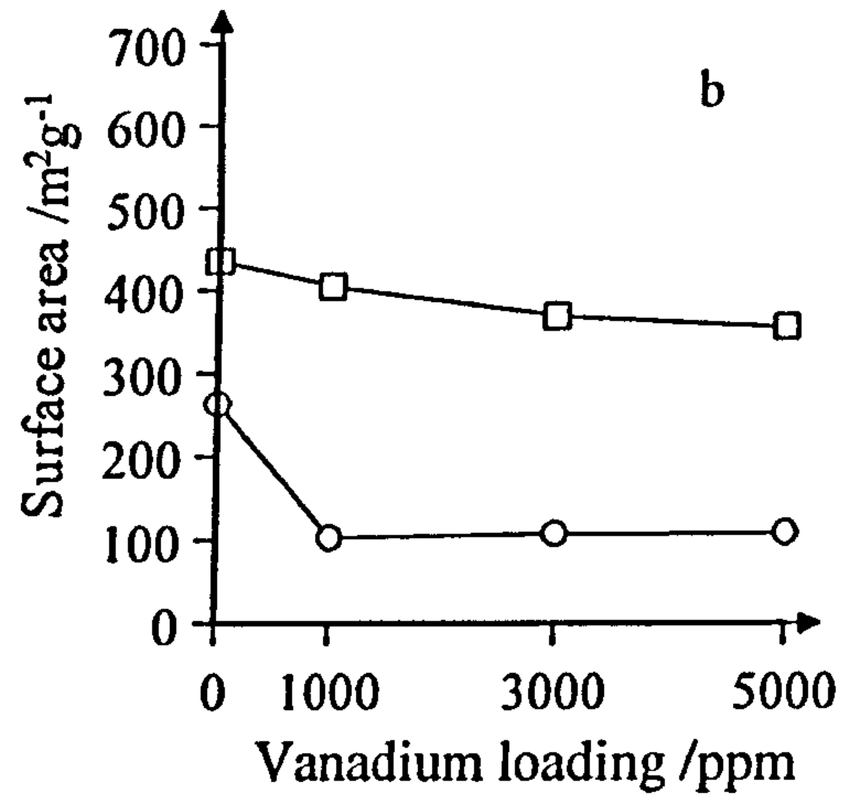

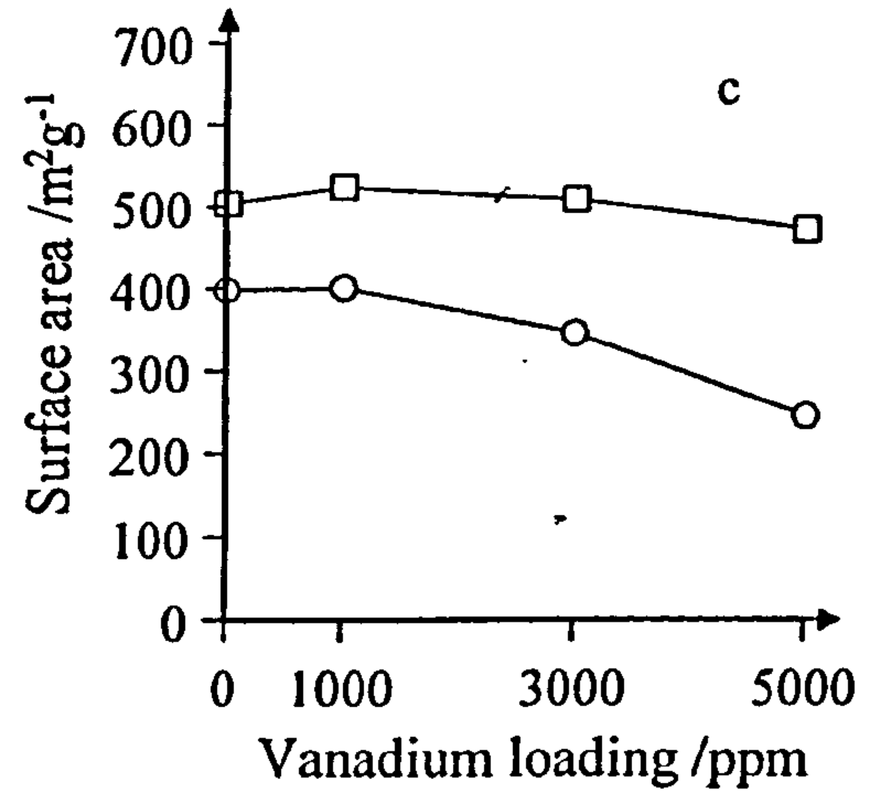

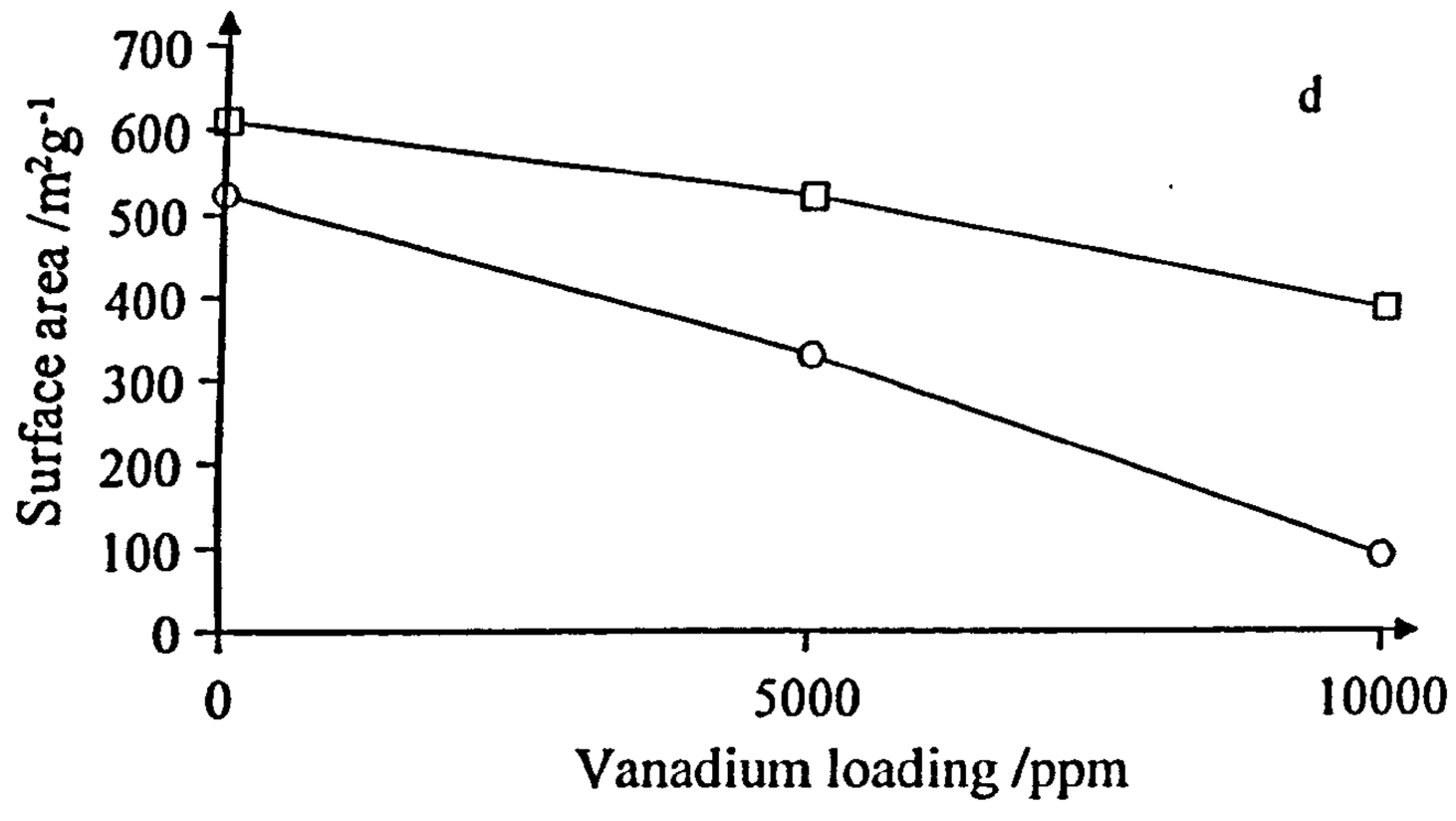

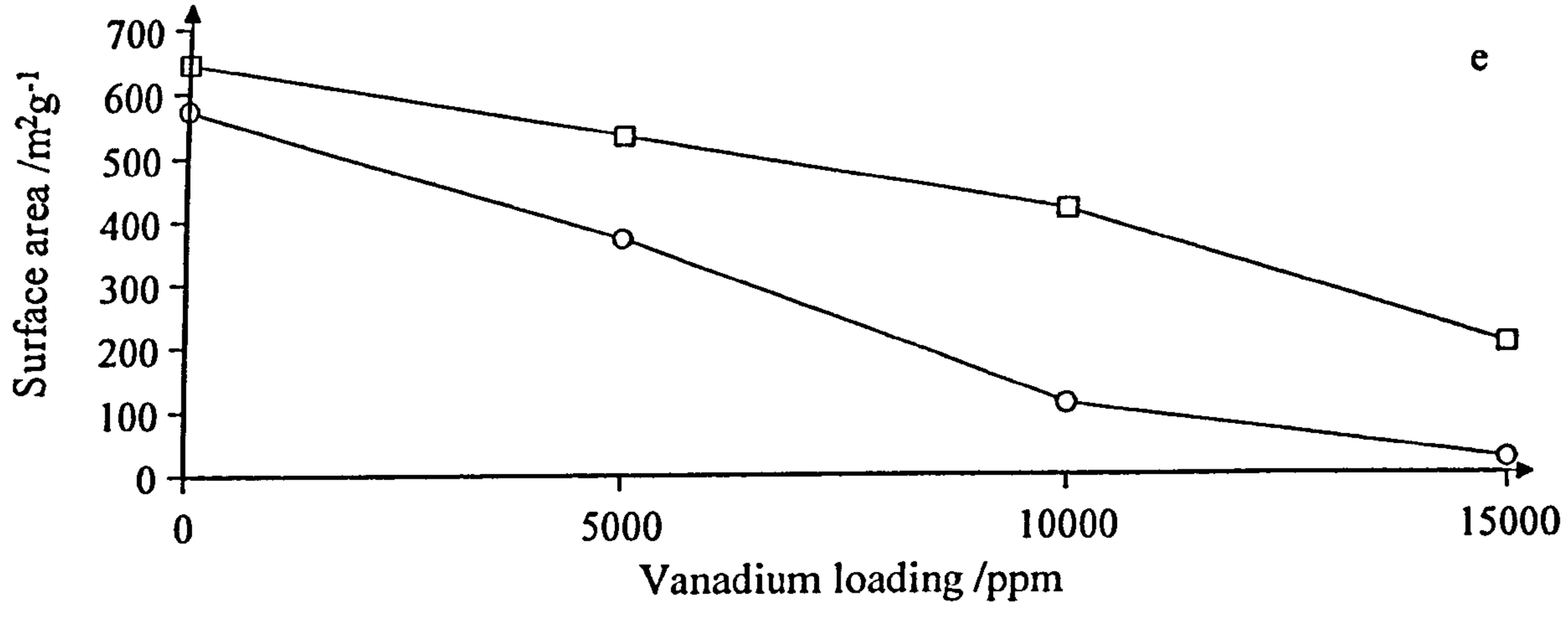

Figure 5.14 Steam treatment data presented in Table 5.5. □ represents steam treatment at 750°C, and ○ represents steam treatment at 800°C. Plot (a) represents data for H-Y, (b) represents data for 1.5LaH-Y, (c) represents data for 2.6LaH-Y, (d) represents data for 5.0LaH-Y and (e) represents data for 8.6LaH-Y. The lines in the figures have no significance other than as a guide to the general trends.

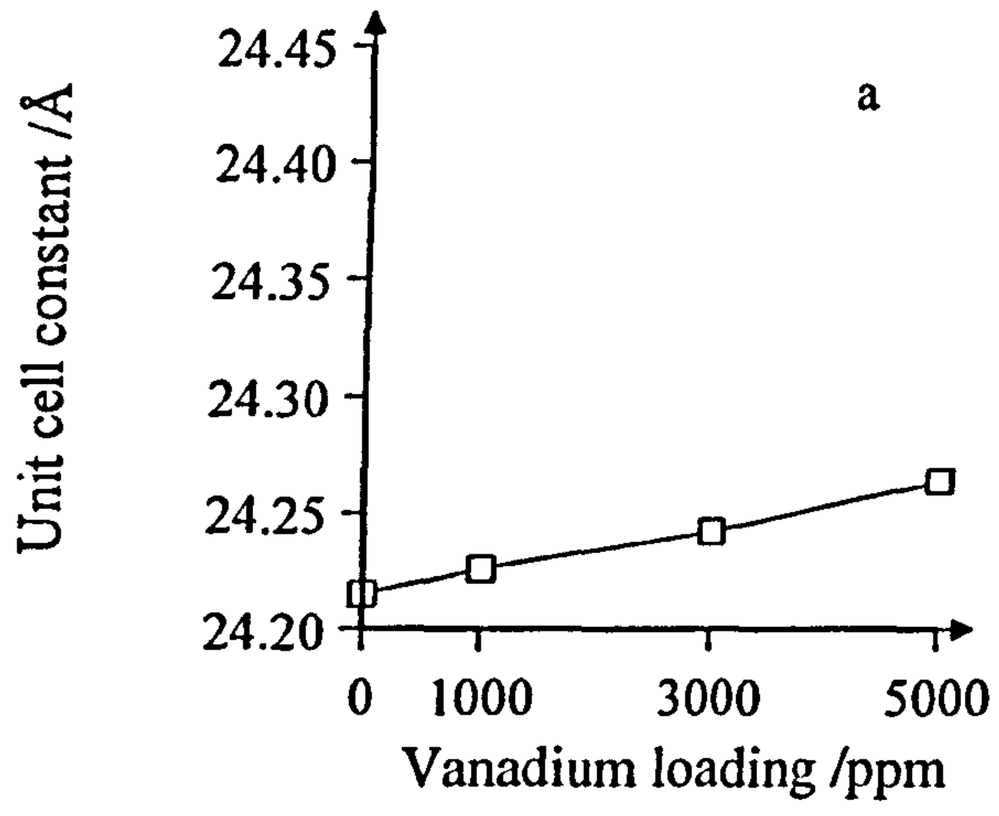

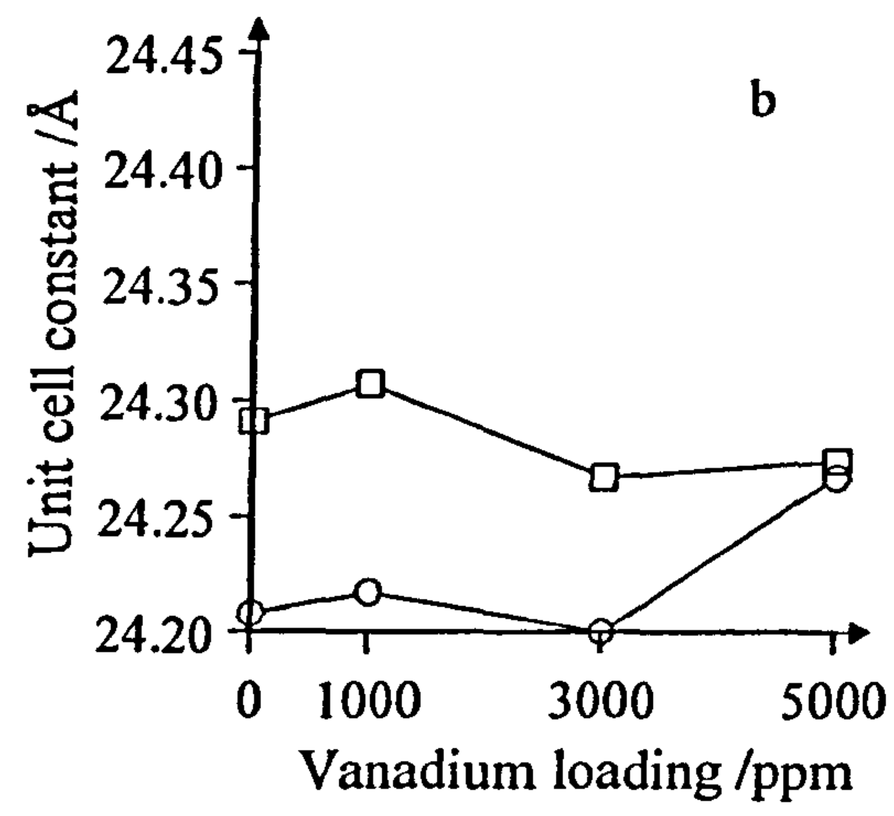

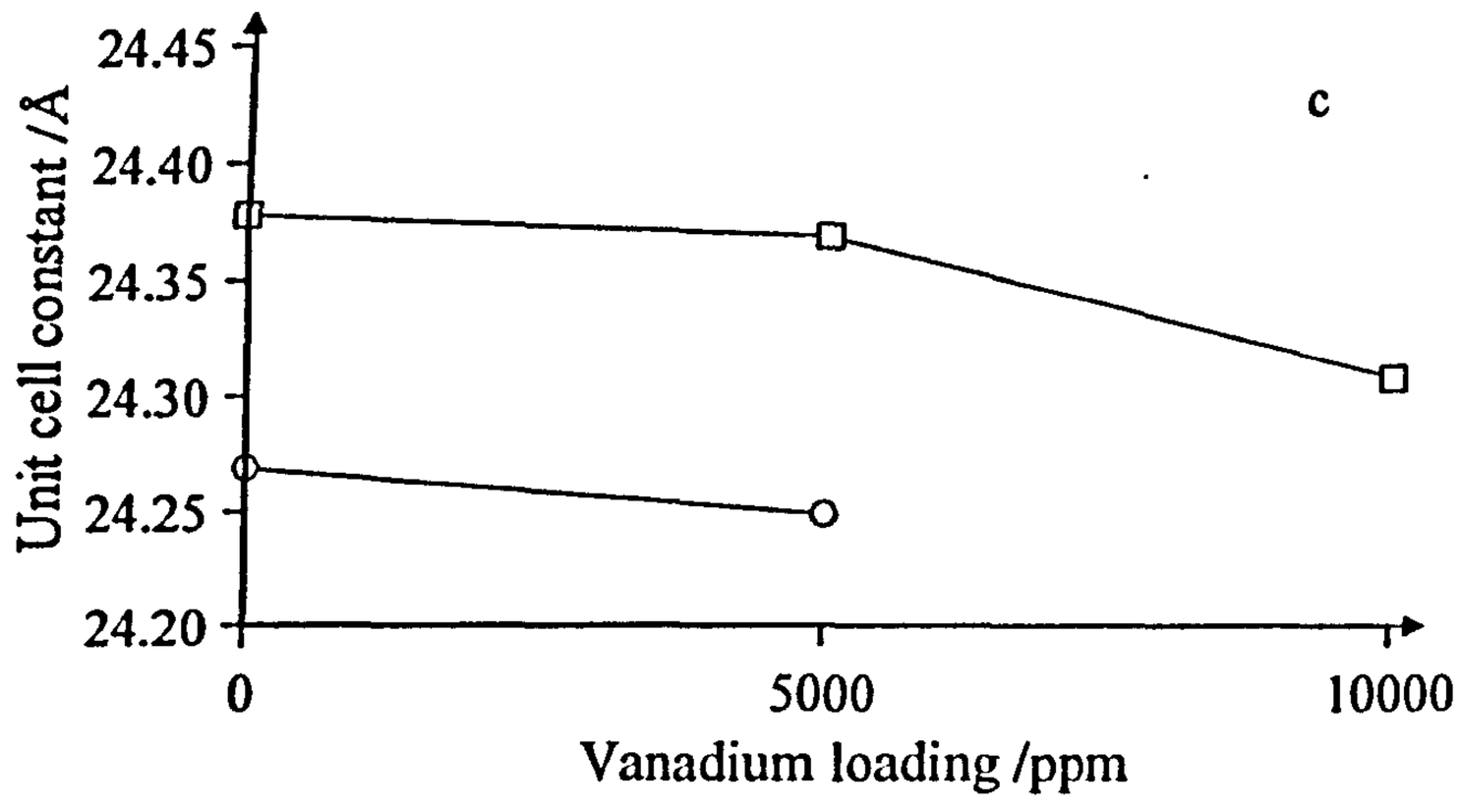

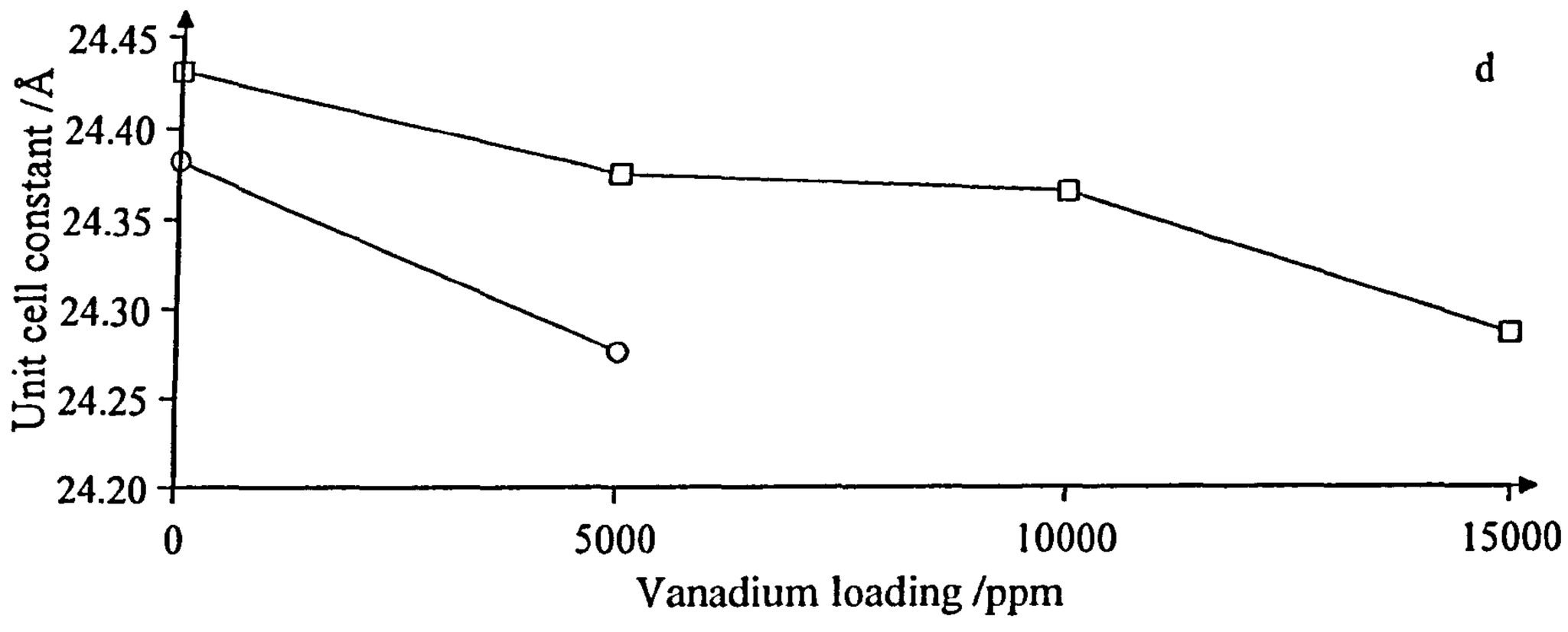

Figure 5.15 Steam treatment data presented in Table 5.5. □ represents steam treatment at 750°C, and ○ represents steam treatment at 800°C. Plot (a) represents data for 1.5LaH-Y, (b) represents data for 2.6LaH-Y, (c) represents data for 5.0LaH-Y and (d) represents data for 8.6LaH-Y. The lines in the figures have no significance other than as a guide to the general trends.

For the 5.0LaH-Y (c) and 8.6LaH-Y (d) samples the unit cell constant tends to fall as the vanadium loading is increased. The unit cell constant results for the 2.6LaH-Y (c) sample do not show any consistent trends with increasing vanadium loading, although most of the observed changes in unit cell constant are within the limits of experimental error.

The ^{27}Al MAS NMR spectra recorded for the 8.6LaH-Y samples at both reaction temperatures and at all vanadium loadings are given in Figure 5.16. The first column of spectra ((a), (c), (e) and (g)) have been steam treated at 750°C and the second column of spectra ((b), (d), (f) and (h)) have been steam treated at 800°C. Moving down a column of spectra shows the effect of increasing vanadium loading and moving across shows the effect of increasing temperature.

It can be seen that as the vanadium loading is increased then the framework aluminium resonance, centred at $\delta(^{27}\mathrm{Al}) \sim 60$ ppm, becomes relatively less intense and less well resolved. This indicates that increased destruction to the zeolite-Y lattice has occurred and this is consistent with the surface area measurements (Figure 5.14 (e)). The same is true at both reaction temperatures. The decrease in the framework aluminium is accompanied by an increase in non-framework aluminium species with an increase in the resonances centred at $\delta(^{27}\mathrm{Al}) \sim 30$ ppm, $\delta(^{27}\mathrm{Al}) \sim 0$ ppm. There is also a noticeable increase in the very broad resonance which spans some 400-500 ppm as the vanadium loading increases.

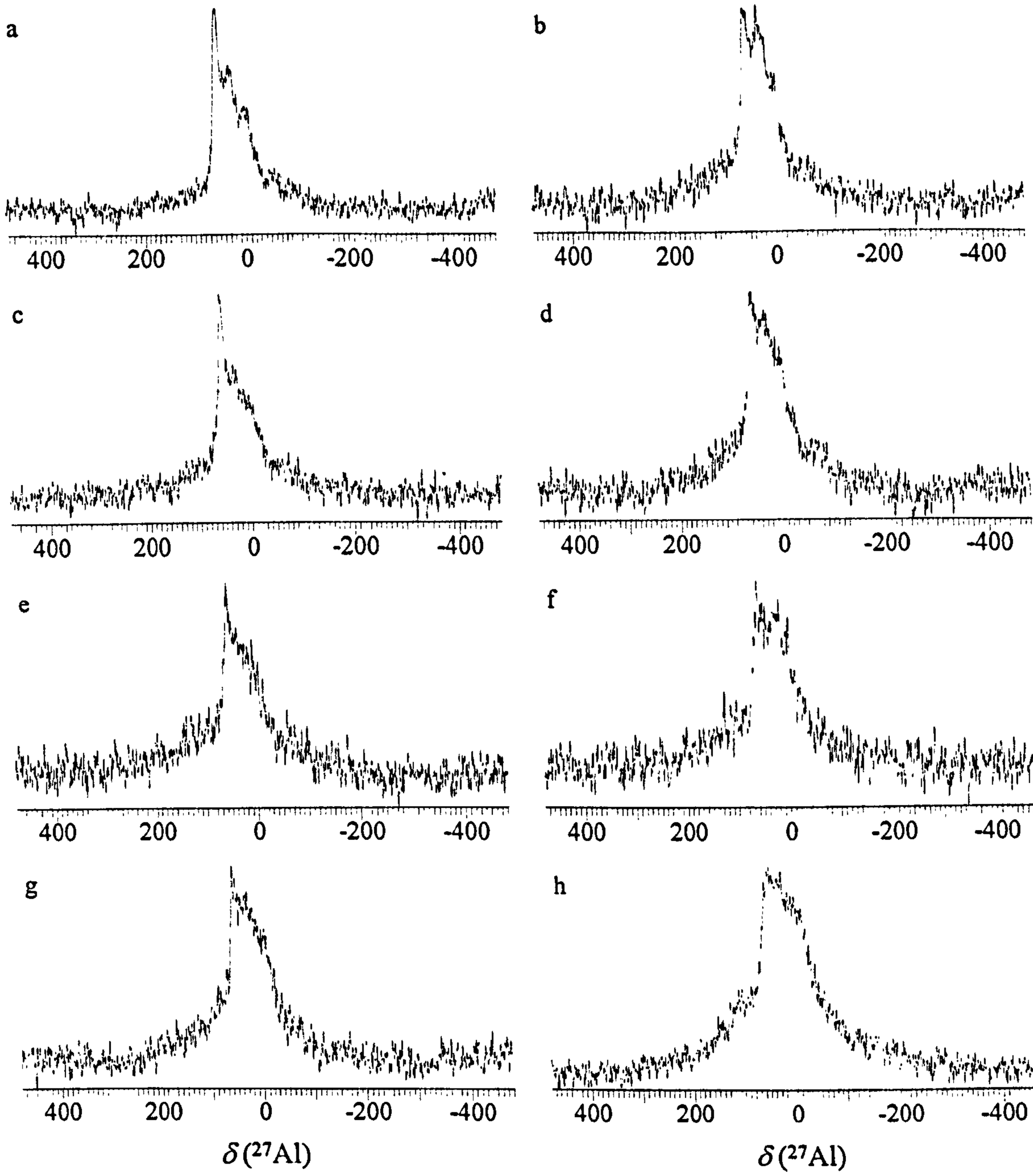

Figure 5.16 ^{27}Al MAS NMR spectra observed for 8.6LaH-Y samples at 104.169 MHz, all spectra were filtered through an exponential window prior to Fourier transformation. For all spectra the external reference was a 0.1 mol dm^{-3} aqueous solution of $[Al(H_2O)_6]^{3+}$, pulse delay = 1 s, pulse width = 2 μs, spinning frequency ~ 8 kHz, number of scans = 6000, except for (h) = 54 000 scans, (g) = 12 358 scans, and (d) and (f) = 8000 scans. Samples (a), (c), (e) and (g) steam treated at 750°C for 5 hours using air as a carrier gas. Samples (b), (d), (f) and (h) steam treated at 800°C for 5 hours using air as a carrier gas. (a) and (b) free from vanadium contamination, (c) and (d) contaminated with 5000 ppm vanadium, (e) and (f) with 10 000 ppm vanadium, and (g) and (h) 15 000 ppm vanadium.

Effect of increasing temperature

Figure 5.17 shows the XRD patterns for a sample of 8.6LaH-Y contaminated with 5000 ppm vanadium and steam treated at 750°C (a) and 800°C (b) for 5 hours using air as a carrier gas. The increase in temperature results in an observed decrease in the amount of crystalline material. The same is true for other lanthanum ion-exchanged samples at all vanadium loadings, as can be confirmed from Figure 5.14. It can also be seen from Figure 5.15, where data is available, that an increase in temperature results in an additional decrease in the unit cell constant. The ^{27}Al MAS NMR spectra reflect these changes and it can be seen from Figure 5.16 that increasing the temperature results in a decrease in the framework aluminium resonance and a corresponding increase in the non-framework resonances.

5.2.2 Zeolite-Y Samples and Different Treatment Conditions

Specific investigations relating to different treatment conditions, for example changing the steam to air ratio, were carried out for the 2.6LaH-Y sample. The reproducibility of the results obtained from different batches of this sample have already been discussed in Chapter 4. Table 5.6 summaries the results of the investigations: the carrier gas was air. No experiments were performed at steam to carrier gas ratios of 10, 20, and 30 % steam because the carrier gas flow rates needed to achieve these ratios would have been too high and the sample would have been blown out of the furnace system.

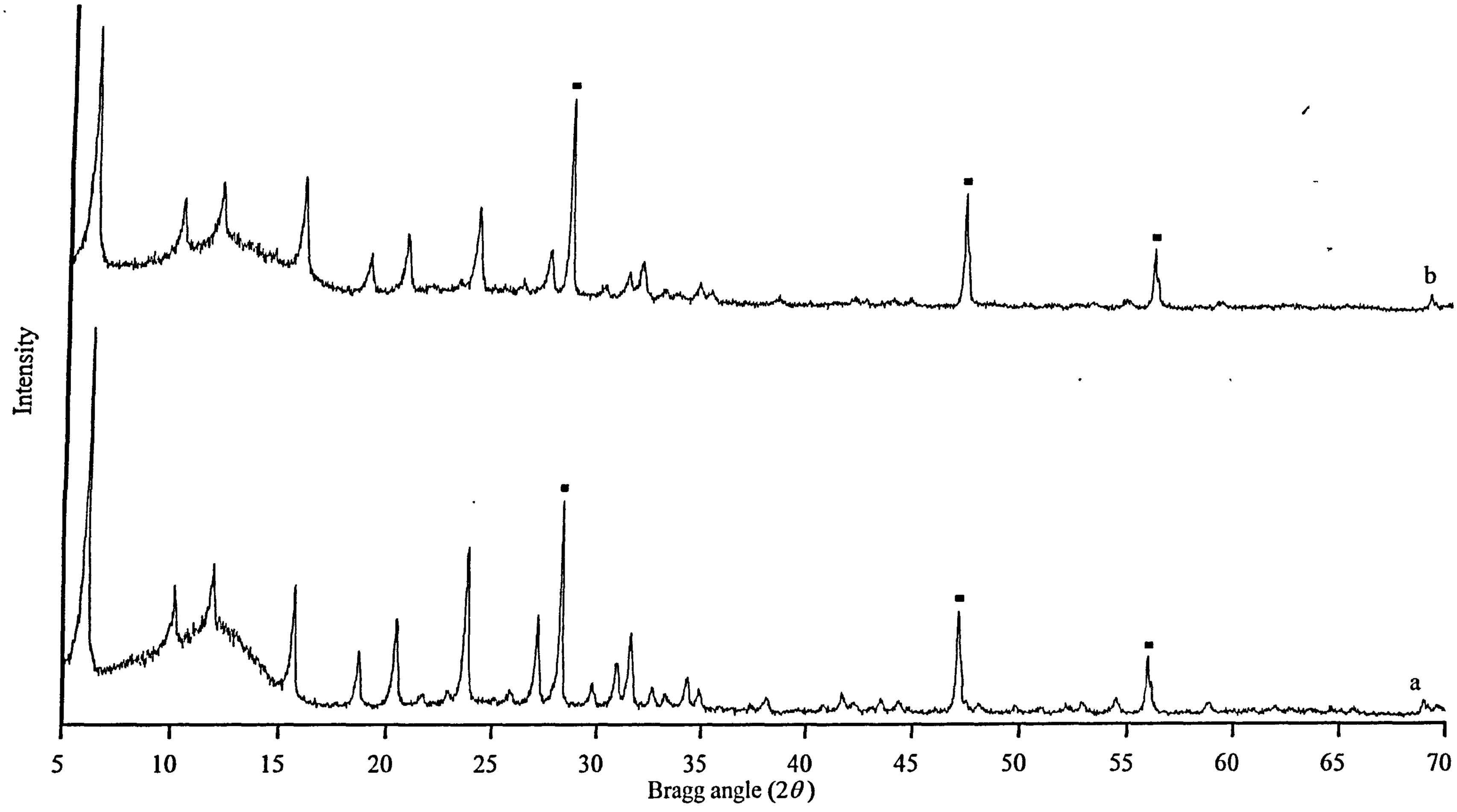

Figure 5.17 XRD patterns recorded for 8.6LaH-Y contaminated with 5000 ppm vanadium and steam treated at (a) 750°C and (b) 800°C for 5 hours using air as a carrier gas. ■ labels the diffraction peaks for the silicon standard.

Reaction conditions	Steam/gas ratio /% steam	Vanadium loading /ppm	Unit cell constant /Å (±0.035Å)	Surface area /m^2g^{-1} (±10%)
800/5/AIR	0	5000	24.261	649
	50		24.281	495
	60		24.299	440
	70		24.253	399
	80		-	151
	100		-	146
800/5/AIR	0	10 000	24.269	666
	40		24.275	206
	50		24.258	128
	60		24.263	122

Table 5.6 Reaction conditions, surface area and unit cell constant data for 2.6LaH-Y samples steam treated at differing steam to carrier gas ratios, and two different vanadium loadings. Omissions appear in the unit cell constant data due to insufficient crystalline material remaining, after treatment, for accurate determination.

Figure 5.18 shows plots of both the surface area and unit cell constant data presented in Table 5.6 as a function of steam to carrier gas ratio. It can be seen that as the steam to carrier gas ratio is increased then there is a decrease in zeolite-Y crystallinity (decreasing surface area), at both vanadium loadings. The XRD patterns obtained for these steam-treated samples also reflect this change in zeolite-Y crystallinity. The decrease in surface area is not linear and the behaviour of the sample contaminated with 5000 ppm vanadium shows a steady decrease in surface area from 0-70 % steam and then a sharp decrease as the steam to carrier gas ratio is increased to 80 % steam. Above 80 % steam the change in surface area is relatively small. It can be noted that measurement of surface area in the region of 70 % to 80 % steam will be particularly sensitive to the steam to

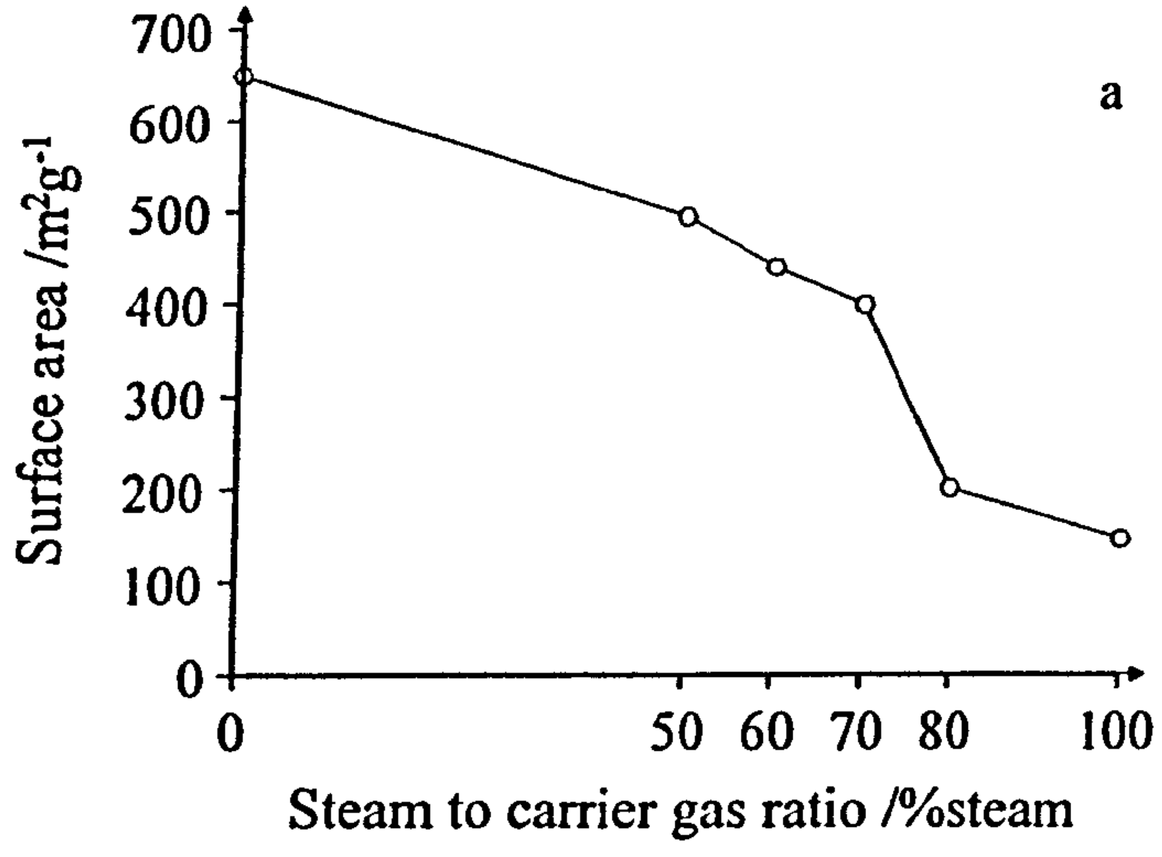

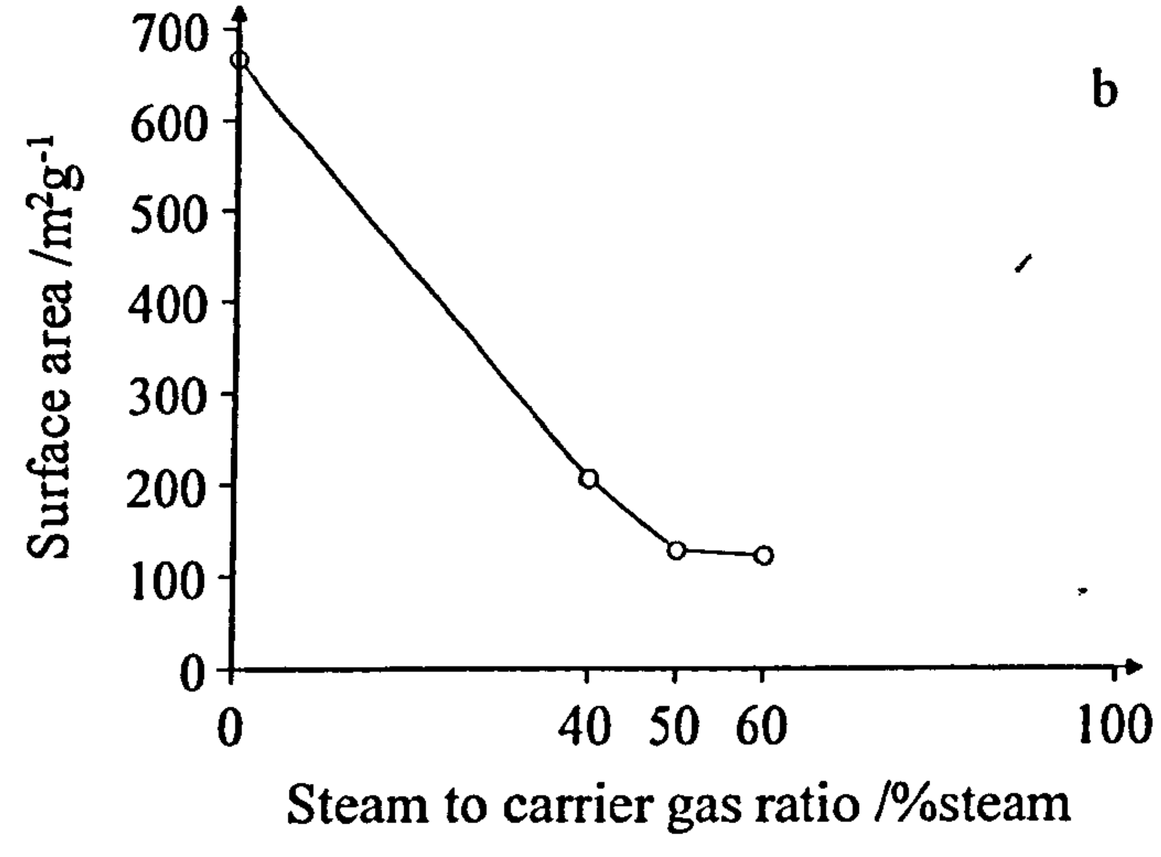

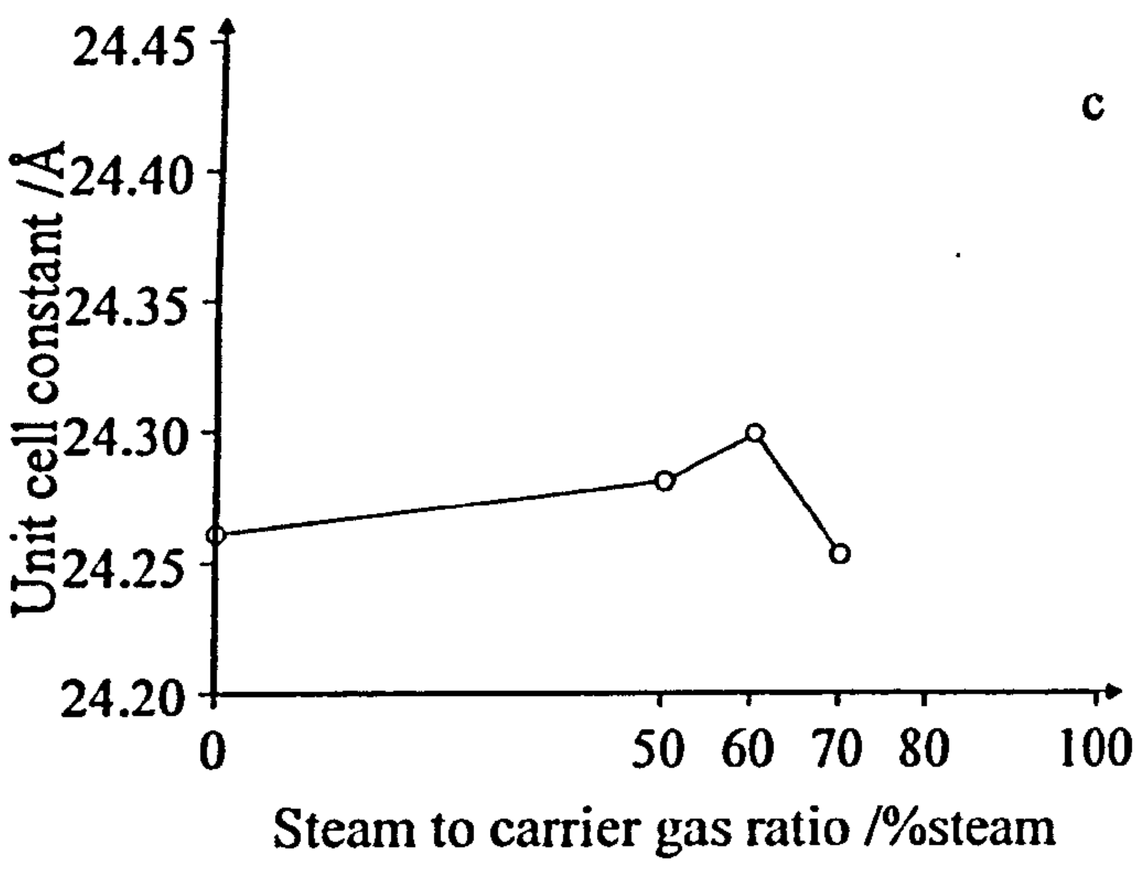

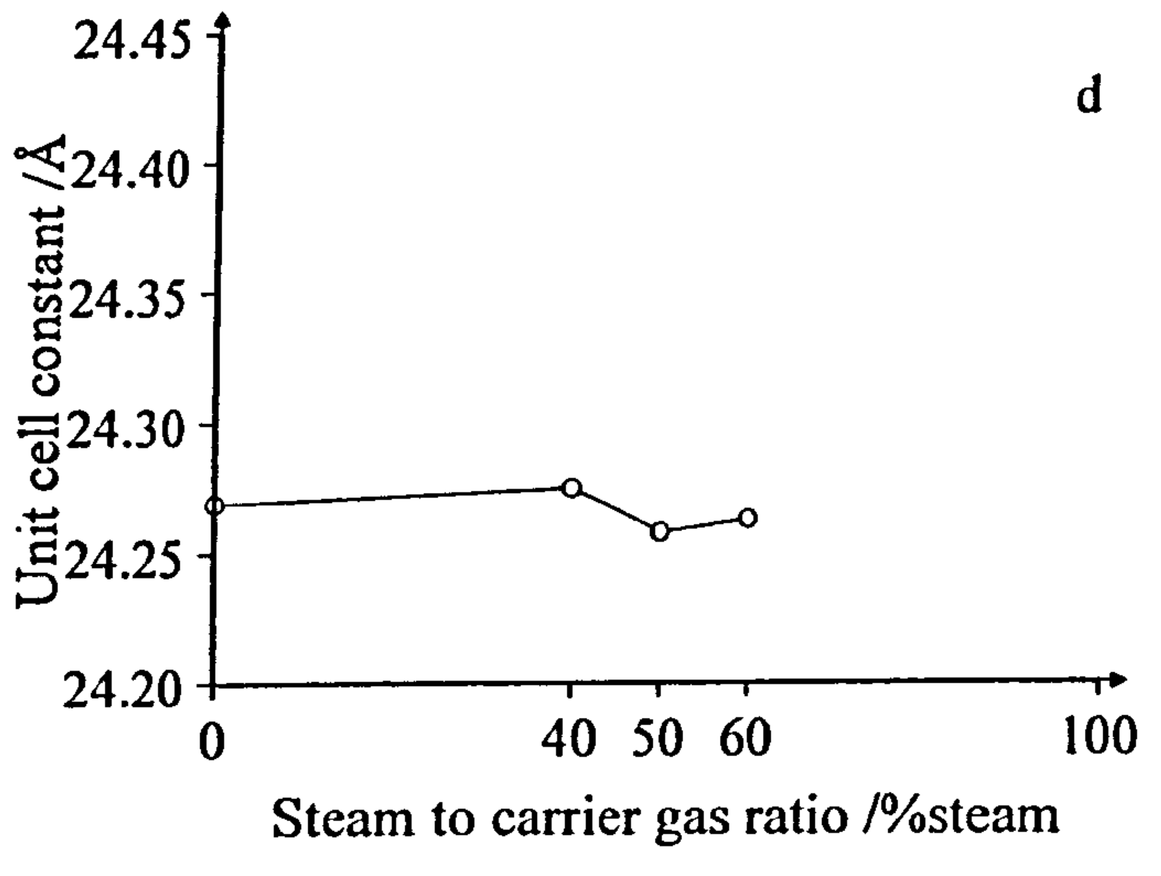

Figure 5.18 Steam treatment data presented in Table 5.7. Plots (a) and (c) represent data for a 2.6LaH-Y sample contaminated with 5000 ppm vanadium and steam treated at 800°C for 5 hours, and (b) and (d) represent data for a similar sample contaminated with 10 000 ppm vanadium and steam treated at 800°C for 5 hours. The lines in the figures have no significance other than as a guide to the general trends.

carrier gas ratio. This will be an additional factor determining the reproducibility of results in this region. For the sample contaminated with 10 000 ppm vanadium it appears that changes in surface area become relatively small at the lower steam to carrier gas ratio of *ca.* 40% (as indicated earlier experiments could not be carried out at steam to carrier gas ratios of less than 40%). Overall the results suggest that the range of steam to gas ratios over which significant changes in zeolite-Y crystallinity occur depend on vanadium loading: the higher the loading the narrower the range measured from zero steam.

The unit cell constant data indicates that calcination of the samples results in a sharp decrease in the unit cell constant. This decrease is maintained, within the limits of experimental error, for the steam-treated samples. The ^{27}Al MAS NMR spectra recorded for the samples, contaminated with 5000 ppm vanadium, and steam treated at 800°C for 5 hours are given in Figure 5.19. The spectra reflect the changes that were deduced from the XRD and surface area measurements. There is a decrease in the framework aluminium sites, centred at $\delta(^{27}\text{Al}) \sim 60$ ppm and an increase in the non-framework aluminium sites, centred at $\delta(^{27}\text{Al}) \sim 30$ and ~ 0 ppm, together with the broad signal between $\delta(^{27}\text{Al}) \sim -250 - 250$ ppm. It can be noted that a distinct difference between the calcined and steam-treated spectra is observed. It can be seen that the form of the ^{27}Al NMR spectra for the calcined sample in the chemical shift region of 30 ppm is better resolved when compared to similar regions in the steam treated samples. The reason for this behaviour is not clear.

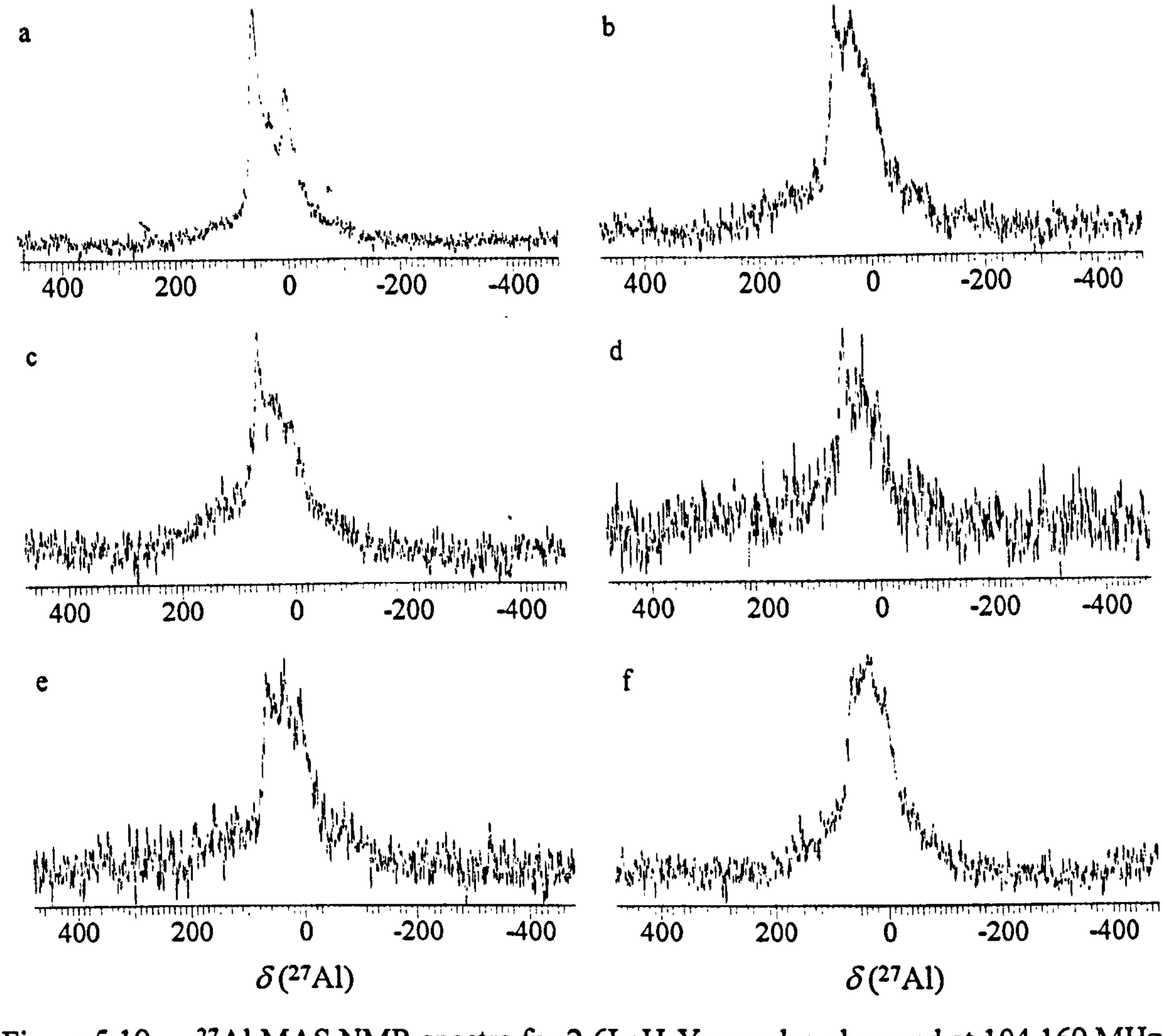

Figure 5.19 ^{27}Al MAS NMR spectra for 2.6LaH-Y samples observed at 104.169 MHz, all spectra were filtered through a exponential window prior to Fourier transformation. For all spectra the external reference was a 0.1 mol dm^{-3} aqueous solution of $[Al(H_2O)_6]^{3+}$, pulse delay = 1 s, pulse width = 2 μs, spinning frequency ~ 8 kHz, number of scans = 10 000, except for (c) = 7315 scans. The samples were steam treated at 800°C for 5 hours using air as a carrier gas with a steam to carrier gas ratio of (a) 0 % steam, (b) 50 % steam, (c) 60 % steam, (d) 70 % steam, (e) 80 % steam, and (f) 100 % steam.

Effect of nitrogen as a carrier gas

A series of experiments were carried out for the 5.0LaH-Y and 8.6LaH-Y samples in which nitrogen gas, rather than air, was used as the carrier gas. The samples were steam treated at 750°C and 800°C for 5 hours at the standard steam to carrier gas ratio (80 % steam).

Table 5.7 gives the surface area and unit cell constant data for the steam-treated samples, also included are the results for samples steam-treated using air as a carrier gas (Table 5.5) for ease of comparison. All of this information is presented in graphical form in Figure 5.20.

The samples steam treated under a nitrogen atmosphere (solid data points) show the same general trends as for those treated under air (open data points): that is there is a loss of surface area (zeolite-Y crystallinity) as both the vanadium loading and temperature are increased. These observations are valid for both the 5.0LaH-Y and 8.6LaH-Y samples. In more detail, however, there is an important difference between the samples treated at 750°C and 800°C. At the lower of these two temperatures it is clear that the presence of the nitrogen atmosphere lessens the destructive effect of the presence of vanadium. In contrast at 800°C the measured surface areas are essentially the same irrespective of whether the steaming is carried out in an air or nitrogen atmosphere.

Sample	Reaction conditions	Vanadium loading /ppm	Unit cell constant /Å (±0.035Å)	Surface area /m^2g^{-1} (±10%)
5.0LaH-Y	750/5/80/AIR	0	24.378	610
		5000	24.369	520
		10 000	24.308	386
	750/5/80/N_2	0	24.412	617
		5000	24.350	560
		10 000	24.328	497
	800/5/80/AIR	0	24.269	523
		5000	24.249	330
		10 000	-	96
	800/5/80/N_2	0	24.309	526
		5000	24.224	317
		10 000	-	111
8.6LaH-Y	750/5/80/AIR	0	24.431	646
		5000	24.375	535
		10 000	24.366	420
	750/5/80/N_2	0	24.441	658
		5000	24.430	628
		10 000	24.400	564
	800/5/80/AIR	0	24.382	574
		5000	24.276	373
		10 000	-	112
	800/5/80/N_2	0	24.349	560
		5000	24.304	344
		10 000	-	121

Table 5.7 Unit cell constant and surface area data for the 5.0LaH-Y and 8.6LaH-Y samples steam treated under either an air or nitrogen atmosphere.

Omissions appear in the unit cell constant data due to insufficient crystalline material remaining, after treatment, for accurate determination.

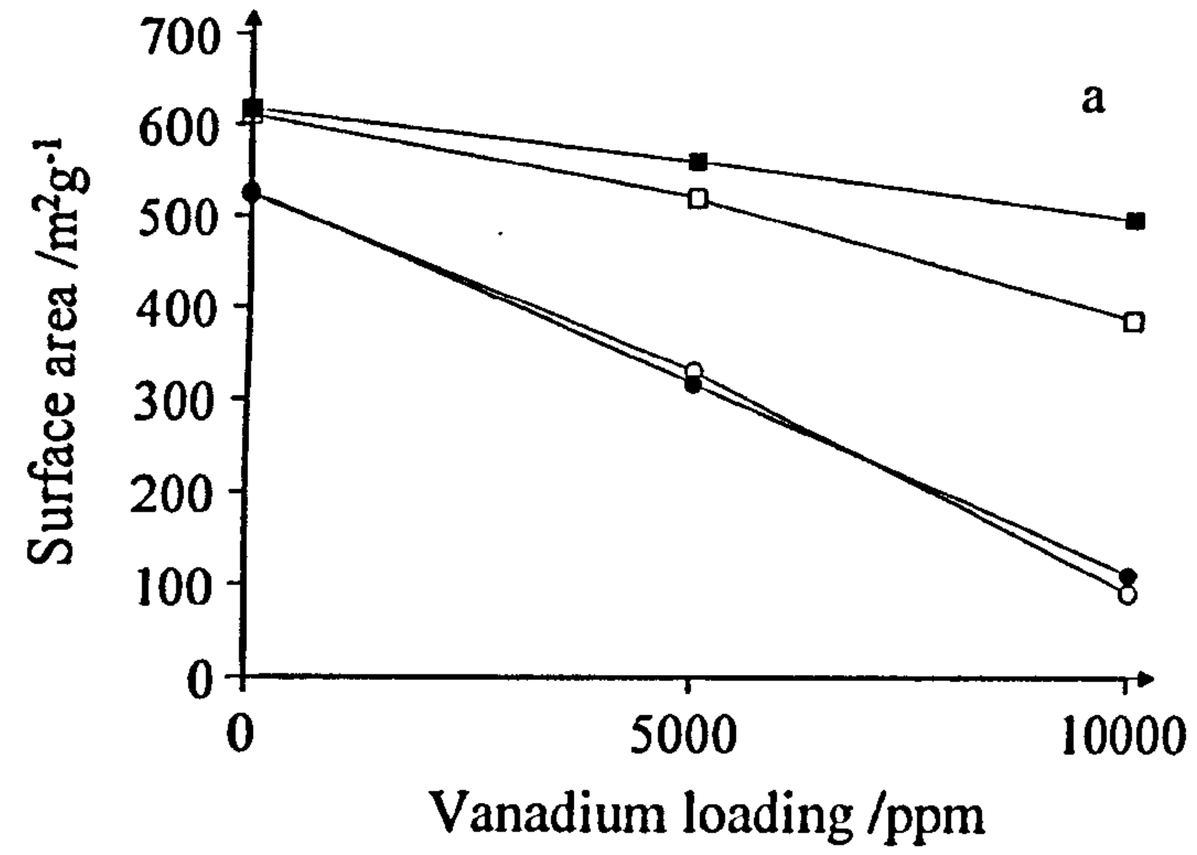

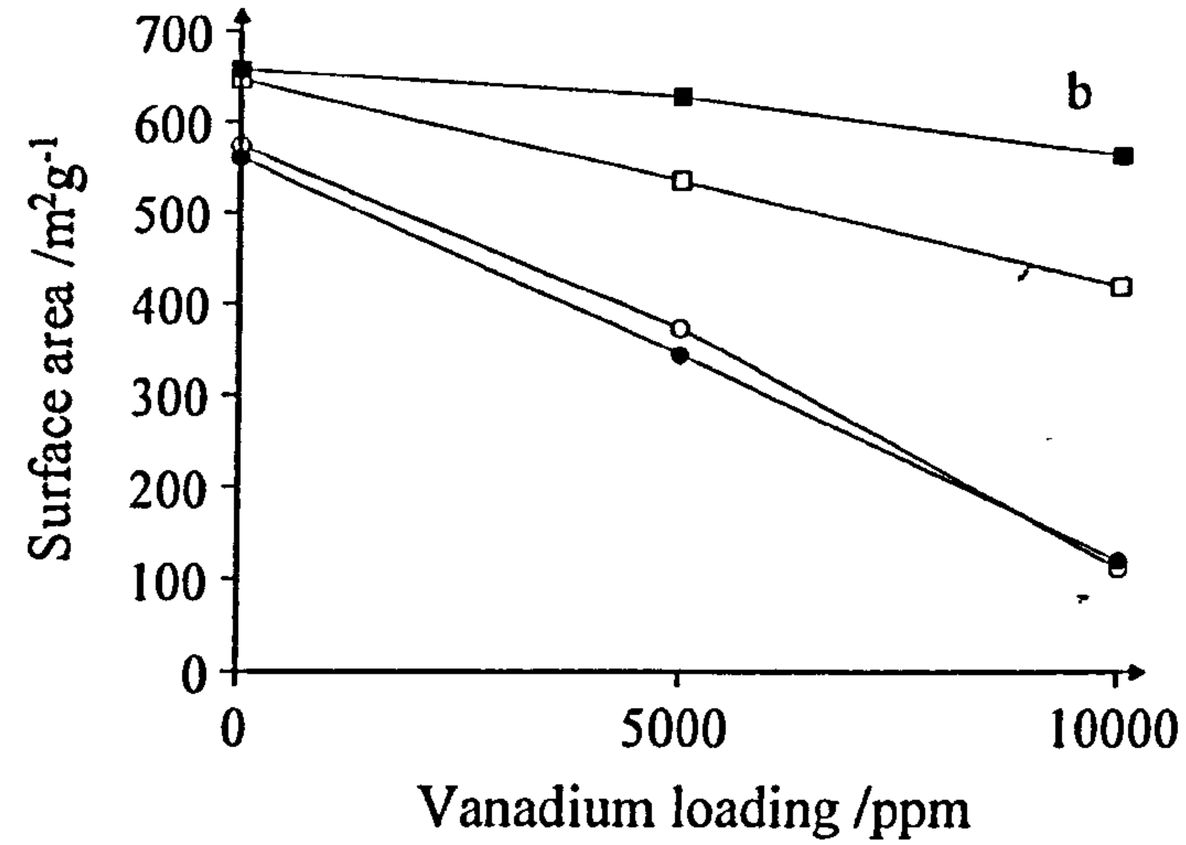

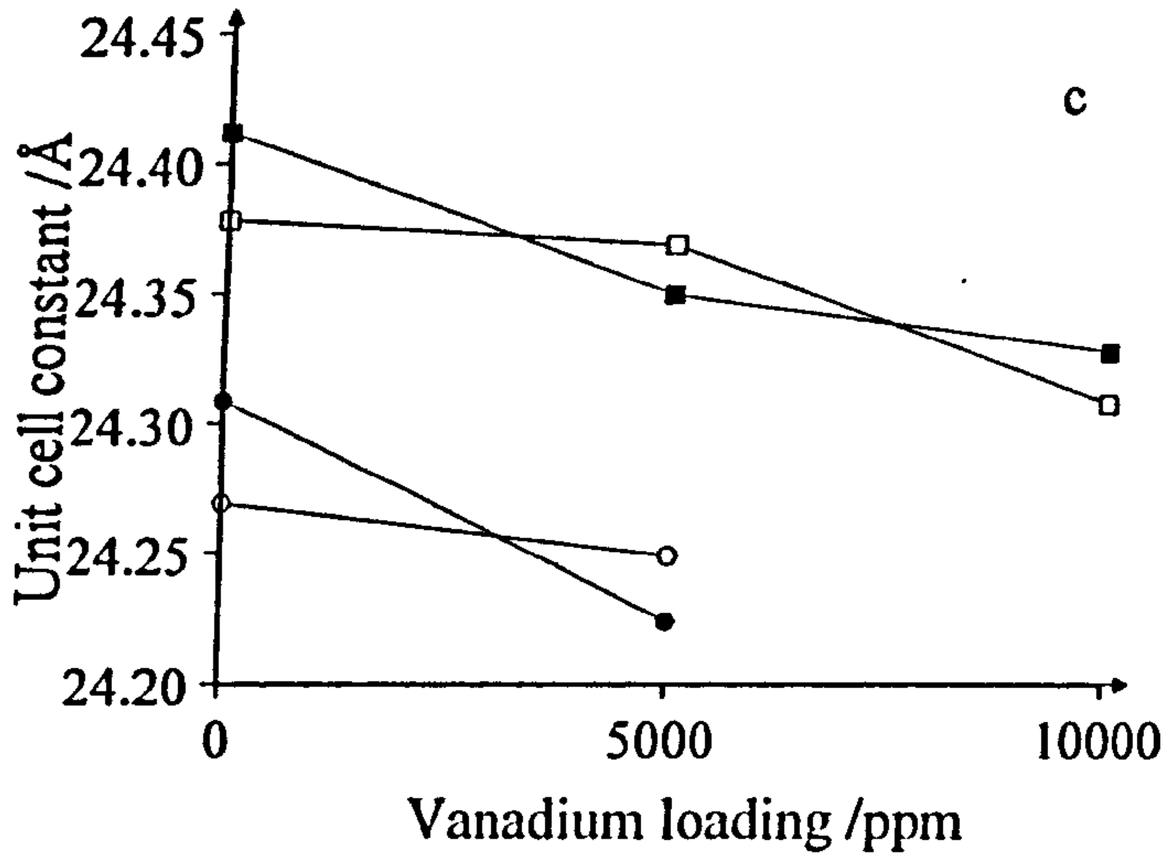

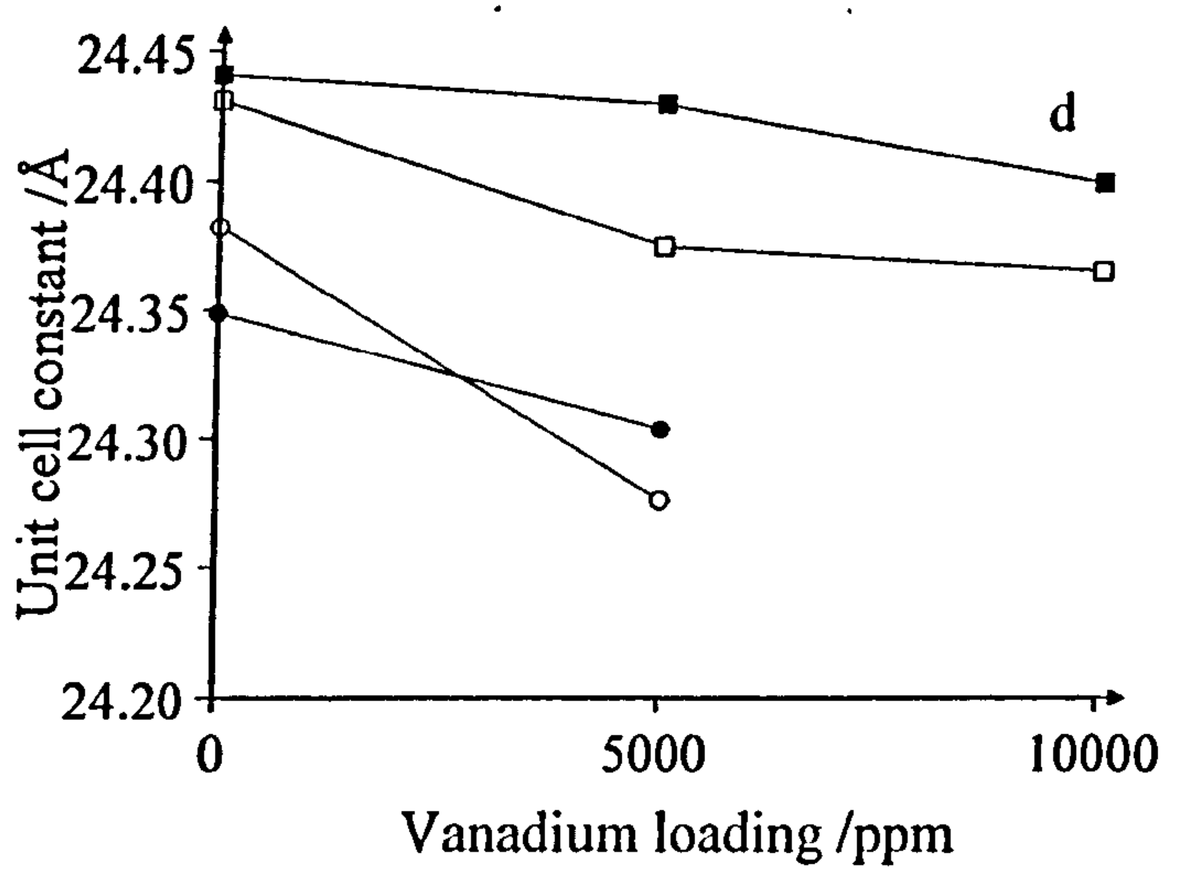

Figure 5.20 Steam treatment data presented in Table 5.8. Plots (a) and (c) represent data for 5.0LaH-Y steam treated at 750°C (□ and ■) and 800°C (○ and ●) for 5 hours using air as a carrier gas (□ and ○) and nitrogen as a carrier gas (■ and ●). (b) and (d) represent data for 8.6LaH-Y steam treated at 750°C (□ and ■) and 800°C (○ and ●) for 5 hours using air as a carrier gas (□ and ○) and nitrogen as a carrier gas (■ and ●).

A change from an air to a nitrogen atmosphere removes a source of oxygen from the treatment system. On the basis of the results described above it is thus possible to speculate that the presence of gaseous oxygen, at least at 750°C, has an influence on the mechanism by which vanadium interacts with lanthanum stabilised zeolite-Y: that is stability is favoured in a more reducing atmosphere. At 800°C the presence of oxygen gas is not as critical. This could suggest, at this higher temperature, that sufficient oxygen is derived from the steam or the lattice of the zeolite-Y.

Despite a literature search, no reports could be found in the open literature which describe comparative experiments between air and nitrogen as carrier gases: reported work simply focussed upon air, nitrogen or an inert atmosphere. For example, Wormsbecher and co-workers[21] worked with nitrogen as a carrier gas using a similar experimental arrangement to ourselves (Section 4.5), Maugé and co-workers[2] worked with air as a carrier gas, again in a fluidised arrangement, and Breck and Skeels[22] steam-treated under a static atmosphere using a conventional oven (the steam was passed directly over shallow beds of zeolite sample).

Pompe and co-workers[23] working with an experimental arrangement which involved a complex cycle of reducing (CH_4) and oxidising (air) atmospheres, to simulate both the riser-cracker and regenerator part of the FCCU, suggested the role of 'extra oxygen', and its origin, was important in the mechanism of vanadium-induced destruction of the zeolite-Y lattice. Working with mixtures of V_2O_5 and RE-Y type zeolites, they proposed that V_2O_5 attacks the RE component of the zeolite-Y forming a low melting RE-vanadate. The formation of vanadate requires more oxygen than the V_2O_5 can supply and so it was proposed that the extra oxygen needed for this reaction could derive from the zeolite-Y lattice; in other words vanadate formation leads to the loss of zeolite-Y crystallinity. It should be noted that lanthanum vanadate formation has been observed in the present work and this important observation will be discussed further in Section 5.2.3. As already stated our results show that steam treatment at 750/5/80/N_2 has benefits in terms of retention of zeolite-Y crystallinity over treatments at 750/5/80/AIR. It is feasible that the difficulty of forming $LaVO_4$ in the nitrogen atmosphere is related to this observed retention of zeolite-Y crystallinity.

5.2.3 Further Results and Discussion

Overall the results for the model series of samples based on zeolite-Y are similar to those observed for the commercial FCC samples (Section 5.1). This strongly supports the view that zeolite-Y by itself is a useful model for investigating the behaviour of the more complex commercial catalyst. For both types of catalyst it has been observed that, (1) increasing vanadium loading results in a loss of zeolite-Y crystallinity, (2) increasing temperature also results in a loss of zeolite-Y crystallinity and (3) an increase in RE (lanthanum for the model zeolite-Y samples) ion-exchange level increases the resistance of the zeolite-Y to destruction in the presence of steam.

The relationship that exists between RE ion-exchange level and vanadium loading is relatively complex and this is further complicated by the fact that each of the differently RE ion-exchanged samples have different stabilities with respect to one another; that is, steam treatment, in the absence of vanadium, results in samples which contain differing amounts of crystalline material. This can be confirmed, for example, by the zeolite-Y results in Figure 5.11 (a). The plot of surface area versus lanthanum ion-exchange level clearly shows that increased lanthanum ion-exchange level results in increased surface area, or increased amounts of crystalline zeolite-Y. To summarise, each of the lanthanum ion-exchanged samples has a different base stability towards steam, and this stability increases with increasing lanthanum ion-exchange level. This behaviour needs to be taken into account when considering the results for samples steam treated in the presence of vanadium.

In general it has been demonstrated that an increase in vanadium level results in loss of zeolite-Y crystallinity (Figure 5.14). This loss of crystallinity will depend upon both the effects of steam treatment and the influence of vanadium. It is of direct interest to explore the consequences of assuming that these two factors are largely independent of one another: in other words to assume that any loss of zeolite-Y crystallinity due to steam treatment will be the same irrespective of whether vanadium is present or not. Surface area measurements can be used for this purpose. In particular the difference between the surface area of a steam-treated sample with no vanadium present and that for a sample

contaminated with a given amount of vanadium, will provide an operational measure of the effect of the presence of vanadium alone.

It is convenient to consider samples with a 5000 ppm vanadium loading. Figure 5.21 shows a plot of the difference in surface area between samples with no vanadium loading and those loaded with 5000 ppm vanadium as a function of lanthanum ion-exchange level. Results for samples steam treated at 750°C, as well as 800°C, are included in the diagram.

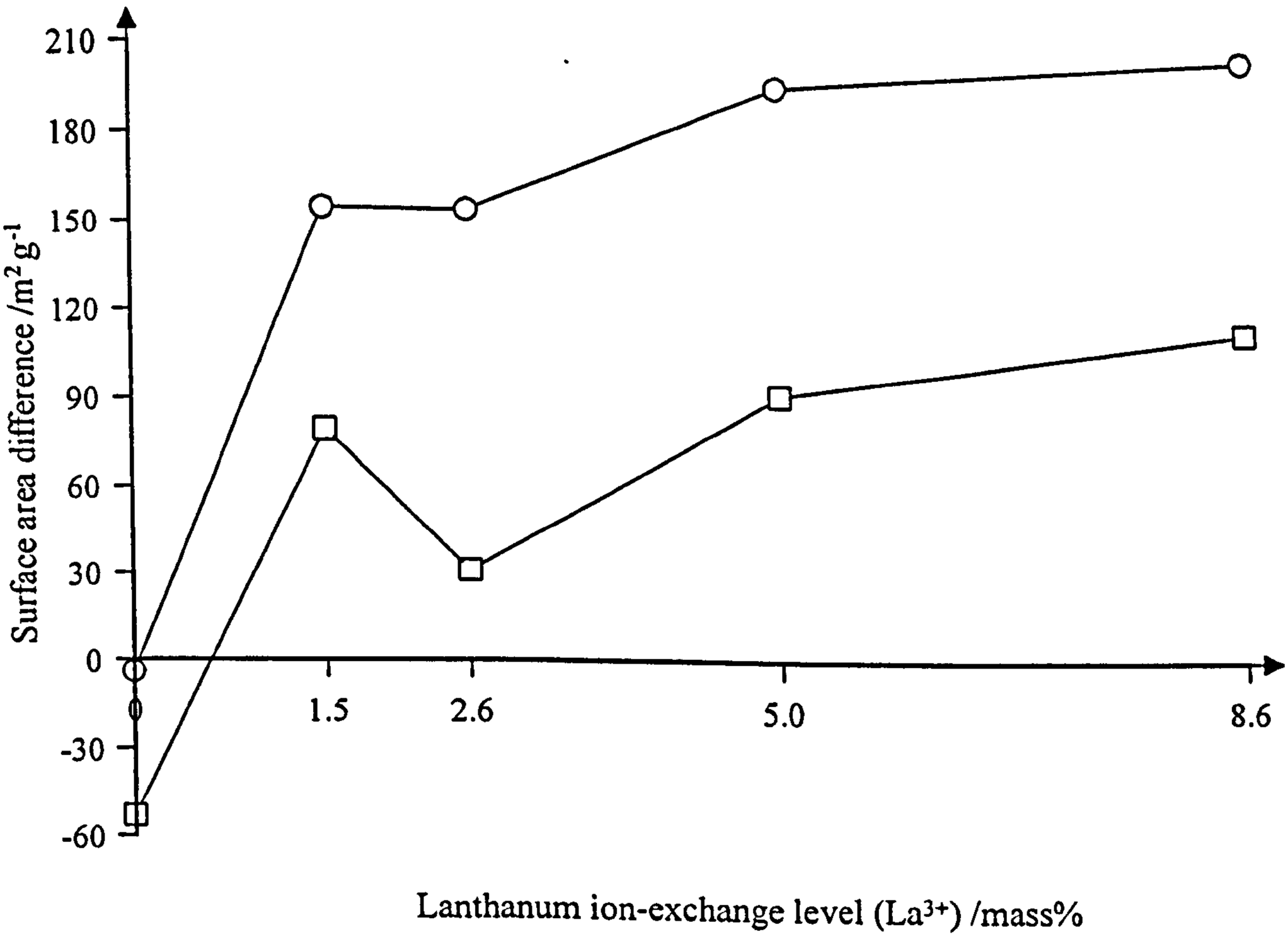

Figure 5.21 A plot of the difference in surface area obtained between samples with no vanadium loading and those loaded with 5000 ppm vanadium as a function of lanthanum ion-exchange level. □ represent steam treatment at 750°C, O steam treatment at 800°C.

The general behaviour at both reaction temperatures is similar and, as expected, there is greater loss of zeolite-Y crystallinity at the higher temperature. The negative values obtained for the H-Y samples arise because of the increase in surface area that was observed upon the introduction of vanadium (Figure 5.14 (a)). As was stated earlier this is

probably due to the recrystallisation of the amorphous material rather than any stabilising effect of the vanadium.

In more detail as the lanthanum ion-exchange level increases at either temperature then so does the amount of destruction caused to the zeolite-Y lattice by the presence of vanadium. However, it is important to note that at both treatment temperatures, but particularly at the lower temperature, the amount of destruction caused to the zeolite-Y lattice for the 2.6LaH-Y sample is distinctly less than might be anticipated from the general trend. This observation is contrary to expectation since REs generally improve the zeolite-Y stability towards thermal and hydrothermal treatment. This behaviour will be discussed in more detail shortly in terms of the more general mechanism to be discussed below.

A possible mechanism for the effect of vanadium on the stability of lanthanum-exchanged zeolite-Y is as follows. Vanadium deposited upon the surface of the zeolite-Y migrates to the lanthanum ions present within the zeolite-Y lattice, a reaction takes place, and the lanthanum is removed from the zeolite-Y in the form of a lanthanum/vanadium compound. This has the effect of removing the stabilising effect that the lanthanum ions provide, so that the zeolite-Y becomes thermally unstable, and lattice collapse proceeds through a thermal/hydrothermal mechanism. In essence this mechanism has features similar to those suggested by Pompe and co-workers.[23] Given that in outline this mechanism is correct then the presence of lanthanum/vanadium compounds would be expected to be observed. With this in mind, ^{51}V MAS NMR spectra were recorded for the 8.6LaH-Y samples contaminated with 15 000 ppm vanadium and steam treated at both 750°C and 800°C (Figure 5.22).

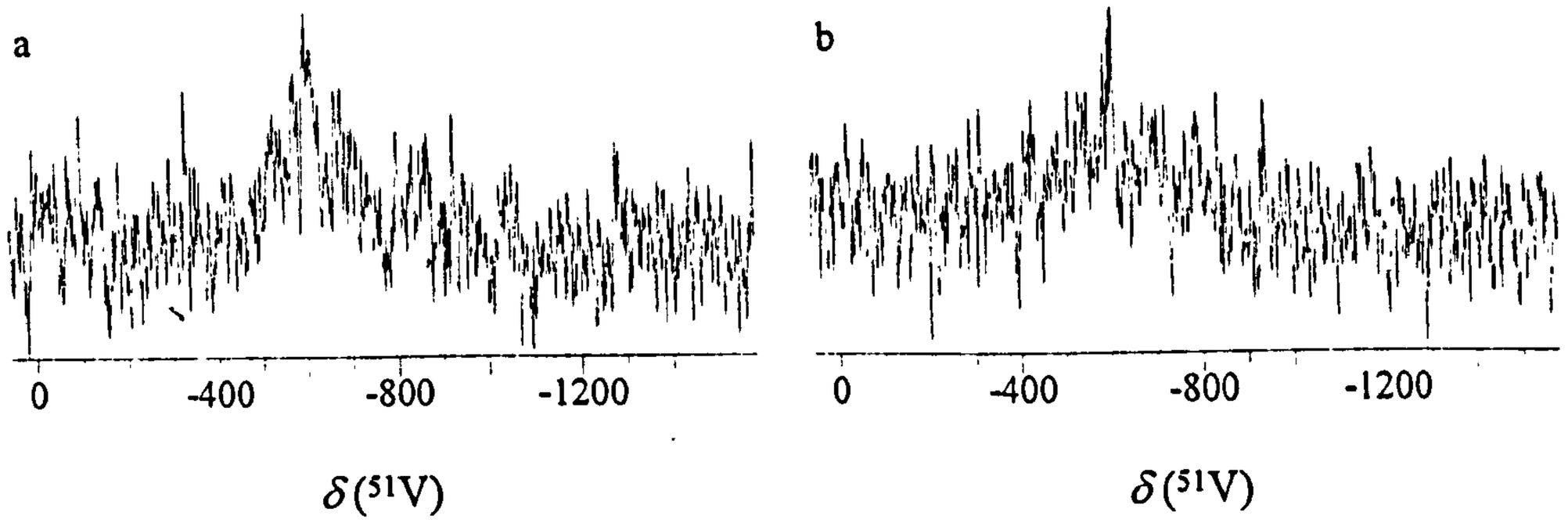

Figure 5.22 ^{51}V MAS NMR spectrum observed at 105.075 MHz. An exponential filter was used prior to Fourier transformation. The spectra were recorded with pulse delay = 1 s, pulse width = 2 μs, spinning frequency ~ 7 kHz and external reference liquid $VOCl_3$. The spectra are for samples of 8.6LaH-Y contaminated with 15 000 ppm vanadium and steam treated for 5 hours using air as a carrier gas (a) 750°C, number of scans = 230 000 and $\delta(^{51}V)$ = -600 ppm, and (b) 800°C, number of scans = 227 000 and $\delta(^{51}V)$ = -607 ppm.

Both spectra have poor signal to noise, even after exponential filtering. This is due to the low amount of vanadium present in these samples. (Increasing the signal to noise by increasing the number of scans was not feasible: a twofold increase would require over 10 days of signal averaging). Spectrum (b), for the 8.6LaH-Y sample steam treated at 800°C, shows the emergence of a single resonance centred at $\delta(^{51}V)$ = -607 ppm. This is in good agreement with the chemical shift for lanthanum vanadium oxide ($LaVO_4$) reported to be $\delta(^{51}V)$ = -610±10 ppm by Lapina and co-workers.[24] A similar resonance also appears at $\delta(^{51}V)$ = -600 ppm for the sample steam treated at 750°C.

In an effort to obtain a 'better resolved' signal the ^{51}V MAS NMR spectrum for a sample of 2.6LaH-Y loaded with 20 000 ppm vanadium and steam treated at 800°C for 5 hours using air as a carrier gas was measured (Figure 5.23). The XRD pattern showed that no zeolitic crystalline material remained after steam treatment, this was also reflected in the surface area result which was found to be 17 m^2g^{-1}.

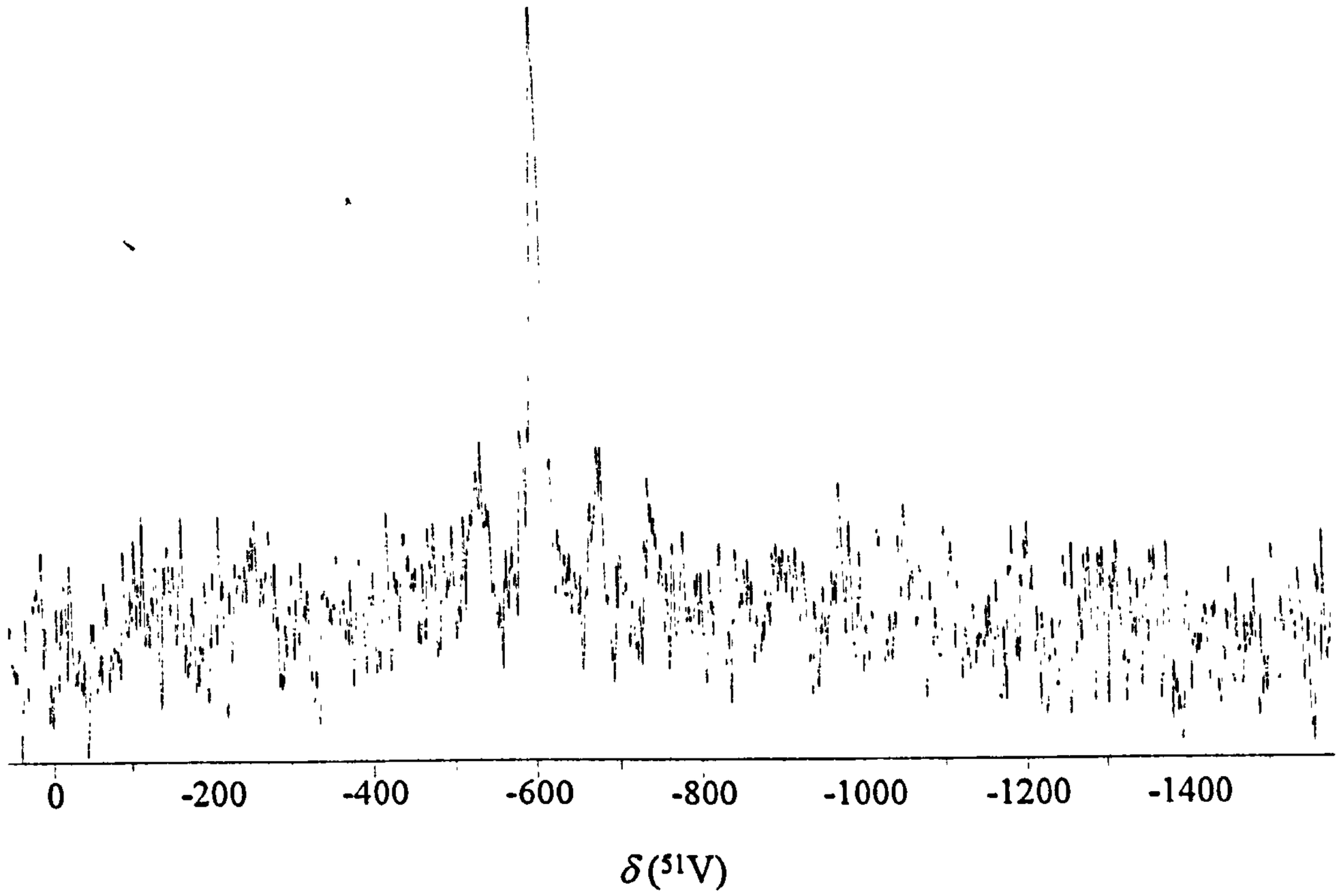

Figure 5.23 ^{51}V MAS NMR spectrum observed at 105.075 MHz. An exponential filter was used prior to Fourier transformation. The spectrum is for a sample of 2.6LaH-Y contaminated with 20 000 ppm vanadium and steam treated at 800°C for 5 hours using air as a carrier gas, and recorded with a pulse delay = 1 s, pulse width = 2 μs, number of scans = 244 000, spinning frequency ~ 7 kHz and external reference liquid $VOCl_3$.
$\delta(^{51}V)$ = -607±8 ppm.

It can be seen that there is a single sharp resonance centred at $\delta(^{51}V)$ = -607±8 ppm. The spectrum has improved to such an extent that sidebands are visible, equally spaced either side of the central transition. The position of the main resonance is in good agreement with that reported for $LaVO_4$[24] and with the less well resolved resonances in Figure 5.22.

As already described in Section 5.2.2, Pompe and co-workers[23] working with mixtures of V_2O_5 and RE-Y type zeolites observed the formation of $LaVO_4$ and concluded that vanadium migrates to the RE component of the zeolite-Y forming a low melting RE-vanadate. It was suggested that the extra oxygen needed for $LaVO_4$ formation came from the zeolite-Y lattice and this was responsible for the reduction in zeolite-Y

crystallinity. It is interesting that RE-vanadates have also been observed by other workers[5,25,26] and have provided the basis for other mechanistic proposals. Maugé and co-workers[25] working with highly-exchanged lanthanum zeolite-Y observed the formation of $LaVO_4$ upon hydrothermal treatment in the presence of vanadium. They also recognised the need for additional oxygen for $LaVO_4$ formation, but in contrast to the proposals put forward by Pompe and co-workers[23], suggested that the extra oxygen would come from the stabilising La-O(H)-La links across zeolite cages (Section 2.2.1). RE complexes are thought to give RE exchanged zeolites added thermal stability[27,28] and removal of these linkages would lead to thermal instability and, hence, increased destruction of the zeolite. Anderson and co-workers[26] observed the formation of $EuVO_4$ for vanadium contaminated europium-exchanged zeolite-Y and Occelli,[5] working with a commercial CREY type catalyst (mixed RE source), reported the formation of $CeVO_4$. In both cases mechanisms were put forward which mirrored the proposals put forward by Maugé and co-workers.[25]

If the formation of $LaVO_4$ is important in the mechanism by which vanadium interacts with RE stabilised zeolite-Y then it could be argued that the accessibility of vanadium to lanthanum (or vice versa) will be a critical factor. In a very simplified picture, if it is assumed that there is an even distribution of lanthanum throughout the zeolite-Y lattice, then the probability of any given vanadium species contacting and reacting with a lanthanum ion will increase as the lanthanum ion-exchange level for the zeolite increases. This increase would not be expected to be linear since there would come a point when lanthanum was in such excess that all vanadium would react. This picture is consistent with the general trend depicted in Figure 5.21 with a 'plateau' region emerging at high lanthanum ion exchange levels. The position of this plateau will depend upon the vanadium concentration, with an increase in vanadium concentration causing the plateau to move to higher lanthanum ion-exchange levels.

The simple picture developed above, however does not explain the behaviour in the region up to 2.6 mass% ion-exchange level for lanthanum. In this case it is interesting to consider the number of lanthanum ions per unit cell. Table 5.8 gives the calculated number of La^{3+} ions per unit cell for zeolite-Y for each of the differently lanthanum ion-exchanged

samples. These values are subject to uncertainty since a fully dehydrated zeolite-Y was assumed for the purposes of the calculation.

Sample	Approximate number of La^{3+} ions per unit cell (±1)
1.5LaH-Y	1
2.6LaH-Y	2
5.0LaH-Y	5
8.6LaH-Y	8

Table 5.8 The approximate number of La^{3+} ions per zeolite-Y unit cell for each of the differently lanthanum ion-exchanged samples.

It can be seen for the 1.5LaH-Y sample that, statistically, there is only one lanthanum ion per unit cell. Maugé and co-workers[2] gave evidence for a dimeric lanthanum complex which bridges across sodalite cages involving bridging hydroxyls and framework oxygens (Figure 2.7). The presence of such a species was proposed to account for the fact that RE-exchanged samples showed superior thermal stability over other ion-exchanged forms of zeolite-Y. Clearly for the 1.5LaH-Y samples the presence of such complexes would be limited due to the probability of there only being one lanthanum ion per unit cell. Interestingly, for the 2.6LaH-Y sample it can be seen that on a statistical basis, there are approximately two lanthanum ions per unit cell, so the possibility of at least one of these complexes per unit cell is increased. The behaviour observed in Figure 5.21, may reflect, therefore, the fact that below approximately 2.6 mass% lanthanum ion-exchange level the vanadium has a relatively greater effect on the zeolite-Y lattice. Above this value the presence of two or more lanthanum ions per unit cell mitigates the effect of the vanadium. In other words as the lanthanum ion-exchange level becomes greater than 2.6 mass% stability is favoured by the formation of a dimeric species of lanthanum. This type of observation has not been made previously in the literature, although it must be remembered that it rests on the assumption that the effect of steam treatment and vanadium contamination are largely independent of one another.

Figure 5.24 presents the surface area difference for the commercial FCC samples in the same manner as that for the model zeolite-Y surface area data. The graph contains data for vanadium loadings of 2000 ppm (□) and 4000 ppm (■) vanadium at 788°C. The values in parentheses give the RE concentration in terms of RE^{3+}, for comparison with the La^{3+} concentrations used in the zeolite-Y model system. These values must be regarded as approximate since, in the absence of any further information, the relative molecular mass of an RE^{3+} ion was assumed to be 139.

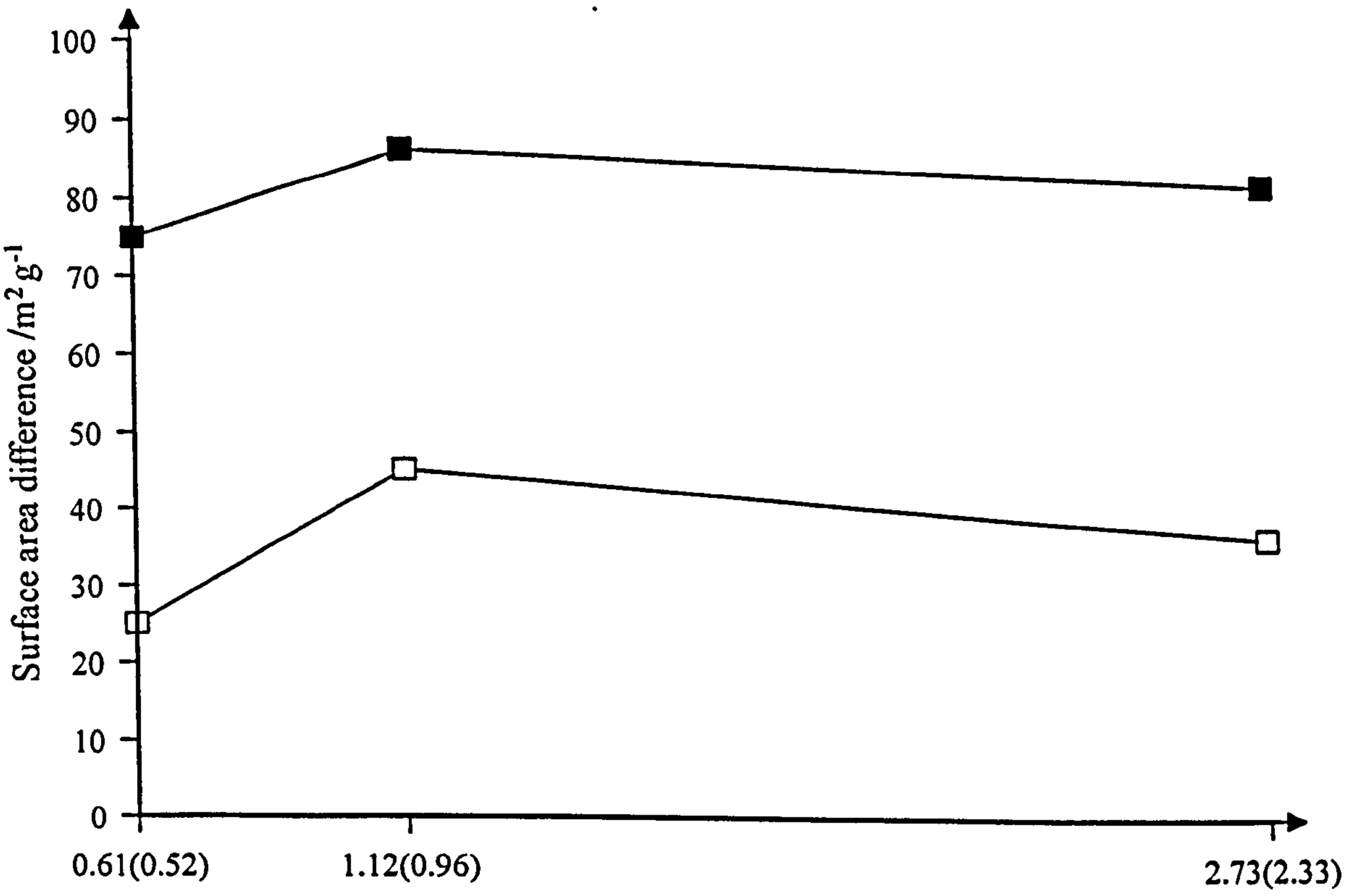

Figure 5.24 A plot of the difference in surface area obtained by taking away the surface area of the steam treated commercial FCC samples contaminated with 2000 ppm vanadium (□) and 4000 ppm vanadium (■) from the surface area of the steam-treated vanadium free samples. □ and ■ represent steam treatment at 788°C. The values in parentheses give the approximate RE concentration in terms of RE^{3+}, for comparison with La^{3+} concentrations used in the zeolite-Y model systems.

The rare earth concentrations incorporated into these FCC samples are typical of the lower La^{3+} concentrations incorporated in the model zeolite-Y samples. The shape of the curves generated from the simple model are similar, in terms of trends, to those presented for the model zeolite-Y samples. The results show an increase in the amount of destruction caused to the zeolite-Y lattice as the RE loading is increased, then a decrease as the number of RE^{3+} ions per unit cell approaches two.

In conclusion, a mechanism has been suggested to explain the loss of zeolite-Y crystallinity due to the presence of vanadium. The mechanism involves the removal of the RE ions, and hence the stabilising effect of these ions, by vanadium. It is supported by the observation of $LaVO_4$ within samples after hydrothermal treatment in the presence of vanadium. Further discussion of this mechanism is given in Chapter 6. It should also be noted that investigations, centred around changing the experimental conditions, rather than catalyst composition, have provided information regarding vanadium species responsible for the loss of zeolite-Y crystallinity. Results have shown that decreasing the temperature, decreasing the steam to carrier gas ratio and working under a nitrogen atmosphere all have benefits with regard to the retention of zeolite-Y crystallinity.

5.3 Retention of Zeolite-Y Crystallinity

In view of the results, and observations, drawn from the studies of the commercial FCC and model zeolite-Y systems, a series of experiments were designed to investigate whether the loss of zeolite-Y crystallinity in the presence of vanadium could be controlled. A key component of the investigation was to deposit RE ions onto the surface of the catalyst prior to contamination with vanadium and steam treatment. In this way it could be investigated whether an 'extra' source of RE could react directly with vanadium and so prevent vanadium/zeolite-Y interaction. Two different RE ions (lanthanum and cerium) were used in the experiments which were based on the commercial FCC catalyst alpha-56. Full details of the procedures used for the preparation and steam treatment of the samples can be found in Chapter 4.

5.3.1 Alpha-56 Prior to Steam Treatment

The level of vanadium contamination was chosen to be high (10 000 ppm) such that without any protection the zeolite-Y crystallinity would be substantially destroyed. The results of the vanadium experiments are summarised in Table 5.9. This table gives the mass percentage and source of the RE ions deposited onto the FCC catalyst, as well as the computed unit cell constant determined for a given sample prior to steam treatment. To avoid any confusion in future discussion the REs deposited upon the surface of a catalyst sample will be referred to as 'free' in order to distinguish them from the RE ions which are ion-exchanged into the zeolite-Y.

Vanadium loading /ppm	Free rare earth loading /mass%	Rare earth source	Unit cell constant /Å (±0.04Å)
0	0	-	24.67
10 000			24.67
0	1.0	$LaCl_3$	24.65
10 000			24.67
10 000	2.0	$LaCl_3$	24.66
	1.0	$La(NO_3)_3$	24.67
	1.0	$CeCl_3$	24.68

Table 5.9 Details of the experiments carried out for the commercial alpha-56 catalyst, including the computed values of unit cell constants prior to steam treatment.

A selection of XRD patterns for the samples contaminated with 10 000 ppm vanadium, and prior to steam treatment are given in Figure 5.25 (the XRD patterns for samples with no vanadium did not significantly differ from these). All of the XRD patterns in the figure are similar although there is some evidence that the samples which had free REs deposited upon their surfaces do show small reductions in levels of the zeolite-Y component ((b), (c),

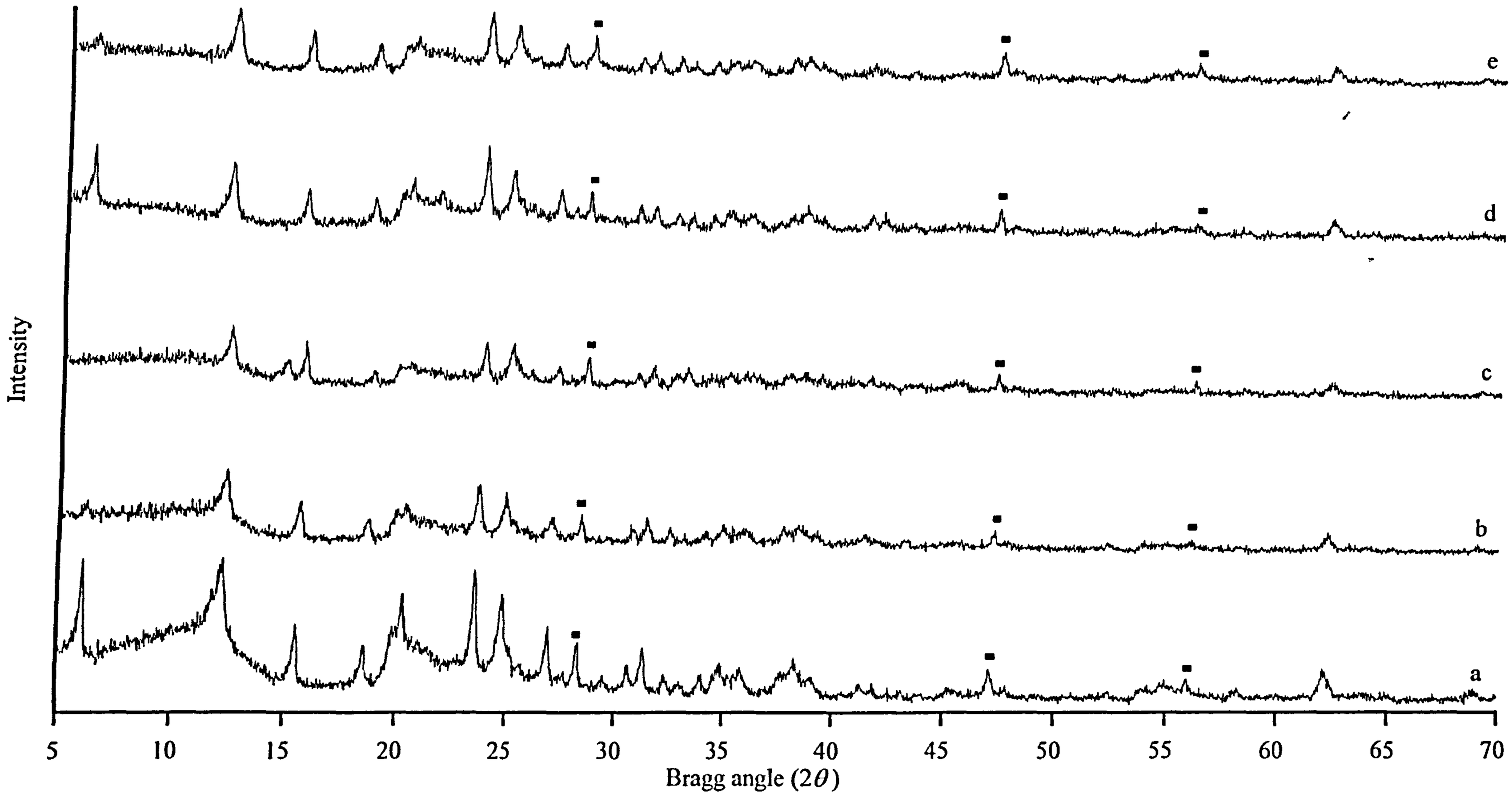

Figure 5.25 XRD patterns recorded for alpha-56 contaminated with 10 000 ppm vanadium (a) alpha-56 without free rare earths, (b) alpha-56 loaded with 1.0 mass% lanthanum from $LaCl_3$, (c) alpha-56 loaded with 2.0 mass% lanthanum from $LaCl_3$, (d) alpha-56 loaded with 1.0 mass% lanthanum from $La(NO_3)_3$ and (e) alpha-56 loaded with 1.0 mass% cerium from $CeCl_3$. ■ labels the diffraction peaks for the silicon standard.

(d) and (e)). However, the surface areas of the untreated samples were not determined in order to prevent contamination of the surface area equipment, therefore, this reduction could not be quantified. It can be noted that there is also the appearance of a diffraction peak at 14.5°, in 2θ, for the sample loaded with 2.0 mass% lanthanum (c). This is not related to the zeolite-Y phase and the phase responsible for this new diffraction peak could not be identified using the JCPDS data base; although it is reasonable to suggest that it contains lanthanum.

Since the RE ions were deposited upon the surface of the catalyst from an aqueous solution it is possible that ion-exchange into the zeolite-Y lattice could occur. This would change the characteristics of the catalyst samples as well as lowering the surface concentration of free RE. However, if large-scale ion-exchange had occurred then this would be expected to cause increases in the unit cell constant. It can be seen from Table 5.9 that the changes, if any, in the unit cell constant are small and certainly within the limits of experimental error. It is reasonable to suggest that the majority of the deposited REs are present upon the surface of the catalyst and any ion-exchange is relatively minor.

5.3.2 Alpha-56 following Steam Treatment

The main experimental work involved steam treatment of the samples under standard conditions, (that is, steam treatment at 750°C and 800°C for 5 hours using air as a carrier gas), although a limited parallel investigation was undertaken where the atmosphere was changed from air to nitrogen. A series of control experiments were also performed in order to evaluate any changes to the FCC samples due to the deposition of REs. The surface area and unit cell constant data obtained for the steam-treated samples of the control experiments together with a series of free RE-loaded samples are given in Table 5.10. These results will be referred to in the discussion that follows.

Reaction conditions	Vanadium loading /ppm	Surface rare earth loading /mass%	Rare earth source	Unit cell constant /Å (±0.04Å)	Surface area /m^2g^{-1} (±10%)
Untreated	0	0	-	24.67	228
750/5/80/AIR				24.43	184
800/5/80/AIR				24.37	165
Untreated	10 000			24.67	-
750/5/80/AIR				24.33	52
800/5/80/AIR				-[a]	13
Untreated	0	1.0	$LaCl_3$	24.67	-
750/5/80/AIR				-	173
800/5/80/AIR				-	146
Untreated	10 000			24.65	-
750/5/80/AIR				-	147
800/5/80/AIR				-	95

[a] Insufficient crystalline material remained for a unit cell constant determination for the alpha-56 sample contaminated with 10 000 ppm vanadium and steam treated at 800°C.

Table 5.10 Surface area and unit cell constant data for steam-treated alpha-56 samples.

As a first step it is important to consider how the alpha-56 catalyst responds to a vanadium loading as high as 10 000 ppm. Figure 5.26 gives the XRD patterns recorded for four of the samples in Table 5.10: these are, samples with and without vanadium contamination, and steam-treated at both 750°C and 800°C for 5 hours using air as a carrier gas. These patterns are plotted with the same intensity scale (this approach is also used for all of the other figures involving XRD patterns in this section: Figures 5.26 to 5.30). It can be recalled from Section 3.1.3 that this allows direct comparison of peak intensities (area under the peaks) for the differently treated samples and gives an approximate 'by eye' method for assessing the amount of crystalline zeolite-Y material remaining in each sample. It can be seen that the steam-treated alpha-56 sample behaved as would be

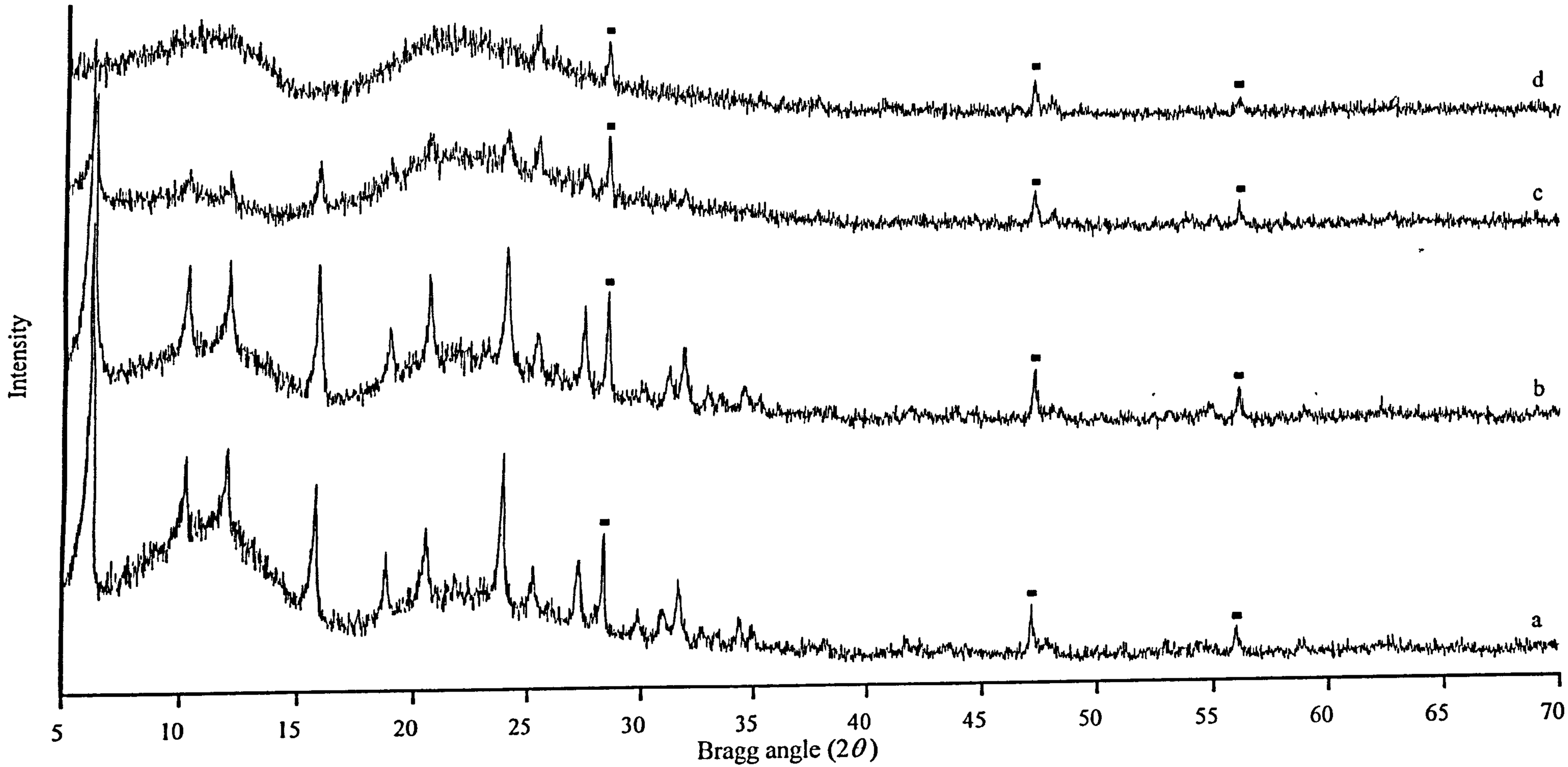

Figure 5.26 XRD patterns recorded for alpha-56 steam treated at (a) 750°C, without vanadium contamination, (b) 800°C, without vanadium contamination, (c) 750°C, contaminated with 10 000 ppm vanadium and (d) 800°C, contaminated with 10 000 ppm vanadium. ■ labels the diffraction peaks for the silicon standard. The XRD patterns are plotted with the same intensity scale.

predicted (c.f. the results in Section 5.1). Reductions in zeolite-Y crystallinity are observed with an increase in temperature, and upon the introduction of vanadium. Furthermore it is apparent that 10 000 ppm vanadium causes considerable damage to the zeolite-Y lattice. This destruction is also very clearly seen in the surface area data (Table 5.10). The unit cell constant data follows the expected trends: steam treatment resulting in a general decrease in the unit cell constant, with additional decreases observed as the reaction temperature is increased and upon the introduction of vanadium.

The steam treatment of alpha-56 in the presence of 1.0 mass% free lanthanum, but with no vanadium contamination, can now be considered. The XRD patterns recorded for the samples steam treated at 750°C and 800°C for 5 hours using air as a carrier gas are given in Figure 5.27. Steam treatment in the presence of free lanthanum clearly results in the formation of new crystalline phases. It can also be noted that in both patterns the relative intensity of the diffraction peak at 23.7° in 2θ, which is due to the zeolite-Y component, is much larger than would be expected given the intensities of the other zeolite-Y diffraction peaks. (In this context it is useful to compare with the XRD patterns recorded for samples without any surface lanthanum, that is Figure 5.26 (a) and (b)). It seems likely that one of the additional phases present has a significant diffraction peak in the region of 23.7°, in 2θ, and that this is augmenting the zeolite-Y diffraction peak. As will be discussed later there is evidence that suggests this phase is more likely to be due to a form of crystalline aluminosilicate rather than a lanthanum-containing phase.

Overall the XRD patterns appear to indicate that in the presence of free lanthanum there is a significant reduction in zeolite-Y crystallinity. However, the surface areas measured for the two samples were found to be similar and directly comparable in magnitude to that determined for the alpha-56 sample with no free lanthanum. This apparent discrepancy between the two types of measurement is surprising. One possibility is that the surface area measurements are influenced by other crystalline components that are formed on steam treatment.

At least four new phases can be observed for the alpha-56 samples treated with free lanthanum; the diffraction peaks for these phases are labelled in the XRD patterns in

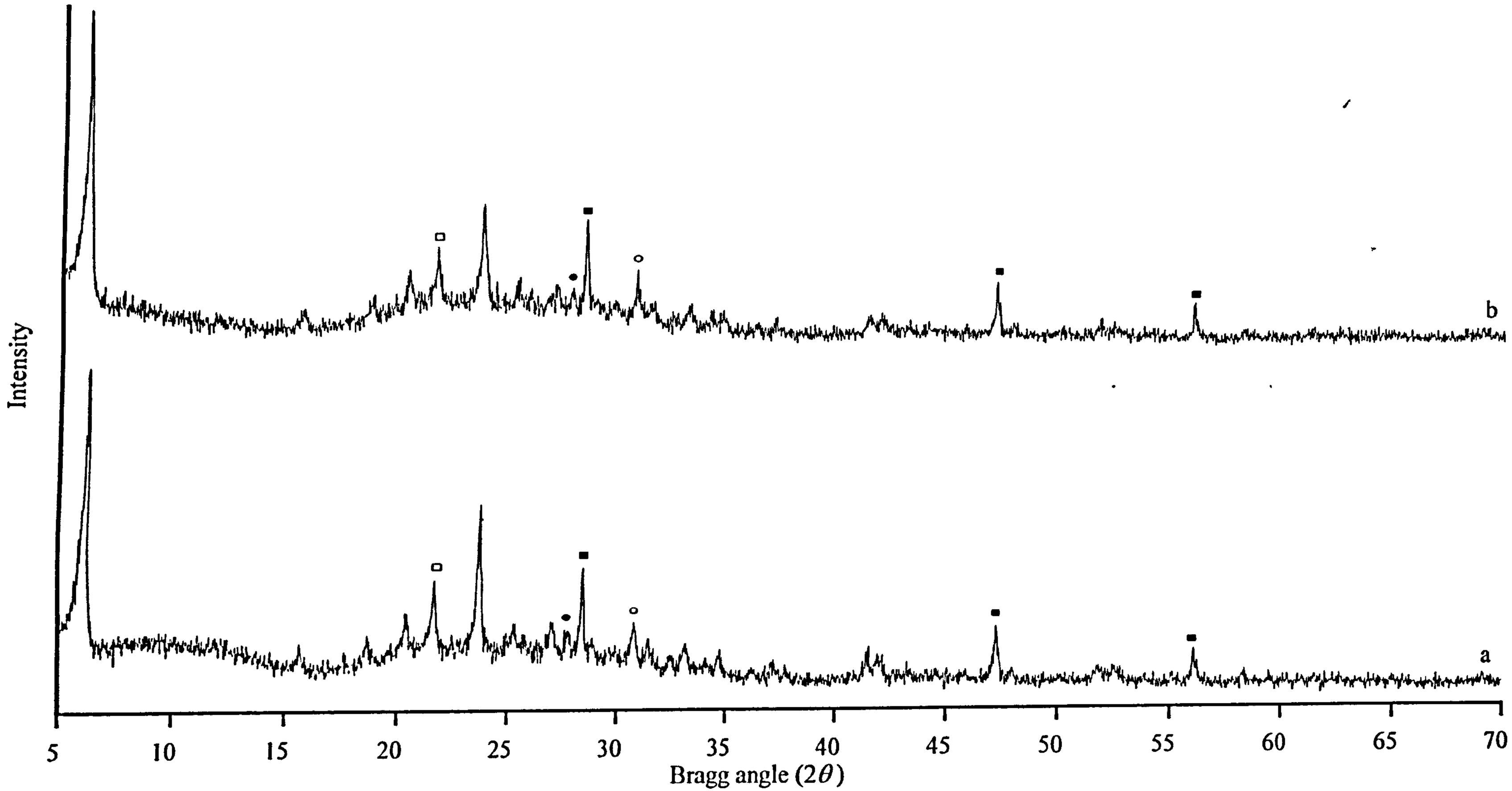

Figure 5.27 XRD patterns recorded for alpha-56 loaded with 1.0 mass% lanthanum from $LaCl_3$ and steam treated at (a) 750°C and (b) 800°C for 5 hours using air as a carrier gas. □ labels the diffraction peaks due to a cubic silica phase, ○ labels diffraction peaks due to La_2O_3, ● labels the diffraction peaks due to an unknown phase and ■ labels the diffraction peaks for the silicon standard. The XRD patterns are plotted with the same intensity scale.

Figure 5.27. The phase with a diffraction peak at 23.7° in 2θ could not be positively identified, although, it is worth noting that an aluminosilicate, JCPDS reference No. 39-1380, corresponding to $AlSi_{0.5}O_{2.5}$ has a strong diffraction peak at this Bragg angle and, given the relative intensity of the other diffraction peaks in the XRD pattern of this material, only the diffraction peak found at 23.7° would be visible. Results presented later in this section indicate that this unknown phase is unlikely to contain RE elements. A further phase (diffraction peak labelled ● 27.5° in 2θ) could also not be positively identified. This phase was found to be absent for samples treated in the presence of free cerium as described later.

The phase present in the steam treated samples with diffraction peaks labelled □ is possibly due to a cubic silica phase (JCPDS reference No. 27-0605). The formation of such a phase is interesting, since it is also one of the major products, together with mullite, observed when a sample of alpha-54 is completely degraded by severe heat treatment (1400/48/AIR) as described later in Section 5.4.1 (Figure 5.35). Similarly the same silica and mullite phases were also observed when the clay component of the catalyst was treated at 1400/48/AIR. The formation of this cubic silica phase has also been observed for silica (quartz) support materials loaded with 9.5 mass% lanthanum and calcined under a nitrogen atmosphere; it was not observed for steam-treatment under a nitrogen atmosphere, nor was it observed for treatment under air. Similarly it was not observed when both surface lanthanum and vanadium were both present.

Overall it seems that the presence of free lanthanum may be promoting the formation of cubic silica; although it is not clear where the material needed for the formation of this phase originates. An additional investigation, using just the clay component of the catalyst, was undertaken to see if the material needed for the formation of the phase originated from the non-zeolitic components of the catalyst, rather than from the zeolite-Y component. Two experiments were performed, steam treatment of the clay component at 800°C for 5 hours using air as a carrier gas both with, and without, the presence of 1.0 mass% free lanthanum. The two XRD patterns obtained were identical and the formation of the cubic silica phase was not observed indicating that the non-zeolitic components are not important. It is possible that the formation of the cubic silica phase may result from

'degraded' zeolite-Y: for example, if the surface lanthanum reacts with zeolite-Y to form an aluminosilicate, as suggested earlier, then free 'silica' may recrystallise to form a cubic phase.

The formation of lanthanum oxide, La_2O_3, (peaks labelled O, Figure 5.27) provides good evidence that a large portion of the lanthanum deposited upon the surface of the FCC catalyst remains on the surface and ion-exchange remains at a minimum. If large scale ion-exchange had resulted from the experimental procedure then levels of free lanthanum, on the surface of the catalyst, would be expected to be below the detection limits of the XRD diffractometer. This phase has also been observed on silica support materials loaded with 9.5 mass% lanthanum and steam treated under identical conditions (Section 5.4.3).

It finally remains to consider the effect of vanadium in the presence of free lanthanum. XRD patterns recorded for the alpha-56 sample loaded with 1.0 mass% free lanthanum and 10 000 ppm vanadium and steam treated at 750°C ((a) and (c)) and 800°C ((b) and (d)) for 5 hours under both an air ((a) and (b)) and a nitrogen ((c) and (d)) atmosphere are given in Figure 5.28. Considering the samples steam treated under an air atmosphere ((a) and (b)), it can be seen that an additional diffraction peak, at 26°, in 2θ, (labelled ▲) is observed compared with the free lanthanum-loaded samples steam treated in the absence of vanadium (Figure 5.27). This diffraction peak can been assigned to the formation of mullite. This is not an unexpected result since it is known that vanadium acts as a mineralising agent for the formation of mullite,[5] and mullite formation has been observed for zeolite-Y samples when steam treated in the presence of vanadium in this work (Figure 5.13 (d)). Diffraction peaks due to zeolite-Y are still present, and as anticipated, a reduction in their relative intensity is observed as the temperature is increased. The presence of diffraction peaks due to zeolite-Y indicates that the presence of free lanthanum does control to some extent the destructive effect of vanadium towards zeolite-Y. The zeolite-Y diffraction peaks are less well-defined than those for the corresponding alpha-56 sample steam treated in the absence of vanadium (Figure 5.27), indicating that the free lanthanum species are not 100% efficient at preventing the vanadium-induced destruction of the zeolite-Y lattice. However, the diffraction peaks for the sample steam treated at

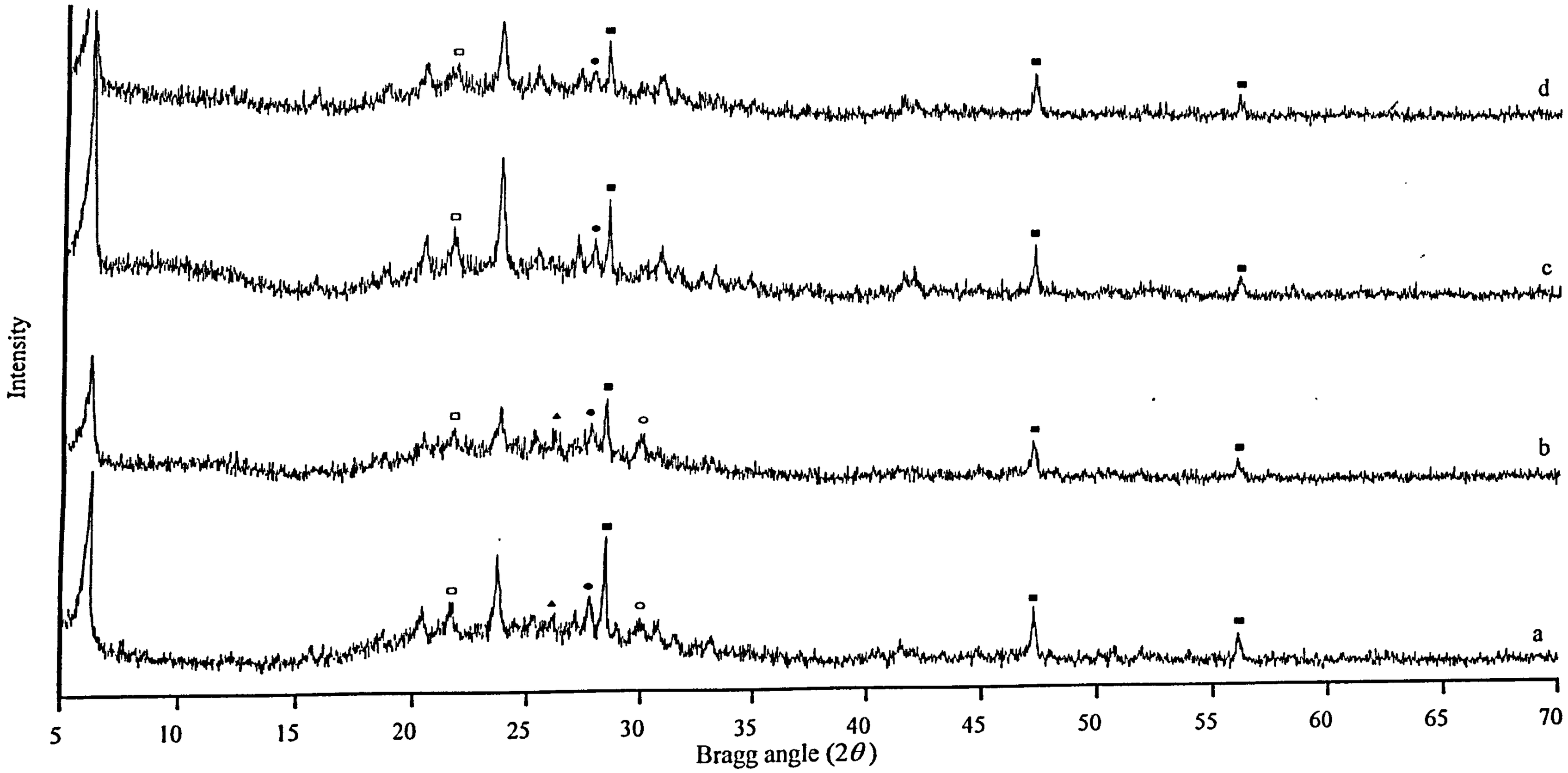

Figure 5.28 XRD patterns recorded for alpha-56 loaded with 1.0 mass% free lanthanum, contaminated with 10 000 ppm vanadium and steam treated at (a) 750°C and (b) 800°C for 5 hours using air as a carrier gas, and (c) 750°C and (d) 800°C for 5 hours under a nitrogen atmosphere. □ labels the diffraction peaks due to a cubic silica phase, O labels diffraction peaks due to La_2O_3, ● labels the diffraction peaks due to an unknown phase, ▲ labels the diffraction peaks due to mullite and ■ labels the diffraction peaks for the silicon standard. The XRD patterns are plotted with the same intensity scale.

800°C (Figure 5.28 (b)) are significantly larger in area than for the sample steam treated without free lanthanum species but in the presence of vanadium (Figure 5.26 (d)). This is clear evidence that the presence of free lanthanum species does offer the zeolite-Y lattice some protection from vanadium. It can also be seen that there is a reduction in the La_2O_3 (diffraction peaks labelled O) phase for the sample steam treated in the presence of vanadium (Figure 5.28) compared to the samples that were free from vanadium (Figure 5.27), this could be due to the combination of lanthanum with vanadium.

Steam treatment under a nitrogen atmosphere (Figure 5.28 (c) and (d)), does not result in the formation of either mullite or La_2O_3, but it is noticeable that the zeolite-Y diffraction peaks are significantly more intense than the corresponding alpha-56 sample steam treated under an air atmosphere (Figure 5.28 (a) and (b)), at both reaction temperatures. For the model zeolite-Y, 5.0LaH-Y and 8.6LaH-Y (Figure 5.20), it was found that relative increases in zeolite-Y crystallinity were observed at 750°C for steam treatment under a nitrogen atmosphere; by contrast at 800°C similar crystallinity was observed. This may be a function of the lower ion-exchange level (~ 2.33 mass% RE^{3+}) for the commercial sample.

Figure 5.29 gives the two XRD patterns recorded for the alpha-56 sample contaminated with 10 000 ppm vanadium and loaded with 2.0 mass% free lanthanum. The patterns are very similar to those recorded for the equivalent steam-treated samples loaded with 1.0 mass% free lanthanum, although the zeolite-Y concentration is markedly lower. This was anticipated in view of the effect that depositing 1.0 mass% free lanthanum had on the zeolite-Y crystalline lattice.

Changing the source of the lanthanum ions from $LaCl_3$ to $La(NO_3)_3$ had little overall effect upon the steam-treated samples. The XRD patterns obtained were very similar to those obtained for the sample loaded with 1.0 mass% free lanthanum from $LaCl_3$ (Figure 5.28(a) and (b)), both in terms of which phases were present and their relative amounts. Interesting differences were obtained, however, when the RE ion was changed from lanthanum to cerium. Figure 5.30 gives the XRD patterns obtained when a sample of alpha-56 contaminated with 10 000 ppm vanadium and loaded with 1.0 mass% free cerium and

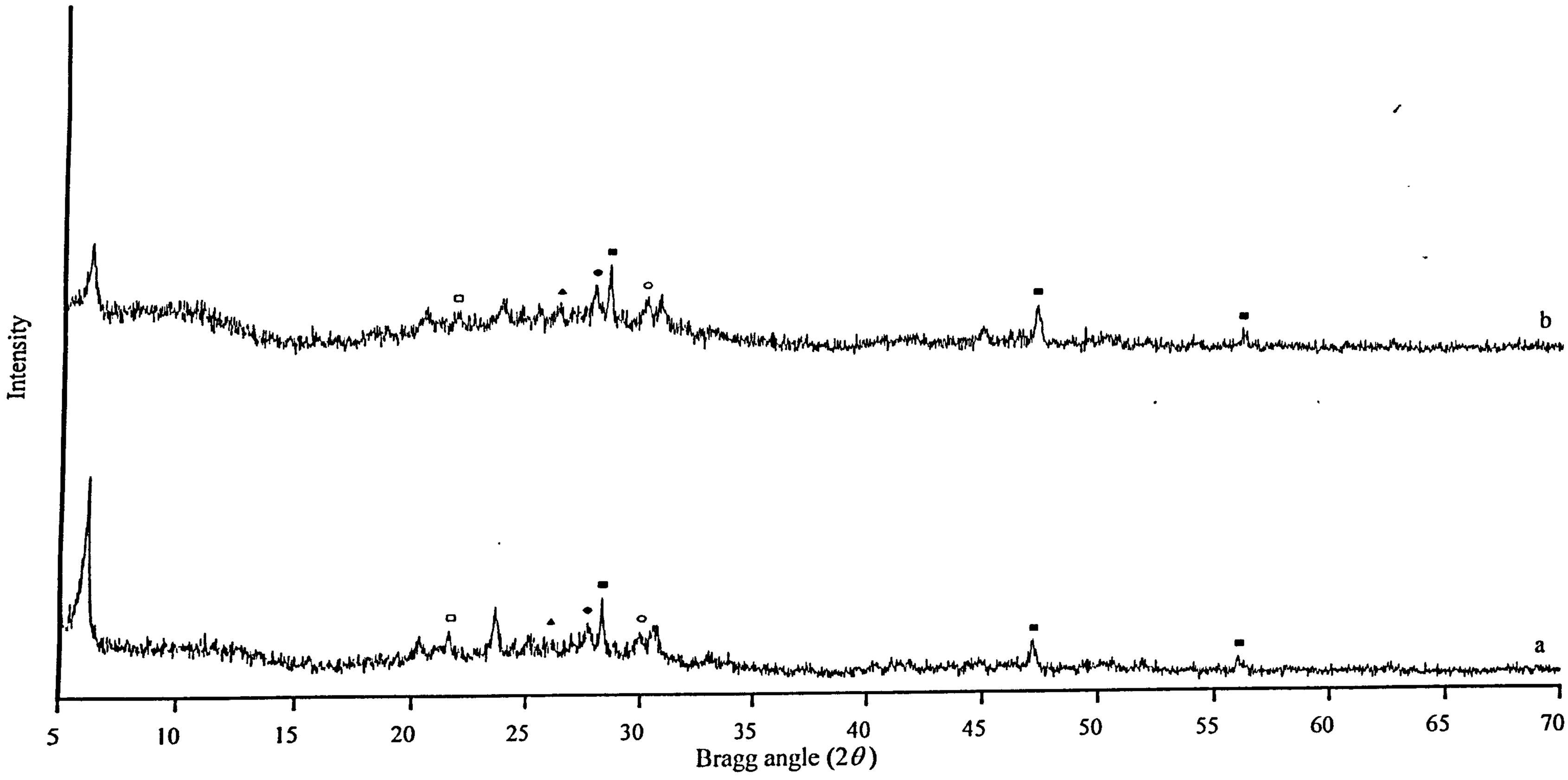

Figure 5.29 XRD patterns recorded for alpha-56 loaded with 2.0 mass% lanthanum from $LaCl_3$, contaminated with 10 000 ppm vanadium and steam treated at (a) 750°C and (b) 800°C for five hours under an air atmosphere. □ labels the diffraction peaks due to a cubic silica phase, ○ labels diffraction peaks due to La_2O_3, ● labels the diffraction peaks due to an unknown phase, ▲ labels the diffraction peaks due to mullite and ■ labels the diffraction peaks for the silicon standard. The XRD patterns are plotted with the same intensity scale.

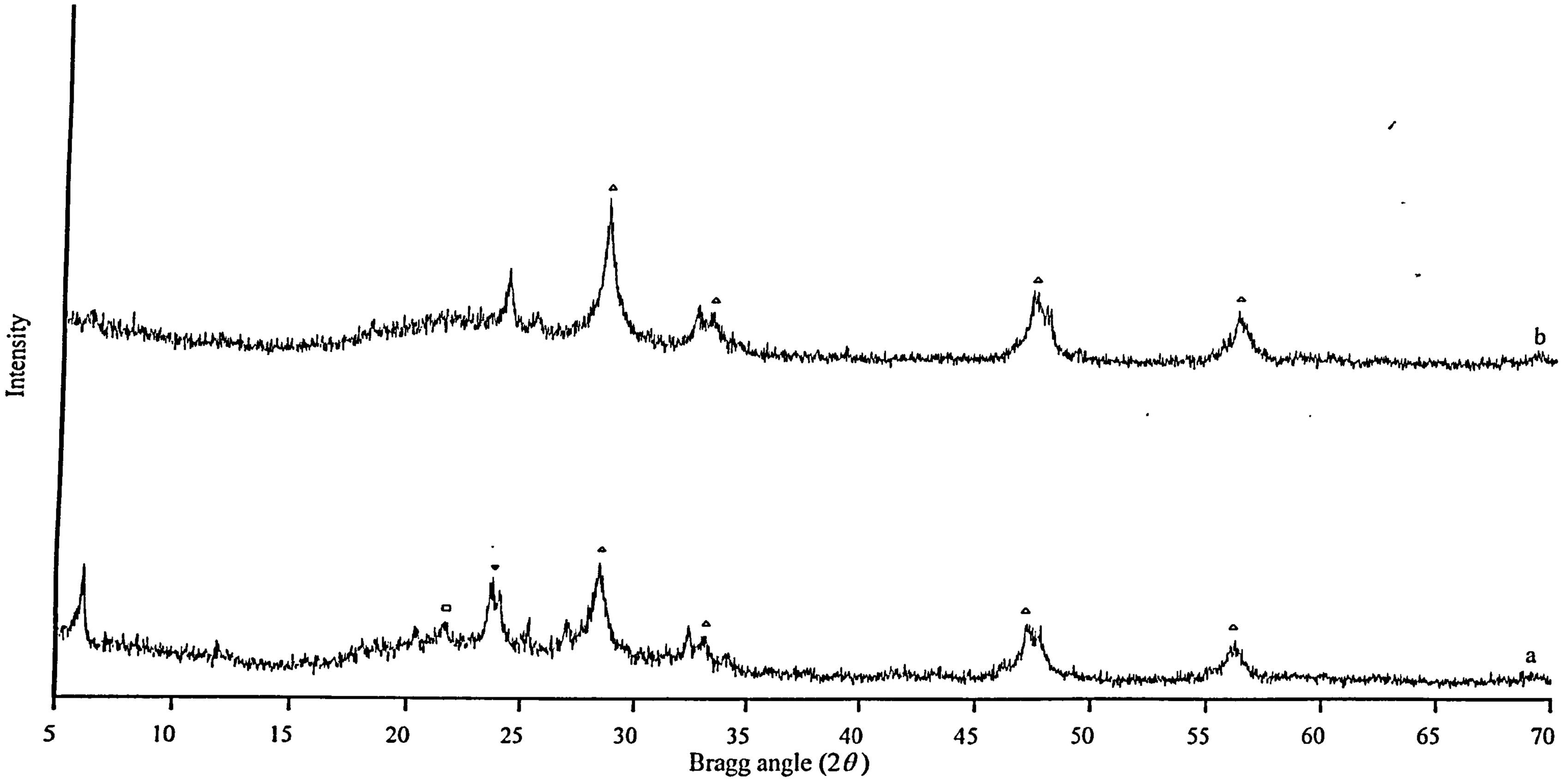

Figure 5.30 XRD patterns recorded for alpha-56 loaded with 1.0 mass% cerium from $CeCl_3$, contaminated with 10 000 ppm vanadium and steam treated at (a) 750°C and (b) 800°C for five hours using air as a carrier gas. □ labels the diffraction peaks due to a cubic silica phase, △ labels diffraction peaks due to CeO_2 and ▼ labels the diffraction peaks due to an unknown phase. The XRD patterns are plotted with the same intensity scale.

steam treated for 5 hours under an air atmosphere. It can be seen that, for both samples, very little crystalline zeolite-Y material remains. This suggests that the presence of free cerium is more detrimental to the zeolite-Y lattice than free lanthanum. Relatively large diffraction peaks due to the formation of cerium oxide (CeO_2) are observed (labelled Δ) and correspond to JCPDS reference file No. 04-0593. There is also the formation of a second phase, which could not be identified, with a diffraction peak (labelled ▼) at 23.5°, in 2θ; this phase was only observed for the sample steam treated at 750°C and was not observed with any of the free lanthanum loaded samples. The relatively strong diffraction peak at 23.7°, in 2θ, still remains with the free cerium-loaded samples which suggest that this phase is more likely an aluminosilicate rather than a RE containing phase. In addition the absence of the diffraction peak ($2\theta = 27.5°$) for the unknown, labelled ●, observed for the lanthanum loaded samples confirms that this peak is due to a separate phase rather than being one of several peaks characterising a particular phase.

5.3.3 Summary

Overall the results demonstrate that significant damage to zeolite-Y crystallinity in a commercial FCC sample is caused by steam treatment in the presence of free REs. Furthermore, steam treatment in the presence of free cerium causes greater loss of crystallinity than similar treatment in the presence of free lanthanum. The loss of zeolite-Y crystallinity, after steam treatment, in the presence of free REs is not fully understood, however, the formation of acids, from reaction of the RE balancing ions with steam, may be responsible for the adverse effects. Zeolite-Y is known to be unstable in strong acidic conditions.[29] The formation of strong acids does not, however, explain why greater loss of zeolite-Y crystallinity is observed in the presence of free cerium. For both the free cerium- and free lanthanum-loaded samples an equivalent number of Cl^- ions are present.

The presence of free lanthanum does, however, have a positive effect (relatively speaking) on the retention of zeolite-Y crystallinity with steam treatment in the presence of vanadium. It is also the case that changing the steaming atmosphere from air to nitrogen further reduces the destructive effect of vanadium. This result does have encouraging

implications for developing a more vanadium tolerant catalyst and is an area which could benefit from further research. It would be useful to determine the role of the RE counter ions (here only chloride (Cl^-) and nitrate (NO_3^-) ions have been used) and it could be that the introduction of REs from an alternative source may produce interesting results. Similarly, investigations into alternative cations and methods of introducing the cations onto the surface of an FCC catalyst would be relevant.

The use of RE containing compounds as effective metal passivators has been reported in patent form by Kumar.[30] His method involved the dispersion of RE oxides or oxychlorides, ideally lanthanum, throughout a clay/alumina matrix. This RE containing particle could then be incorporated in the catalyst particle or added to the FCCU as an additive and work as a dual function cracking catalyst DFCC (Section 2.2.3). It is interesting that this method of dispersing the RE avoids, at least initially, direct contact with the zeolite-Y component of the catalyst. As the present results indicate this would be advantageous to maintaining the crystallinity (surface area) of the zeolite-Y.

Steam treatment in the presence of free REs resulted in the formation of a variety of new crystalline phases: Table 5.11 summarises the phases which were identified after reaction under differing conditions. It can be seen that, for all free lanthanum-loaded samples, treatment at differing reaction temperatures produces similar product distributions and the phases observed are similar for differently prepared samples. Excess lanthanum is stabilised in the form of La_2O_3 and mullite formation is observed in the presence of vanadium. No mullite formation was observed for the sample loaded with free lanthanum from $La(NO_3)_3$, however, the XRD patterns were rather noisy and its observation may have been hindered. Treatment of the free lanthanum-loaded samples under a nitrogen atmosphere only results in the formation of cubic silica. A further phase, which could not be identified, was found to be common to all of the lanthanum-loaded samples.

Significant differences were observed when free cerium was deposited upon the surface. Different product distributions were observed after treatment at 750°C and 800°C. The cerium was stabilised in the form of CeO_2. There was also an additional phase which could not be positively identified.

Free RE loading /mass% and source	Vanadium loading /ppm	Reaction conditions			
		750/5/80/AIR	800/5/80/AIR	750/5/80/N_2	800/5/80/N_2
1.0 $LaCl_3$	0	Cubic SiO_2 La_2O_3	Cubic SiO_2 La_2O_3	×	×
1.0 $LaCl_3$	10 000	Cubic SiO_2 La_2O_3 Mullite	Cubic SiO_2 La_2O_3 Mullite	Cubic SiO_2	Cubic SiO_2
2.0 $LaCl_3$	10 000	Cubic SiO_2 La_2O_3 Mullite	Cubic SiO_2 La_2O_3 Mullite	×	×
1.0 $La(NO_3)_3$	10 000	Cubic SiO_2 La_2O_3	Cubic SiO_2 La_2O_3	×	×
1.0 $CeCl_3$	10 000	Cubic SiO_2 CeO_2	CeO_2	×	×

Table 5.11 Summary of the identified crystalline phases formed on the surface of alpha-56 following deposition of free REs, with and without vanadium, after treatment under differing conditions. Experiments were not carried out for the boxes labelled with crosses.

5.4 Silica and Alumina Support Materials

This section describes results obtained from the steam treatment of both the silica and α-alumina support materials. Samples were prepared with an emphasis on characterising the vanadium/lanthanum chemistry which occurs in the presence of these samples. The results are compared with those from similar experiments for a completely degraded FCC sample.

5.4.1 Samples without Steam Treatment

For both the silica and α-alumina support materials, four different combinations of vanadium/lanthanum were deposited upon the surface of each support material. These combinations were chosen so that particular features of vanadium/lanthanum chemistry could be observed, both with the support material and between the individual vanadium and lanthanum components. Full details of the preparation methods, as for other samples in this section, can be found in Section 4.3.

Alumina support material

Figure 5.31 shows the XRD patterns recorded for four parent samples based upon the α-alumina support material. These samples were then used for subsequent treatment experiments.

Pattern (a) is for α-alumina (corundum) which has been dried at 110°C and is in good agreement with the JCPDS reference pattern No. 10-0173. The same α-alumina phase is present as the major phase in all XRD patterns presented in Figure 5.31.

Pattern (b) is for α-alumina which has had 1 mass% vanadium deposited upon its surface. It can be seen that this pattern is identical to that for α-alumina (Figure 5.31 (a)). This may have been anticipated since vanadium levels of 1 mass% are significantly lower than the 4 mass% detection limits of the X-ray diffractometer. A ^{51}V MAS NMR spectrum

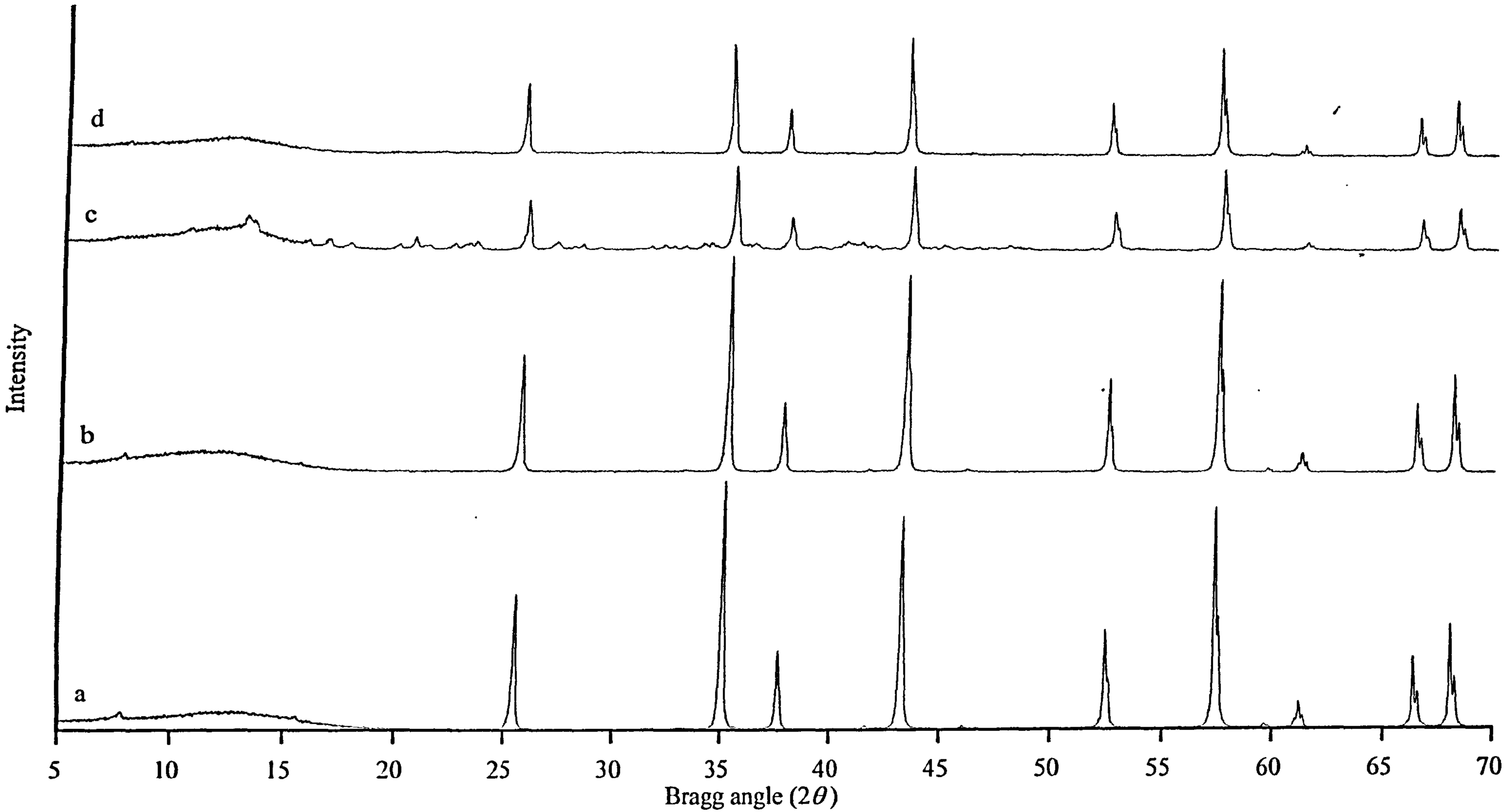

Figure 5.31 XRD patterns recorded for four parent samples based upon the α-alumina support material. (a) α-alumina, (b) α-alumina loaded with 1 mass% vanadium, (c) α-alumina loaded with 11.0 mass% lanthanum, and (d) α-alumina loaded with 1 mass% vanadium and 11.0 mass% lanthanum.

could not be observed for this sample. This is probably due to the vanadium being in the +4 oxidation state at this stage. It has been shown by Anderson and co-workers[31] that vanadyl naphthenate 3% is stabilised as octahedral VO^{2+} species on the surface of a europium-exchanged zeolite-Y, and that the VO^{2+} species was found to be stable even after calcination at 540°C. It seems likely that vanadyl naphthenate 3%, deposited in a similar manner, would also be stabilised as a vanadium (IV) species on the α-alumina.

Vanadium (IV) species are paramagnetic and this will cause severe distortion to the ^{51}V MAS NMR spectrum and, particularly at low concentrations, make such a spectrum unobservable.

For the α-alumina sample with 11.0 mass% lanthanum deposited upon its surface (Figure 5.31 (c)) two observations can be made: first, the emergence of additional diffraction peaks within the XRD pattern and second, a significant reduction in the intensity from the diffraction peaks due to the α-alumina phase. The loss of intensity from the α-alumina phase is an indication of some form of interaction between the deposited lanthanum and the α-alumina, forming new phases. None of the new phases present could be positively identified even after a thorough cross-reference with the JCPDS data base with all combinations of the available elements (La, Cl, Al, O, H). This suggests that no single phase is present but rather an array of phases, all contributing to the new diffraction peaks observed in the XRD pattern (Figure 5.31 (c)).

When both 11.0 mass% lanthanum and 1 mass% vanadium are deposited upon the surface of the α-alumina (Figure 5.31 (d)), the diffraction peaks which were present due to the deposition of lanthanum on the surface (Figure 5.31 (c)) disappear and only the diffraction peaks due to α-alumina remain. The loss of these diffraction peaks suggests that vanadium/lanthanum interactions are occurring even under the relatively mild preparation conditions (Section 4.3). The vanadium/lanthanum compounds are not visible in the XRD pattern because either their levels are below the detection limits of the X-ray diffractometer or they may be amorphous and, as a result, invisible to the XRD technique. The ^{51}V MAS NMR spectrum of this sample (Figure 5.32) shows a single broad resonance centred at $\delta(^{51}V) = -615$ ppm. The signal is very weak (the signal to noise is approximately ~2:1) but nonetheless is indicative of the presence of a vanadium compound. No vanadium signal

was observed for the sample which had only vanadium deposited upon the α-alumina. It is thus reasonable to infer that the NMR signal observed in Figure 5.32 is associated with the presence of a 'lanthanum/vanadium compound'. In fact the observed ^{51}V chemical shift is in good agreement with that for $LaVO_4$ reported as $\delta(^{51}V) = -610 \pm 10$ ppm by Lapina and co-workers.[24] Despite the poor quality of the spectrum, it is reasonable to conclude that $LaVO_4$ is present.

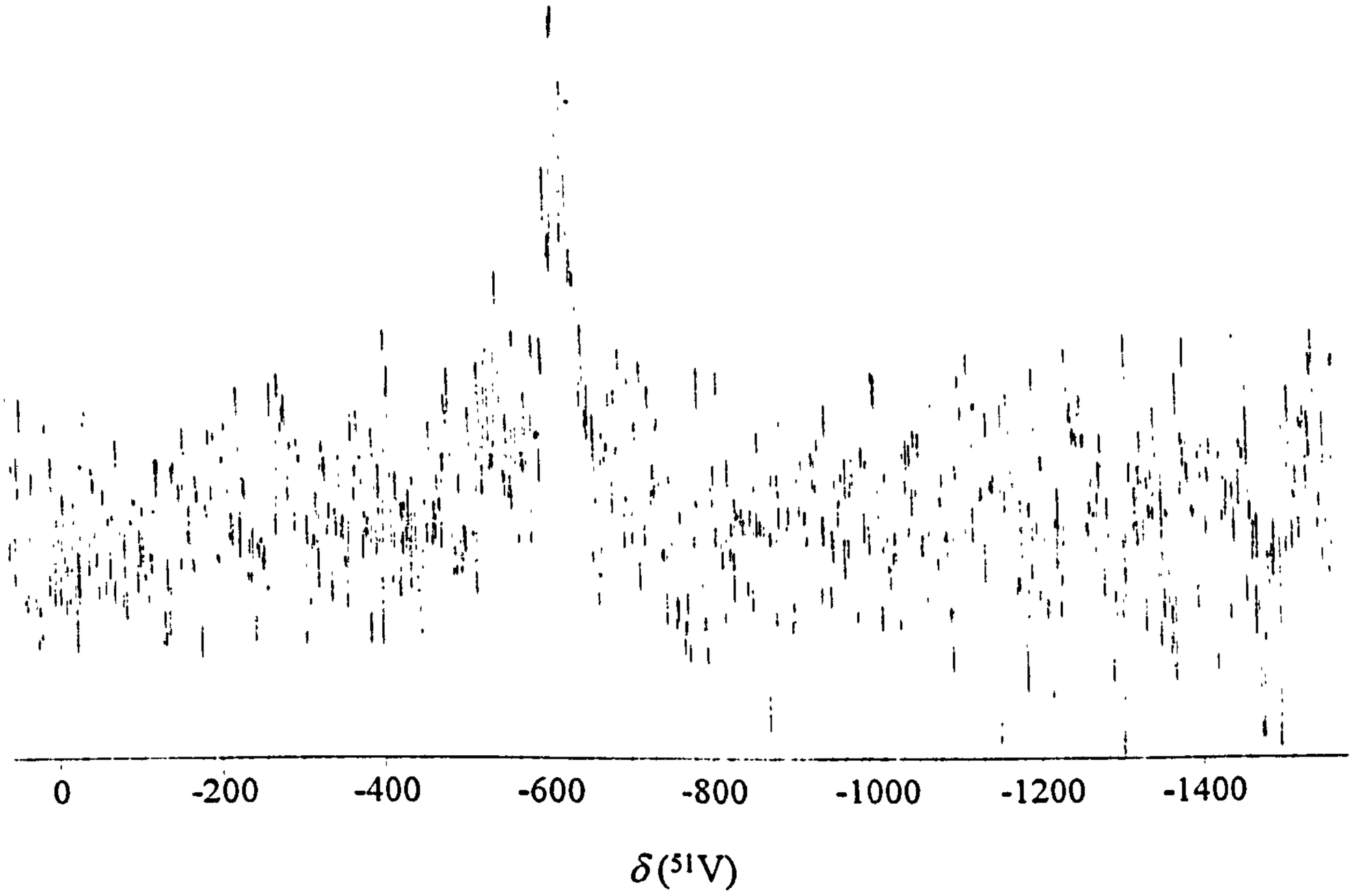

Figure 5.32 ^{51}V MAS NMR spectrum observed at 105.075 MHz for a sample of α-alumina loaded with 11.0 mass% lanthanum followed by 1 mass% vanadium. The FID was filtered through an exponential window prior to Fourier transformation in order to increase sensitivity. External reference liquid $VOCl_3$, pulse delay = 1 s, pulse width = 2 μs, number of scans = 62 000, spinning frequency ~ 7 kHz, and $\delta(^{51}V) = -615$ ppm.

Silica support materials

The results obtained for these materials compare directly with those obtained in the α-alumina studies. Figure 5.33 gives the XRD patterns recorded for the four parent samples. The very intense diffraction peak centred at 26.5° in 2θ has in all of the patterns been truncated level with the intensity of the diffraction peak centred at 20.5° in 2θ: in this way less intense diffraction peaks are more easily seen.

Pattern (a) is for silica (quartz) dried at 110°C and is in good agreement with the JCPDS reference pattern No. 33-1161 for quartz. Pattern (b) is for silica which has had 1 mass% vanadium deposited upon its surface and is, as expected, identical to that in (a). For the sample with 9.5 mass% lanthanum deposited upon its surface (Figure 5.33 (c)) additional low-intensity diffraction peaks appear in the XRD pattern: similar behaviour was noted for the corresponding α-alumina sample. However, as previously, these additional diffraction peaks could not be positively related to known phases using the JCPDS data base. In the presence of vanadium these extra diffraction peaks disappear (Figure 5.33(d)) and this again suggests an interaction between vanadium and lanthanum even under the relatively mild preparation conditions. The ^{51}V MAS NMR spectrum (Figure 5.34) is very similar to that observed for the equivalent α-alumina sample (Figure 5.32), that is a single broad signal centred at $\delta(^{51}V)$ = -606 ppm which is typical of the presence of $LaVO_4$.

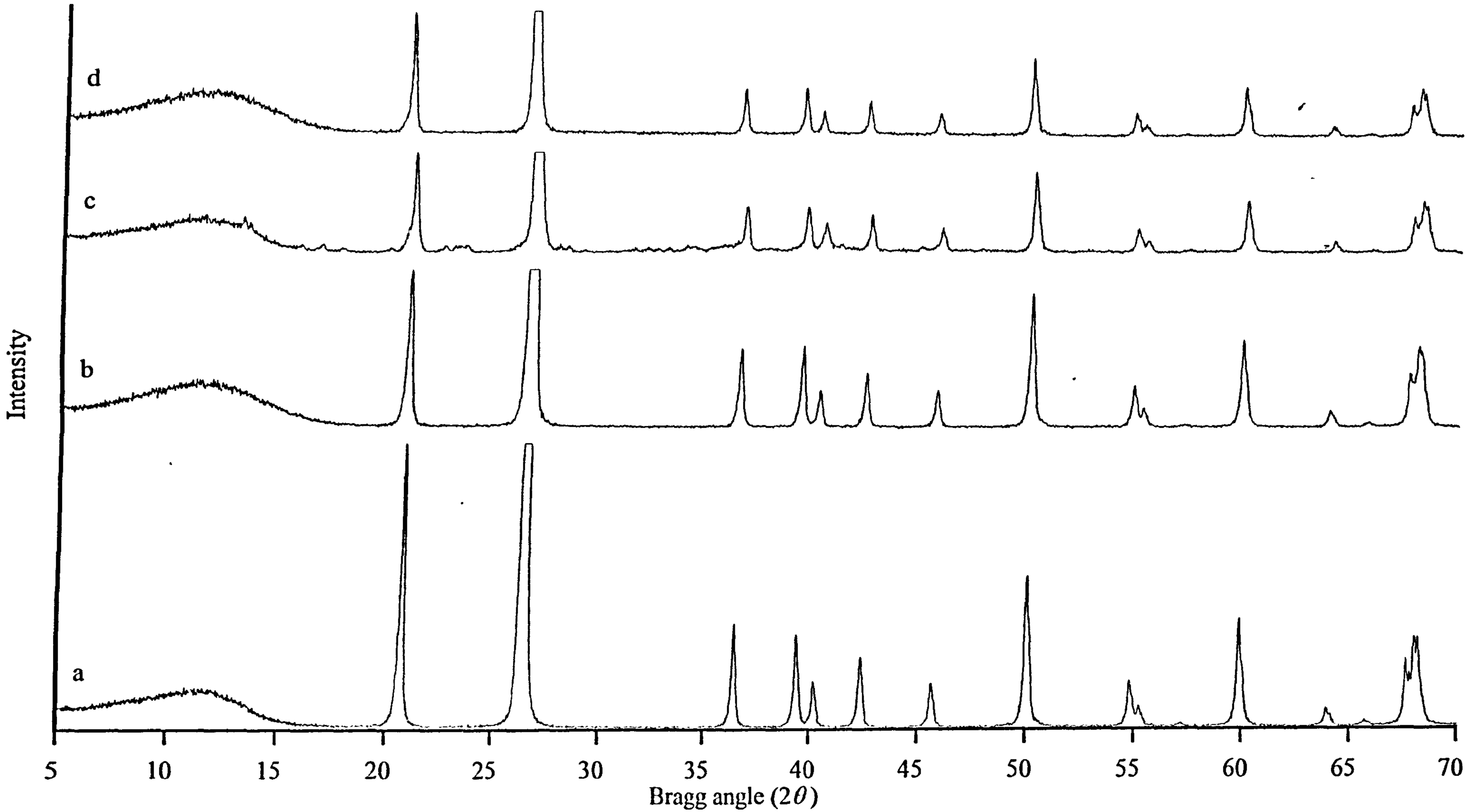

Figure 5.33 XRD patterns recorded for four parent samples based upon the silica support material. (a) silica, (b) silica loaded with 1 mass% vanadium, (c) silica loaded with 9.5 mass% lanthanum, and (d) silica loaded with 1 mass% vanadium and 9.5 mass% lanthanum.

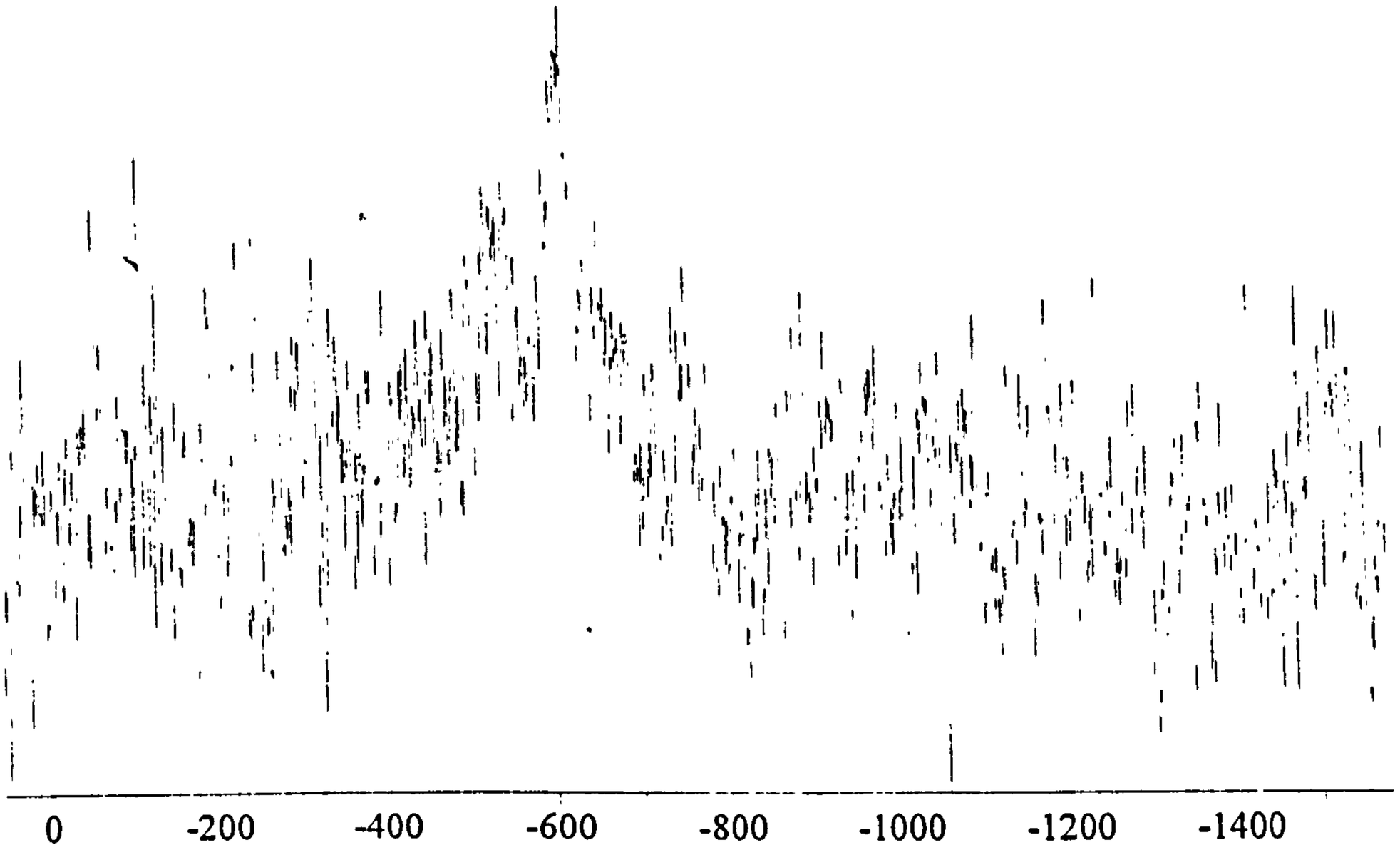

Figure 5.34 ^{51}V MAS NMR spectrum observed at 105.075 MHz for a sample of silica loaded with 9.5 mass% lanthanum followed by 1 mass% vanadium. The FID was filtered through an exponential window prior to Fourier transformation in order to increase sensitivity. External reference liquid $VOCl_3$, pulse delay = 1 s, pulse width = 2 μs, number of scans = 57 000, spinning frequency ~ 7 kHz, and $\delta(^{51}V)$ = -606 ppm.

Completely Degraded FCC samples

Complete destruction of the catalyst (alpha-54) was achieved by severe heat treatment, 1400/48/AIR, (Section 4.4). This treatment caused the various components of the catalyst to recrystallise into silica and mullite (Figure 5.35). The XRD pattern recorded from this degraded sample loaded with 1.0 mass% vanadium remained unchanged from that shown in Figure 5.35. A ^{51}V MAS NMR spectrum could not be observed for the sample although, given the relatively low vanadium concentration and the mixed nature of the RE ions, this was not unexpected.

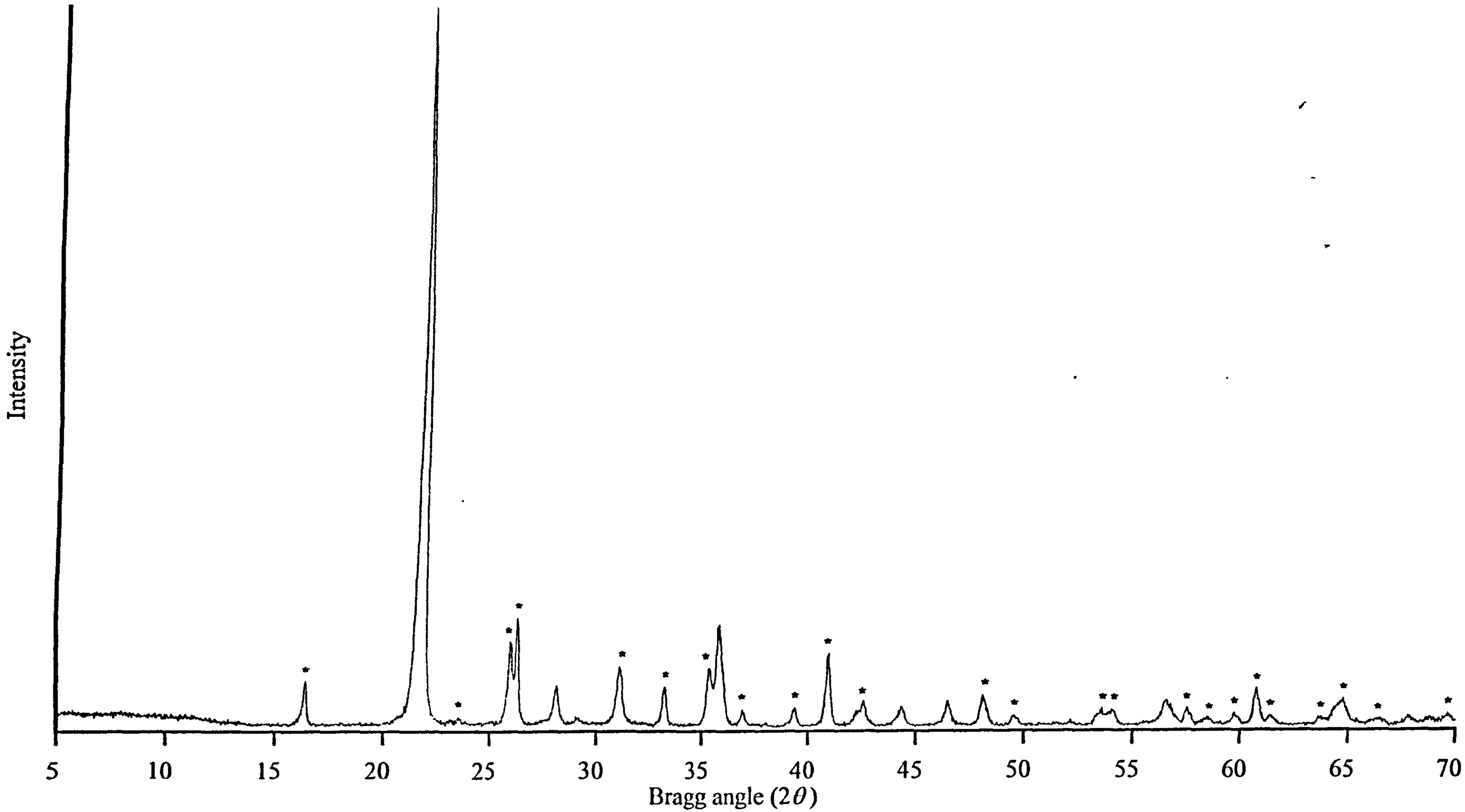

Figure 5.35 XRD pattern recorded for a sample of completely degraded alpha-54, after treatment at 1400°C for 48 hours. ★ labels diffraction peaks due to mullite, unlabelled diffraction peaks are due to silica.

5.4.2 Calcination and steam treatment: alumina support material

Samples in the absence of vanadium and lanthanum

The samples in this series essentially act as a control and were either calcined or steam treated at 800°C for five hours under both air and nitrogen atmospheres. The experimental treatments are summarised in Table 5.12.

Sample	Treatment
ALU#1	800/5/0/AIR
ALU#2	800/5/80/AIR
ALU#3	800/5/0/N_2
ALU#4	800/5/80/N_2

Table 5.12 The experimental conditions used for the treatment of α-alumina support materials with no vanadium or lanthanum present.

In all cases the recorded XRD patterns did not deviate from that presented in Figure 5.31 (a) for α-alumina dried at 110°C, the treatment precursor. This result is consistent with the fact that corundum is a stable α-alumina phase at temperatures in excess of 800°C.[32]

Samples with 1 mass% vanadium only

The samples were subject to the same experimental treatments, as listed in Table 5.12 for the dried α-alumina samples. The XRD patterns recorded for these samples were similar to those reported for the dried α-alumina in that the only phase detectable was that of α-alumina, and all patterns were similar to that recorded for the treatment precursor in Figure 5.31 (b). It is likely that vanadium compounds could not be detected because the concentrations were below the detection limits of the X-ray diffractometer.

Figure 5.36 shows the ^{51}V MAS NMR spectrum for the sample steam treated at 800°C under a nitrogen atmosphere. It can be seen that there are no visible resonances. This is probably due to vanadium being stabilised as a series of compounds. If a single phase was present the vanadium concentration should be sufficient for a signal to be observed given the number of scans collected. No attempt was made to record further spectra in this series of samples.

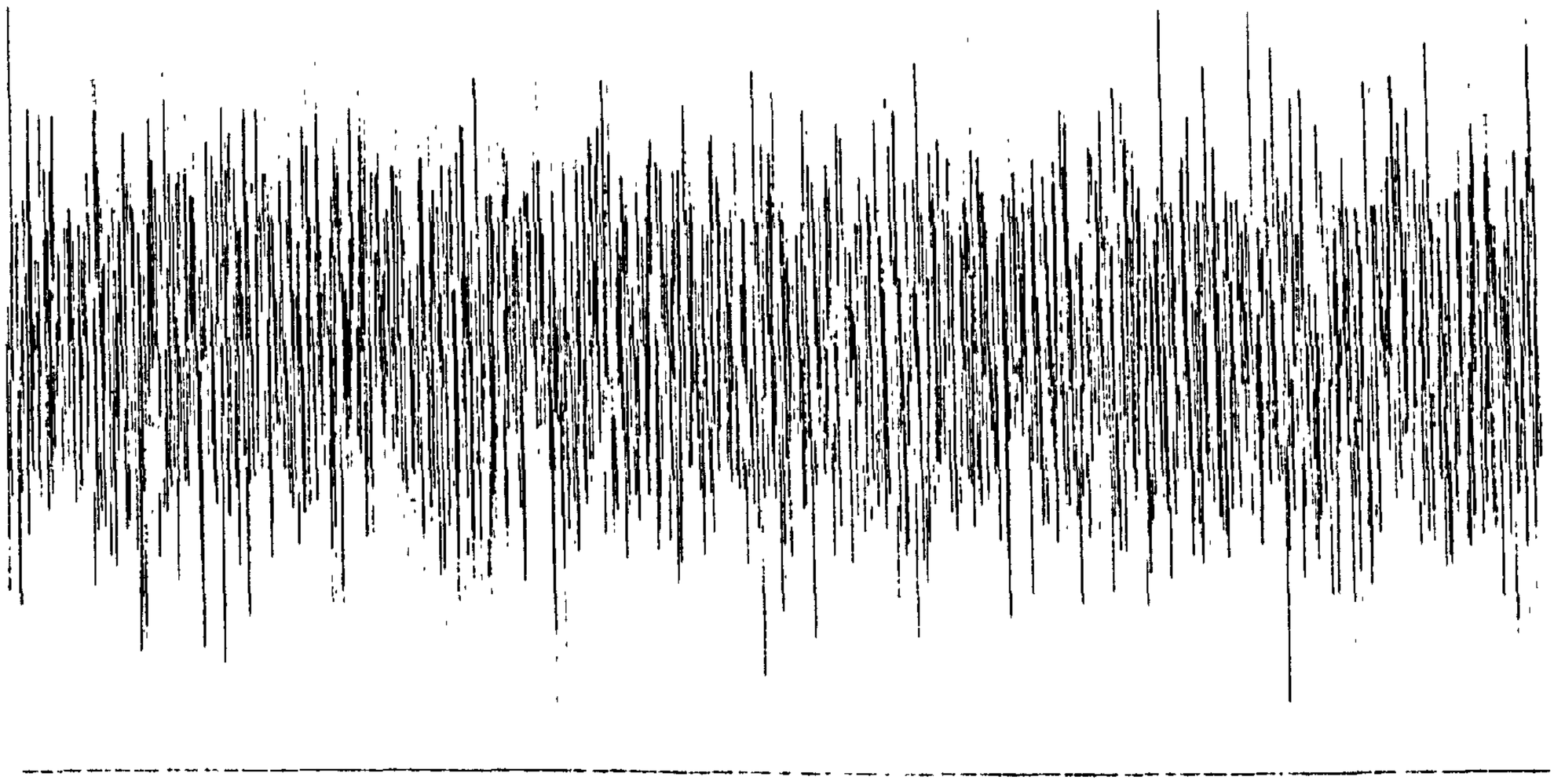

Figure 5.36 ^{51}V MAS NMR observed at 105.075 MHz for a sample of α-alumina support material loaded with 1 mass% vanadium only and steam treated at 800°C under a nitrogen atmosphere. External reference liquid $VOCl_3$, pulse width = 2 μs, pulse delay = 1 s, number of scans = 54 000, and spinning frequency ~ 7 kHz.

Samples loaded with 11.0 mass% lanthanum only

Lanthanum-loaded samples were subject to a full array of experimental conditioning (Table 5.13) included calcination and steam treatment at 750°C and 800°C under both an air and nitrogen atmosphere.

Sample	Treatment
ALU#9	750/5/0/AIR
ALU#10	750/5/80/AIR
ALU#11	800/5/0/AIR
ALU#12	800/5/80/AIR
ALU#13	750/5/0/N_2
ALU#14	750/5/80/N_2
ALU#15	800/5/0/N_2
ALU#16	800/5/80/N_2

Table 5.13 The experimental conditions used for the treatment of α-alumina support material loaded with 11.0 mass% lanthanum only. (It can be noted that this table also applies to the silica support material: Section 5.4.3.)

Considering first the samples that were treated using air as a carrier gas, the four XRD patterns for these samples are given in Figure 5.37, the patterns are presented from a Bragg angle of 18° in 2θ to aid with the resolution of the patterns. These samples show the formation of new well-resolved crystalline phases. Calcination of the samples (Figure 5.37 (a) and (b)) at both 750°C and 800°C results in the formation of lanthanum oxychloride (LaOCl) indicated in the XRD patterns as ■, and is consistent with the JCPDS reference pattern No. 08-0477 for this material. LaOCl has a tetragonal unit cell and the structure consists of a sheet of coplanar oxygen atoms with a sheet of chlorine atoms on each side with the lanthanum atoms between the Cl-O-Cl sheets.[33] Comparing XRD patterns (a) and (b) (Figure 5.37) it can be seen that levels of the new LaOCl phase remain approximately constant and its formation appears independent of temperature, possibly indicating that all of the deposited lanthanum is present in the new LaOCl phase at this stage.

The introduction of steam into the system results again in the formation of LaOCl together with two additional new phases, namely lanthanum aluminium oxide ($LaAlO_3$), indicated

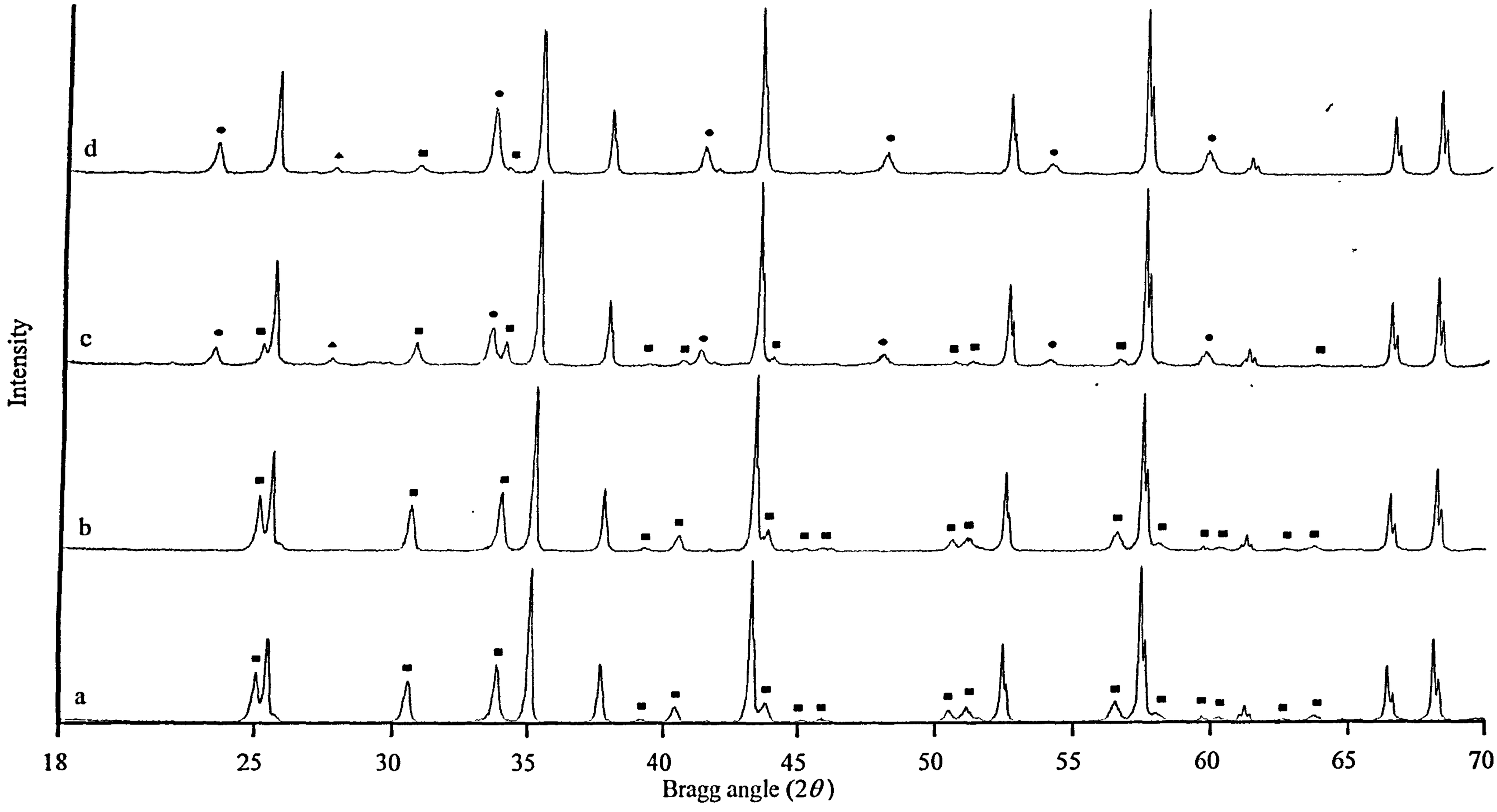

Figure 5.37 XRD patterns recorded for α-alumina support material loaded with 11.0 mass% lanthanum only, treated as follows (a) 750/5/0/AIR, (b) 800/5/0/AIR, (c) 750/5/80/AIR, and (d) 800/5/80/AIR. ■ indicates peaks due to LaOCl, ● indicates peaks due to $LaAlO_3$, ▲ indicates an unknown component, and unlabelled peaks are due to α-Al_2O_3.

in the XRD patterns as ●, and an unknown, but relatively small, component indicated as ▲. The $LaAlO_3$ phase is consistent with the JCPDS reference pattern No. 31-0022 for $LaAlO_3$. $LaAlO_3$ has a rhombohedral unit cell and is an example of the rhombohedral tilt system, with a small tilt angle ($\alpha=\beta=\gamma=90.1°$), making it slightly distorted from the ideal perovskite structure.[34] The unknown phase could not be identified after a thorough cross-reference with the JCPDS data base; although, as stated earlier, identification of a crystalline phase from a single diffraction peak is difficult and often unreliable. The formation of $LaAlO_3$ when steam is introduced is also accompanied by a reduction in the relative intensity of the LaOCl diffraction peaks, when these diffraction peaks are compared with those for the calcination experiments. It can also be seen that increasing the temperature from 750°C to 800°C results in the increased formation of the $LaAlO_3$ phase, and a further reduction in that for LaOCl, with at 800°C only the strongest diffraction peaks due to the LaOCl phase being observable. Thus under hydrothermal conditions, and in particular at the higher temperature of 800°C, the formation of $LaAlO_3$, rather then LaOCl is favoured.

Similar observations were made for samples that were treated under a nitrogen atmosphere. The XRD patterns for the four samples treated under this atmosphere are shown in Figure 5.38. Calcination of the samples again results in the formation of LaOCl (indicated as ■ within the XRD patterns) as the only detectable lanthanum phase (Figure 5.38 (a) and (b)). The amount formed again seems independent of temperature with similar levels present at both 750°C and 800°C. The introduction of steam results in the formation of $LaAlO_3$ (indicated as ● within the XRD patterns) and the same unidentified phase (indicated as ▲ within the XRD patterns) together with LaOCl (Figure 5.38 (c) and (d)). As seen with the samples that were treated using air as a carrier gas, increasing the temperature from 750°C to 800°C results in increased amounts of $LaAlO_3$ at the expense of the LaOCl phase.

It is interesting to compare the relative amounts of LaOCl and $LaAlO_3$ for samples that have been hydrothermally treated under a nitrogen atmosphere with those similarly treated but using air as a carrier gas (compare Figure 5.37 (c) with Figure 5.38 (c) and Figure 5.37 (d) with Figure 5.38 (d)). It can be seen that the relative amount of LaOCl, at both 750°C

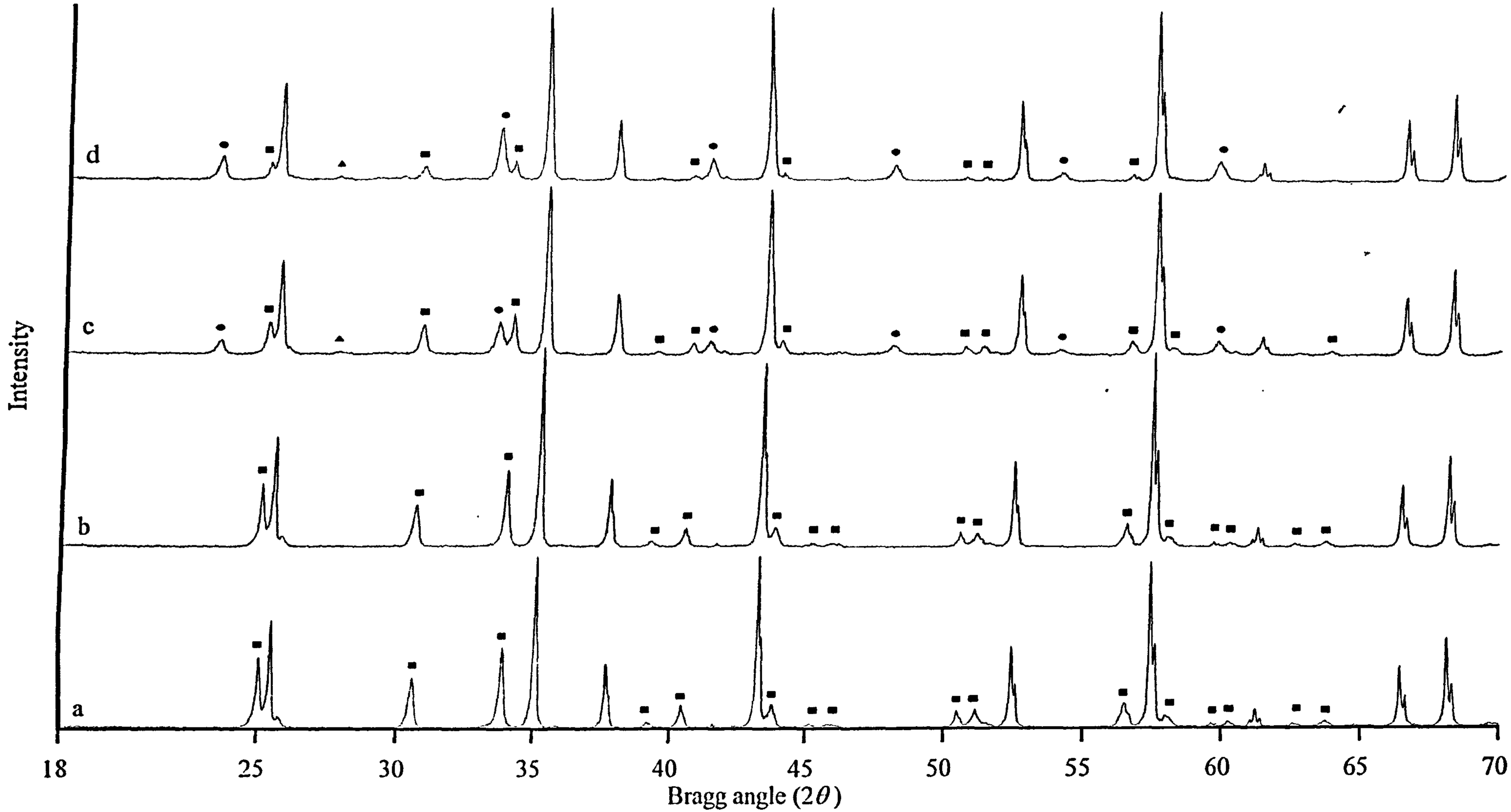

Figure 5.38 XRD patterns recorded for α-alumina support materials loaded with 11.0 mass% lanthanum only, treated as follows (a) 750/5/0/N_2, (b) 800/5/0/N_2, (c) 750/5/80/N_2, and (d) 800/5/80/N_2. ■ indicates peaks due to LaOCl, ● indicates peaks due to $LaAlO_3$, ▲ indicates an unknown component, and unlabelled peaks are due to α-Al_2O_3.

and 800°C, is greater when the samples are steam treated under a nitrogen atmosphere with the corresponding levels of $LaAlO_3$ being reduced. This suggests that the role of external oxygen may be important in the formation of $LaAlO_3$. When the external oxygen source is removed the formation of $LaAlO_3$ is reduced and the remaining lanthanum is stabilised in the form of LaOCl.

Samples loaded with 1 mass% vanadium and 11.0 mass% lanthanum

These samples were also subjected to a full array of treatment conditions (Table 5.13). Figure 5.39 shows the XRD patterns recorded for four experiments that were performed using air as a carrier gas. It can be seen that additional diffraction peaks appear and these can be assigned to four distinct crystalline phases depending on conditions.

Calcination of the samples (Figure 5.39 (a) and (b)) results in the formation of LaOCl (indicated as ■ in the XRD patterns) and two forms of lanthanum vanadium oxide, namely $LaVO_4$ (indicated in the XRD patterns as □) and $LaVO_3$ (indicated as O in the XRD patterns).

$LaVO_4$ is a vanadium (V) species and best corresponds to JCPDS reference pattern No. 23-0324, and has a monoclinic unit cell with the monazite ($CePO_4$) structure.[35] $LaVO_3$ is a vanadium (III) species corresponding to JCPDS reference pattern No. 11-0024, and has a cubic unit cell with the perovskite structure.[36]

The formation of $LaVO_3$ under the given experimental conditions was not anticipated since these were predominantly oxidising. As was stated earlier, it would be expected that vanadium should be present as a vanadium (IV) species. Reduction (or a form of disproportionation) of vanadium from +4 to +3 must therefore have occurred during calcination rather than within the preparative procedure. It can be noted that the formation of $LaVO_3$ is dependent upon the reaction temperature and its formation increases as the reaction temperature is increased from 750°C to 800°C.

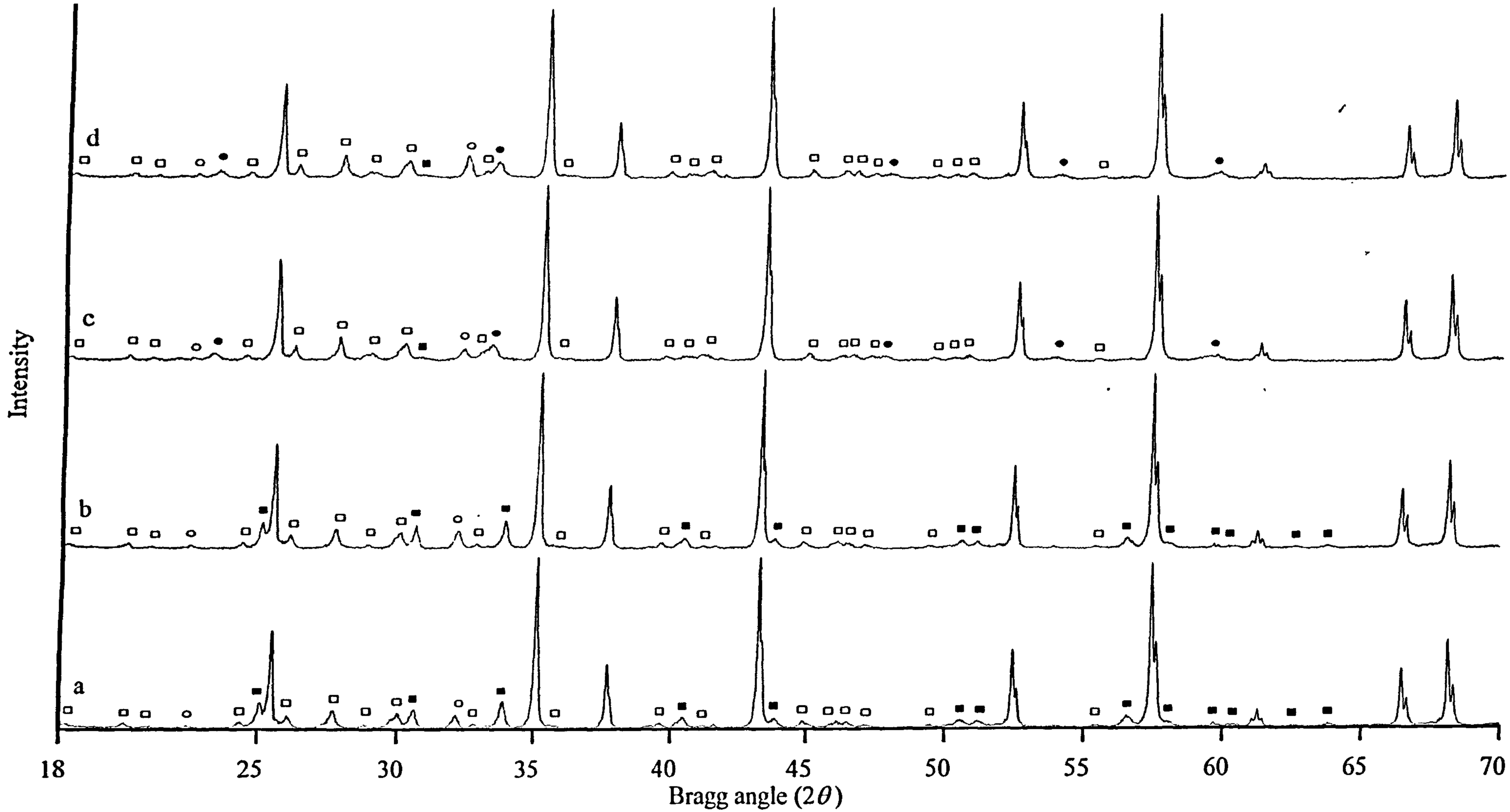

Figure 5.39 XRD patterns recorded for α-alumina support materials loaded with 1 mass% vanadium and 11.0 mass% lanthanum, treated as follows (a) 750/5/0/AIR, (b) 800/5/0/AIR, (c) 750/5/80/AIR, and (d) 800/5/80/AIR. ■ indicates peaks due to LaOCl, ● indicates peaks due to $LaAlO_3$, □ indicates peaks due to $LaVO_4$, ○ indicates peaks due to $LaVO_3$, and unlabelled peaks are due to α-Al_2O_3.

The formation of $LaVO_4$ is consistent with the vanadium being oxidised from the +4 to +5 oxidation state. Its formation is probably dependent on the amount of vanadium present, and therefore independent of the reaction temperature.

The remaining lanthanum upon the surface of the support material is present as LaOCl under calcination conditions. This is consistent with the observations made for the α-alumina support materials loaded with 11.0 mass% lanthanum only, cf. Figure 5.37 (a) and (b).

The ^{51}V MAS NMR spectra for the two calcined samples are given in Figure 5.40 (a) and (b). In both spectra it can be seen that there is a central line surrounded by weak rotational sidebands: for the sample treated at 750°C (Figure 5.40 (a)) $\delta(^{51}V) = -613\pm6$ ppm and for the sample treated at 800°C (Figure 5.40 (b)) $\delta(^{51}V) = -612\pm6$ ppm. Both resonances are in good agreement with that reported for $LaVO_4$[24] (the improvement in signal to noise for spectrum (b) over spectrum (a) is due to more extensive signal averaging in the latter case). There is no evidence for the presence of $LaVO_3$ in these spectra. This is not unexpected since vanadium (III) compounds, which have two unpaired 3d electrons, are paramagnetic.

Steam treatment of the samples results in the formation of LaOCl, $LaAlO_3$ (indicated in the XRD patterns as ●) together with $LaVO_4$ and $LaVO_3$ (Figure 5.39 (c) and (d)). As seen with the calcined samples the formation of $LaVO_3$ is temperature dependent with increased levels found at 800°C. The levels of $LaVO_4$ again appear to remain constant with temperature.

The excess lanthanum (lanthanum not combined with vanadium) is present mainly as $LaAlO_3$ with only trace amounts of LaOCl present. This is consistent with the observations made for the α-alumina support materials loaded with 11.0 mass% lanthanum. However, when both lanthanum and vanadium are present the amounts of both $LaAlO_3$ and LaOCl also appear to remain constant with increasing temperature. This is in contrast to the behaviour observed with samples that only had lanthanum deposited upon their surfaces; in this case levels of $LaAlO_3$ increased at the expense of LaOCl as the temperature increased from 750°C to 800°C (Figure 5.37 (c) and (d)).

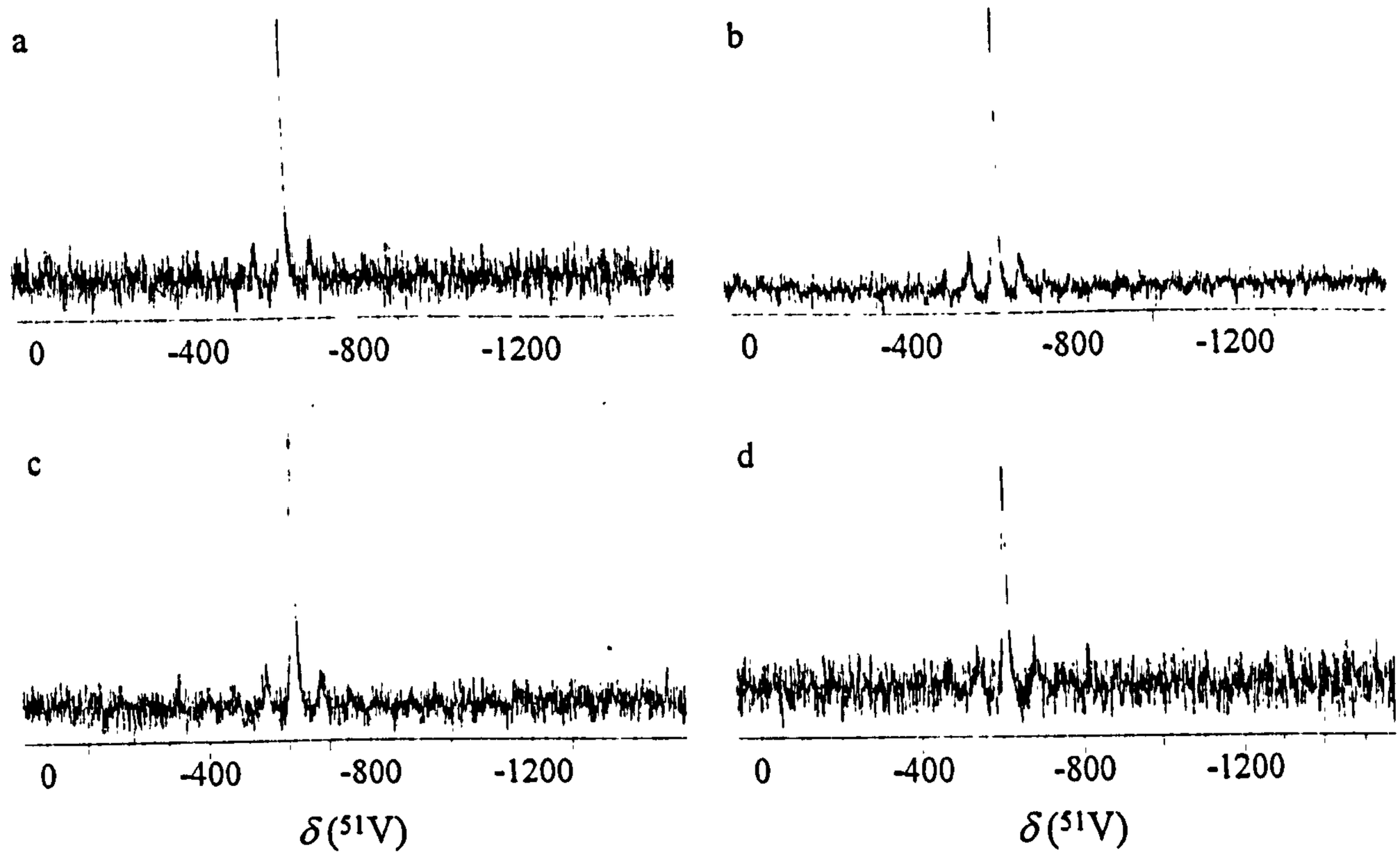

Figure 5.40 ^{51}V MAS NMR spectra observed at 105.075 MHz for α-alumina loaded with 1 mass% vanadium and 11.0 mass% lanthanum treated as follows

(a) 750/5/0/AIR, number of scans = 47 000, $\delta(^{51}V)$ = -613±6 ppm,

(b) 800/5/0/AIR, number of scans = 159 239, $\delta(^{51}V)$ = -612±6 ppm,

(c) 750/5/80/AIR, number of scans = 58 000, $\delta(^{51}V)$ = -613±6 ppm, and

(d) 800/5/80/AIR, number of scans = 62 000, $\delta(^{51}V)$ = -611±6 ppm.

External reference liquid $VOCl_3$, pulse delay = 1 s, pulse width = 2 μs and the spinning frequency ~ 7 kHz.

The ^{51}V MAS NMR spectra for the steam treated samples (Figure 5.40 (c) and (d)) are very similar to those recorded for the calcined samples (Figure 5.40 (a) and (b)). Both show a single resonance: $\delta(^{51}V)$ = -613±6 ppm for the sample steam treated at 750°C and $\delta(^{51}V)$ = -611±6 ppm for the sample steam treated at 800°C, and this confirms the presence of $LaVO_4$ in both cases. The spectra also confirm that similar levels of $LaVO_4$ are present for both the calcined and steam treated samples.

Figure 5.41 shows the XRD patterns recorded for four samples that have been treated under a nitrogen atmosphere. Calcination of the samples again results in the formation of LaOCl, $LaVO_4$ and $LaVO_3$, although when these patterns (Figure 5.41 (a) and (b)) are compared with the calcined samples using air as a carrier gas (Figure 5.39 (a) and (b)) it can be seen

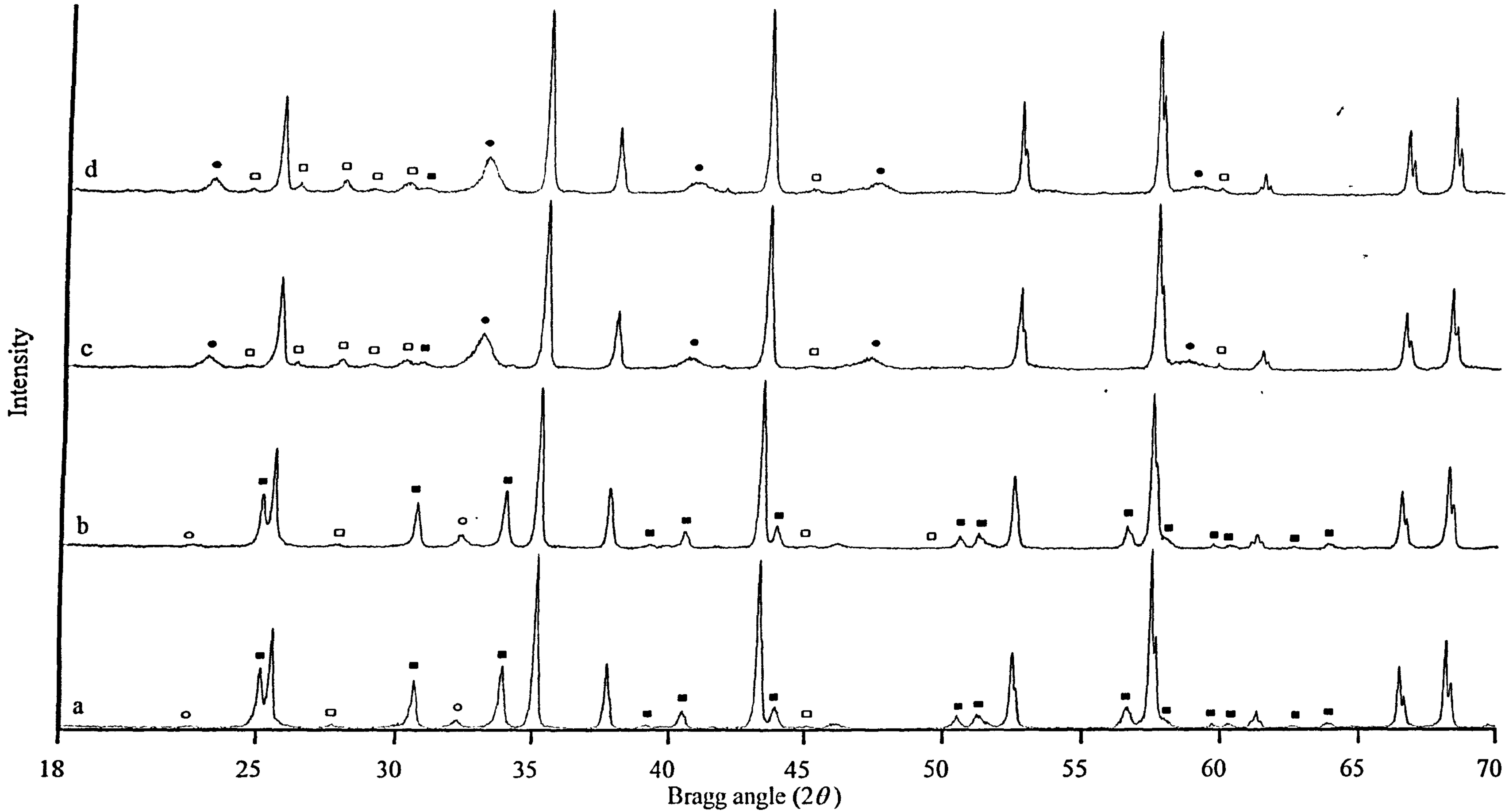

Figure 5.41 XRD patterns recorded for α-alumina support materials loaded with 1 mass% vanadium and 11.0 mass% lanthanum, treated as follows (a) 750/5/0/N_2, (b) 800/5/0/N_2, (c) 750/5/80/N_2, and (d) 800/5/80/N_2. ■ indicates peaks due to LaOCl, ● indicates peaks due to $LaAlO_3$, □ indicates peaks due to $LaVO_4$, ○ indicates peaks due to $LaVO_3$, and unlabelled peaks are due to α-Al_2O_3.

that there are changes in the relative amounts of these compounds. For the samples calcined under nitrogen there is a significant reduction in the observed levels of $LaVO_4$ and $LaVO_3$ and a large increase in the levels of LaOCl. The reduction in $LaVO_4$ may be expected since its formation requires the oxidation of vanadium (IV) to vanadium (V) and the conditions are less favourable for oxidation than for the samples calcined in air. Increased production of LaOCl is consistent with reduced levels of both $LaVO_4$ and $LaVO_3$.

The ^{51}V MAS NMR spectra for the calcined samples (Figure 5.42 (a) and (b)) also reflect the decrease in levels of $LaVO_4$. Both spectra are beginning to show the emergence of a resonance, centred at $\delta(^{51}V)$ = -608 ppm for the sample calcined at 750°C and centred at $\delta(^{51}V)$ = -607 ppm for the sample calcined at 800°C. The significant reduction in signal to noise over the samples that were calcined in air (Figure 5.40 (a) and (b)) after a similar number of scans, provides clear evidence for reduced levels of $LaVO_4$. Significantly no evidence for additional vanadium species could be found; this may be due to the vanadium being in the +4 oxidation state, or the presence of many vanadium species present in small amounts and indistinguishable from the background noise.

Hydrothermal treatment of the samples under a nitrogen atmosphere (Figure 5.41 (c) and (d)) results in the formation of just three crystalline phases: LaOCl, $LaAlO_3$ and $LaVO_4$, rather than the four that were observed for the samples steam treated using air as a carrier gas (Figure 5.39 (c) and (d)). There was no evidence for the presence of $LaVO_3$ in any significant amounts.

The amount of the $LaAlO_3$ phase remains relatively constant with increasing temperature; this is consistent with the behaviour when similar samples were steam treated in air. Overall the general amount of this phase increases compared to samples that were steam treated in air (compare, Figure 5.39 (c) with Figure 5.41 (c) and Figure 5.39 (d) with Figure 5.41 (d)). This is expected since under a nitrogen atmosphere a decrease in the $LaVO_4$ phase is observed and so greater amounts of free lanthanum are available to form $LaAlO_3$.

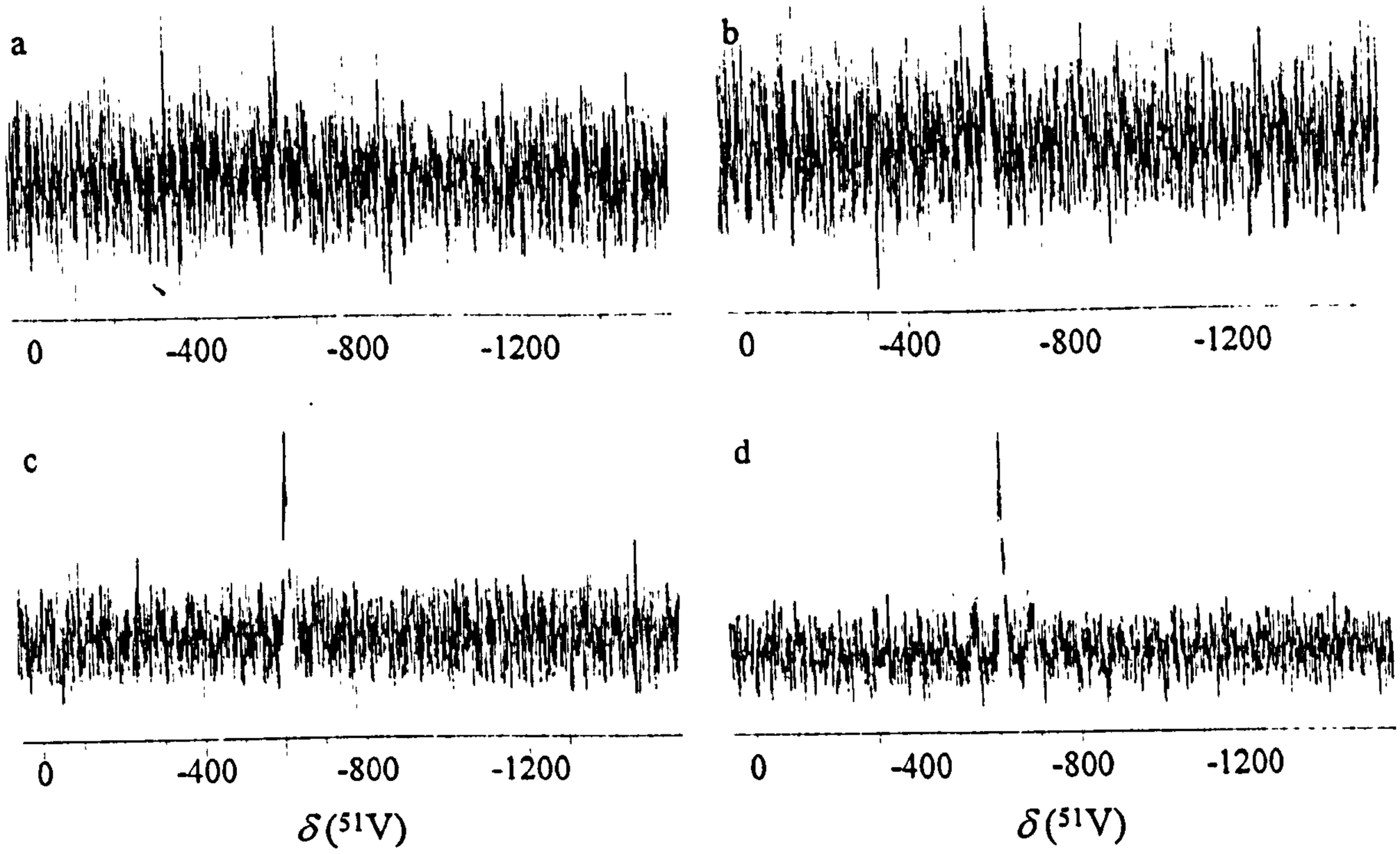

Figure 5.42 ^{51}V MAS NMR spectra observed at 105.075 MHz for the α-alumina loaded with 1 mass% vanadium and 11.0 mass% lanthanum treated as follows

(a) 750/5/0/N_2, number of scans = 55 000, $\delta(^{51}V)$ = -608 ppm,

(b) 800/5/0/N_2, number of scans = 57 841, $\delta(^{51}V)$ = -607 ppm,

(c) 750/5/80/N_2, number of scans = 65 000, $\delta(^{51}V)$ = -612±6 ppm, and

(d) 800/5/80/N_2, number of scans = 58 000, $\delta(^{51}V)$ = -612±6 ppm. External reference liquid $VOCl_3$, pulse delay = 1 s, pulse width = 2 μs and spinning frequency ~ 7 kHz.

Interestingly there is a significant increase in the concentration of $LaVO_4$ for the samples that have been steam treated compared to samples that were calcined, this is an indication of the increased oxidising conditions under a hydrothermal environment. However, there is still significantly less $LaVO_4$ formed compared to samples that were treated in air. This indicates a decrease in oxidative conditions as the atmosphere changes to nitrogen. These results are also reflected in the ^{51}V MAS NMR spectra for the two samples that have been steam treated under a nitrogen atmosphere (Figure 5.42 (c) and (d)). There is a single resonance at $\delta(^{51}V)$ = -612±5 ppm for the sample steam treated at 750°C (Figure 5.42 (c)) and a single resonance at $\delta(^{51}V)$ = -612±6 ppm for the sample steam treated at 800°C

(Figure 5.42 (d)) both confirming the presence of $LaVO_4$. Comparing these spectra with those for the calcined samples (Figure 5.42 (a) and (b)) it can be seen that there is a large increase in signal to noise, for similar scan times, indicating the presence of increased amounts of $LaVO_4$. Comparing the spectra with those for the steam-treated samples using air as a carrier gas (Figure 5.40 (c) and (d)) it can be seen that there is a general decrease in signal to noise, after similar scan times, indicating reduced levels of $LaVO_4$ when the samples are treated under a nitrogen atmosphere. A reduction in the amount of $LaVO_4$ indicates that vanadium may be present in other forms: but the are not detectable either by XRD or MAS NMR.

Summary and further discussion

A summary of the crystalline phases identified for the α-alumina samples loaded with 11.0 mass% lanthanum, with and without vanadium, after treatment under differing conditions is given in Table 5.14. It can be seen that after calcination the excess lanthanum is stabilised as LaOCl, this is true regardless of vanadium contamination. However, after steam treatment the formation of $LaAlO_3$ is favoured. Treatment, in the presence of vanadium always results in the formation of $LaVO_4$. A second vanadium phase, $LaVO_3$, is also observed, except when the samples are steam treated under nitrogen.

For the $LaAlO_3$ phase that is observed after steam treatment, it is the case that the diffraction peaks move to lower Bragg angles in the presence of vanadium. Table 5.15 details the changes in 2θ for the strongest diffraction peak which occurs at ~ 33.3°. It can be seen that the position of this diffraction peak for the samples treated without vanadium is relatively constant at ~ 33.3°, but it decreases to ~ 33.1° after steam treatment in air and ~ 32.9° after steam treatment in nitrogen for the vanadium loaded samples. (The diffraction peaks due to the α-alumina and other phases present within the samples remain in their expected positions, ruling out the possibility of any systematic errors). $LaAlO_3$ can exist with an alternative crystal structure to that reported, the structure is still based on the rhombohedral tilt system but the tilt angle is much greater at 60.1°; however, the XRD pattern for this system is greatly different from that observed, thus ruling out a

Vanadium loading /mass%	Treatment conditions							
	750/5/0/AIR	800/5/0/AIR	750/5/80/AIR	800/5/80/AIR	750/5/0/N_2	800/5/0/N_2	750/5/80/N_2	800/5/80/N_2
0	LaOCl	LaOCl	LaOCl $LaAlO_3$	LaOCl $LaAlO_3$	LaOCl	LaOCl	LaOCl $LaAlO_3$	LaOCl $LaAlO_3$
1	LaOCl $LaVO_4$ $LaVO_3$	LaOCl $LaVO_4$ $LaVO_3$	LaOCl $LaAlO_3$ $LaVO_4$ $LaVO_3$	LaOCl $LaAlO_3$ $LaVO_4$ $LaVO_3$	LaOCl $LaVO_4$ $LaVO_3$	LaOCl $LaVO_4$ $LaVO_3$	LaOCl $LaAlO_3$ $LaVO_4$	LaOCl $LaAlO_3$ $LaVO_4$

Table 5.14 Crystalline phases identified when α-alumina loaded with 11.0 mass% lanthanum, with and without vanadium, is exposed to differing treatment conditions.

Treatment Conditions	Vanadium loading /mass%	Observed 2θ position
750/5/80/AIR	0	33.30
800/5/80/AIR		33.30
750/5/80/N_2		33.37
800/5/80/N_2		33.31
750/5/80/AIR	1.0	33.09
800/5/80/AIR		33.13
750/5/80/N_2		32.80
800/5/80/N_2		32.92

Table 5.15 The changes in the observed 2θ position for $LaAlO_3$ phases observed after steam treatment of α-alumina samples loaded with 11.0 mass% lanthanum, with and without vanadium.

simple phase change. The movement of the diffraction peaks is probably related to the incorporation of vanadium into the $LaAlO_3$ lattice; although direct evidence for this suggestion is not available. It is interesting to note that the largest change in the position of the diffraction peak is found under nitrogen; it can be recalled that steam treatment under nitrogen results in decreased amounts of $LaVO_4$, and no $LaVO_3$, when compared to treatment in air, thus making more vanadium available for incorporation into the $LaAlO_3$ lattice.

Since lanthanum aluminium oxide ($LaAlO_3$) is formed only in the presence of steam it can be suggested that the following reaction takes place

$$2\ LaOCl + Al_2O_3 + H_2O \rightarrow 2\ LaAlO_3 + 2\ HCl \qquad (5.1)$$

The observation that an increase in reaction temperature from 750°C to 800°C results in an increase of $LaAlO_3$ at the expense of LaOCl indicates that the progress of the reaction depends on temperature. Interestingly Ropp and Carrol[37] in a study of the direct reaction

between La_2O_3 and alumina found that the formation of $LaAlO_3$ started at 400°C and was complete at 800°C,

$$La_2O_3 + Al_2O_3 \dashrightarrow 2\,LaAlO_3 \qquad (5.2)$$

It is worth commenting that lanthanum-stabilised aluminas have been the focus of considerable study due to their potential use in three-way catalytic converters.[38-44] For this purpose γ-alumina has been the phase of interest due to its relatively large surface area. Doping with lanthanum has been shown to hinder the change to α-alumina that is normally observed after prolonged exposure to elevated temperatures (800°C to 1000°C). For example, Shkrabina and co-workers[38] found that lanthanum doped γ-alumina contained greater amounts of γ-alumina after heat treatment over a range of temperatures than a similar sample that was lanthanum free. Typically lanthanum nitrate solutions have been the favoured source of lanthanum for doping purposes. This is possibly due to the difficulty in removing surface chloride ions if lanthanum trichloride solution is used as an alternative. γ-Al_2O_3 treated with lanthanum nitrate solution yields lanthanum oxide (La_2O_3) directly on heat treatment and then at higher temperatures, and in accord with equation 5.2, $LaAlO_3$ is also formed.

5.4.3 Calcination and steam treatment: silica support

A similar series of investigations to those carried out for the α-alumina support were carried out for the silica support material. The results are outlined below and more detail is given in areas for which distinct differences in behaviour were found.

The results from both the treatment of the silica support materials free from surface lanthanum and vanadium, and the silica support materials loaded with 1.0 mass% vanadium, are similar in nature to those reported for the corresponding α-alumina support materials. The XRD patterns obtained did not differ from those reported for the steam-treatment precursors (Figure 5.33 (a) and (b)). This was an anticipated since it is known that the quartz phase is stable at temperatures in excess of those employed here,[32] and vanadium concentrations are below the detection limits of the X-ray diffractometer.

The ^{51}V MAS NMR spectrum recorded for the sample steam treated at 800°C using air as a carrier gas did not show the presence of any vanadium signals.

Samples loaded with 9.5 mass% lanthanum only

The samples in this series were subject to a full array of experiments (listed in Table 5.13 where the label ALU can simply be replaced by SIL). The XRD patterns recorded for the four samples treated using air as a carrier gas are given in Figure 5.43. The patterns are displayed from 15°, in 2θ, to aid with the resolution of the patterns. As was the case with the treatment precursors the very intense diffraction peak at 26.5°, in 2θ, has been truncated level with the diffraction peak at 20.5°, in 2θ, to aid with the observation of new crystalline phases. Presentation of patterns in this format will be maintained for the remainder of this section.

For the samples that have been calcined (Figure 5.43 (a) and (b)) it can be seen that two new additional phases result from the treatment of the samples. The formation of LaOCl (indicated as ■ in the XRD patterns) and an unidentified phase (indicated as ▼ in the XRD patterns) are observed. The presence of LaOCl is consistent with the behaviour observed for the α-alumina support material treated under identical conditions (Figure 5.38 (a) and (b)): the XRD pattern is consistent with JCPDS reference pattern 08-0477. However, with the α-alumina support material the only detectable phase after calcination was LaOCl, here the LaOCl phase is accompanied by a second phase although this could not be identified. Increasing the temperature from 750°C to 800°C results in a decrease in the amount of the LaOCl phase, this is accompanied with an increase in the unknown phase. The decrease in the LaOCl phase suggests that the unidentified phase may contain lanthanum.

Steam treatment of the samples in air (Figure 5.43 (c) and (d)) again results in the formation of LaOCl and the same unidentified phase that was present in the calcined samples, together with a third phase (indicated in the XRD patterns as Δ). This phase can be assigned to lanthanum oxide (La_2O_3) (corresponding to JCPDS reference pattern

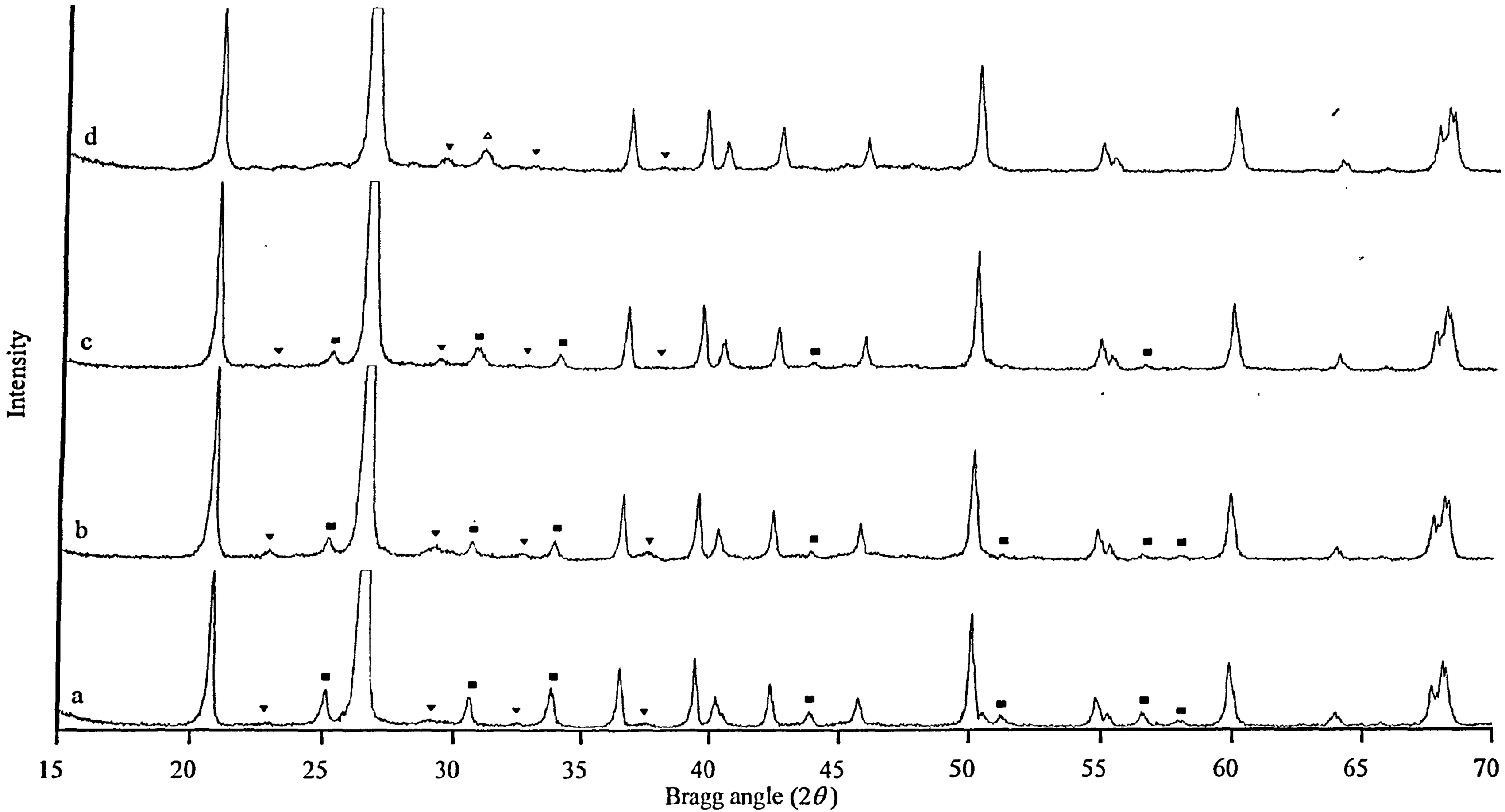

Figure 5.43 XRD patterns recorded for silica support materials loaded with 0 mass% vanadium and 9.5 mass% lanthanum, treated as follows (a) 750/5/0/AIR, (b) 800/5/0/AIR, (c) 750/5/80/AIR, and (d) 800/5/80/AIR. ■ indicates peaks due to LaOCl, Δ indicates peaks due to La_2O_3, ▼ indicates an unknown component, and unlabelled peaks are due to the silica support material.

No. 08-0477) but it should be noted that only a single diffraction peak is visible in the XRD patterns. Identification of a phase from a single diffraction peak is unreliable, but it can be noted that for La_2O_3 all other diffraction peaks would be relatively weak and probably not observable. Increasing the temperature from 750°C to 800°C results in a decrease in the concentration of LaOCl with little or none of this phase present at 800°C.

The four XRD patterns recorded for the samples treated under a nitrogen atmosphere are given in Figure 5.44. Calcination of the samples (Figure 5.44 (a) and (b)) results in the formation of LaOCl (indicated as ■ in the XRD patterns) and an unidentified phase (indicated as ▼ in the XRD patterns) the same as that observed when the samples were calcined in air (Figure 5.43 (a) and (b)). There are also two other additional phases. One of these, which is formed at both reaction temperatures, is an alternative phase of silica (indicated as ◇) and corresponds to JCPDS reference pattern No. 27-0605. This assignment is based on the presence of only one diffraction peak but, given the amount of material present, no other diffraction peaks from this phase would be expected to be observed. Treatment at 800°C results in the formation of a second unidentified phase (indicated as ◆).

It can be seen that the levels of LaOCl are relatively low when compared to the samples that were calcined using air as a carrier gas, and increasing the temperature has little effect on these levels. The amount of the unidentified phase, indicated as ▼, increases with increasing temperature; similar behaviour was observed for treatment in air. The amount of the alternative silica phase shows a large decrease as the temperature is increased.

Hydrothermal treatment of the samples under a nitrogen atmosphere (Figure 5.44 (c) and (d)) results in the formation of three crystalline phases: La_2O_3, indicated as Δ, and two unidentified phases, indicated as ▼ and ◆, with only one of these phases (indicated as ◆) being identifiable at 800°C. The concentration of La_2O_3 remains constant with increasing temperature.

It is clear from all of the results described above that the chemistry of lanthanum on silica support materials is more complex than on α-alumina support materials. The XRD

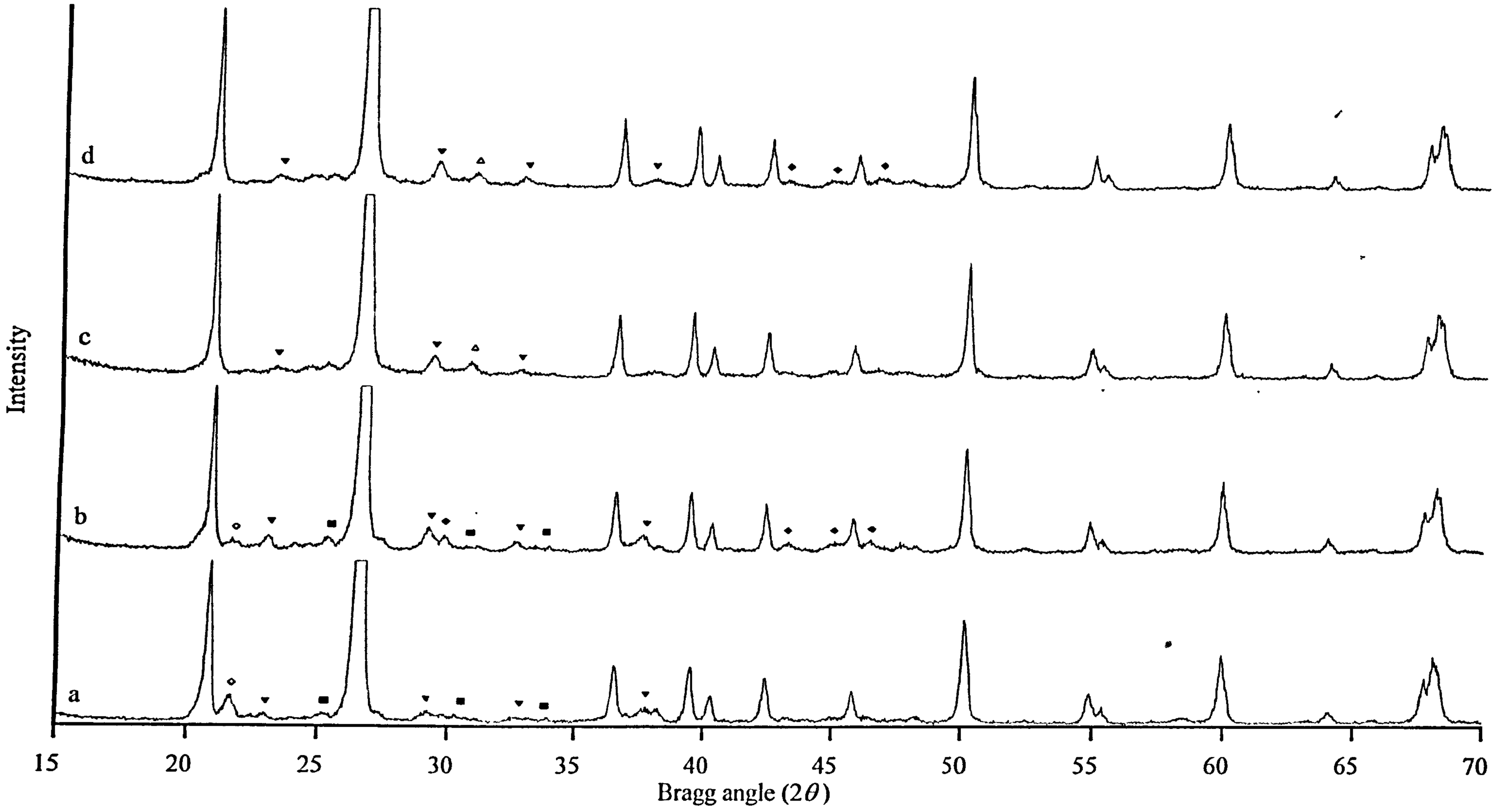

Figure 5.44 XRD patterns recorded for silica support materials loaded with 9.5 mass% lanthanum only, treated as follows (a) 750/5/0/N_2, (b) 800/5/0/N_2, (c) 750/5/80/N_2, and (d) 800/5/80/N_2. ■ indicates peaks due to LaOCl, △ indicates peaks due to La_2O_3, ◇ indicates peaks due to SiO_2, ▼ and ◆ indicate unknown components, and unlabelled peaks are due to the silica support material.

patterns indicate the formation of more phases (a portion of which could not be identified) and the background suggests that other amorphous phases may also be present.

Samples loaded with 1 mass% vanadium and 9.5 mass% lanthanum

These samples were subject to calcination and steam treatment at both 750°C and 800°C in both air and nitrogen atmospheres (listed in Table 5.13).

Figure 5.45 shows four XRD patterns recorded for the samples treated using air as a carrier gas. Calcination of the samples (Figure 5.45 (a) and (b)) results in the formation of two crystalline phases. LaOCl (indicated as ■) and $LaVO_4$ (indicated as □). The $LaVO_4$ phase observed is the same as that observed for the α-alumina support material. Its formation is independent of reaction temperature; similar observations were made for the α-alumina support materials under similar conditions (Figure 5.39 (a) and (b)). The amount of LaOCl formed remains relatively constant as the reaction temperature is increased. For the silica support materials loaded with 9.5 mass% lanthanum only, and treated under identical conditions, the lanthanum was present in the form of LaOCl and a second phase which could not be identified (Figure 5.43 (a) and (b)), no evidence for this unidentified phase could be found for the samples in the presence of vanadium.

The ^{51}V MAS NMR spectra for the calcined samples are given in Figure 5.46 (a) and (b). It can be seen that both exhibit a single resonance centred at $\delta(^{51}V) = -613\pm10$ ppm for the sample calcined at 750°C, and centred at $\delta(^{51}V) = -613\pm9$ ppm for the sample calcined at 800°C, both confirming the presence of $LaVO_4$. Comparing the two spectra it can be seen that similar amounts are present at both reaction temperatures in agreement with the XRD results.

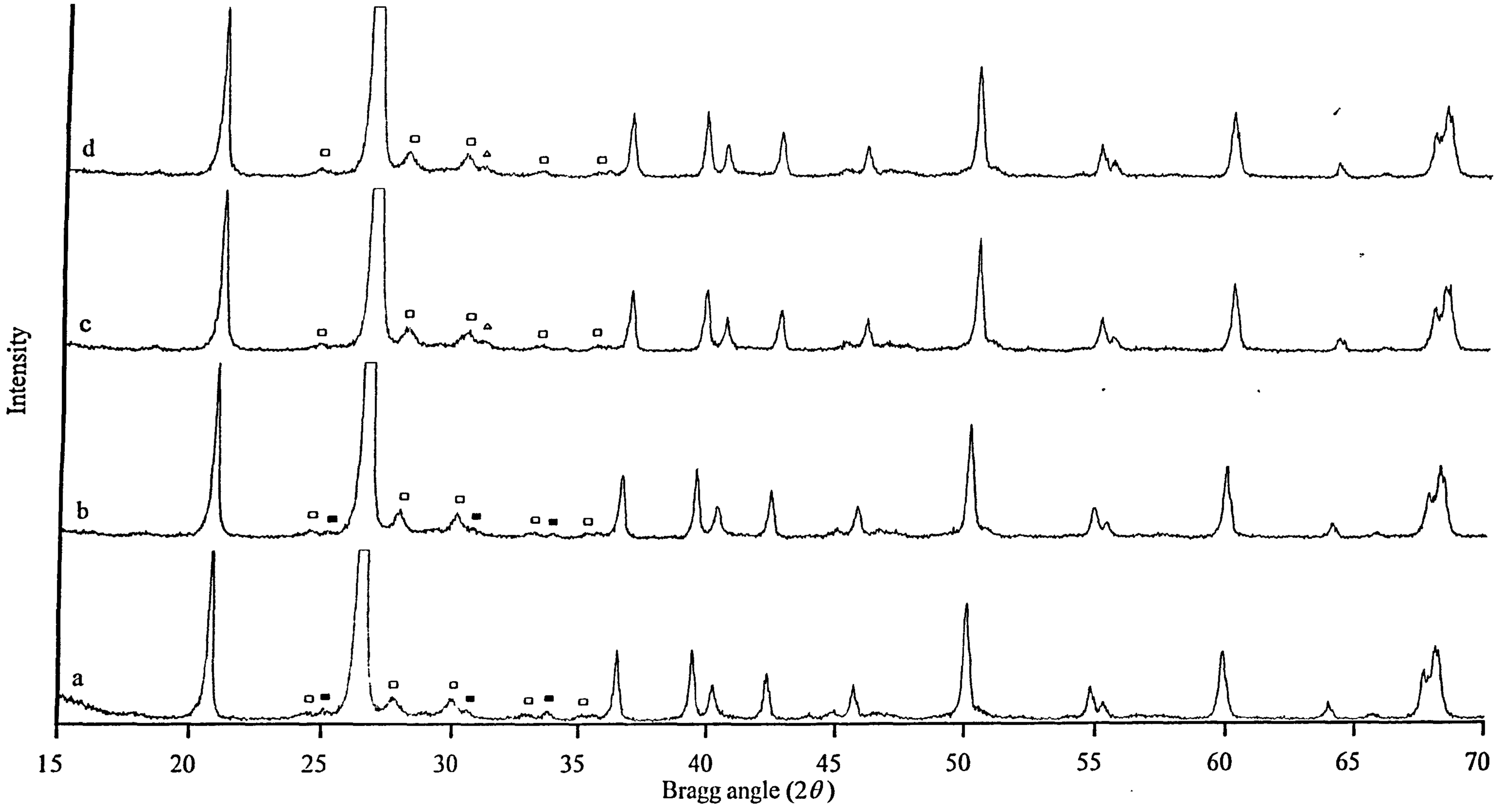

Figure 5.45 XRD patterns recorded for silica support materials loaded with 1 mass% vanadium and 9.5 mass% lanthanum, treated as follows (a) 750/5/0/AIR, (b) 800/5/0/AIR, (c) 750/5/80/AIR, and (d) 800/5/80/AIR. ■ indicates peaks due to LaOCl, Δ indicates peaks due to La_2O_3, □ indicates peaks due to $LaVO_4$, and unlabelled peaks are due to the silica support material.

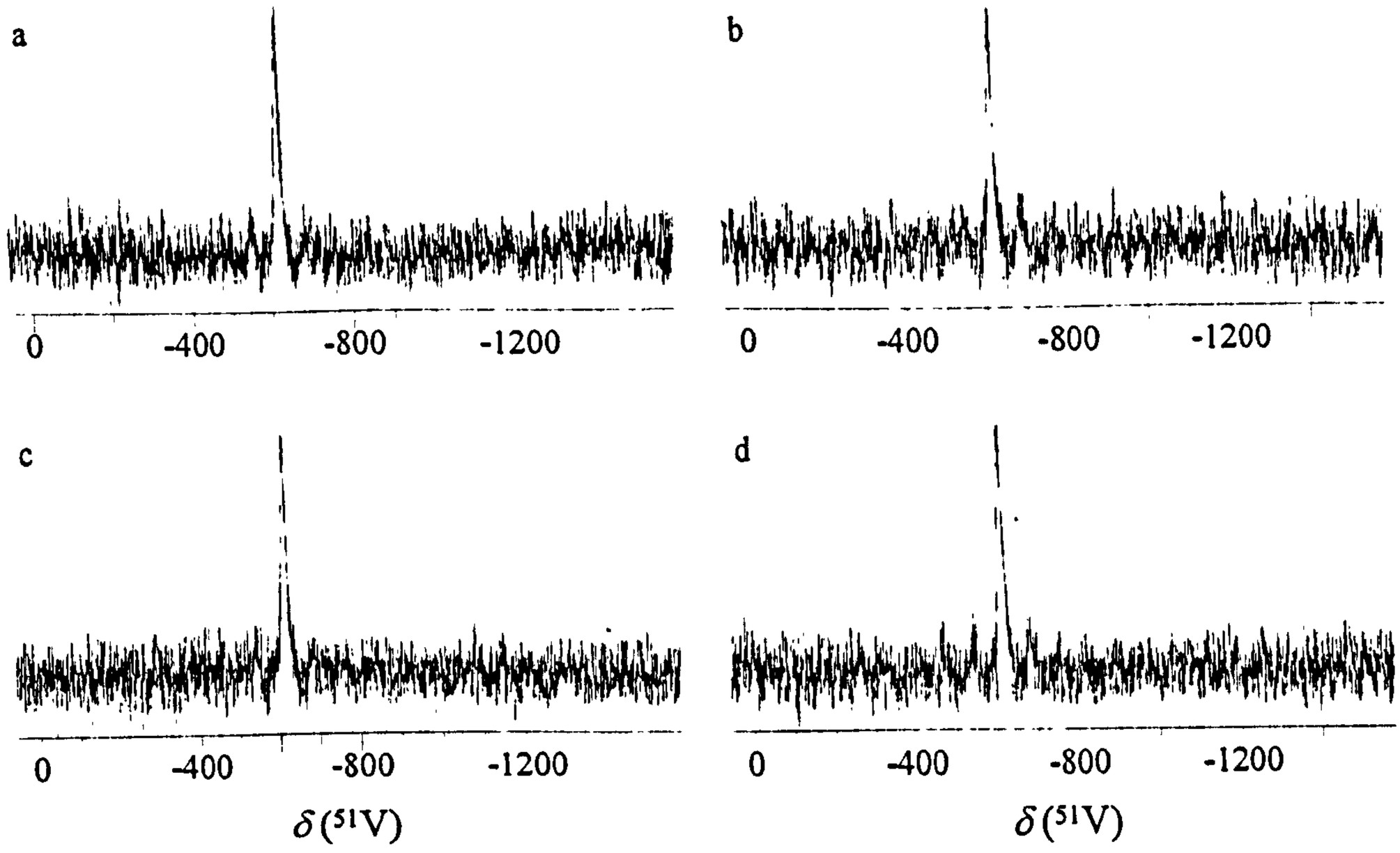

Figure 5.46 ^{51}V MAS NMR spectra observed at 105.075 MHz for the silica support materials loaded with 1 mass% vanadium and 9.5 mass% lanthanum treated as follows (a) 750/5/0/AIR, number of scans = 54 000, $\delta(^{51}V)$ = -613±10 ppm, (b) 800/5/0/AIR, number of scans = 47 000, $\delta(^{51}V)$ = -613±9 ppm, (c) 750/5/80/AIR, number of scans = 54 000, $\delta(^{51}V)$ = -612±8 ppm, and (d) 800/5/80/AIR, number of scans = 54 000, $\delta(^{51}V)$ = -612±9 ppm. External reference liquid $VOCl_3$, pulse delay = 1 s, pulse width = 2 μs and spinning frequency ~ 7 kHz.

Steam treatment of the samples (Figure 5.45 (c) and (d)) again results in two crystalline phases. However, under hydrothermal conditions the lanthanum is present as La_2O_3 (indicated as Δ) rather than LaOCl as observed when the samples where calcined. The amount of the $LaVO_4$ phase remains constant with temperature; furthermore, comparison with the samples that were calcined shows similar levels of $LaVO_4$ under all reaction conditions (Figure 5.45). Similar levels of the La_2O_3 phase are present under both reaction conditions.

The ^{51}V MAS NMR spectra for the steam-treated samples are given in Figure 5.46 (c) and (d). As observed with the calcined samples, both spectra show a single resonance, centred at $\delta(^{51}V)$ = -612±8 ppm for the sample calcined at 750°C and centred at $\delta(^{51}V)$ = -612±9 ppm for the sample calcined at 800°C, again confirming the presence of $LaVO_4$. Comparison of the spectra with the calcined samples confirms that similar amounts of $LaVO_4$ are observed under all reaction conditions. This is also consistent with the results obtained for the α-alumina support materials (Figure 5.40); although in the present case no evidence is found for the formation of $LaVO_3$.

The XRD results for the samples treated under a nitrogen atmosphere are given in Figure 5.47. Calcination of the samples (Figure 5.47 (a) and (b)) results in the formation of four detectable crystalline phases. For the sample that was calcined at 750°C diffraction peaks due to LaOCl (indicated as ■) and $LaVO_4$ (indicated as □) are visible, increasing the temperature to 800°C results in the loss of these two phases and the appearance of diffraction peaks assigned to two unidentified phases (indicated as ▼ and ◆) first observed for the silica support materials loaded with 9.5 mass% lanthanum only (it can be noted that the phase labelled ◆ only became apparent at the higher temperature of 800°C).

The ^{51}V MAS NMR spectra for the calcined samples reflect the reduction in concentration of $LaVO_4$ (Figure 5.48 (a) and (b)) as the temperature is increased. It can be seen that both show a single resonance, centred at $\delta(^{51}V)$ = -610±9 ppm for the sample calcined at 750°C and centred at $\delta(^{51}V)$ = -612 ppm for the sample calcined at 800°C, confirming the presence of $LaVO_4$. There is a large reduction in signal to noise as the temperature is increased, indicating reduced amounts of $LaVO_4$. This is not accompanied by the emergence of any further detectable resonances which suggests that a portion of the vanadium, at both reaction temperatures, is invisible to both MAS NMR and XRD.

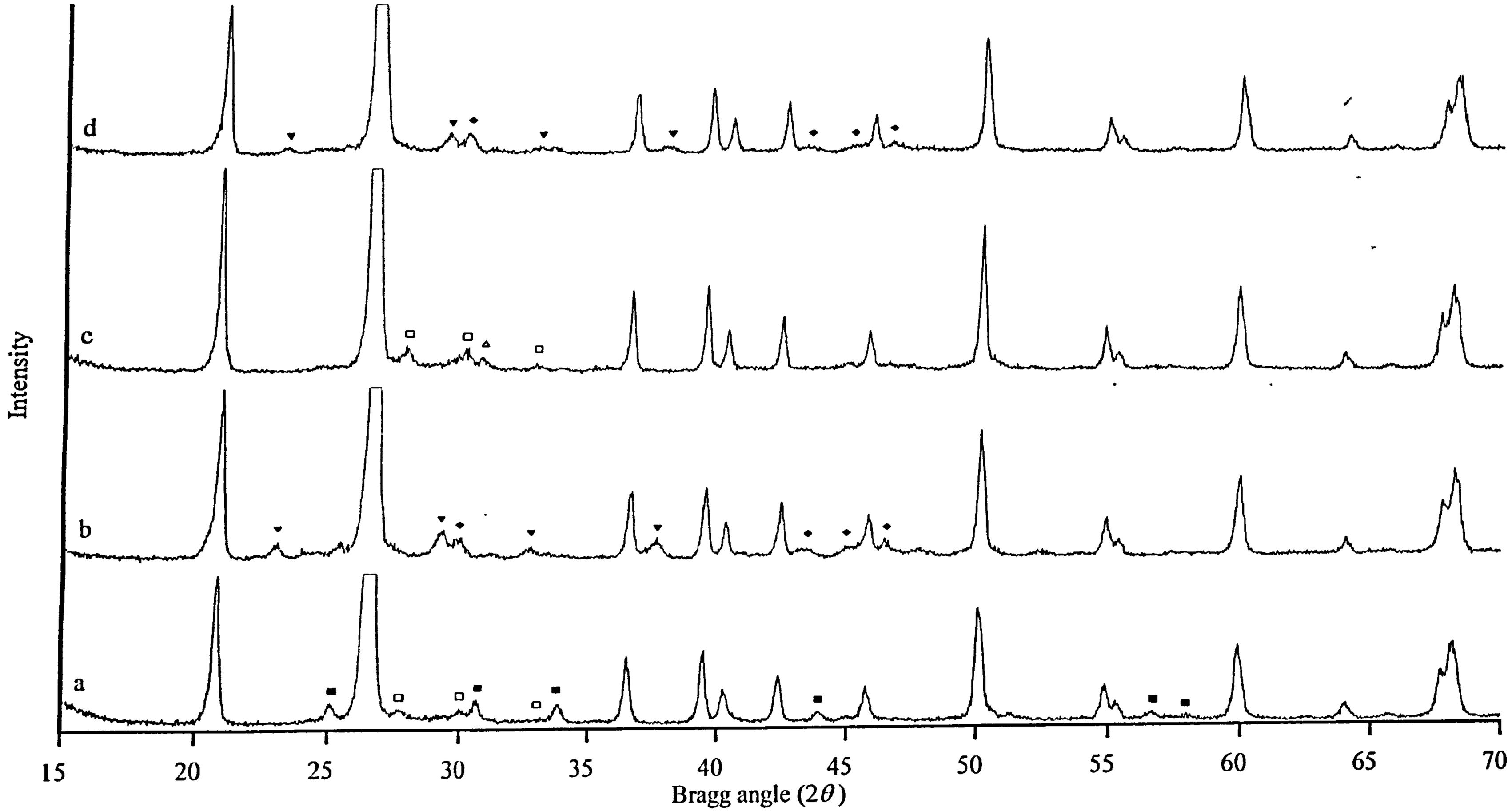

Figure 5.47 XRD patterns recorded for silica support materials loaded with 1 mass% vanadium and 9.5 mass% lanthanum, treated as follows (a) 750/5/0/N_2, (b) 800/5/0/N_2, (c) 750/5/80/N_2, and (d) 800/5/80/N_2. ■ indicates peaks due to LaOCl, Δ indicates peaks due to La_2O_3, □ indicates peaks due to $LaVO_4$, ▼ and ◆ indicate unknown components, and unlabelled peaks are due to the silica support material.

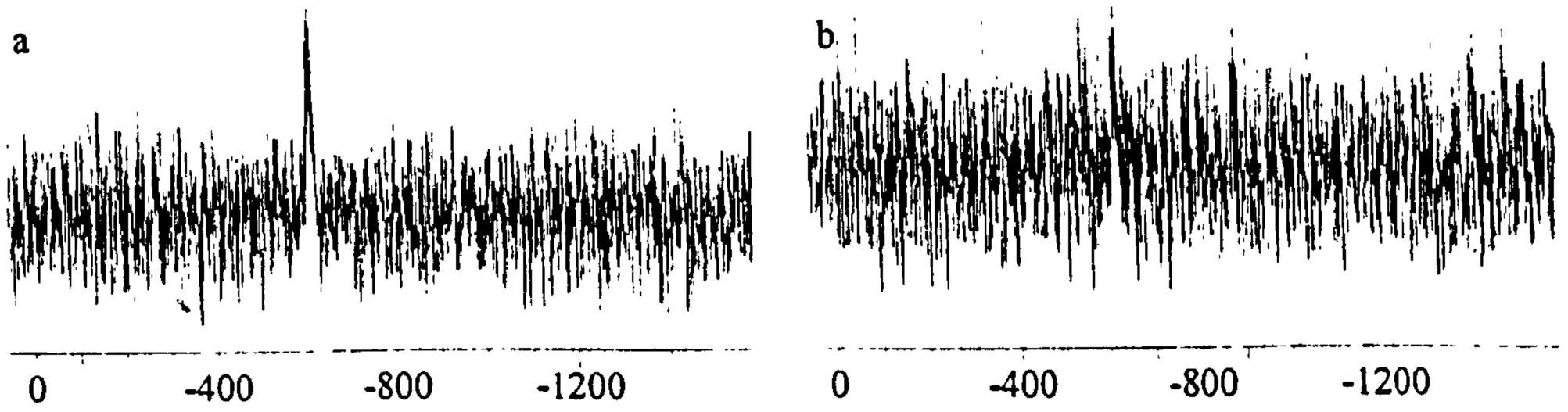

Figure 5.48 ^{51}V MAS NMR spectra observed at 105.075 MHz for the silica support materials loaded with 1 mass% vanadium and 9.5 mass% lanthanum treated as follows at (a) 750/5/0/N_2, number of scans = 57 000, $\delta(^{51}V)$ = -610±9 ppm, (b) 800/5/0/N_2, number of scans = 58 000, $\delta(^{51}V)$ = -612 ppm, (c) 750/5/80/N_2, number of scans = 50 000, $\delta(^{51}V)$ = -612±8 ppm, and (d) 800/5/80/N_2, number of scans = 54 000, $\delta(^{51}V)$ = -612 ppm. External reference liquid $VOCl_3$, pulse delay = 1 s, pulse width = 2 μs and spinning frequency ~ 7 kHz.

Reduced levels of $LaVO_4$ under a nitrogen atmosphere are consistent with the observations for the α-alumina support materials, and was attributed to the conditions being less favourable for the oxidation of vanadium from vanadium (IV) to vanadium (V). However, a further reduction as the temperature was increased from 750°C to 800°C was not observed for the α-alumina support materials. This decrease probably indicates that vanadium favours stability in some other form (not detectable by XRD or MAS NMR).

Steam treatment of the samples results in the formation of four different crystalline phases. $LaVO_4$ is formed at 750°C, increasing the temperature to 800°C results in a loss of this phase. This is consistent with the observations for the calcined samples. At 750°C the

formation of La_2O_3 is favoured over LaOCl, as for the calcined samples (Figure 5.47). At 800°C steam treatment results in the formation of the two unidentified phases, indicated as ▼ and ◆.

The ^{51}V MAS NMR spectra for the two steam treated samples are given in Figure 5.48. Both contain a single resonance centred at $\delta(^{51}V)$ = -612±8 ppm for the sample calcined at 750°C and centred at $\delta(^{51}V)$ = -612 ppm for the sample calcined at 800°C, confirming the presence of $LaVO_4$. The reduction in levels of $LaVO_4$ can be seen by the reduction in signal to noise as the temperature is increased from 750°C to 800°C. It can also be seen that increased levels of $LaVO_4$ are present for the steam-treated samples compared to those that were calcined. This is consistent with the observations for the α-alumina support materials (Figure 5.42), and is attributed to hydrothermal conditions being more oxidising.

Table 5.16 summarises the crystalline compounds observed after differing treatments of the silica support material loaded with 9.5 mass% lanthanum, both with and without vanadium.

5.4.4 Treatment of the Completely Degraded FCC Sample

Samples that were free from vanadium contamination were treated at 800°C under both air and nitrogen atmospheres (Table 5.12). These samples were essentially control experiments. The XRD patterns recorded did not significantly differ from that of the untreated sample presented in Figure 5.35.

Samples that were contaminated with 1 mass% vanadium were subject to a full array of treatment experiments (Table 5.13). Similarly, the XRD patterns recorded did not differ from the untreated sample (Figure 5.35). Figure 5.49 shows the ^{51}V MAS NMR spectrum recorded for the sample steam treated at 800°C using air as a carrier gas. No further NMR spectra were recorded in this series due to limited spectrometer time (Figure 5.49 was achieved by signal averaging for ~ 4 days).

Vanadium loading /mass%	Treatment conditions							
	750/5/0/AIR	800/5/0/AIR	750/5/80/AIR	800/5/80/AIR	750/5/0/N_2	800/5/0/N_2	750/5/80/N_2	800/5/80/N_2
0	LaOCl	LaOCl	LaOCl	La_2O_3	LaOCl SiO_2	LaOCl SiO_2	La_2O_3	La_2O_3
1	LaOCl $LaVO_4$	LaOCl $LaVO_4$	La_2O_3 $LaVO_4$	La_2O_3 $LaVO_4$	LaOCl $LaVO_4$	-	La_2O_3 $LaVO_4$	-

Table 5.16 Crystalline phases identified when silica loaded with 9.5 mass% lanthanum, with and without vanadium, is exposed to differing treatment conditions.

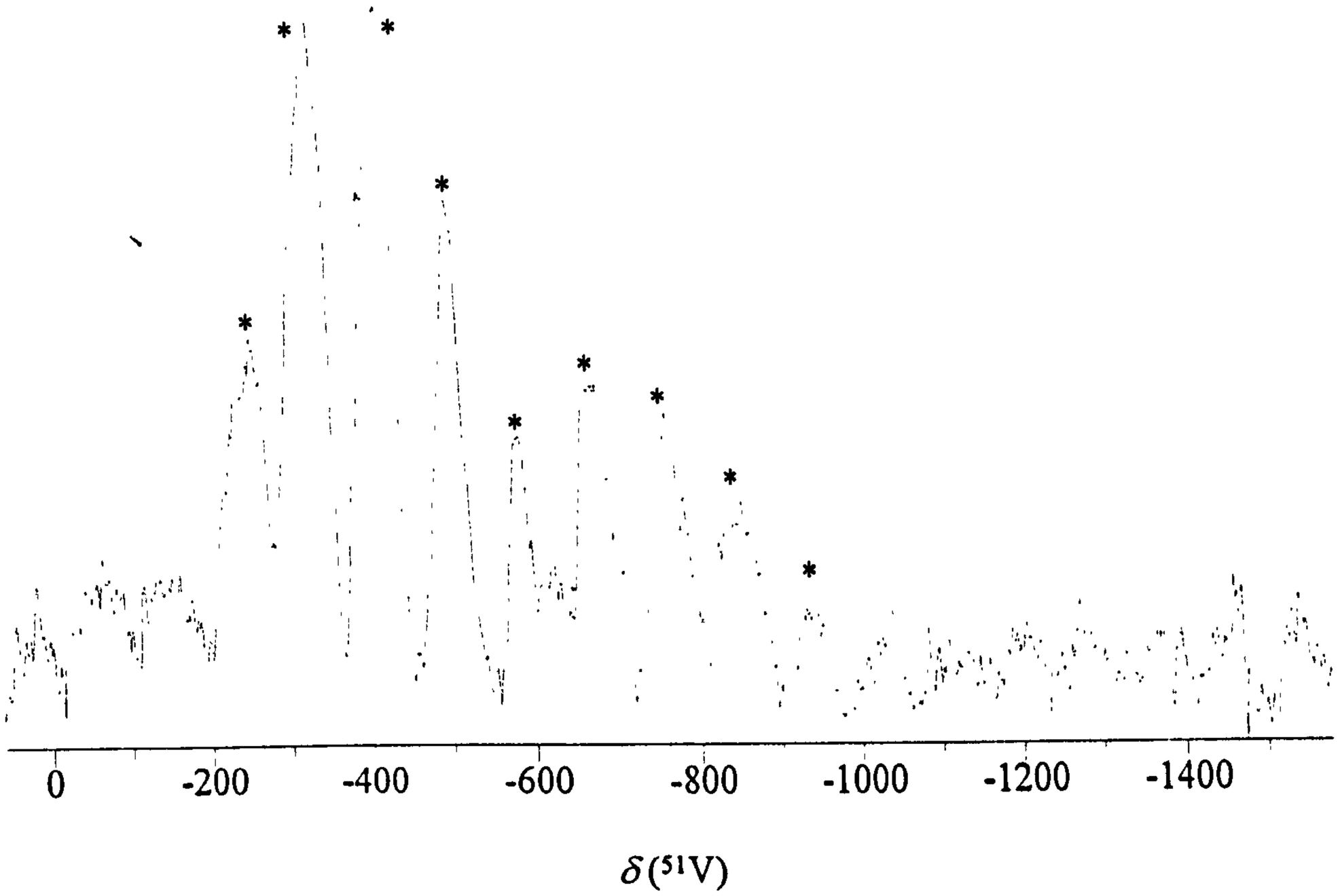

Figure 5.49 ^{51}V MAS NMR spectrum observed at 105.075 MHz for a sample of completely degraded alpha-54 contaminated with 1 mass% vanadium. The FID was filtered through an exponential window prior to Fourier transformation in order to increase sensitivity. External reference liquid $VOCl_3$, pulse delay = 1 s, pulse width = 2 μs, number of scans = 334 000, spinning frequency ~ 9 kHz. * labels signals separated by ~ 9 kHz.

It can be seen that the spectrum is relatively complicated and may contain contributions from several differently co-ordinated vanadium species. Two resonance signals can be identified within the spectrum. The resonance peaks, labelled *, are all present due to a single vanadium compound, this follows since all the peaks are separated by ~ 9 kHz, the spinning frequency. The overall form of the rotational sideband pattern is very similar to that for V_2O_5. The ^{51}V MAS NMR spectrum for this compound (although at a slower spinning frequency) is shown in Figure 5.50 and $\delta(^{51}V)$ = -610±10ppm. It is reasonable to suggest, therefore, that one of the resonance signals in Figure 5.49 is due to the presence of V_2O_5.

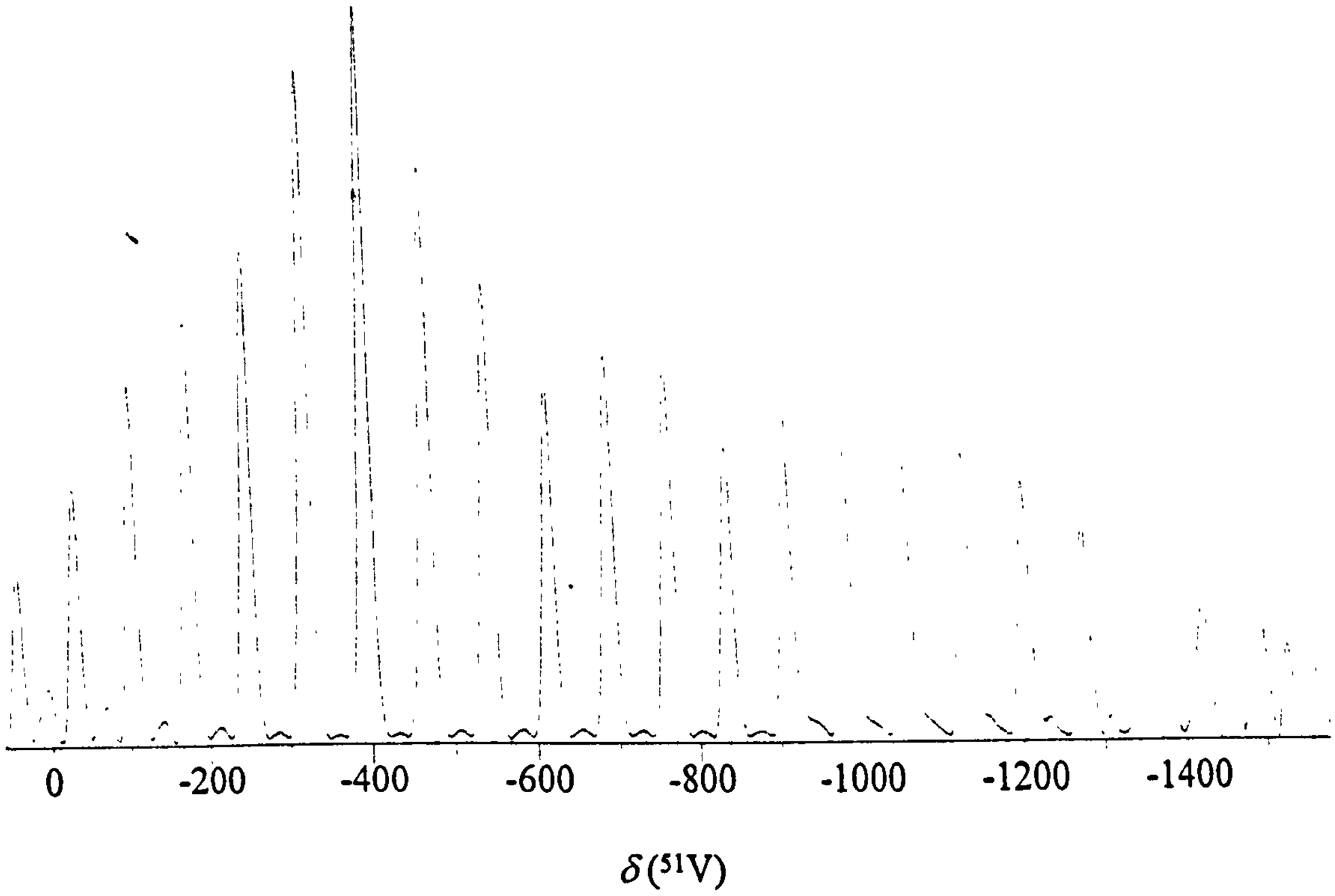

Figure 5.50 ^{51}V MAS NMR spectrum observed at 105.075 MHz for a sample of V_2O_5. External reference liquid $VOCl_3$, pulse delay = 1 s, pulse width = 2 μs, number of scans = 1000, spinning frequency ~ 7 kHz.

The second signal which can be identified in Figure 5.49 has no sideband manifold and $\delta(^{51}V) \sim$ -625 ppm. The resonance is thus more shielded than would be expected for $LaVO_4$. A strong possibility is that the resonance could be associated with vanadium in the mullite lattice. It is known that vanadium can be incorporated into the mullite lattice[5,19-20] although the levels are generally thought to be relatively small.

Based on the ^{51}V MAS NMR results presented in Sections 5.2 and 5.4, and those to be presented in Section 5.5, it might have been expected that resonance signals due to the presence of $CeVO_4$ ($\delta(^{51}V)$ = -435 ppm) and $LaVO_4$ ($\delta(^{51}V)$ = -610 ppm) would have been observed. From the spectrum it is not clear whether these compounds are present because resonance signals from these compounds would be masked by the spinning sideband manifold of V_2O_5. However it may be the case that the RE present in the zeolite-Y lattice, when forced to redistribute upon severe heat treatment, may have formed very stable compounds (possibly oxides) which do not react with the vanadium dopant.

5.4.5 Summary

Of the series of samples for each support material those containing lanthanum only and lanthanum combined with vanadium produced the most interesting results. The other series of samples essentially acted as controls.

For the samples with only vanadium present both XRD and MAS NMR did not identify the presence of any specific vanadium species. For samples that were loaded with both lanthanum and vanadium the presence of $LaVO_4$ was observed, to some extent, for all samples. The amount present was found to be a function of the treatment atmosphere, with the greatest levels being found when air was used as a carrier gas. Hydrothermal conditions were also found to aid the formation of $LaVO_4$ under a nitrogen atmosphere. Both observations indicate that the formation of $LaVO_4$ is related to the oxidising capability of the atmosphere.

Two distinct differences were observed which relate to vanadium/lanthanum chemistry on the two support materials. Firstly for the α-alumina support materials the formation of $LaVO_3$ was observed, except with samples that were hydrothermally treated under a nitrogen atmosphere: no evidence could be found for the formation of $LaVO_3$ on the silica support materials. Secondly with the silica support material it was observed, under a nitrogen atmosphere, that the formation of $LaVO_4$ was decreased when the temperature was increased from 750°C to 800°C (Figures 5.47 and 5.48), for the α-alumina support materials similar amounts were observed at both reaction temperatures (Figures 5.41 and 5.42). Both of these observations were not anticipated in view of the reaction conditions employed. The formation of $LaVO_3$ requires reduction of vanadium from vanadium (IV) to vanadium (III) and the reaction conditions, particularly under an air atmosphere, are predominantly oxidising; the mechanism by which reduction of vanadium occurs is unclear. For the effect of temperature on the formation of $LaVO_4$ it would be expected that at the higher reaction temperature the oxidising atmosphere would be relatively unaltered and similar levels of $LaVO_4$ would be formed. This suggests that on silica support materials, at 800°C, vanadium is present in a form other than $LaVO_4$. Interestingly, a nitrogen atmosphere and a temperature of 800°C were the only conditions that an unknown

phase (indicated by ◆) was observed. This phase cannot contain vanadium since it was also observed for the silica support materials loaded with 9.5 mass% lanthanum (Figure 5.44). It may be that this phase represents a stable lanthanum-containing compound and the vanadium is unable to compete successfully for the lanthanum. The same may be true for other phases that are present on the surface of the silica support materials. On the α-alumina support materials the vanadium may be able to compete with greater success and $LaVO_4$ formation is facile. It is certainly true that with the α-alumina support materials that as the amounts of lanthanum/vanadium containing compounds increases, then the levels of the lanthanum-containing compounds reduces, as would be predicted.

For the completely degraded samples the ^{51}V MAS NMR spectrum suggest the presence of V_2O_5. The fate of the RE ions, redistributed after thermal treatments, is not clear.

5.5 General Rare Earth Chemistry

In order to gain more information about the RE/vanadium chemistry that has been observed for the zeolite-Y and support material (silica and α-alumina) samples, a series of solid state reactions were performed using differing combinations of RE and vanadium containing compounds (Table 4.7). Significantly larger molar quantities of vanadium were used for these reactions, and this facilitated the detection of new crystalline phases by both XRD and ^{51}V MAS NMR. The reactions were carried out using a horizontal tube furnace arrangement (Section 4.4), with similar reaction conditions to those used for the zeolite-Y and support material samples; that is, calcination and steam treatment at 800°C for five hours using both air and nitrogen atmospheres.

5.5.1 Preparation of $LaVO_4$

Preparation of this material was of direct interest for characterisation purposes. It was also of interest to expose this compound to hydrothermal treatments, similar to those used for the catalytic samples. The method of preparation has been described in Section 4.4.

It should be noted that the reaction is highly exothermic and thus an arc melting method of preparation[45-49] would have been preferable to carrying out the reaction in a sealed quartz container. (Arc melting was not available to us).

A lime green powder was obtained from the reaction of V_2O_5 with La_2O_3 and this was confirmed to be almost phase pure $LaVO_4$ by XRD (Figure 5.51). The two small diffraction peaks, labelled ◆, are not due to the $LaVO_4$ phase, nor to V_2O_5 or La_2O_3; these peaks are probably due to contamination from the quartz container. The ^{51}V MAS NMR spectrum obtained for $LaVO_4$ is given in Figure 5.52. It can be seen that the spectrum consists of a single sharp resonance, centred at $\delta(^{51}V) = -611 \pm 6$ ppm, with equally spaced spinning-sidebands either side of the central line. The chemical shift is in good agreement with that reported by Lapina and co-workers[24] for $LaVO_4$.

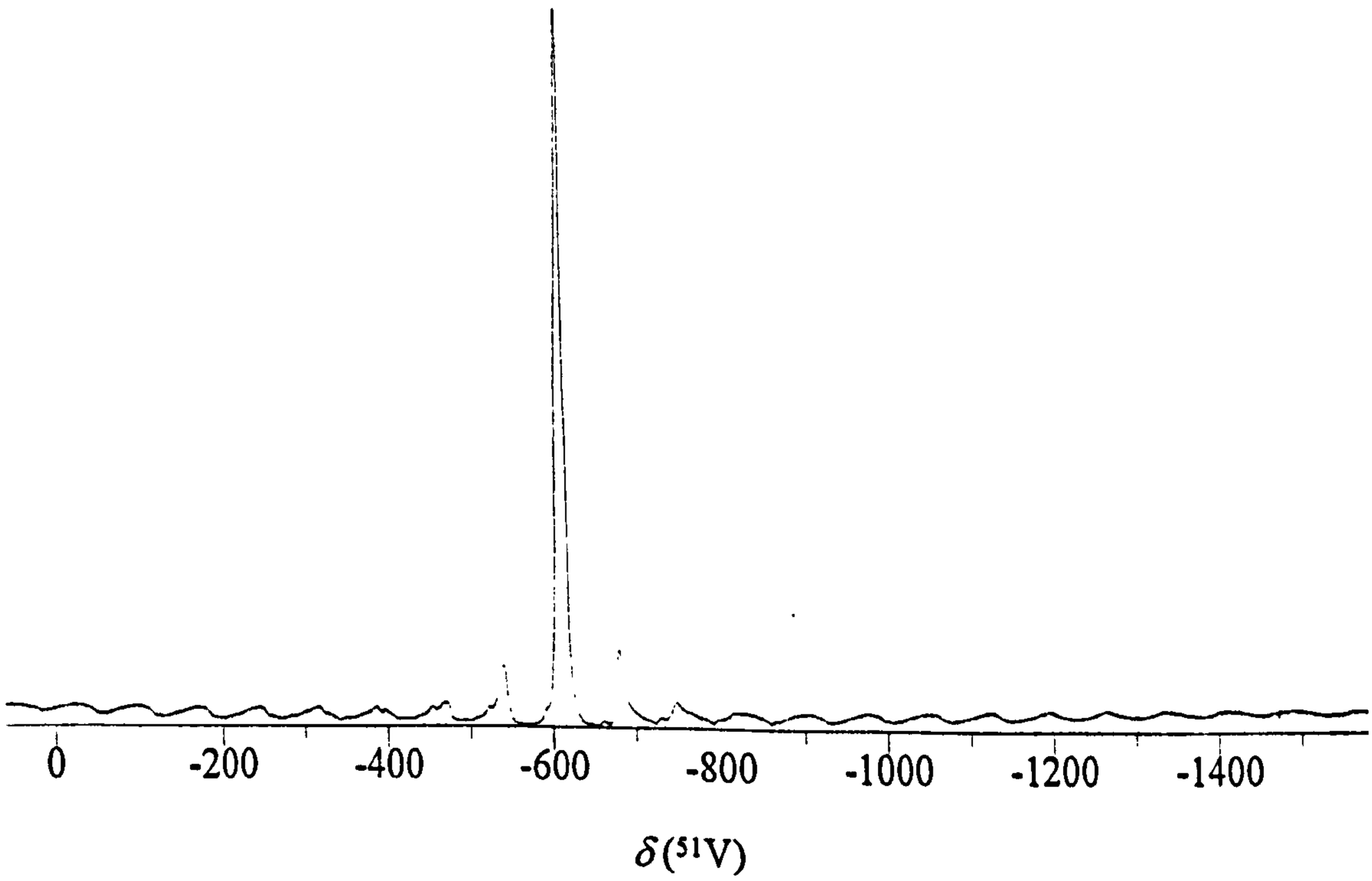

Figure 5.52 ^{51}V MAS NMR spectrum observed at 105.075 MHz for a sample of $LaVO_4$. Spectrum recorded using a pulse delay = 1 s, pulse width = 2 μs, number of scans = 2000, spinning frequency ~ 7.5 kHz, external reference liquid $VOCl_3$ and $\delta(^{51}V) = -611 \pm 6$ ppm.

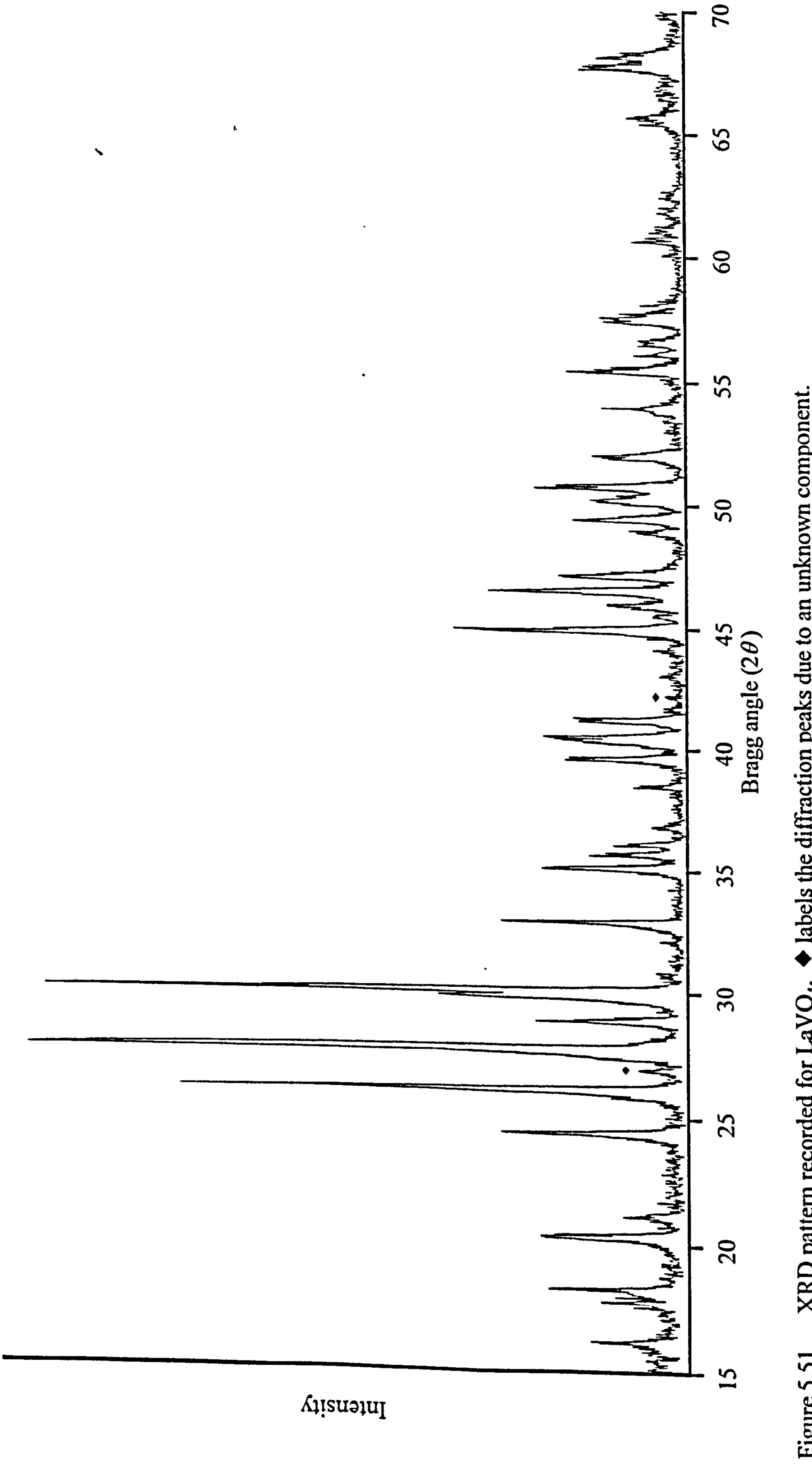

Figure 5.51 XRD pattern recorded for $LaVO_4$. ◆ labels the diffraction peaks due to an unknown component.

The second-order nature of the central line has been analysed in detail and quadrupolar parameters extracted are in good agreement with broad line studies.[50] These parameters have also been calculated with reasonable success via *ab initio* methods based on the known structure of $LaVO_4$.[51]

Steam treatment of the $LaVO_4$ phase, by itself, had little effect upon the $LaVO_4$ phase: the XRD pattern and ^{51}V MAS NMR spectrum obtained were similar to those presented in Figures 5.51 and 5.52.

5.5.2 Reactions Involving Vanadyl Naphthenate 3%

Four different RE containing compounds were reacted with vanadyl naphthenate 3% (Table 4.7). Only the results from the reactions involving $LaCl_3$ and $CeCl_3$ will be discussed in detail here. The reactions carried out with $La(NO_3)_3$ and La_2O_3 were found to be considerably more complex: a short summary of these reactions are given later in this section.

Reaction of vanadyl naphthenate 3% with lanthanum trichloride

Calcination of a mixture of vanadyl naphthenate 3% with lanthanum trichloride at 800°C for 5 hours using air as a carrier gas resulted in the formation of two crystalline phases (Figure 5.53(a)), LaOCl (peaks labelled ■) and $LaVO_4$ (peaks labelled ◆). Steam treatment at 800°C for 5 hours using air as a carrier gas (Figure 5.53(b)) again resulted in the formation of LaOCl (peaks labelled ■) and $LaVO_4$ (peaks labelled ◆) together with a third unidentified phase (peaks labelled ▲). The LaOCl phase, corresponding to JCPDS reference file No. 08-0477, is the same as that observed on the surface of the α-alumina support materials (Section 5.4) when treated under similar reaction conditions. The ^{51}V MAS NMR spectra obtained for the two treated samples are given in Figure 5.54(a) and (b). Figure 5.54(a), for the calcined sample, is similar to that reported for $LaVO_4$ in Section 5.5.1 (Figure 5.52) with a single sharp resonance centred at $\delta(^{51}V) = -610\pm6$ ppm, confirming the XRD result that vanadium is present as $LaVO_4$. The introduction of steam

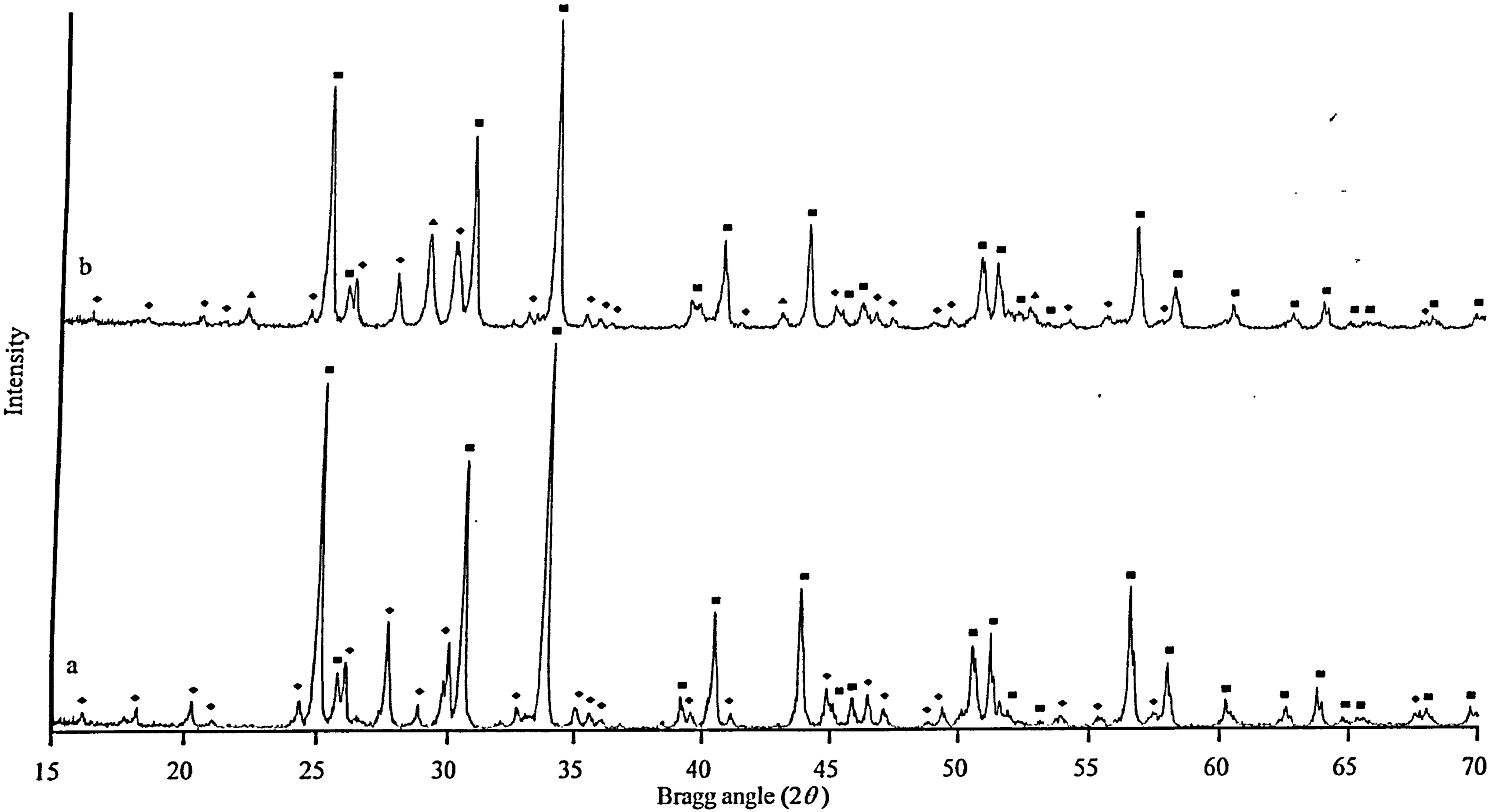

Figure 5.53 XRD patterns recorded for a mixture of vanadyl naphthenate 3% and lanthanum trichloride treated at (a) 800/5/0/AIR, and (b) 800/5/80/AIR. ■ labels the diffraction peaks due to LaOCl, ◆ labels the diffraction peaks due to $LaVO_4$, and ▲ labels the diffraction peaks due to an unknown component.

into the system results in an additional small resonance in the ^{51}V MAS NMR spectrum (Figure 5.54(b)) centred at $\delta(^{51}V)$ = -571±11 ppm. This ^{51}V MAS NMR result points to the unidentified phase found in the corresponding XRD pattern to be a vanadium-containing compound. In this context it is interesting that on a qualitative basis there seems to be relatively less $LaVO_4$ in the XRD pattern for the steam-treated material (Figure 5.53(b)). Lapina and co-workers,[24] have observed a ^{51}V NMR resonance signal: $\delta(^{51}V)$ = -570 ppm for experiments involving V_2O_5 supported on MgO or Al_2O_3. They concluded that this signal was probably due to surface clusters in which the vanadium was in a distorted tetrahedral environment. It is not clear whether surface clusters are important in the present work, nonetheless it seems that the unidentified crystalline compound may have vanadium in a similar distorted geometry. Table 5.17 summarises the XRD and ^{51}V MAS NMR data for this compound.

X-ray diffraction data	^{51}V MAS NMR data
Diffraction peaks observed at:	Single resonance observed at:
22, 28.5, 43 and 57.5°, in 2θ	$\delta(^{51}V)$ = -571±11 ppm

Table 5.17 XRD and ^{51}V MAS NMR data obtained for the unidentified phase observed after steam treatment of $LaCl_3$ with vanadyl naphthenate 3%.

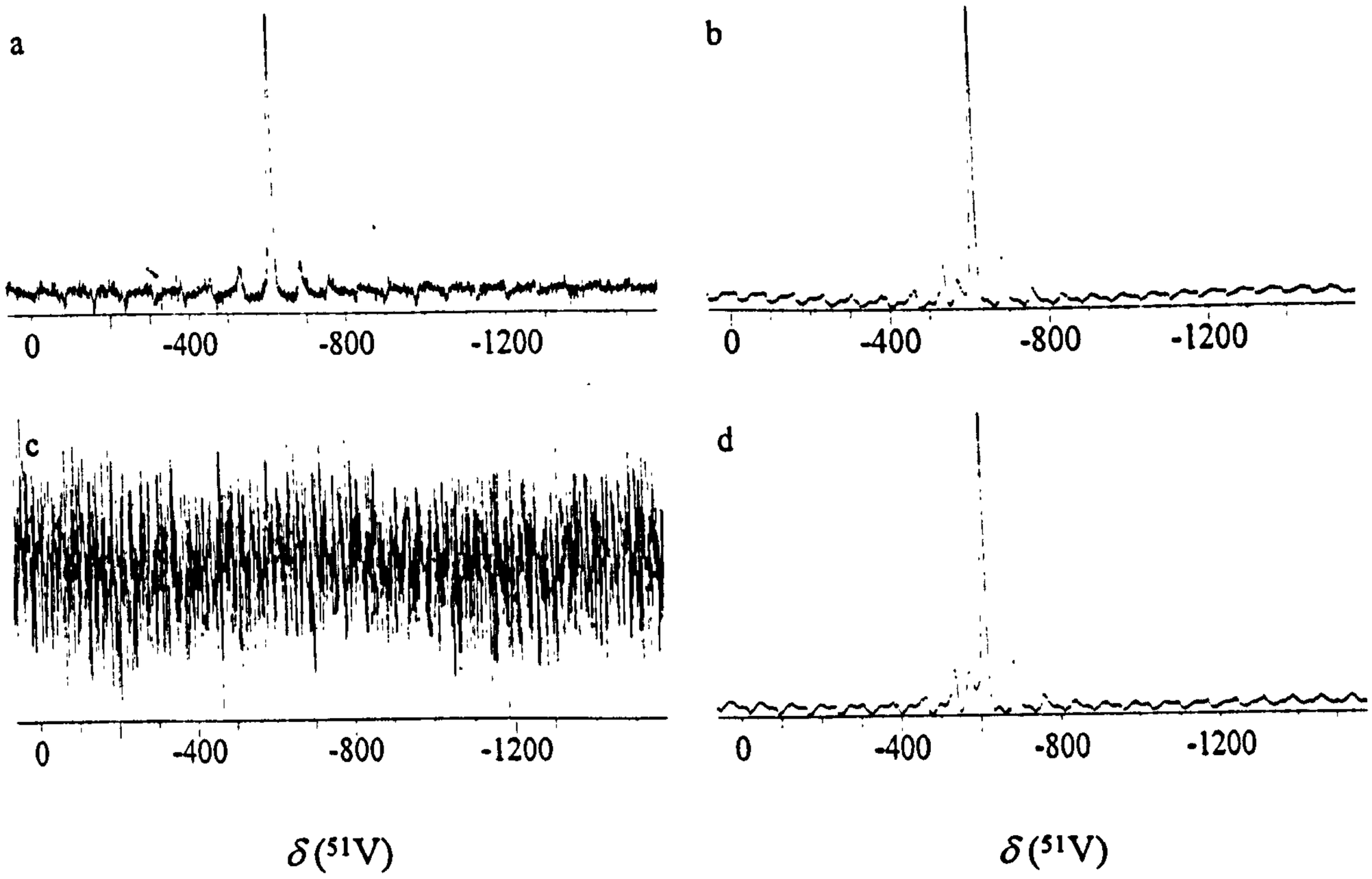

Figure 5.54 ^{51}V MAS NMR spectra observed at 105.075 MHz for a mixture of vanadyl naphthenate 3% and lanthanum trichloride treated under differing conditions. Spectra recorded using a pulse delay = 1 s, pulse width = 2 μs, spinning frequency ~ 7.5 kHz and external reference liquid $VOCl_3$. With the mixture treated at (a) 800/5/0/AIR, number of scans = 7407 and $\delta(^{51}V)$ = -610±6 ppm, (b) 800/5/80/AIR, number of scans = 10 000, $\delta(^{51}V)$ = -611±5 ppm and $\delta(^{51}V)$ = -571±11 ppm, (c) 800/5/0/N_2, number of scans = 10 000, and (d) 800/5/80/N_2, number of scans = 61 000, $\delta(^{51}V)$ = -610±6 ppm and $\delta(^{51}V)$ = -571 ppm.

Calcination of the vanadyl naphthenate 3% and lanthanum trichloride mixture at 800°C for 5 hours under a nitrogen atmosphere had a marked effect on the product distribution (Figure 5.55(a)) with effectively only LaOCl being formed. Positive evidence for vanadium containing species could not be found, this is reflected in the ^{51}V MAS NMR spectrum (Figure 5.54(c)) where no vanadium signals could be detected. It is probable that the vanadium could be present in a single, or series, of paramagnetic compounds.

Steam treatment under a nitrogen atmosphere (Figure 5.55(b)) produced a similar product distribution to that observed for the sample steam treated using air as a carrier gas. That is,

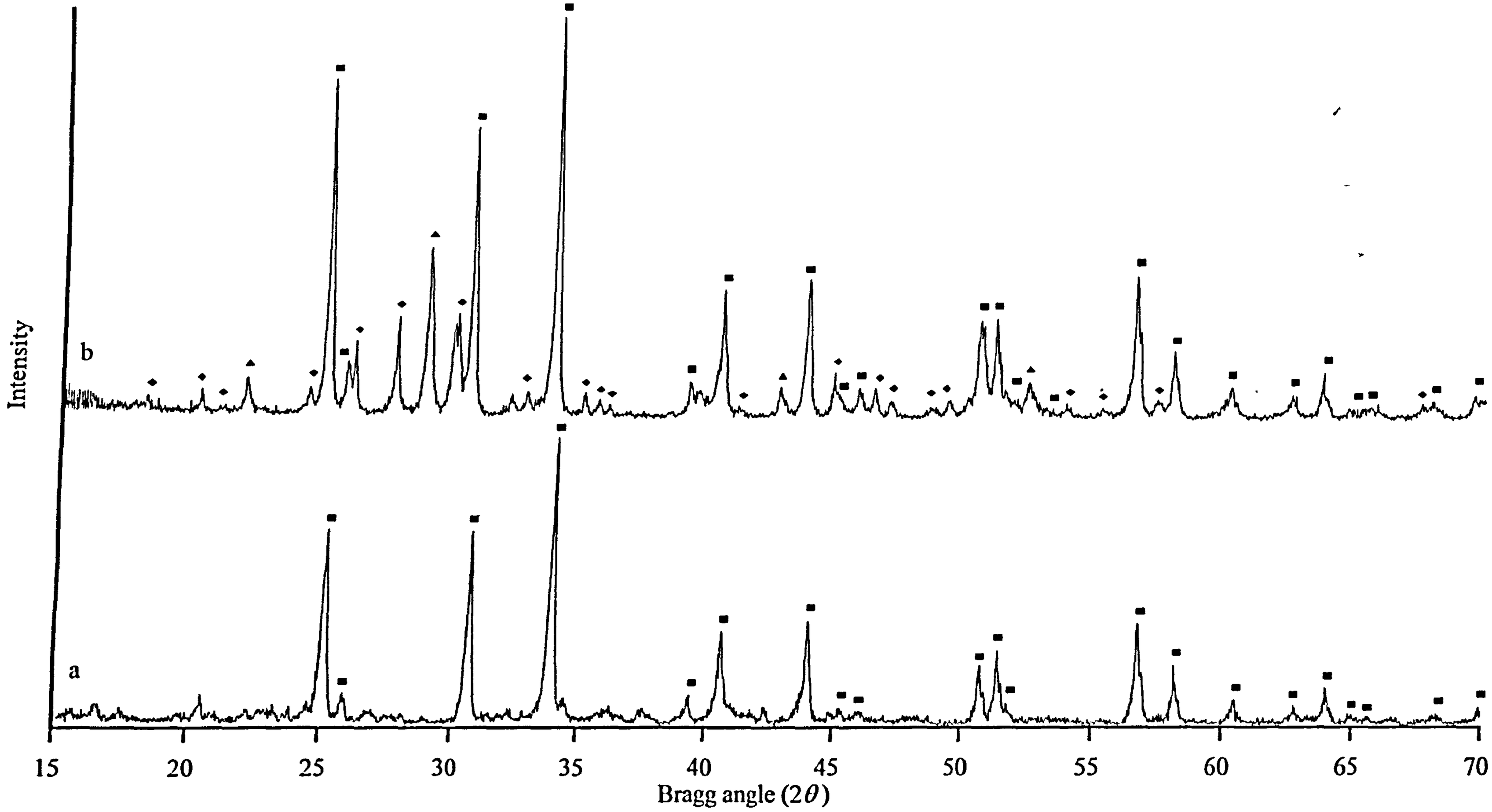

Figure 5.55 XRD patterns recorded for a mixture of vanadyl naphthenate 3% and lanthanum trichloride treated at (a) 800/5/0/N_2, and (b) 800/5/80/N_2. ■ labels the diffraction peaks due to LaOCl, ◆ labels the diffraction peaks due to $LaVO_4$, and ▲ labels the diffraction peaks due to an unknown component.

the formation of LaOCl (peaks labelled ■), $LaVO_4$ (peaks labelled ◆) together with an unidentified compound, as already discussed (peaks labelled ▲). This similarity in product distribution is also observed in the ^{51}V MAS NMR spectrum (Figure 5.54(d)), where a similar MAS spectrum is observed to that obtained for the sample steam treated under air.

The results from the reaction of vanadyl naphthenate 3% and lanthanum trichloride show that under conditions that favour the oxidation of the vanadium from an oxidation state of +4 to +5, then $LaVO_4$ is the major vanadium containing reaction product. Under conditions were oxidation of the vanadium is not favoured (800/5/0/N_2) then vanadium remains in a lower oxidation state. This behaviour is similar to that observed on the surface of the support materials where the concentration of $LaVO_4$ was dependent upon the severity of the oxidative conditions (Section 5.4). Interestingly, steam treatment also results in the formation of a second vanadium-containing species (but not positively identified); this was not found with the silica and α-alumina support materials. The formation of LaOCl was common to all experiments.

Reaction of vanadyl naphthenate 3% with cerium trichloride

Treatment of vanadyl naphthenate 3% with cerium trichloride using air as a carrier gas gave well defined results. Both calcination and steam treatment (Figure 5.56) resulted in the formation of CeO_2 (peaks labelled □, corresponding to JCPDS data base file No. 04-0593) and $CeVO_4$ (peaks labelled ◇ corresponding to JCPDS data base file No. 12-0757). An interesting point is the oxidation state of the excess cerium, here the cerium is oxidised from cerium (III) to cerium (IV); furthermore there is no evidence for the formation of an oxychloride. $CeVO_4$ is a paramagnetic compound since cerium (III) has a single unpaired electron in the 4f shell.

The ^{51}V MAS NMR spectra, for the samples treated in air, are comparable and in both cases consist of a single resonance centred at $\delta(^{51}V)$ = -437±7 ppm (calcined sample Figure 5.57(a)) and $\delta(^{51}V)$ = -435±7 ppm (steam treated sample Figure 5.57(b)) with equally spaced spinning-sidebands either side of the central transition. There is no report of $\delta(^{51}V)$ for $CeVO_4$ in the literature: clearly from the present work $\delta(^{51}V)$ = -436±7 ppm.

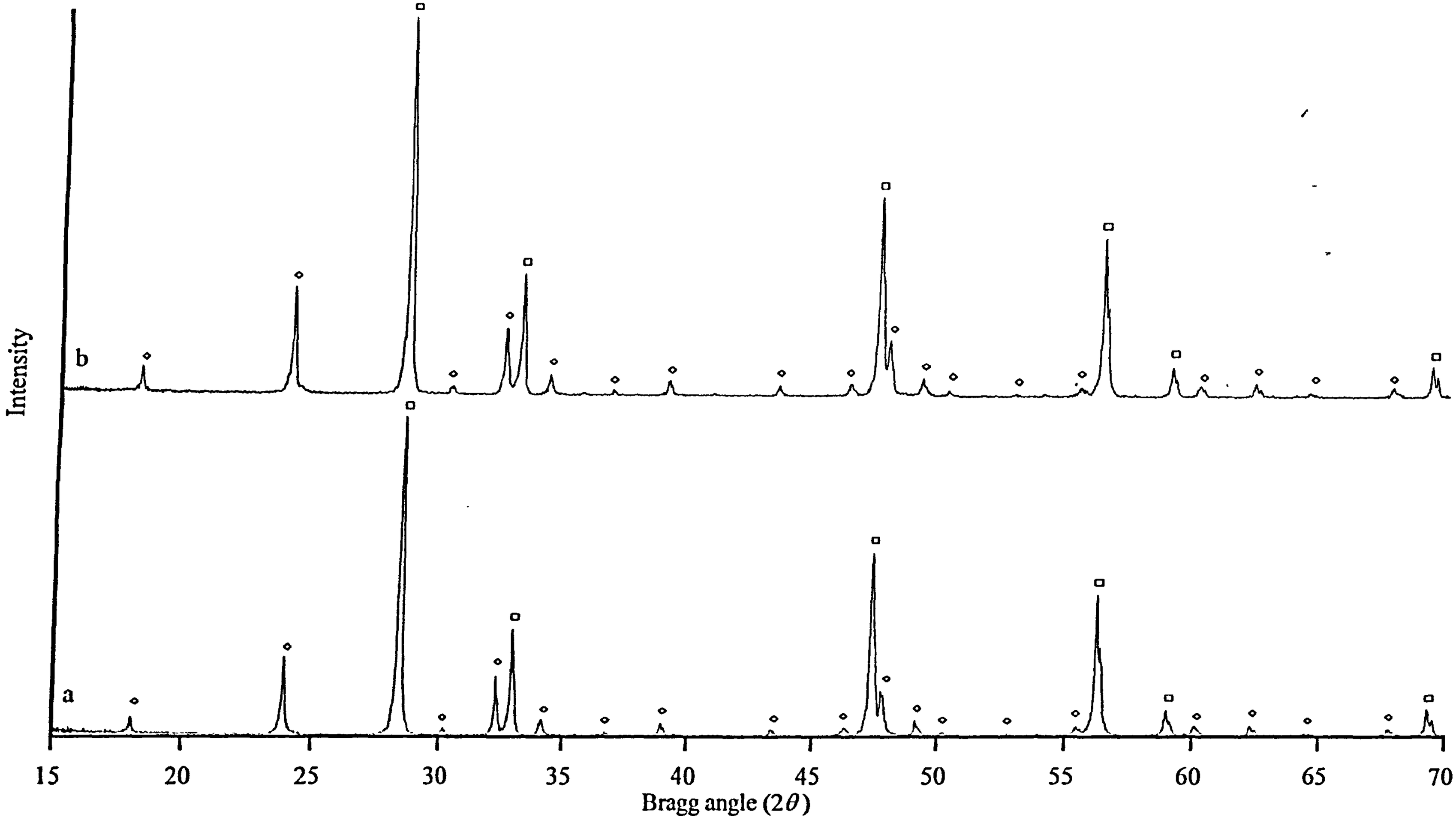

Figure 5.56 XRD patterns recorded for a mixture of vanadyl naphthenate 3% and cerium chloride treated at (a) 800/5/0/AIR, and (b) 800/5/80/AIR. □ labels the diffraction peaks due to CeO_2, ◇ labels the diffraction peaks due to $CeVO_4$.

The enhancement of the spinning sideband manifold is typical of that expected for the MAS NMR spectrum of a paramagnetic solid.[52]

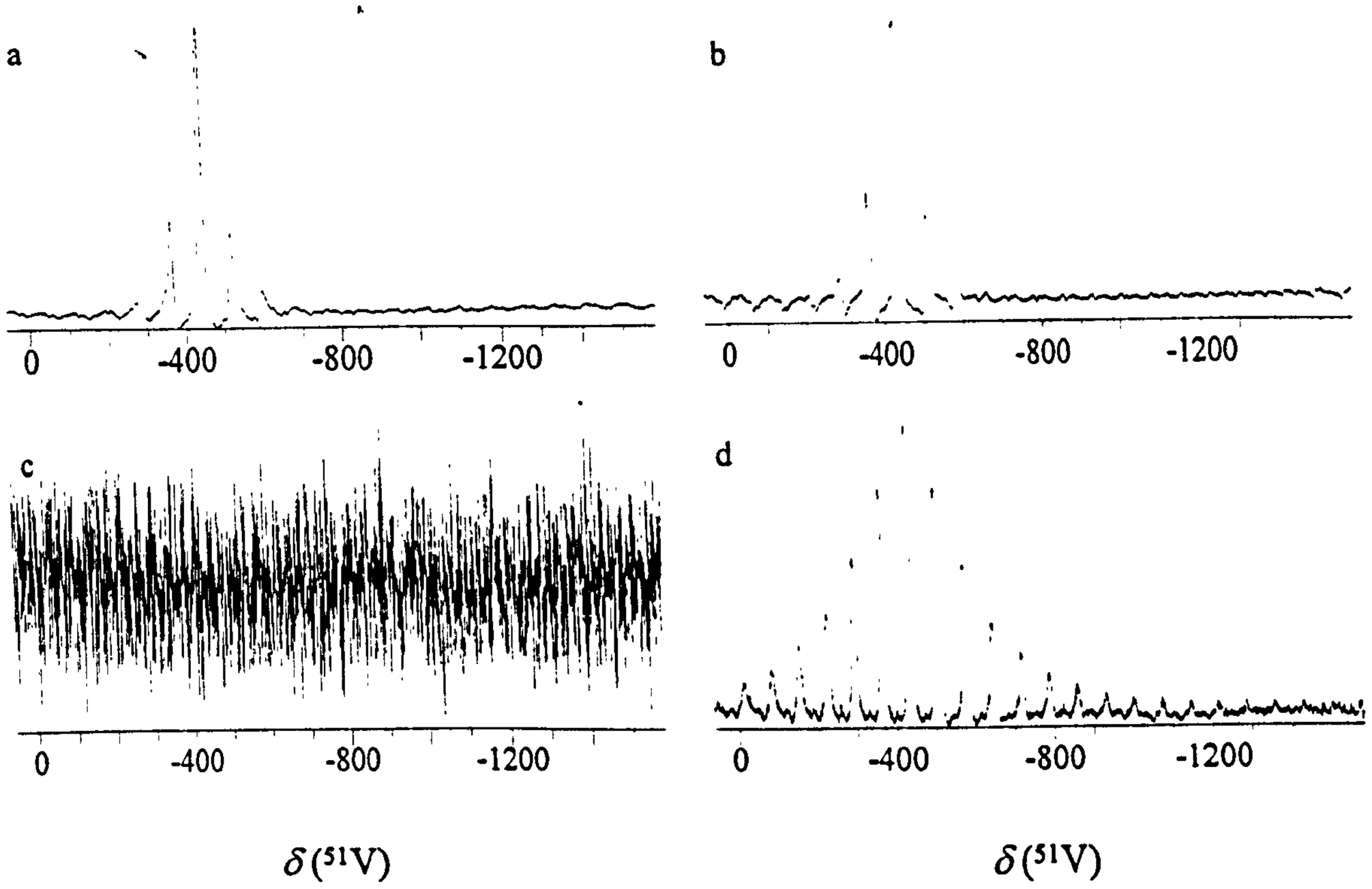

Figure 5.57 ^{51}V MAS NMR spectra observed at 105.075 MHz for a mixture of vanadyl naphthenate 3% and cerium trichloride treated under differing conditions. Spectra recorded using a pulse delay = 1 s, pulse width = 2 μs, spinning frequency ~ 7.5 kHz and external reference liquid $VOCl_3$. With the mixture treated at (a) 800/5/0/AIR, number of scans = 9000 and $\delta(^{51}V)$ = -437±7 ppm, (b) 800/5/80/AIR, number of scans = 9500, $\delta(^{51}V)$ = -435±7 ppm, (c) 800/5/0/N_2, number of scans = 61 000, and (d) 800/5/80/N_2, number of scans = 9000, $\delta(^{51}V)$ = -435±6 ppm.

Steam treatment under a nitrogen atmosphere produces a similar product distribution to treatment under an air atmosphere (Figure 5.58(b)) with CeO_2 (peaks labelled □) and $CeVO_4$ (peaks labelled ◇) observed. The ^{51}V MAS NMR spectrum observed (Figure 5.57(d)), however, is markedly different from that for the samples treated under air. In general the spinning sideband manifold in a paramagnetic solid is influenced by the distribution of paramagnetic ions within the solid.[52] It is thus difficult to see why the observed MAS NMR spectra should change so markedly if it is due solely to $CeVO_4$: it

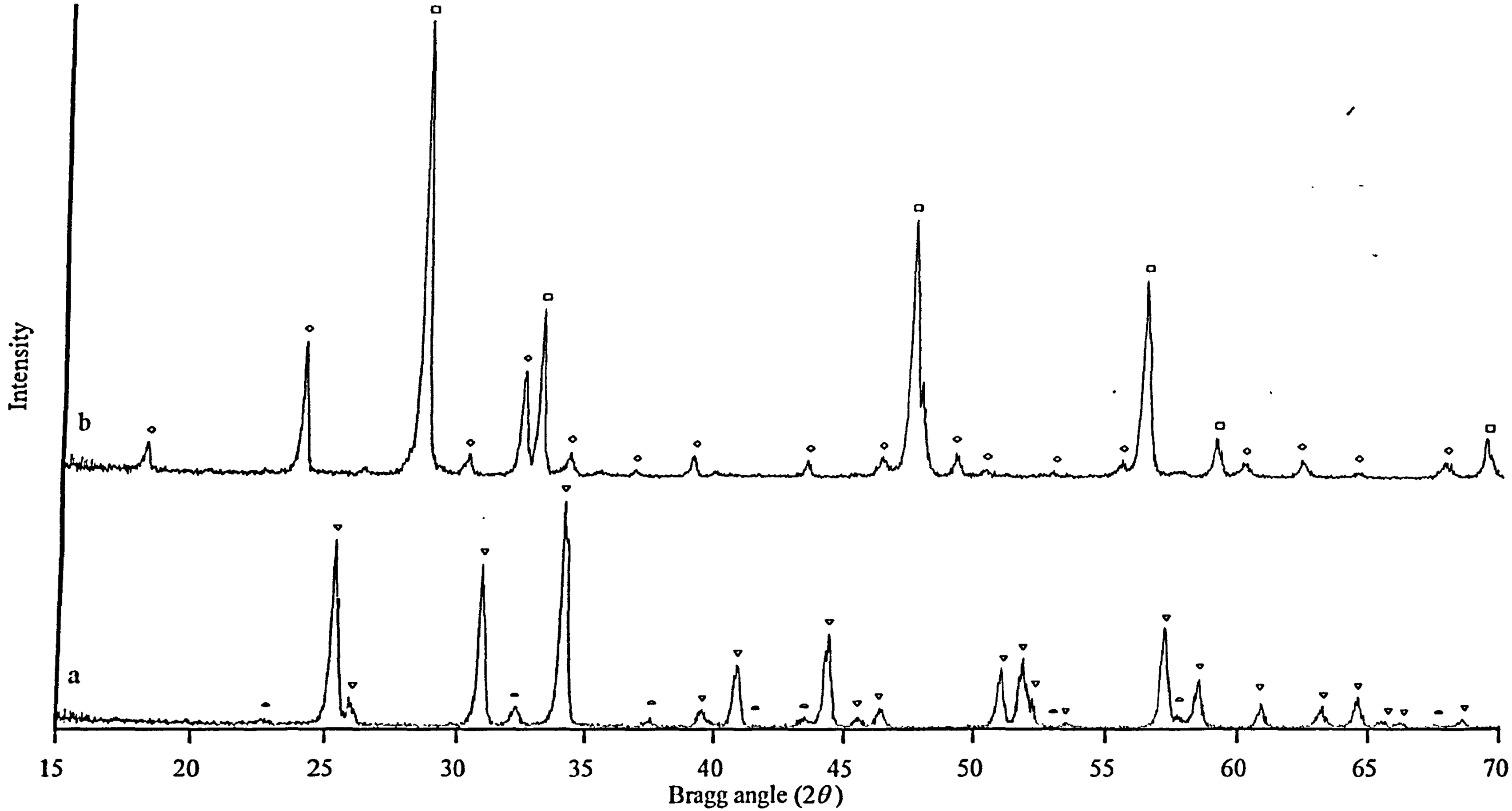

Figure 5.58 XRD patterns recorded for a mixture of vanadyl naphthenate 3% and cerium chloride treated at (a) 800/5/0/N_2, and (b) 800/5/80/N_2. □ labels the diffraction peaks due to CeO_2, ◇ labels the diffraction peaks due to $CeVO_4$, ▽ labels the diffraction peaks due to CeOCl, ▲ labels the diffraction peaks due to $CeVO_3$, and Δ labels the diffraction peaks due to an unknown component.

suggests that additional paramagnetic centres are present. In this context the less oxidising atmosphere may be relevant; this is an area for further investigation.

Calcination under a nitrogen atmosphere (Figure 5.58(a)) results in the formation of CeOCl (peaks labelled ∇), a cerium (III) compound, together with $CeVO_3$ (peaks labelled ▲, corresponding to JCPDS data base reference No. 31-0343), a vanadium (III) compound. The presence of $CeVO_3$ is significant in that the reduction of vanadium within the vanadyl naphthenate 3% system is identified. Reduction of vanadyl naphthenate 3% from vanadium (IV) to vanadium (III) was also observed on the surface of the silica and α-alumina support materials after treatment under these reaction conditions. The XRD pattern also shows evidence for a third crystalline phase (peaks labelled Δ), however, this phase could not be positively identified. The ^{51}V MAS NMR spectrum obtained for the calcined sample (Figure 5.57(c)) does not show the presence of any vanadium signals. This suggests that the vanadium is present in a series of compounds some of which may be paramagnetic.

Reaction of vanadyl naphthenate 3% with lanthanum nitrate and lanthanum oxide

These reactions were complex producing at least five crystalline compounds (a portion of which could not be identified) depending on conditions. In both cases lanthanum oxide (La_2O_3) was a predominant phase in the XRD patterns and $LaVO_4$ was formed in conditions which favoured the oxidation of vanadium (IV) to vanadium (V) (treatment under air and steam treatment under nitrogen). The ^{51}V MAS NMR spectra were complex and could not be interpreted in a straightforward manner. It can be noted that for comparable treatments the product distributions were similar, this was reflected in both the XRD and ^{51}V MAS NMR spectra. These reactions will not be discussed further here.

Summary and further discussion

Table 5.18 summarises the compounds identified when $LaCl_3$ and $CeCl_3$ are reacted with vanadyl naphthenate 3% under differing experimental conditions.

RE containing reactants	Treatment conditions			
	800/5/0/AIR	800/5/80/AIR	800/5/0/N_2	800/5/80/N_2
$LaCl_3$	LaOCl $LaVO_4$	LaOCl $LaVO_4$	LaOCl	LaOCl $LaVO_4$
$CeCl_3$	CeO_2 $CeVO_4$	CeO_2 $CeVO_4$	CeOCl $CeVO_3$	CeO_2 $CeVO_4$

Table 5.18 A summary of the compounds identified, after differing treatments, when $LaCl_3$ and $CeCl_3$ are reacted with vanadyl naphthenate 3%.

One immediate feature of the results is the formation of $REVO_4$ compounds for reaction conditions that favour the oxidation of vanadium (IV) to vanadium (V) (800/5/0/AIR, 800/5/80/AIR, and 800/5/80/N_2). For the reactions which involved calcination under a nitrogen atmosphere, no vanadium-containing compounds could be identified for the $LaCl_3$ reaction and, $CeVO_3$ was confirmed to be present for the reaction of $CeCl_3$. In addition to these identified phases it can also be recalled that, for the reactions involving $LaCl_3$, steam treatment also resulted in a second vanadium-containing compound (Table 5.17) and a number of unassigned diffraction peaks remained in the pattern recorded for the samples calcined under nitrogen (Figure 5.55(a)). For the reaction involving $CeCl_3$ steam treatment resulted in the formation of $CeVO_4$ alone, however, calcination under a nitrogen atmosphere did result in one compound which could not be identified (Figure 5.58(a)).

The similarity in the product distributions observed after reaction at 800/5/0/AIR, 800/5/80/AIR, and 800/5/80/N_2 strongly suggests that the oxygen associated with the steaming regime plays a significant role in determining the product distribution. Indeed, for the $LaCl_3$ and $CeCl_3$ reactions, under a nitrogen atmosphere, the only source of extra oxygen is that from steam. For reactions where no external oxygen is available (800/5/0/N_2) no vanadium species could be identified for the vanadyl naphthenate 3% and $LaCl_3$ reaction, and vanadium was found in the form of $CeVO_3$ for the reaction of vanadyl naphthenate 3% and $CeCl_3$. In the latter case vanadium has been reduced from a +4 oxidation state to +3 oxidation state.

5.5.3 Reaction of Vanadyl Phthalocyanine with Lanthanum Trichloride

Treatment of vanadyl phthalocyanine with lanthanum trichloride using air as a carrier gas resulted in a similar product distribution as for the corresponding experiment with vanadyl naphthenate 3%. That is, calcination (Figure 5.59(a)) resulted in the formation of $LaVO_4$ (peaks labelled ◆) and LaOCl (peaks labelled ■). Steam treatment resulted in the formation of $LaVO_4$ and LaOCl, together with an unidentified phase (peaks labelled ▲), which was the same as that observed from the steam treatment of $LaCl_3$ and vanadyl naphthenate 3% (Table 5.17). The ^{51}V MAS NMR spectra (Figure 5.60(a) and (b)) indicate the formation of $LaVO_4$, but a further resonance in the region of $\delta(^{51}V) = -570$ ppm was not observed.

Figure 5.61 (a), (b), and (c) shows the XRD patterns recorded for the samples treated under a nitrogen atmosphere: (a) is for the sample treated at 800/5/0/N_2 and (b) and (c) are both for treatment at 800/5/80/N_2. For the latter conditions two differently coloured phases were present within the sample holder (a black phase (b) and an off white phase (c)); these were easily separated.

Calcination under a nitrogen atmosphere (Figure 5.61(a)) resulted in the formation of LaOCl (peaks labelled ■). No other phases could be positively identified. The ^{51}V MAS NMR spectrum (Figure 5.60(c)) shows the presence of at least two vanadium signals. A relatively well resolved signal is observed at $\delta(^{51}V) = -365 \pm 17$ ppm, together with spinning sidebands, and a much broader signal centred between $\delta(^{51}V) = -100$ to -200 ppm. In both cases these signals are to high frequency of the chemical shift ranges expected for vanadates.[24] Further work is required to assign these resonances.

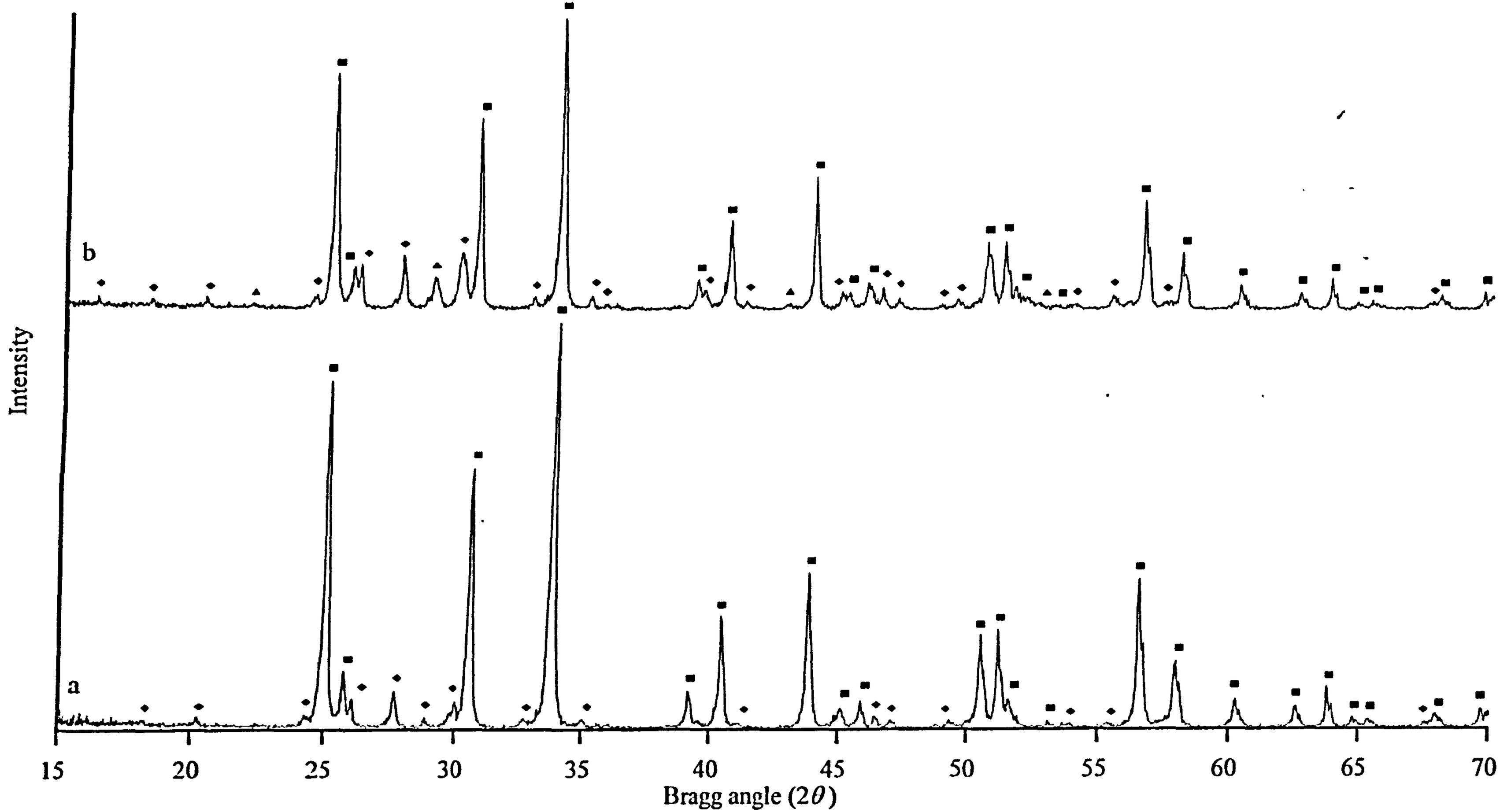

Figure 5.59 XRD patterns recorded for a mixture of vanadyl phthalocyanine and lanthanum trichloride treated at (a) 800/5/0/AIR, and (b) 800/5/80/AIR. ■ labels the diffraction peaks due to LaOCl, ◆ labels the diffraction peaks due to $LaVO_4$, and ▲ labels the diffraction peaks due to an unknown component.

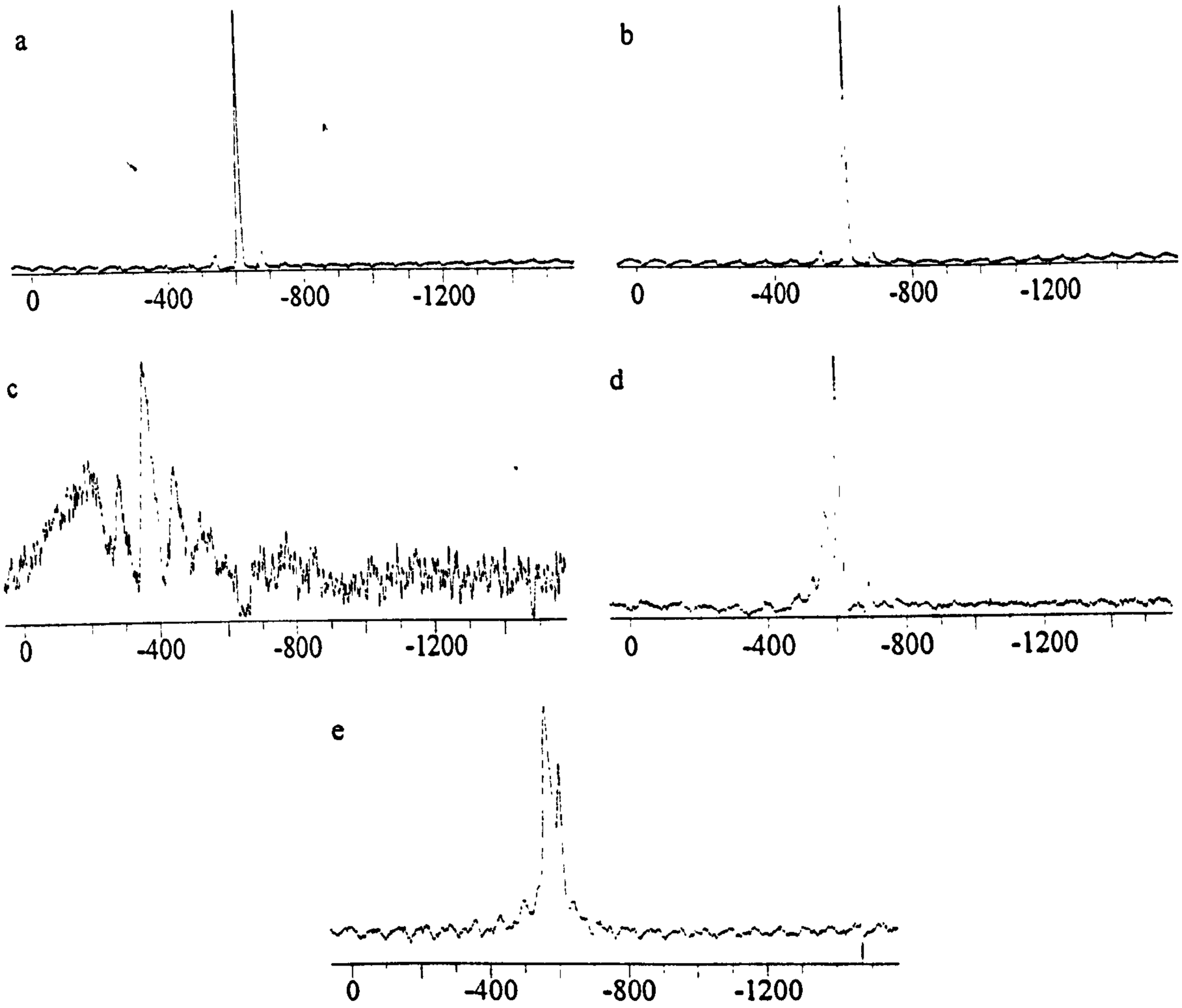

Figure 5.60 ^{51}V MAS NMR spectra observed at 105.075 MHz for a mixture of vanadyl phthalocyanine and lanthanum trichloride treated under differing conditions. Spectra recorded using a pulse delay = 1 s, pulse width = 2 μs, spinning frequency ~ 7.5 kHz and external reference liquid $VOCl_3$. Spectra (c), (d), and (e) were filtered through an exponential window prior to Fourier transformation. With the mixture treated at (a) 800/5/0/AIR, number of scans = 4241 and $\delta(^{51}V)$ = -611±4 ppm, (b) 800/5/80/AIR, number of scans = 9000, $\delta(^{51}V)$ = -611±4 ppm, (c) 800/5/0/N_2, number of scans = 12 122, $\delta(^{51}V)$ = -365±17 ppm, (d) 800/5/80/N_2, number of scans = 68 500, $\delta(^{51}V)$ = -570±20 ppm, $\delta(^{51}V)$ = -611±6 ppm, and (e) 800/5/80/N_2, number of scans = 10 000, $\delta(^{51}V)$ = -571±20 ppm, $\delta(^{51}V)$ = -611±9 ppm.

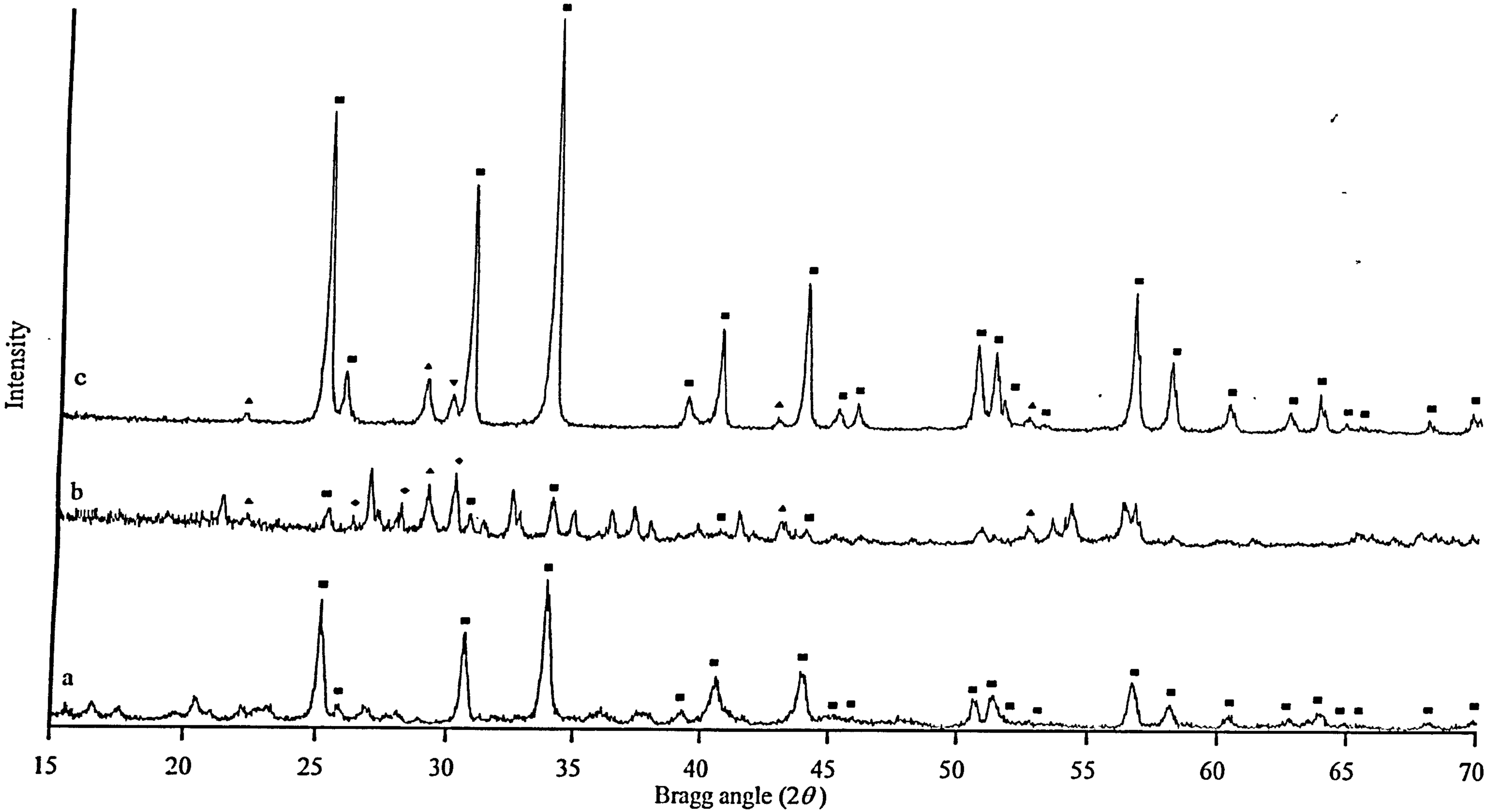

Figure 5.61 XRD patterns recorded for a mixture of vanadyl phthalocyanine and lanthanum trichloride treated at (a) 800/5/0/N_2, and (b) and (c) 800/5/80/N_2. ■ labels the diffraction peaks due to LaOCl, ◆ labels the diffraction peaks due to $LaVO_4$, and ▲ and ▼ label diffraction peaks due to unknown components.

As already indicated steam treatment under a nitrogen atmosphere gave rise to two easily separated phases. Considering first the black phase (Figure 5.61(b)), it can be seen that the diffraction peaks due to LaOCl (peaks labelled ■), $LaVO_4$ (peaks labelled ◆), and the same unidentified compound found in the corresponding vanadyl naphthenate 3% investigation (Table 5.17) (peaks labelled ▲) are observed. In addition there are several unlabelled peaks which could not be identified. It can be seen that the concentration of $LaVO_4$ with respect to the unidentified compound is relatively low; this is also reflected in the ^{51}V MAS NMR spectrum (Figure 5.60(d)) where the signal, centred at $\delta(^{51}V)$ = -570±20 ppm, has a greater intensity with respect to the signal for $LaVO_4$, centred at $\delta(^{51}V)$ = -611±6 ppm.

Considering the off-white phase (Figure 5.61(c)), it can be seen that the majority of this phase is found as LaOCl (peaks labelled ■). The ^{51}V MAS NMR spectrum recorded for this phase (Figure 5.60(e)) shows the presence of the same two vanadium signals ($\delta(^{51}V)$ = -571±20 ppm) and ($\delta(^{51}V)$ = -611±9 ppm) observed for the black phase. However the intensity distribution is markedly changed with considerably less $LaVO_4$ present: indeed the XRD pattern is unable to detect the presence of this compound. It might be expected that reaction of $LaCl_3$ with vanadyl phthalocyanine should give a similar product distribution to that from the reaction with $LaCl_3$ and vanadyl naphthenate 3%, particularly since the vanadium is found in a similar environment. This was found to be the case with the samples that were treated using air as a carrier gas (Table 5.18), the same holds for the sample calcined under a nitrogen atmosphere. Close inspection of the two XRD patterns (Figure 5.60(a) and Figure 5.55) shows that the two patterns are very similar, with the major phase being LaOCl (peaks labelled ■), and furthermore most of the unlabelled peaks found in these two patterns correspond well. As already discussed the major difference between the two reactions is found after treatment at $800/5/80/N_2$.

5.5.4 Reaction of Vanadium (V) Oxide with Lanthanum Trichloride

The main feature of this reaction was the formation of $LaVO_4$ under all reaction conditions. In this case the oxidation of vanadium is not a barrier to the formation of $LaVO_4$, even after calcination under a nitrogen atmosphere. Apart from this main feature this reaction proved

to be complex with the production of a number of phases, depending upon conditions, which were difficult to identify.

5.5.5 Summary

Overall the reactions between various RE- and vanadium-containing compounds have produced an array of differing reaction products. It has been seen that in conditions which favour the oxidation of vanadium (IV) to vanadium (V) then $REVO_4$ is the major vanadium species present, this was the case with all six different combination of reactants. The formation of other vanadium-containing phases was particularly favoured for the reactions involving $La(NO_3)_3$, La_2O_3, and V_2O_5. The unidentified vanadium phase in Table 5.17 (observed after reaction of $LaCl_3$ with vanadyl naphthenate 3% and vanadyl phthalocyanine) may be vanadium in a distorted tetrahedral environment.

References

1 J.W. Roelofsen, H. Mathies, R.L. de Groot, P.C.M. van Woerkom and H. Anga Gaur, *Stud. Surf. Sci. Catal.*, 1986, **28**, 337.

2 F. Maugé, P. Gallezot, J-C. Courcelle, P. Engelhard and J. Grosmangin, *Zeolites*, 1986, **6**, 261.

3 D.J. Rawlence, K. Gosling, L.H. Staal and A.P. Chapple, *Preparation of Catalysts V*, G. Pomcelet, P.A. Jacobs, P. Grange and B. Delmon, Ed., Elsevier, 1991, 407.

4 H. Klein, H. Fuess and M. Hunger, *J. Chem. Soc. Faraday Trans.*, 1995, **91**, 1813.

5 M.L. Occeli, *Catal. Rev.-Sci. Eng.*, 1991, **33**, 241.

6 P.J. Grobet, H. Geerts, M. Tielen, J.A. Martens and P.A. Jacobs, *Zeolites as Catalysts, Sorbents and Detergent Builders*, H.G. Karge and J. Weitkamp, Ed., 1989, Elsveir, 645.

7 G. Engelhardt and D. Michel, *High-Resolution Solid-State NMR of Silicates and Zeolites*, John Wiley and Sons, Chichester, 1987.

8 J-P. Gilson, G.C. Edwards, A.W. Peters, K. Rajagopalan, R.F. Wormsbecher, T.G. Roberie and M.P. Shatlock, *J. Chem. Soc., Chem. Commun.*, 1987, 91.

9 D. Freude, E. Brunner, H. Pfeifer, H.-G. Jerschkewitz, U. Lohse and G. Oehlmann, *Chem. Phys. Letters*, 1987, **139**, 325.

10 A. Samoson, E. Lippmaa, G. Engelhardt, U. Louse and H.-G. Jerschkewitz, *Chem. Phys. Letters*, 1987, **134**, 589.

11 R.D. Shannon, K.H. Gardner, R.H. Staley, G. Bergeret, P. Gallezot and A. Auroux, *J. Phys. Chem.*, 1985, **89**, 4778.

12 J. Klinowski, C.A. Fyfe and G.C. Gobbi, *J. Chem. Soc., Faraday Trans.*, 1985, **81**, 3003.

13 D. Freude, T. Fröhlich, M. Hunger, H. Pfeifer and G. Scheler, *Chem. Phys. Letters*, 1983, **98**, 263.

14 D. Freude, T. Fröhlich, H. Pfeifer and G. Scheler, *Zeolites*, 1983, **3**, 171.

15 J. Klinowski, J.M. Thomas, C.A. Fyfe and G.C. Gobbi, *Nature*, 1982, **296**, 533.

16 C.V. McDaniel and P.K. Maher, *Zeolite Chemistry and Catalysis*, ACS Monograph 171, J.A. Rabo, Ed., 1976, ACS, Washington, D.C., 285.

17 L. Bragg, G.F. Claringbull and W.H. Taylor, *Crystal Structures of Minerals*, G. Bell and Sons Ltd, 1965.

18 P. Gallezot, B. Feron, M. Bourgogne and Ph: Engelhard, *Zeolites: Facts, Figures, Future Part B*, P.A. Jacobs and R.V. van Santen, Ed., Elsevier, 1989, 1281.

19 M.L. Occeli and J.M. Stencel, *Zeolites as Catalysts, Sorbentsand Detergent Builders*, H.G. Kerge and J. Weitkamp, Ed., 1989, Elsvier, 127.

20 G.Y. Meng and R.A. Haggins, *Mat. Res. Bull.*, 1983, **18**, 581.

21 R.F. Wormsbecher, A.W. Peters and J.M. Maselli, *J. Catal.*, 1986, **100**, 130.

22 D.W. Breck and G.W. Skeels, *Molecular Sieves II*, ACS Symposium Series 40, J.R. Katzer, Ed., 1977, Washington, D.C., 271.

23 R. Pompe, S. Järås and N-G. Vannerberg, *Appl. Catal.*, 1984, **13**, 171.

24 O.B. Lapina, V.M. Mastikhin, A.A. Shubin, V.N. Krasilnikov and K.I. Zamaraev, *Prog. Nucl. Magn. Reson. Spectrosc.*, 1992, **224**, 457.

25 F. Maugé, J.C. Courrcelle, Ph. Engelhard, P. Gallezot and J. Grosmangin, *Proceedings 7th International Zeolite Conference*, Y. Murakami, A. Iijima and J.W. Ward, Ed., 1986, **28**, 803.

26 M.W. Anderson, M.L. Occelli and S.L. Suib, *J. Catal.*, 1989, **118**, 31.

27 H. Bremer, W. Mörke, R. Schödel and F. Vogt, *Moleculer Sieves*, Advan. Chem. Ser. 121, W.H. Meier and J.B. Uytterhoeven, Ed., 1973, ACS. Washington, D.C., 249.

28 J.V. Smith, J.M. Bennet and E.M. Flanigen, *Nature*, 1967, **215**, 241.

29 B.W. Wojciechowski and A. Corma, *Catalytic Cracking Catalysts, Chemistry and Kinetics*, 1986, Marcel Dekker Inc., New York.

30 R. Kumar, **U.S. Patent No. 5, 194, 413**, 1993.

31 M.W. Anderson, M.L. Occelli and S.L. Suib, *J. Catal.*, 1990, **122**, 374.

32 N.N. Greenwood and A. Earnshaw, *Chemistry of the Elements*, Pergamon Press, Oxford, 1984.

33 A.F. Wells, *Structural Inorganic Chemistry*, (3rd edn), Oxford University Press, 1962.

34 H. Megaw, *Crystal Structures: A Working Approach*, W.B. Saunders Company, Philadelphia, London, Toronto, 1973.

35 R.C. Ropp, *J. Electrochem. Soc.*, 1968, **9**, 155.

36 R.W.G. Wyckoff, *Crystal Structures*, Interscience Publishers, Second Edition, Volume 2, 1964.

37 R.C. Ropp and B. Carrol, *J. Amer. Ceram. Soc.*, 1980, **63**, 416.

38 R.A. Shkrabina, N.A. Koryabkina, V.A. Ushakov, M. Lausberg, E.M. Moroz and Z.R. Ismagilov, *Kinetics and Catalysis*, 1996, **37**, 109.

39 V.A. Ushakov, O.A. Kirichenko, R.A. Shkrabina, N.A. Koryabkina, M. Lausberg, E.M. Moroz and Z.R. Ismagilov, *Kinetics and Catalysis*, 1996, **37**, 130.

40 L. Wachowski, P. Kirszensztejn and R. Lopatka, *Cat. Lett.*, 1995, **32**, 123.

41 J.S. Church, N.W. Cant and D.L. Trimm, *App. Cat. A: Gen.*, 1993, **101**, 105.

42 L.P. Haack, C.R. Peters, J.E. deVries and K. Otto, *App. Cat. A: Gen.*, 1992, **87**, 103.

43 L.P. Haack, J.E. deVries, K. Otto and M.S. Chattha, *App. Cat. A: Gen.*, 1992, **82**, 199.

44 I.I.M. Tijburg, J.W. Geus and H.W. Zandbergen, *J. Mater. Sci.*, 1991, **26**, 6479.

45 R. Pankajavalli and O.M. Sreedharan, *Materials Lett.*, 1995, **24**, 247.

46 Y. Kimishima, M. Takahashi, K. Okada, H. Ishikawa and Y. Ichiyanagi, *J. Magnetism and Magnetic Materials*, 1995, **140-144**, 1185.

47 J. Kikuchi, H. Yasuoka, Y. Kokubo and Y. Ueda, *J. Physical Soc. Japan*, 1994, **63(10)**, 3577.

48 G. Ranga Rao and D.D. Sarma, *Mod. Phys. Lett. B*, 1990, **4(4)**, 277.

49 B.C. Tofeild and W.R. Scott, *J. Solid State chem.*, 1974, **10**, 183.

50 M. Mortimer, E.A. Moore and C. Wigglesworth, unpublished work.

51 E.A. Moore, M. Mortimer and C. Wigglesworth, unpublished work.

52 A. Nayeen and J.P. Yesinowski, *J. Chem. Phys.*, 1988, **89**, 4600.

Chapter 6

Conclusions

6 Summary and Overall Conclusions

The overall aim of the work has been to gain a better understanding of the chemistry of zeolite-Y in the presence of vanadium and, in particular, to investigate the loss of zeolite-Y crystallinity in the presence of this metal.

Initial studies focussed on a series of three commercial FCC type catalysts (Section 5.1) that only differed in the levels of REs ion-exchanged into the zeolite-Y (Table 5.1). The investigations clearly showed that steam treatment, with and without the presence of vanadium, resulted in changes to the levels of crystalline zeolite-Y present; changes to the unit cell constant for the zeolite-Y were also observed. The observed changes in surface area and unit cell constant for the steam-treated and untreated catalysts are given in Table 5.2. The magnitudes of the observed changes are closely linked to a number of factors, namely the specific RE ion-exchange level within the zeolite-Y lattice, the level of vanadium contamination and the reaction temperature.

With regard to the levels of crystalline zeolite-Y remaining after given treatment conditions, investigations into the behaviour of commercial FCC type catalysts (Section 5.1), under simulated conditions, showed in general that (i) increasing the RE ion-exchange level within the zeolite-Y lattice increases the resistance of the zeolite-Y to destruction by hydrothermal treatment (Figures 5.2(a), (c) and (e) and 5.4), (ii) increasing the vanadium loading on the catalyst results in increased loss of zeolite-Y crystallinity (Figures 5.3(a), (c) and (e) and 5.5), and (iii) increasing the temperature results in increased destruction to the zeolite-Y lattice (Figures 5.2(a), (c) and (e), 5.3(a), (c) and (e), and 5.6). In terms of the observed changes to the unit cell constant after treatment, it was found that (i) increasing the RE ion-exchange level increases the observed unit cell constant (Figure 5.2(b), (d), and (f)), (ii) increasing the vanadium loading results in a decrease in the unit cell constant (Figure 5.3(b), (d), and (f)), and (iii) increasing the reaction temperature has the effect of further reducing the unit cell constant (Figure 5.2(b), (d), and (f) and 5.3(b), (d), and (f)).

Against the background of the studies of the commercial catalysts detailed investigations were then carried out for zeolite-Y by itself as a model system. This had important advantages. In particular, it was possible to greatly increase the levels of vanadium to which the zeolite-Y could be exposed whilst still maintaining the loading at realistic levels in commercial terms. In turn, this allowed the use of ^{51}V MAS NMR as a powerful characterisation technique. Similarly ^{27}Al MAS NMR became more informative since only contributions from the aluminium associated with the zeolite-Y were observed; with commercial FCC catalysts other forms of non zeolitic aluminium (matrix/clay, particle binder) are present all of which would contribute to, and hence complicate, the ^{27}Al MAS NMR spectrum.

A series of five zeolite-Y samples were prepared with a range of lanthanum ion-exchange levels from 0 to 8.6 mass% lanthanum. Initially, the same general investigations as those performed on the commercial FCC samples were carried out. The surface area measurements and unit cell constant data for these steam-treated samples are given in Table 5.5. The changes in surface area (zeolite-Y crystallinity) and unit cell constant mirror the behaviour observed for the commercial FCC catalysts. This can be confirmed from Figures 5.10 to 5.17. This result is important in its own right since it confirms the validity of using zeolite-Y by itself as an effective model for the study of vanadium/FCC chemistry. It can be noted that the general type of behaviour observed for both the commercial FCC and the model zeolite-Y samples was found to be typical of that reported by other workers in the field.[1-10] Detailed comparisons were not always possible, however, because of variations in composition of the samples used.

A relatively large range of lanthanum ion-exchange levels was investigated for the model zeolite-Y system and, as a consequence, it was possible to observe that the increase in zeolite-Y stability conferred by increasing the RE ion-exchange level was not linear in this region (Figure 5.11(a) and (c)). It was found that there was a large increase in relative stability as the lanthanum ion-exchange level was increased from 0 to *c.a.*3 mass% lanthanum whilst at higher levels the effect was markedly less pronounced. This behaviour was observed for samples steam treated at both reaction temperatures, and both with and without the presence of vanadium.

A range of experiments was carried out for the model zeolite-Y samples which involved changing treatment conditions other than just that of temperature (Section 5.2.2). The results from experiments where the carrier gas was changed from air to nitrogen are of particular interest and are given in Table 5.8. It is important to note that the zeolite-Y samples treated under nitrogen and with respect to (i) increasing RE ion-exchange, (ii) increasing vanadium loading, and (iii) increasing reaction temperature, behave in a similar manner to comparable samples steam treated with air as a carrier gas. In more detail there is, increasing zeolite-Y stability with increases in RE ion-exchange level, and decreasing zeolite-Y stability with increases in the vanadium loading and reaction temperature. Returning to specific results when the carrier gas was nitrogen it was found that, at the higher reaction temperature (800°C), similar levels of crystalline zeolite-Y remained after steam treatment under both air and nitrogen atmospheres. However, at the lower reaction temperature (750°C), and in the presence of vanadium, it was found that significantly larger amounts of crystalline zeolite-Y remained after steam treatment under a nitrogen atmosphere than under an air atmosphere. In the absence of vanadium similar levels of crystalline zeolite-Y remained after treatments under both atmospheres (Figure 5.20). Changing from an air to a nitrogen atmosphere removes a source of oxygen from the system. Clearly at the lower reaction temperature, and in the presence of vanadium, external oxygen plays an important role in the interaction of vanadium with the zeolite-Y lattice. At the higher reaction temperature, the role of external oxygen appears to be less critical.

The model zeolite-Y samples (2.6LaH-Y) were also subjected to a series of experiments where the steam to carrier gas ratio was changed from the standard value of 80 % steam (Section 5.2.2). The carrier gas was air and separate experiments were carried out with vanadium loadings of 5000 and 10 000 ppm vanadium at a reaction temperature of 800°C (Table 5.6 and Figures 5.18 and 5.19). At the lower of the vanadium loadings it was found that increasing the steaming ratio resulted in a steady decrease in surface area (zeolite-Y crystallinity) until a value of 80 % steam was reached. In the region of this steam to carrier gas ratio a relatively large decrease in surface area was observed. For the samples treated in the presence of 10 000 ppm vanadium it was found that a marked change in surface area

occurred at a much lower steam to carrier gas ratio, that is below 40 % steam. These results indicate that for any given vanadium loading there is a steam to gas ratio above which enhanced damage to the zeolite-Y lattice occurs.

The experimental results outlined above provide new information on the behaviour of zeolite-Y under an array of different treatment conditions. These include the level of RE ion-exchanged into the zeolite-Y lattice, the vanadium loading to which the catalyst is exposed, the treatment temperature, the percentage steam used during treatments, and the atmosphere that the treatments are carried out under. At one level the results can be used to suggest optimum conditions for enhancing the useful life time of the zeolite-Y component of a commercial FCC catalyst: (i) the RE ion-exchange level should be sufficiently high to provide the zeolite-Y with protection form thermal and hydrothermal treatments, the results indicate that this should be at least *c.a.* 3 mass% RE, (ii) the vanadium loading must be maintained at minimal levels, (iii) the treatment temperature should be as low as is acceptable, (iv) the steam to carrier gas ratio should be as low as possible, and (v) the treatment atmosphere should be as oxygen free as possible. Although these suggestions would go some way to prolonging the life time of the zeolite-Y they do not take into account the harsh realities of a modern working FCCU. For example, it must not be forgotten that during the cracking reaction the catalyst particles become coated with carbonaceous material (coke). These deposits prevent contact between the catalyst particle and fresh reactants. To overcome this problem the catalyst particles are transferred to the regenerator part of the FCCU for removal of 'carbon' surface deposits and this is achieved by hydrothermal treatments at elevated temperatures and under an oxidising atmosphere. Clearly the percentage steam, the treatment temperature, and percentage oxygen in the atmosphere are all critical factors during the removal of coke, and reductions in these factors lessens the ability of the regenerator to remove coke form the surface of the catalyst. A catalyst particle which cannot contact fresh reactants is equally as ineffective as a catalyst particle with reduced levels of crystalline zeolite-Y. Similarly with regard to reducing vanadium loadings to which the catalyst particles are exposed, this can be achieved with prudent selection of crude oil sources, however, high quality crudes are the most expensive, and their price will inevitably increase with time. Vanadium loadings are

controlled by the removal of spent catalyst and replacement with fresh catalyst. Again this is an expensive procedure and cost limits the amount of spent catalyst which can be removed, and hence the average vanadium loading on the catalyst particles. Ideally what is required is a catalyst particle which can withstand both the harsh conditions of an FCCU and the presence of vanadium. In order to achieve this a full understanding of the mechanism by which vanadium reacts destructively with the zeolite-Y catalyst is required.

A key step in the more detailed analysis of the model zeolite-Y result was to make the basic assumption that the amount of destruction caused to the zeolite-Y lattice by hydrothermal treatment and that caused by the presence of vanadium, were essentially independent of one another. Surface area measurements provided a quantitative means of exploring the consequences of this assumption. Specifically, if the difference in surface area between a sample loaded with vanadium and the same sample with no vanadium present is taken, then this provides a measure of the change in surface area due to the presence of vanadium alone. For example, Figure 5.21 provides results for steam-treated model zeolite-Y samples with 5000 ppm vanadium contamination. One immediate result of this approach is that it is observed that a given vanadium level causes a greater decrease in surface area at the higher reaction temperature. This may reflect the increased physical mobility of vanadium at higher temperatures, but an enhanced chemical reactivity of vanadium cannot be ruled out. Another interesting result of the analysis is that there is an overall trend to increased destruction to the zeolite-Y lattice as the RE ion-exchange level is increased. This was interpreted to indicate that a RE-vanadium compound, or at least the formation of such a compound, may be responsible for the destruction caused to the zeolite-Y lattice. In simple terms if RE ions are removed from the zeolite-Y lattice then the influence that these RE ions have on the stability of the zeolite-Y lattice is also removed. It can be recalled that lanthanum bridging complexes are thought to give lanthanum ion-exchanged zeolite-Y samples added thermal stability[11] (Section 2.1.1, Figure 2.7).

To summarise a possible mechanism for vanadium-induced destruction to the zeolite-Y lattice involves the migration of vanadium from the surface of the catalyst to the RE ions present within the zeolite-Y lattice, a reaction takes place and the RE ions are removed

from the zeolite-Y lattice in the form of a RE-vanadium compound. As a consequence the zeolite-Y becomes thermally and hydrothermally less stable and more susceptible to thermal collapse. This mechanism has features in common with suggestions put forward by other workers.[1,9,12,13]

The presence of a RE-vanadium compound has been confirmed on three differently steam treated samples. Figures 5.22 and 5.23 show ^{51}V MAS NMR spectra for the three samples and all spectra confirm the presence of $LaVO_4$. If the formation of $LaVO_4$ (in more general terms $REVO_4$) is intrinsically involved in the mechanism of the collapse of the zeolite-Y lattice then the conditions that result in relatively large effects must also be those favourable to the formation of $LaVO_4$.

It has been shown that zeolite-Y crystallinity reduces with increasing temperature, reduces with increasing steam to carrier gas ratio, and at 750°C a nitrogen atmosphere has beneficial effects towards the retention of zeolite-Y crystallinity. In the absence of detailed information (in the open literature) regarding the chemistry and properties of $LaVO_4$ a series of experiments were designed to explore how RE and vanadium compounds would react under similar treatment conditions. Experiments were performed in the presence of α-alumina (Section 5.4.2), in the presence of silica (Section 5.4.3), and a series of solid state reactions were considered between a variety of different RE and vanadium containing compounds (Section 5.5).

Considering the reactions that were performed in the presence of α-alumina, it can be recalled that the α-alumina support material was loaded with different combinations of lanthanum (11.0 mass% lanthanum, from lanthanum trichloride) and vanadium (1 mass% vanadium, from vanadyl naphthenate 3%) prior to reaction (Section 4.3). Treatment in the presence of lanthanum and vanadium resulted, in all cases, in the formation of $LaVO_4$. However, it must be noted that the formation of $LaVO_4$ did not account for 100% of the deposited vanadium. The formation of $LaVO_3$ was also observed, and there was evidence which suggested that some vanadium may be present in a form invisible to both XRD and ^{51}V MAS NMR. Details of the phases identified are given in Table 5.14. Both calcination and steam treatment under an air atmosphere, at both reaction temperatures (750°C and

800°C), resulted in similar levels of $LaVO_4$ being formed (Figures 5.39 and 5.40). Interesting differences were observed when the samples were calcined and steam treated under a nitrogen atmosphere. Under a nitrogen atmosphere the levels of $LaVO_4$ were reduced when compared to those for treatment under air. However, it was evident that steam treatment under nitrogen resulted in greater quantities of $LaVO_4$ than calcination (Figures 5.41 and 5.42). As with the samples treated under air, an increase in temperature had no major effects on the levels of $LaVO_4$ present. It can be noted that when the α-alumina, loaded with vanadium only, was treated no vanadium compounds could be identified.

For the silica support materials, loaded with both lanthanum (9.5 mass% lanthanum, from lanthanum trichloride) and vanadium (1 mass% vanadium, from vanadyl naphthenate 3%), treatment under an air atmosphere resulted in similar levels of $LaVO_4$ being present after calcination and steam treatment, and at both reaction temperatures (Figures 5.45 and 5.46). This behaviour was also observed for the α-alumina support materials but it can be noted that smaller quantities of $LaVO_4$ were found on the silica support materials. Similarly there was evidence that not all of the vanadium was present as $LaVO_4$. Treatment under a nitrogen atmosphere again resulted in the formation of $LaVO_4$, although, an increase in temperature resulted in reduced amounts of $LaVO_4$ being formed. Again no vanadium compounds could be identified after treatment in the presence of only vanadium.

Details of the combinations of reactants used for the unsupported lanthanum/vanadium reactions can be found in Table 4.7, the reactions included calcination and steam treatment under both air and nitrogen atmospheres at 800°C only. In conditions which favoured the oxidation of vanadium from the +4 to +5 oxidation state (800/5/0/AIR, 800/5/80/AIR, and 800/5/80/N_2) then the presence of $LaVO_4$ was observed; reduced levels of $LaVO_4$ were found after treatment under nitrogen. As with the support material samples there was evidence that $LaVO_4$ did not account for 100% of the vanadium present. For reactions carried out at 800/5/0/N_2 the formation of $LaVO_4$ was not noted except for the reaction of vanadium (V) oxide with lanthanum trichloride, for this reaction vanadium is found in a +5 oxidation state prior to reaction. Reactions were the RE ion was changed to cerium resulted in the formation of $CeVO_4$.

The experiments summarised above provide a good deal of information about the chemistry of RE and vanadium under reaction conditions. One overriding feature of all of the results was the formation of $REVO_4$, except under specific conditions for reactions not involving support materials. The formation of $REVO_4$ requires the oxidation of vanadium from the +4 to +5 oxidation state, and since vanadium is deposited as VO^{2+} then the formation of $REVO_4$ also requires three additional oxygen atoms per molecule of $REVO_4$. It seems clear that one source of this oxygen must derive from the support materials: this is particularly apparent for the conditions: $750/5/0/N_2$ and $800/5/0/N_2$. Furthermore, since greater quantities of $REVO_4$ were observed on the α-alumina support material than on the silica support material, this suggests that the oxygen associated with the former is more accessible.

Another source of oxygen derives from steam under hydrothermal conditions. For example, in the absence of support material $REVO_4$ is formed after the treatment $800/5/80/N_2$. It should be re-emphasised that the oxygen associated with steam is also important in the formation of $REVO_4$ in the presence of support materials, for example it was found for either support material that under a nitrogen atmosphere, steam treatment resulted in relative greater quantities of $REVO_4$ being formed.

Returning to the zeolite-Y system, it is important to discuss in more detail the proposal that the formation of $REVO_4$ is responsible for reducing zeolite-Y crystallinity. There are three important factors which must be considered for treatments in the presence of vanadium: (i) an increase in the steam to carrier gas ratio causes increased destruction to the zeolite-Y lattice, (ii) an increase in temperature has the same effect, and (iii) moving to a nitrogen atmosphere results in retention of crystalline zeolite-Y (at least at 750°C).

Considering points (i) and (ii), it might be expected that an increase in temperature or the steam to carrier gas ratio would result in larger amounts of $REVO_4$ being formed. This was not found to be the case, either for treatment in air with both the supported series of reactions, or for the general solid state RE/vanadium investigations. However, the observed reductions in crystalline zeolite-Y with increasing temperature and steam to carrier gas ratio may be related to the formation of greater quantities of $REVO_4$ as a

response to the increased mobility of vanadium. An important factor to remember with the zeolite-Y samples is the fact that the RE component is found, in the main, within the lattice of the zeolite-Y and not on the surface as was with the samples based on support materials. For the zeolite-Y based samples for RE and vanadium to combine they must first contact one another and so diffusion factors may play an important role. Clearly an increase in temperature would increase vanadium mobility, but what of an increase in the steam to carrier gas ratio? Wormsbecher and co-workers[7] have demonstrated the importance of steam with regard to the transport of vanadium through a commercial FCC type catalyst. They showed that vanadium is initially found on the surface of an FCC particle and this remained the case even after calcination at 760°C. However, steam treatment of an equivalent sample resulted in an even distribution of vanadium throughout the FCC particle, thus demonstrating the importance of steam to the mobility of vanadium which is initially deposited upon the surface of the catalyst. It seems reasonable, therefore, to assume that increasing the steam to carrier gas ratio would also increase the mobility of the vanadium. Increasing the ease with which vanadium can contact RE within the zeolite-Y lattice would also increase the removal of RE from the lattice and hence increased destruction to the zeolite-Y lattice would be the end result.

To summarise, with the support-based materials an increase in the reaction temperature of 50°C has little effect upon the levels of $REVO_4$ observed and may reflect that in the temperature range 750-800°C maximum levels of $REVO_4$ are reached, similarly with changes to greater steam to carrier gas ratios. With the zeolite-Y system, where diffusion factors play a more critical role, an increase in the reaction temperature and steam to carrier gas ratio may have a more significant effect due to an increase in the ease with which vanadium can contact the RE component, thus, in this case increased levels of $REVO_4$ would be anticipated. To some extent this is verified by ^{51}V MAS NMR spectroscopy cf. Figure 5.22, but this is an area which requires further investigation.

With regard to the fact that under a nitrogen atmosphere, and at 750°C, greater quantities of crystalline zeolite-Y remain than after similar treatments under air then the results from the RE/vanadium investigations are consistent with the assumption that this is due to reduced levels of $REVO_4$ being formed. For each of the three different sets of samples reduced

levels of $REVO_4$ were recorded under a nitrogen atmosphere when the results were compared to those performed under air.

To summarise a mechanism has been put forward to account for the fact that increased destruction of the zeolite-Y lattice is observed after treatment in the presence of vanadium. That is, the vanadium, initially deposited upon the surface of the catalyst, migrates to the RE component of the catalyst and reacts to form $REVO_4$. The removal of RE (RE bridging complexes) from the zeolite-Y lattice renders that portion of the zeolite-Y thermally and hydrothermally unstable. The observation of $LaVO_4$ upon three differently treated model zeolite-Y samples and the results from investigations into the chemistry of RE with vanadium support this proposed mechanism.

As was stated earlier, the formation of $REVO_4$ compounds have formed the basis for mechanisms put forward by other workers,[1,9,12,13] However, it is also the case that this type of mechanism for the vanadium-induced destruction of zeolite-Y has been questioned by other workers. Wormsbecher and co-workers[7] suggested that the formation of $REVO_4$ compounds was only a by-product of a different reaction and their formation was not critical to the mechanism of attack. As a simple test for this proposal a commercial FCC sample was completely destroyed by thermal treatments (Section 5.4.4). XRD analysis of the destroyed FCC sample confirmed that no crystalline zeolite-Y remained and the amorphous material had recrystallised into silica and mullite (Figure 5.35). This sample was contaminated with vanadium (1 mass% vanadium, from vanadyl naphthenate 3%) and steam treated under differing conditions. The ^{51}V MAS NMR spectrum (Figure 5.49), recorded for the sample steam treated at 800/5/80/AIR, showed the presence of several vanadium environments. The majority of the vanadium was found in a V_2O_5 phase, the remaining vanadium environments could not be positively identified. No evidence for the formation of $LaVO_4$ or $CeVO_4$ was found. This result by itself does not provide definitive proof that the formation of $REVO_4$ compounds is critical in the mechanism by which vanadium causes loss of zeolite-Y crystallinity, however, it does show that REs are present in a form (or forms) which are inaccessible to vanadium in a thermally destroyed catalyst.

Having observed that destruction to the zeolite-Y lattice, in the presece of vanadium, is related to the RE ion-exchange level a series of experiments were designed to prevent reaction of vanadium with the zeolite-Y lattice by the use of a secondary source of REs (Section 5.3). A commercial catalyst, alpha-56, was selected for the experiments. The catalyst had RE ions deposited upon the surface of the catalyst prior to vanadium loading and steam treatment. An unexpected feature of the experiments was the loss of zeolite-Y crystallinity caused by the steam treatment of the sample in the presence of REs alone. It was noted that cerium ions caused greater damage to the zeolite-Y lattice than lanthanum ions. However, it was found that the reaction of vanadium with the zeolite-Y lattice could be controlled in the presence of surface REs, furthermore, treatment under a nitrogen atmosphere provided additional protection to the zeolite-Y lattice, at both reaction temperatures. Clearly if REs are to be used commercially as a method of controlling the vanadium/zeolite-Y reaction then the loss of zeolite-Y crystallinity due to the presence of surface REs must be overcome. This may be a function of the methods used for the introduction of REs to the surface of the catalyst or the sources of RE ions used, this is an area which would benefit from further investigation.

Finally, to summarise a range of different experiments have been carried out with a view to gaining a greater understanding of the vanadium/zeolite-Y system. The results indicate that the levels of REs ion-exchanged into the zeolite-Y lattice are related to the amount of destruction caused to the zeolite-Y by the presence of vanadium. It is proposed that vanadium migrates to the RE component of the zeolite-Y lattice, where the REs (RE bridging complexes) are removed by the formation of $REVO_4$. Removal of RE bridging complexes from the zeolite-Y lattice causes a reduction in thermal and hydrothermal stability of that portion of the zeolite-Y and this results in loss of crystallinity.

References

1 M.L. Occeli, *Catal. Rev.-Sci. Eng.*, 1991, **33**, 241.

2 P.J. Grobet, H. Geerts, M. Tielen, J.A. Martens and P.A. Jacobs, *Zeolites as Catalysts, Sorbents and Detergent Builders*, H.G. Karge and J. Weitkamp, Ed., 1989, Elsveir, 645.

3 P. Gallezot, B. Feron, M. Bourgogne and Ph. Engelhard, *Zeolites: Facts, Figures, Future Part B*, P.A. Jacobs and R.V. van Santen, Ed., Elsevier, 1989, 1281.

4 J-P. Gilson, G.C. Edwards, A.W. Peters, K. Rajagopalan, R.F. Wormsbecher, T.G. Roberie and M.P. Shatlock, *J. Chem. Soc., Chem. Commun.*, 1987, 91.

5 D. Freude, E. Brunner, H. Pfeifer, H.-G. Jerschkewitz, U. Lohse and G. Oehlmann, *Chem. Phys. Letters*, 1987, **139**, 325.

6 A. Samoson, E. Lippmaa, G. Engelhardt, U. Louse and H.-G. Jerschkewitz, *Chem. Phys. Letters*, 1987, **134**, 589.

7 R.F. Wormsbecher, A.W. Peters and J.M. Maselli, *J. Catal.*, 1986, **100**, 130.

8 J. Klinowski, C.A. Fyfe and G.C. Gobbi, *J. Chem. Soc., Faraday Trans.*, 1985, **81**, 3003.

9 R. Pompe, S. Järås and N-G. Vannerberg, *Appl. Catal.*, 1984, **13**, 171.

10 J. Klinowski, J.M. Thomas, C.A. Fyfe and G.C. Gobbi, *Nature*, 1982, **296**, 533.

11 F. Maugé, P. Gallezot, J-C. Courcelle, P. Engelhard and J. Grosmangin, *Zeolites*, 1986, **6**, 261.

12 M.W. Anderson, M.L. Occelli and S.L. Suib, *J. Catal.*, 1989, **118**, 31.

13 F. Maugé, J.C. Courrcelle, Ph. Engelhard, P. Gallezot and J. Grosmangin, *Proceedings 7th International Zeolite Conference*, Y. Murakami, A. Iijima and J.W. Ward, Ed., 1986, **28**, 803.